THESIS APPROVAL

GRADUATE SCHOOL, KASETSART UNIVERSITY

Doctor of Engineering (Mechanical Engineering)

DEGREE

Mechanical Engineering — **FIELD**

Mechanical Engineering — **DEPARTMENT**

TITLE: Investigation of 3D Structure of Turbulent Spot using Liquid Crystals

NAME: Mr. Weerachai Chaiworapuek

THIS THESIS HAS BEEN ACCEPTED BY

-- **THESIS ADVISOR**

(Associate Professor Chawalit Kittichaikarn, D.Phil.)

-- **DEPARTMENT HEAD**

(Associate Professor Chawalit Kittichaikarn, D.Phil.)

APPROVED BY THE GRADUATE SCHOOL ON --

-- **DEAN**

(Associate Professor Gunjana Theeragool, D.Agr.)

THESIS

INVESTIGATION OF 3D STRUCTURE OF TURBULENT SPOT USING LIQUID CRYSTALS

WEERACHAI CHAIWORAPUEK

A Thesis Submitted in Partial Fulfillment of
the Requirements for the Degree of
Doctor of Engineering (Mechanical Engineering)
Graduate School, Kasetsart University
2014

Weerachai Chaiworapuek 2014: Investigation of 3D Structure of Turbulent Spot using Liquid Crystals. Doctor of Engineering (Mechanical Engineering), Major Field: Mechanical Engineering, Department of Mechanical Engineering. Thesis Advisor: Associate Professor Chawalit Kittichaikarn, D.Phil. 177 pages.

This study focuses on a flow visualization of an artificially generated turbulent spot, bypassed under boundary layer transition over flat plate. The experiment was carried out in a low free stream turbulence water tunnel using three visualization techniques, consisting of coating liquid crystals for temperature measurement on surface, slurry liquid crystal for temperature detection in fluid, and milk solution to visualize the structure of turbulent spot. From these techniques, a full mechanism in growth development and heat transfer was well described. Not only the spot celerities of laminar-turbulent interface, but also spreading half angle were informed and compared to those reported by the other researchers. The contour of temperature on the footprint and within the fluid structure as well as heat transfer coefficient, and heat flux were provided instantaneously. The representative structure of turbulent spot was proposed to reveal the average characteristics of turbulent spot. Moreover, the turbulent spot manner under the influence of various adverse pressure gradients was also observed. Therefore, these qualitative and quantitative results may lead to the better understanding in growth and heat transfer mechanism of the turbulent spot and they are helpful for the development of an accurately predictive formula for full evolution of the bypassed transition flow.

____________________ Student's signature

____________________ Thesis Advisor's signature

___ / ___ / ___

ACKNOWLEDGEMENTS

I would like to gratefully thank Assoc. Prof. Dr. Chawalit Kittichaikarn may thesis advisor for advice, help and valuable guidance throughout this study. I would sincerely like to thank Assoc. Prof. Dr. Pongwit Siribodhi, Asst. Prof. Dr. Vejapong Juttijudata, Dr. Chinnapat Thipyopas, Assoc. Prof. Dr. Metta Chareonpanich, Asst. Prof. Duangrudee Chaysuwan and Asst. Prof. Amornrat Lertworasirikul for valuable suggestions and kindly providing the tools for using in this research. Also, I would like to thank K. Umnart Khuntayabhorn for all technical supports.

This research was supported by Kasetsart University Research and Development Institute – KURDI.

Special thanks to my friends, K. 'Ton' Ayudh Mapairote Paleebut, Golf' Suttaya Nongnoi, 'Yossy' Methee Duangsoythong, P' Oatzy, Vorayos Ratanamart, 'Bo' Chayanee Tippayasam, 'Men'Sakol Kongkaew, N' Arch, Jay, Tarn, Tong, Karn etc. for their suggestions and supports.

Finally, I especially wish to express my gratitude to my family, Kitti, Sanga, Noppanan Chaiworapuek as well as 'Butter' Tawika Thareesan and her family who always give me love, patience and support during all my graduate study.

Weerachai Chaiworapuek
May 2014

TABLE OF CONTENTS

LIST OF TABLES

LIST OF FIGURES

LIST OF FIGURES (Continued)

Figure **Page**

LIST OF FIGURES (Continued)

Figure **Page**

LIST OF FIGURES (Continued)

Figure **Page**

LIST OF FIGURES (Continued)

LIST OF FIGURES (Continued)

Figure **Page**

LIST OF FIGURES (Continued)

LIST OF FIGURES (Continued)

LIST OF FIGURES (Continued)

LIST OF ABBREVIATIONS

A	=	Area
APG	=	Adverse pressure gradient
B	=	Blue color signal
C	=	Turbulent spot celerity
C_{BC}	=	Turbulent spot celerity at becalmed region
C_{LE}	=	Turbulent spot celerity at leading edge
C_{TE}	=	Turbulent spot celerity at trailing edge
C_p	=	Specific heat capacity
DNS	=	Direct Numerical Simulation
$\dot{E}_g$	=	Energy source
$\dot{E}_{in}$	=	Energy inflow
$\dot{E}_{st}$	=	Energy storage
f	=	Fluid property
f_L	=	Fluid property in Laminar flow
f_T	=	Fluid property in Turbulent flow
G	=	Green color signal
g	=	number of spots
H	=	Hue signal
HSI	=	Hue, Saturation, Intensity color space
h_x	=	Local heat transfer coefficient
I	=	Intensity signal
K	=	Acceleration parameter
k	=	Thermal conductivity
LP	=	Low pressure
MAPG	=	Mild adverse pressure gradient
Nu_x	=	Local Nusselts number
PIV	=	Particle Image Vocimetry technique
Pr	=	Prandtl number
q	=	Rate of heat transfer
$\dot{q}$	=	Heat flux

LIST OF ABBREVIATIONS (Continued)

$\dot{q}_{avg}$	=	Averaged heat flux
$\dot{q}_l$	=	Heat flux of laminar flow
$\dot{q}_t$	=	Heat flux of turbulent flow
R	=	Red color signal
RGB	=	Red, Green, and Blue color space
Re	=	Reynolds number
$Re_{\theta t}$	=	Reynolds number based on momentum thickness at transition
Re_{x0}	=	Reynolds number at the pivot
S	=	Saturation signal
SAPG	=	Strong adverse pressure gradient
T	=	Temperature
T_s	=	Surface temperature
T_α	=	Free stream temperature
TLCs	=	Thermochromic Liquid Crystals
Tu	=	Free stream turbulence intensity
t	=	Time
U_α	=	Free stream velocity
U_0	=	Free stream velocity at the pivot
V	=	Controlled volume
x	=	Streamwise distance
x_0	=	Streamwise distance from leading edge to the pivot
y	=	Heightwise distance
y_h	=	Height at the hump
ZPG	=	Zero pressure gradient
z	=	Spanwise distance

LIST OF ABBREVIATIONS (Continued)

ξ	=	Conical similarity co-ordinate, x
ξ_0	=	Length of unheated starting section
η	=	Conical similarity co-ordinate, y
ρ	=	Density
Δ	=	Difference
σ	=	Dimensionless propagation rate
β	=	Elevated angle of the roof
γ	=	Intermittency
υ	=	Kinematic viscosity
θ	=	Momentum thickness of laminar boundary layer
θ_0	=	Momentum thickness of laminar boundary layer at the pivot
λ_θ	=	Pressure gradient parameter
α	=	Spreading half angle
δ	=	Thickness of boundary layer
δ_L	=	Thickness of laminar boundary layer
δ_T	=	Thickness of turbulent boundary layer

INVESTIGATION OF 3D STRUCTURE OF TURBULENT SPOT USING LIQUID CRYSTALS

INTRODUCTION

Chaotic level of the flow over flat plate basically depends on Reynolds number - Re. It begins from Laminar and ends up at fully Turbulent. Transition is between them when Reynolds number rises beyond its critical value at 500,000. Under boundary layer transition, burst of turbulence or intermittent spots occur. It has been found that numerical models of both Laminar and Turbulent flow are much developed and capable to apply into many engineering subjects effectively. Conversely, the accuracy of transitional flow in mathematical prediction is still much to be improved so far. The difficulty is primarily due to its high unsteadiness. These result in unsuitable design for machines or systems, involving the transition. Not only components in gas turbine, including compressors, combustion chamber, low and high pressure turbines, but also any other multi-stage turbo machines, this flow directly relates to.

In low pressure - LP turbine, worldwide used, Re has been found around 50,000 in small jet – 500,000 for the largest turbofans, following Hodson and Howell (2005). Because of this range of Reynolds number that appears on the LP blades, boundary layer transition plays an important role significantly on suction side. Curtis *et al*. (1997) reported that this side of the turbine blade generated 60% of the losses of efficiency in these blades. The loss profile is strongly up to the process of boundary layer on these blades, following Jahanmiri (2011). At very low Re, laminar separation occurs on the blade surface and reattachment before trailing tip is not possible. The highest loss is obtained because the airfoil completely separates as shown in Fig. 1. For higher Re, laminar separation ahead of transition is possible. If the separation bubble appears, it will be short and the flow becomes turbulent state after reattachment. Loss is much lower than the previous case in this condition. The lowest in this loss profile is found in the case of fully attached flow with transition. Under this condition, turbulent separation disappears and bypassed transition occurs on the downstream surface.

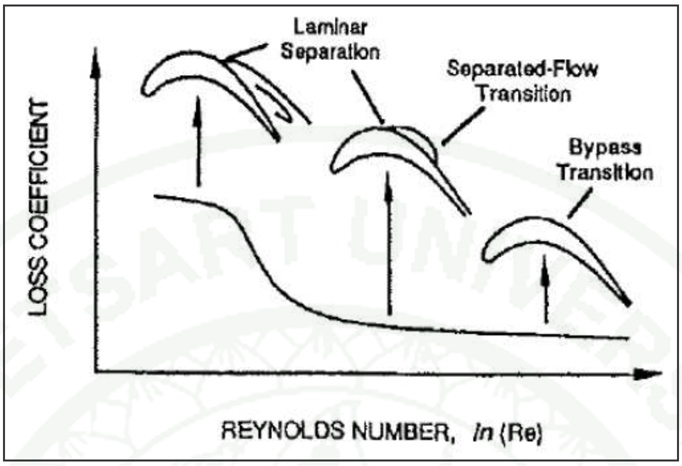

Figure 1 Loss profile of transition on the low pressure turbine at various Reynolds Number.

Source: Jahanmiri (2011)

When turbulent intensity of the freestream flow, for instance in LP turbine, is high enough, Tollmien-Schlichting waves break down and turbulent spot is formed within instabilized boundary layer transition. This spot is found as small turbulent patch, surrounding by laminar flow. The fully turbulent flow is also obtained by merging turbulent spots. Turbulent spot is the mostly significant phenomenon in the boundary layer when the first stage of natural transition is bypassed. With its unsteady fluctuating flow and heat transfer manner, turbulent spot performs as the most complicate part of the boundary layer transition. The improved understanding in its behavior will greatly impact on the development of numerical prediction. Precise calculation is still needed by the turbine designer to break the recent limit of efficiency improvement.

The present study focuses on the investigation of three dimensional structure of artificially generated turbulent spot when it propagates downstream under bypassed boundary layer transition. All experiments were performed in low turbulent water tunnel, set up in Computational Mechanic laboratory – CML at department of Mechanical Engineering, Kasetsart University, to enable three visualization techniques in order to construct the whole structure of turbulent spot. The first technique is the use of coating Thermochromic Liquid Crystals – TLCs, to reveal the structure of thermal footprint of turbulent spot. In the current study, an analytical solution, derived from "Implicit" finite difference approach mutually with method of heat balance for convective heat transfer coefficient and heat flux is firstly proposed. Thus, with this high performance tools, not only the shape of unsteady turbulent spot that are detected in space and time, but also its heat transfer characteristics.

The second technique is carried out by using milk solution as dye to capture shape of turbulent spot body. With its high reflective property, the shape of turbulent spot can be clearly visualized. It is similar to the last technique except the type of dye, changing from milk to slurry TLCs. The technique of applying TLCs as dilute suspension in water can accurately provide both temperature information and fluid tracing even in near wall region, reported by Chaiworapuek and Kittichaikarn (2011). In this technique, spatial distribution of temperature within turbulent spot body will be achieved.

Furthermore, the influence of adverse pressure gradient on turbulent spot is also investigated since it has been known that it affects on retracting of streamwise length of transition zone. Also, representative structures of turbulent spot footprint are proposed so the probable shape is identified and the behavior of the specified substructures are directly comparable. Turbulent spot information, including spot celerities, and half spreading angle will be determined and compare with those reported by the other researchers. Thus, these results could be informed as qualitative and quantitative data into numerical formulas for the flow under boundary layer transition.

OBJECTIVES

1. To visualize a three dimensional structure of turbulent spot. Also, to study the properties of turbulent spot that is a key part of transitional flow.

2. To study the effect of adverse pressure gradient on the onset of artificially generated turbulent spot. These will reveal a controlling mechanism of the size and length of the transitional flow.

3. To apply the temperature measurement technique using slurry liquid crystals into bypassed boundary layer transition.

LITERATURE REVIEW

1. Discovery of turbulent spot

It has been known that the concept of boundary layer transition was firstly introduced over hundred years ago. The transition locates between laminar and turbulent regimes. Typically, due to the complexity and randomness of transitional region, the flow is considered as fully turbulent when it goes beyond laminar zone or the critical Reynolds number. Consequently, the advance predictive formula, used in many engineering applications, is inaccurate because of the absence of the transition. However, in order to obtain the effective numerical formula, insight details of the transitional flow should be properly achieved.

The most important phenomenon within boundary layer transition is found as turbulent spot. It is a turbulent patch, outstandingly presenting the unique flow and heat transfer characteristics. Turbulent spot was firstly reported by Emmons (1961) on basis of visual observation on a water table. He concluded that it was randomly generated and grew uniformly downstream. Emmons also showed that turbulent spot could be directly produced by releasing a water droplet to strike the target surface. His theory relied on four assumptions that were 1. turbulent spot was from point-like breakdown, 2. there was a sharp boundary between the turbulent fluid of a spot and the surrounding laminar flow, 3. it grew with uniform rate, 4. there was no interaction between spots. Hence, boundary layer transition takes place via the formation of these turbulent spots, surrounding by the laminar flow. A fully turbulent boundary layer is formed by merging of these turbulent spots when they propagate downstream. Intermittency term – γ is established to indicate the state of the laminar-turbulent transition. It is a fraction of time during which the flow is turbulent at any particular location. The flow is completely laminar at $\gamma = 0$. Conversely, if $\gamma = 1$, the flow is fully turbulent. So, the state of transition flow is described between 0 to 1. Emmons proposed a linear combination of the flow properties of the boundary layer during transition as

$$f = (1- \gamma)f_L + (\gamma)f_T \tag{1}$$

where the subscripts L and T denote the laminar and fully turbulent state, respectively and f denotes the fluid property.

2. The modes of transition

Generally, boundary layer transition can appear differently, depending on its mechanism. Each of them, classified as "mode", provides a different flow manner, which is very important on the fundamental of fluid mechanics. Four modes of transition are reviewed as the following sections under this topic.

2.1 Natural transition

Natural transition on flat plate normally occurs within a low free stream turbulence flow under suitable level of pressure gradient to avoid the separation. It typically involves in the flow over blade surface of turbo machine. This mode of transition can be simply described as depicted in Fig. 2, after White (1974). This figure shows a full mechanism of laminar-turbulent transition process on the flat plate. The main stages of transition are reviewed as the following paragraph.

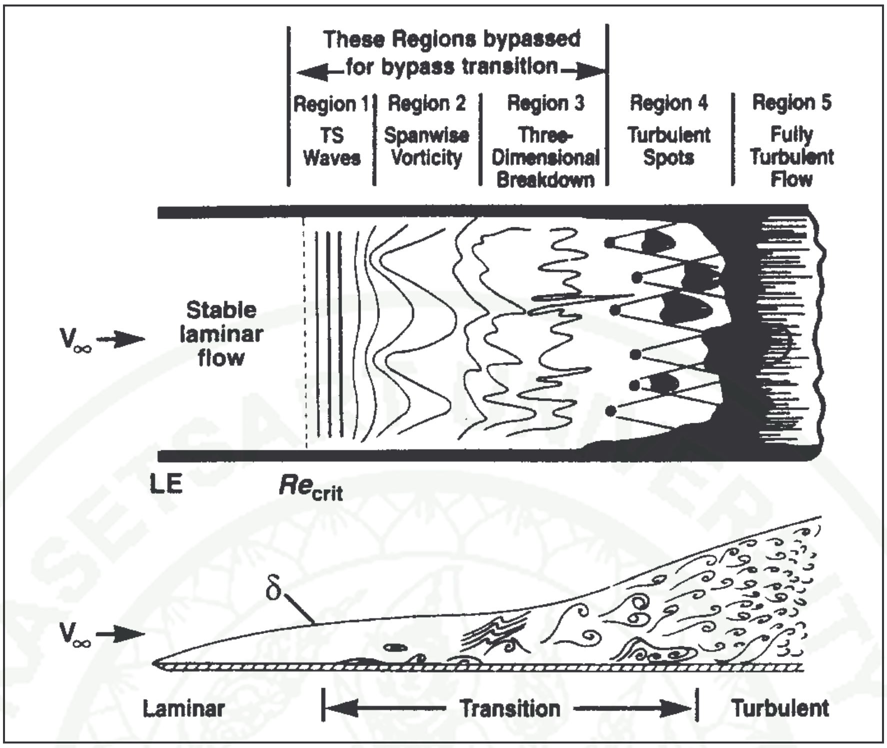

Figure 2 Mechanism of natural transition.

Source: White (1974).

In the first region, as the flow develops beyond the critical Reynolds number, the thickness of laminar boundary layer has grown to the point of where a small disturbance is able to amplify. These disturbances amplify at the near linear rate and the fluctuation motion is largely growing until Tollmein-Schlichting waves are formed. These waves are two dimensional instability waves that propagate downstream at a speed approximately 0.3 – 0.35 of the free stream velocity and with a wavelength several times the boundary layer thickness.

The second stage of natural transition is dominated by a spanwise distortion of the Tollmein-Schlichting waves. They occurred as unstable, laminar, three-dimensional waves and vortices. In this region, three dimensional disturbances grow and the flow reaches a stage where spanwise variations in velocity appear. These were also observed by Klebanoff *et al*. (1962) from their vibrating-ribbon experiment. In region 3, these distortions continue growing in an increasing three dimensional and non linear characteristic. Then, it results in the formation of streamwise vorticity and the generation of hairpin vortices or Λ-eddies. This breakdown zone is narrow, following Dhawan and Narasimha (1958) because the growth rate of the velocity fluctuation is rapid in the previous zone. By visual study, there is no noticeable alteration in the growth rate of one spot due to the presence of another.

In the fourth stage, further high frequency instability appears near the head of the vortex loops, and these disturbances break down to form turbulent spots. They may occur over an area of the plate, not a specific single location. In the other words, this occurs as part, turbulent region among the laminar flow. The turbulent spots, randomly generating from different locations, linearly grow and eventually merge to the others. This stage is clearly visualized by Wu and Durbin (2000), Wallace *et al*. (2010), and Wu and Moin (2010). The details of merging process are also investigated by Elder (1960). However, by measurement of hotwire series, Makita and Nishizawa (2001) indicate that there is an appearance of unique velocity profile in the merging region. This forms the strong spanwise vortices as the head of larger horseshoe vortices at the upper merged region.

The horseshoe or hairpin vortices, generated by the vortical interaction in the merging region are measured to grow higher and start to have stronger structure than those in the non interacting spots. The merging process of all occurring turbulent spot completely forms a fully turbulent boundary layer as shown in region 5. In addition, it is observable in the contribution of Makita and Nishizawa (2001) that the strengthened internal vertical structures in a merged turbulent spot and the turbulent bulge in the fully developed turbulent boundary layer have good similarities in the configurations and coincidence in scales. This interaction of turbulent spots may initiate the turbulent bulges and some longitudinal vortices in the downstream fully developed turbulent boundary layer.

2.2 Bypassed transition.

The first three regions of boundary layer transition can be completely bypassed if the flow is subjected to strong disturbances, either by sufficient amplitude external disturbance or the presence of high free stream turbulence. Under the described conditions, bypassed transition, mainly focusing on the formation of turbulent spot, is formed between laminar and turbulent region. This process outstandingly decreases the length of unstable laminar boundary layer. This mode of transition is usually presented inside gas turbine and involves earlier stage of the flow over the blade surface.

2.3 Separated flow transition

Comparing to the others, this mode is more crucial to low pressure turbine and compressor design. When the flow is influenced by adverse pressure gradient, the separation of a laminar boundary layer may occur. If the level of the pressure gradient is not too strong, the reattachment may appear behind the separating point. This results the closed region of recirculating flow, called "separation bubble", following Roberts (1980). Generally, the flow separated at the detaching point with highly unstable condition, leading to transition as depicted in Fig. 3 where x_s, x_t, x_T and x_r denote point of separation, transition onset, transition completion, and reattachment, respectively.

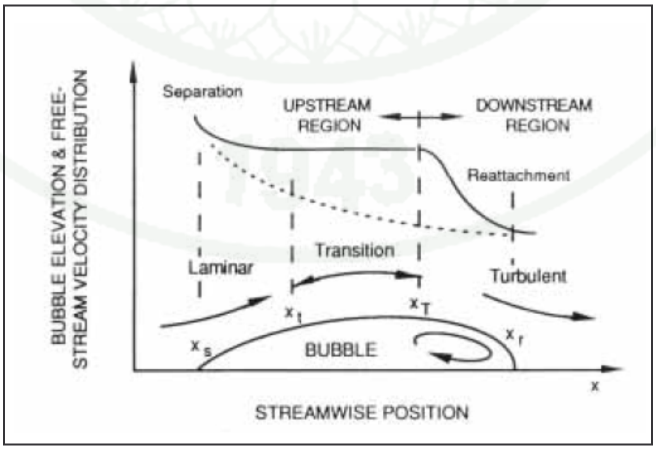

Figure 3 Mechanism of separated flow transition.

Source: Roberts (1980)

2.4 Reverse transition

Reverse transition or relaminarization, particularly important for the gas turbine designer, often occurs in turbomachinery components. It usually takes place on the pressure side near the trailing edge and may occur on the suction side near the leading edge under sufficiently strong acceleration gradients. This mode performs when the skin friction reduces to level of laminar boundary layer. An acceleration parameter is the most commonly accepted parameter used to indicate relaminarization. A fully turbulent equilibrium boundary layer will relaminarize in flows with the acceleration parameter, equal to or greater than about $3 – 3.5 \times 10^{-6}$. By the manner of this mode, a laminar boundary layer, subjected to a sufficiently strong acceleration will remain laminar and not undergo transition to turbulent. The relaminarization is not an instantaneous process so immediately after this mode performs, re-transition occurs.

3. Fundamental of turbulent spot.

3.1 Primary structure of turbulent spot.

After the discovery by Emmons, turbulent spot has been continuously further investigated using many measurement and visualization techniques. Emmons's theory that transition existed via the passage of turbulent spot was firstly confirmed by Schubauer and Klebanoff (1955). Hotwire anemometer was employed to detect the signals of the propagating spot, generating from electrical sparking. Their results showed that turbulent section of turbulent spot started suddenly in velocity and ended with a slow exponential-like fall as depicted in Fig. 4. They found that turbulent spot has an arrowhead shape and propagated down stream with velocity of 0.88 and 0.5 of free stream velocity at leading and trailing edge, respectively. In the mean time, it spread at the half angle - α of 11.3°. Its overhang, appearing at the most downstream, convected at the free stream velocity while its hump, found at the most top was high with distance like a fully developed turbulent boundary layer. Moreover, Schubauer and Klebanoff also discovered an important phenomenon, stable state region like laminar flow, following the passage of turbulence. While the layer was in this state, it was highly stable and no breakdown was likely to appear. This was termed "The recovery trail" or "Becalmed region". This region was expressed as exponential-like, following the fluctuating signals as depicted in Fig. 4.

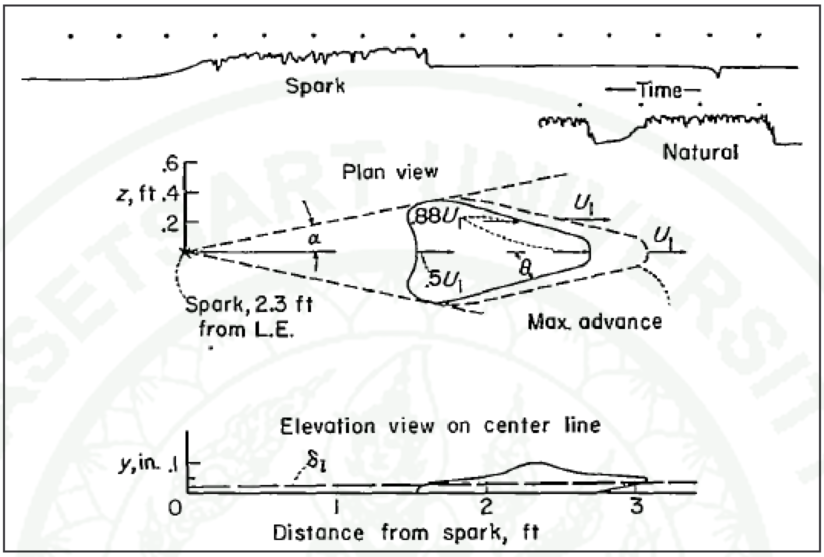

Figure 4 Turbulent spot mechanism.

Source: Schubauer and Klebanoff (1955)

The general features of turbulent spot, reported by Schubauer and Klebanoff were further confirmed by the results, obtained by Elder (1960). The image of turbulent spot was visualized dye sheet, released at the upstream of flat plate. Inside the spot body, a portion of the fluctuating motion is periodic and regular as shown in Fig. 5. The principal of this motion occurred very similar to the horseshoe or hairpin vortices, generally found under turbulent boundary layer. This is clearly supported by the calculation of Wallace *et al*. (2010). Behind this zone, the fluid returned to laminar state and they described the striation in this region that it was caused by the dye, rapidly extended in the flow direction by the high shear near the plate.

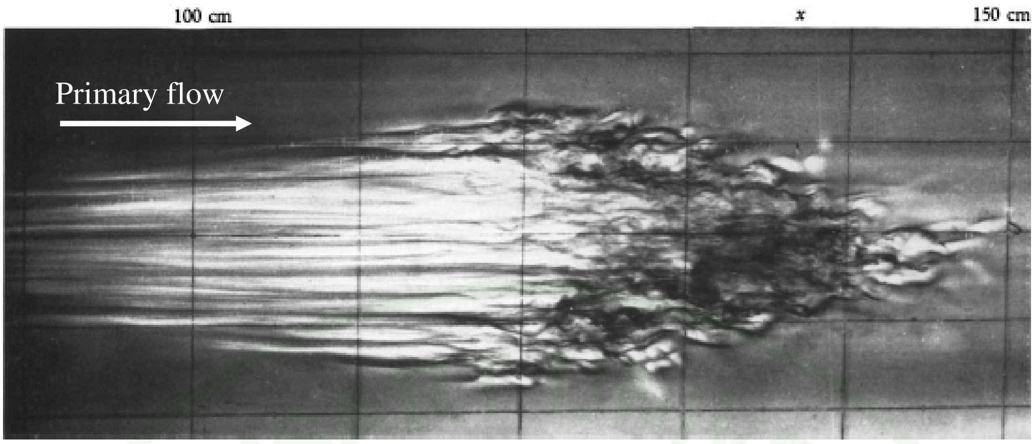

Figure 5 Turbulent spot structure visualized.

Source: Elder (1960)

The shape of turbulent spot structure, reported by Elder was consistent to those obtained later by the other researchers that also employed the dye method. The highlight art work on the spot was carried out by Cantwell *et al*. (1978) who dispersed the aluminum flakes with the dye. With changing in reflective property of the suspension, their fabulous image was obtained as shown in Fig. 6. Also, the turbulent structure, visualized using a boundary layer smoke tunnel by Perry *et al*. (1981), was published as illustrated in Fig. 7. They described that turbulent spot has five very important features, namely (1) the folds, occurring from the vortex flow, (2) the staggered arrangement of these folds, (3) the long tapered tails which trail behind the spot, (4) an appearance of “loop-like” structures after a sufficient development and (5) the characteristic heart-like shape of the spot. Besides, a novel visualization technique that utilized fluorescent dye, excited by a sheet of laser light was employed by Gad-El-Hak *et al*. (1981). This dye was applied due to its specialty that was visible only when subjected by a strong light source of the appropriate wavelength. These results not only presented the flow field on both plan and side views as shown in Fig. 8, but also an entrainment mechanism that made turbulent spot grew downstream. They categorized the different dynamic regions of a spot as depicted in Fig. 9.

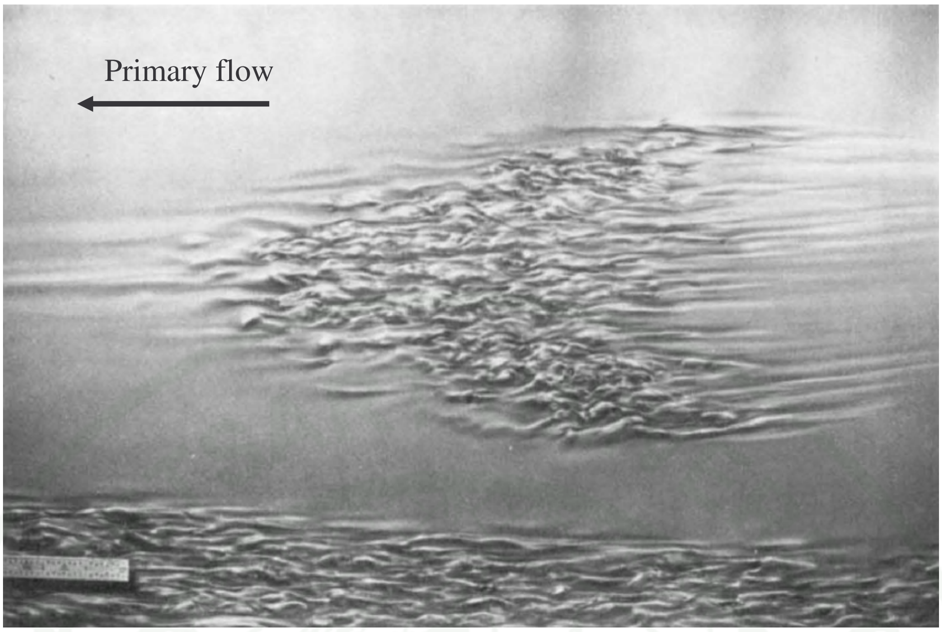

Figure 6 Turbulent spot structure.

Source: Cantwell *et al*. (1978)

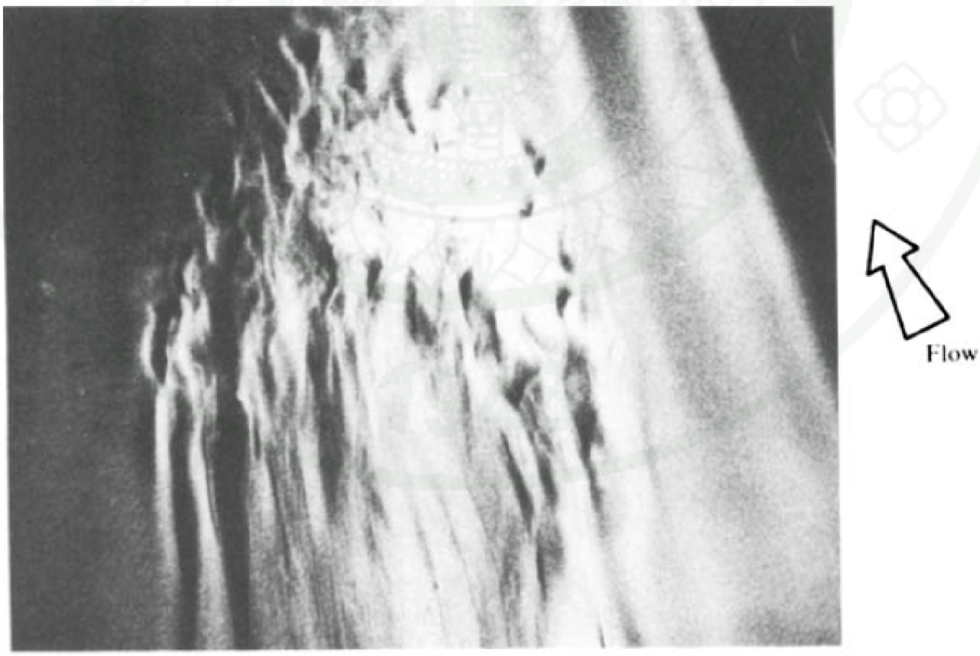

Figure 7 Heart like shape of turbulent spot.

Source: Perry *et al*. (1981)

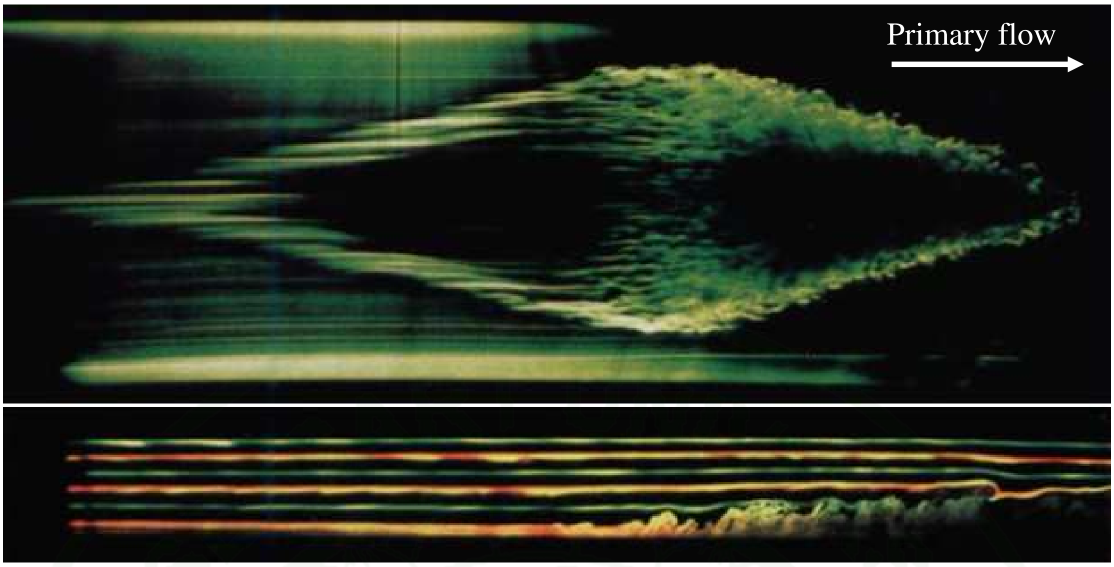

Figure 8 Turbulent spot structure obtained by fluorescence dye.

Source: Gad-El-Hak *et al*. (1981)

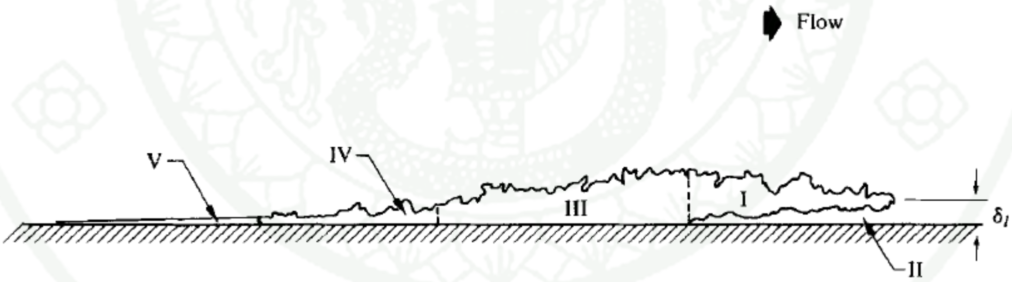

Figure 9 Dynamic regions of turbulent spot.

Source: Gad-El-Hak *et al*. (1981)

In Fig. 9, region I is overhang head, a result of turbulent fluid being swept over the laminar boundary layer. The height of overhang tip corresponds initially to the thickness of laminar boundary layer and later slightly lower at mature stage, following Wygnanski *et al*. (1976) who presented velocity profile inside the spot using hotwire anemometer. Furthermore, Wygnanski *et al*. (1976) also reported that the hump of turbulent spot, found in this region, has a height that corresponded to the thickness of a hypothetical turbulent boundary layer originating at the spark with initial thickness equal to that of the laminar boundary layer at that location. Gad-El-Hak *et al*. (1981) mentioned that this region occurred fairly passive, in agreement with those reported by Cantwell *et al*. (1978) However, the dominant vortex was invisible in their visualizations, which is contrast to the measurement by Chong and Zhong (2006). Fig. 10 presents the contour of vertical velocity, revealing that there is a great single vortex at the upper portion of turbulent spot.

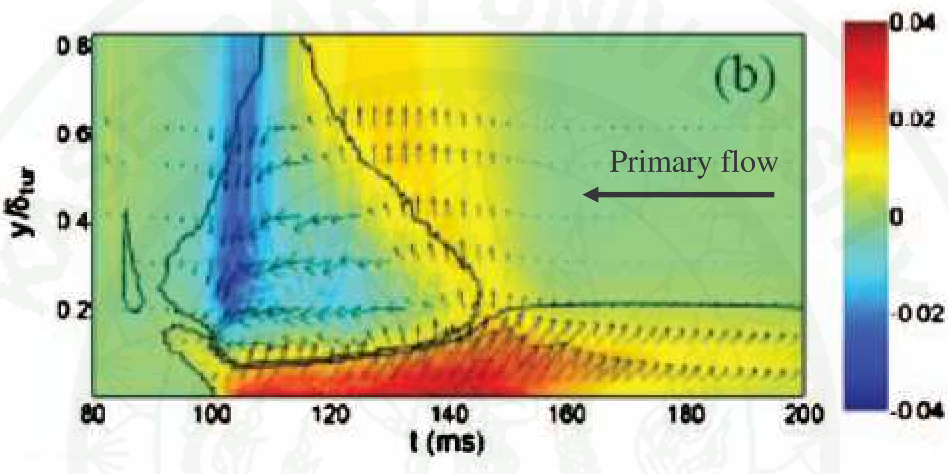

Figure 10 Contour of vertical velocity perturbation.

Source: Chong and Zhong (2006)

Region II in Fig. 9 is directly below region I. This region is a part of laminar boundary layer, not breaking down until the spot body rides over. It is found that a typical turbulence intensity level here is around 10 – 12%, following Chong and Zhong (2006). Also, new fluid is added through here via "gulping" entrainment process, following Cantwell *et al*. (1978). Another process of entrainment, called "nibbling" is found in region III. This region is dynamically very similar to a classical turbulent boundary layer over flat plate. It has a typical intensity level of 7 – 9%. From the figure, it is found that both processes of entrainment are directly connected to this region. Region IV is in the lower part of a turbulent boundary layer-like flow. This region is among turbulent, laminar, and the external potential flow. It is also a part of nibbling process above itself. This produces the growth of the spot in the rear. Finally, region V refers the calmed region, following the spot. Dye streaks in this region aligned with the streamline direction. It is raised by the result of streamwise vortices, lying near wall. Due to the stable velocity profile here, the flow remains laminar state.

Furthermore, an ensemble averaged thermal structure of turbulent spot was firstly constructed using temperature data, yielding from a cold wire by Van Atta and Helland (1980) as shown in Fig. 11. The thermal structure apparently consists of 2 primary portions, the high and low temperature regions that are on the upper and lower parts of turbulent spot, respectively. These results are also compared to the contour of velocity perturbation, obtained by Zilberman *et al* (1977). This correlation was confirmed by the measurement of Antonia *et al*. (1981). They utilized an X-wire and also a cold wire to achieve the instantaneous longitudinal and normal velocity as well as temperature simultaneously. The other turbulence parameters such as rms fluctuations and the second moment turbulent quantities within the spot were further measured using a triple wires probe by Chong and Zhong (2006). However, the general shape, depicted by the temperature and velocity data is also very similar to those obtained by Antonia *et al*. (1981).

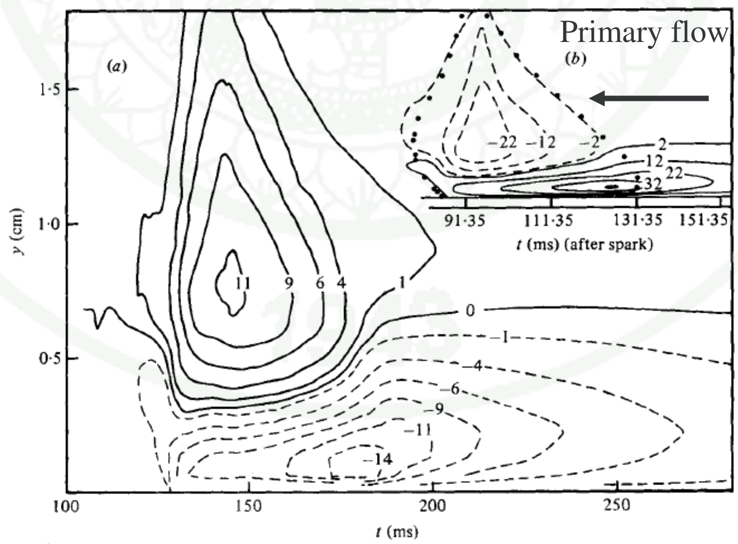

Figure 11 Temperature and velocity structure of turbulent spot.

Source: Van Atta and Helland (1980)

The thermal footprint structure of turbulent spot is firstly proposed using coating thermochromic liquid crystals by Kittichaikarn (1999). The structure was presented by the contour of heat flux, derived from colors, scattering by the liquid crystals as shown in Fig. 12. The footprint structure also appears as streaky, consistent to those obtained within the spot interior. Sabatino and Smith (2002) also obtained the similar results and show that the heat transfer behavior within the footprint was close to the pattern, induced by turbulent boundary layer. The slight difference is possibly caused by a different stage of maturity. Besides, becalmed region are observable at the structure’s trailing. Meanwhile, this region is absent and only trailing edge is detected in ensemble averaged velocity structure at $y/h_0 = 0$ as shown in Fig. 13 by Wygnanski *et al*. (1976). Chong and Zhong (2013) supported the reliability of thermal footprint by comparing to the shear stress footprint, yielding by shear stress sensitive liquid crystals. The liquid crystals successfully displayed the “true” structure on the surface and the shape of these two footprints is in agreement with each others. Moreover, the existence of spanwise overhang of turbulent spot is confirmed by comparing the spreading characteristic at its footprint and the near wall region. The results show that turbulent spot spreads out with different angle at the measuring locations. Also, Kittchaikarn (1999) further described that the variation of spreading angle depends on the state of maturity. This is in agreement with the observation of Wygnanski *et al*. (1976) who concluded that the spot take some time to reach the steady spreading angle. The time of development from its origin to fully mature becomes shorter with increasing Reynolds number.

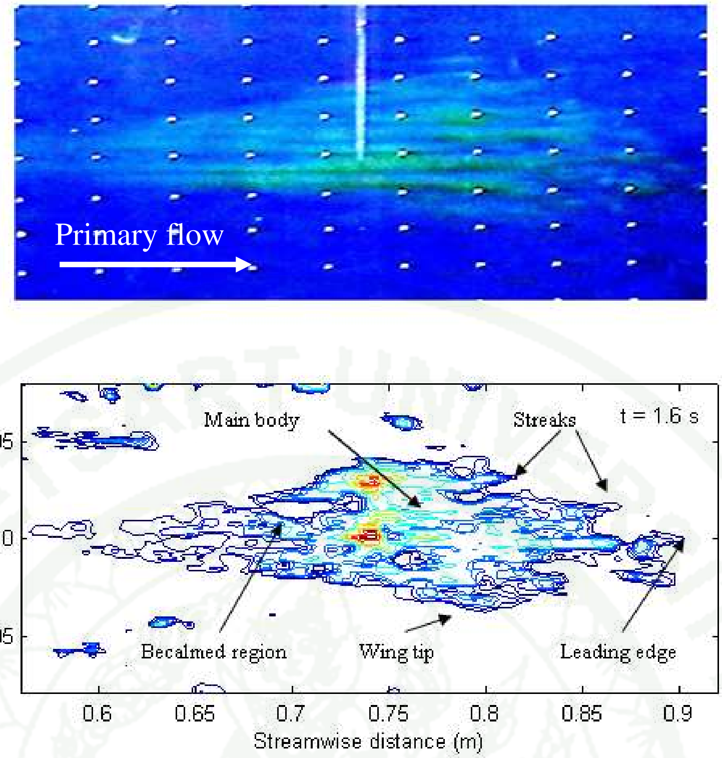

Figure 12 Turbulent spot footprint.

Source: Kittichaikarn (1999)

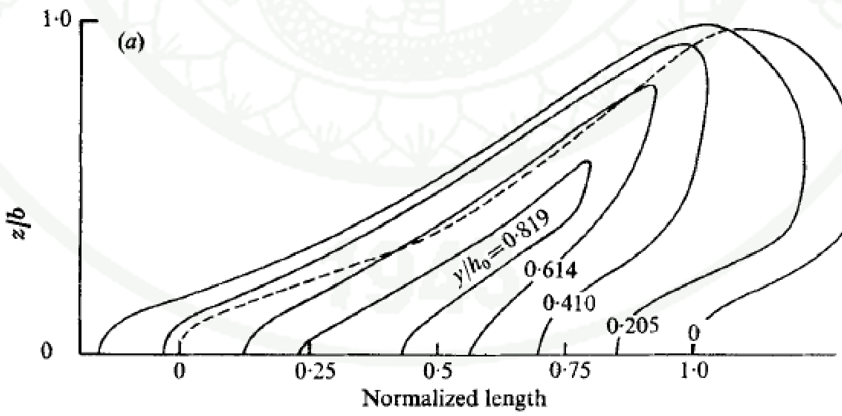

Figure 13 Half structure of turbulent spot.

Source: Wygnanski *et al*. (1976)

The multi-plane stereo particle image velocimetry (MSPIV) technique has been employed by Schröder and Kompenhans (2004) to investigate the spatial and temporal development of turbulent spot. Fig. 14 (a) shows an instantaneous velocity vector field of the spot at a wall distance of y = 4.5 mm. A wavy to streaky structure within the spot is noticeable. When an rms structure, corresponding to an ensemble averaged structure was calculated as shown in Fig. 14 (b), it is found that the turbulent spot, having arrow head shape convects downstream slower than the surrounding laminar flow. The slowest averaged celerity is at the center of the spot, about 0.65 of the free stream. Furthermore, the average substructures, indentified in their contribution, similar to hairpin vortices and streaks with strong shear layers, consistent to those in fully turbulent boundary layer flow, but here they are more orderly.

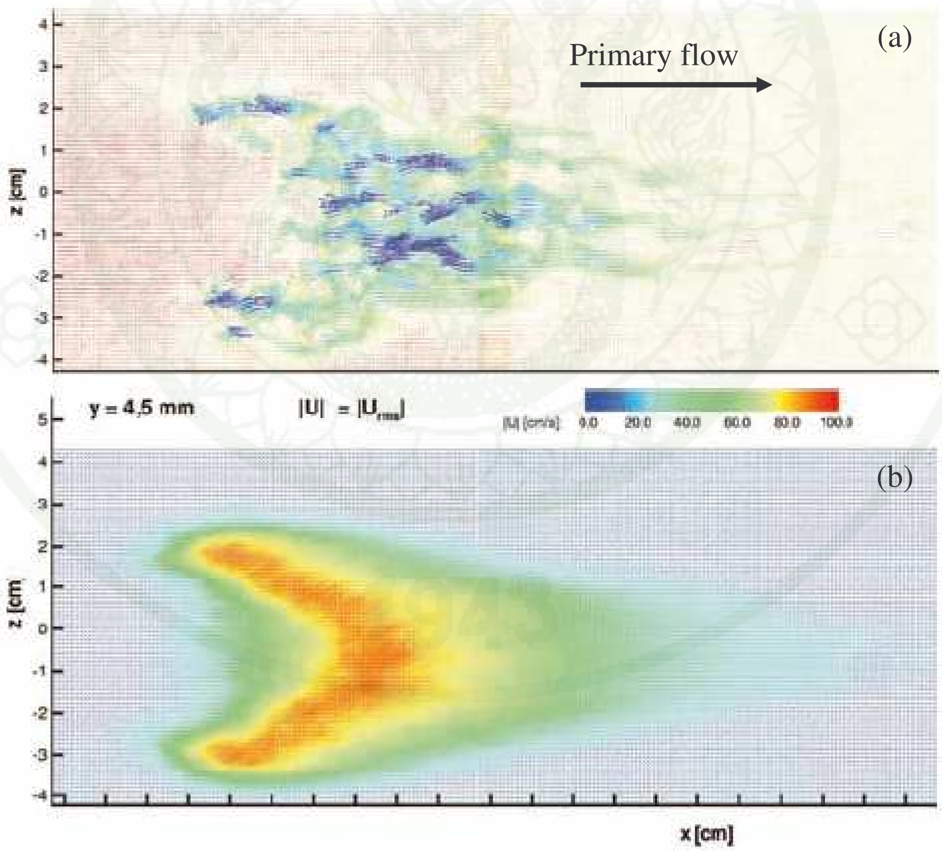

Figure 14 (a) Instantaneous velocity vectors, (b) Ensemble averaged structure.

Source: Schröder and Kompenhans (2004)

3.2 Growth mechanism of turbulent spot.

Under bypassed transition process, turbulent spot is directly induced by either high free stream turbulence intensity or external disturbance. The flow field in the spot depends upon both the distance from its origin or on the time elapsed from its initiation, following Wygnanski *et al*. (1982). The growth mechanism of the spot was early investigated by Wygnanski *et al*. (1976), Cantwell *et al*. (1978), Gad-El-Hak *et al*. (1981), and Perry *et al*. (1981). Wygnanski *et al*. (1976) showed that turbulent spot body consisted of a large eddy, having no way to escape as long as the spot retained its shape as depicted in Fig. 15. From the figure, the entrainment process is found not only at the near wall frontal interface but also along the trailing interface. They also described the behavior of turbulent spot with a shape factor parameter, generally used to determine the nature of the flow within the boundary layer. It was found that the shape factor within its body is about 1.5, the characteristic of a turbulent boundary layer at a low Re. At front, shape factor is decreased from the upstream and then equaled to 1.7 at the tip of overhang leading. This value indicated that fluctuation occurred and these might be partial connection from the upstream pressure wave. The shape factor was about 2.3, which was about the value of stagnation point. At further downstream, the value continued to increase and approached 2.6, the manner of a Blasius laminar boundary layer.

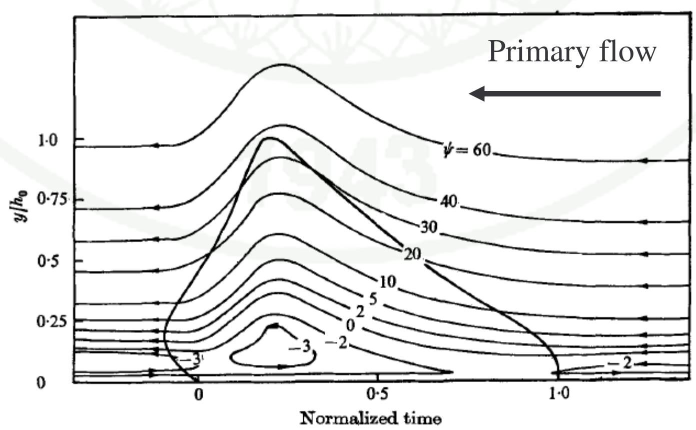

Figure 15 Streamlines through the turbulent spot structure.

Source: Wygnanski *et al*. (1976)

The details of the flow mechanism inside turbulent spot are further investigated by Cantwell *et al*. (1978). They reported that turbulent spot has a structure, comprising two large eddies. The technique of laser-doppler velocity measurements is employed to obtain the sketch of particle trajectories as shown in Fig. 16. The figure is constrained by conical similarity co-ordinates ξ and η, defining as $\xi = x/U_\alpha t$ and $\eta = y/ U_\alpha t$, respectively. They concluded that there are two vortex structures associated with the average spot. The large transverse vortex, denoted as I was identified by Coles and Barkers (1975). This vortex moves along the surface at the velocity of $0.77U_\alpha$. The other, probably found in the measurement of Wygnanski *et al*. (1976) is close to the wall near the rear of the structure at the notation II and convects downstream with the celerity of $0.64U_\alpha$. These eddies are not only the accumulation points of fluid, but also the peak and valley of temperature contour within the spot. This is found when the temperature contour, measured by Van Atta and Helland (1980) was plotted in the conical similarity co-ordinates mutually with the streamlines from Cantwell *et al*. (1978) as shown in Fig. 17. However, it is irrational because the maximum-temperature fluid must come from the layer, closing to the heated floor, whereas the converging particle paths originate from unheated region. Also, the position of the lower cooling maximum is consistent to the near wall eddy. They reasons that this is associated by the entrainment, coming from the cooler regions at the higher position. Cantwell *et al.* (1978) further reported that there are two processes of the entrainment, mainly served to the growth of turbulent spot. More than 80% occurs by the process of "nibbling" along the segment bed, which is the upper rear boundary. This is visualized by the dye layer on the back of the spot as shown in Fig. 8. Besides, the process called "gulping" entrains the remainder through the segment efg, locating at the front of the spot.

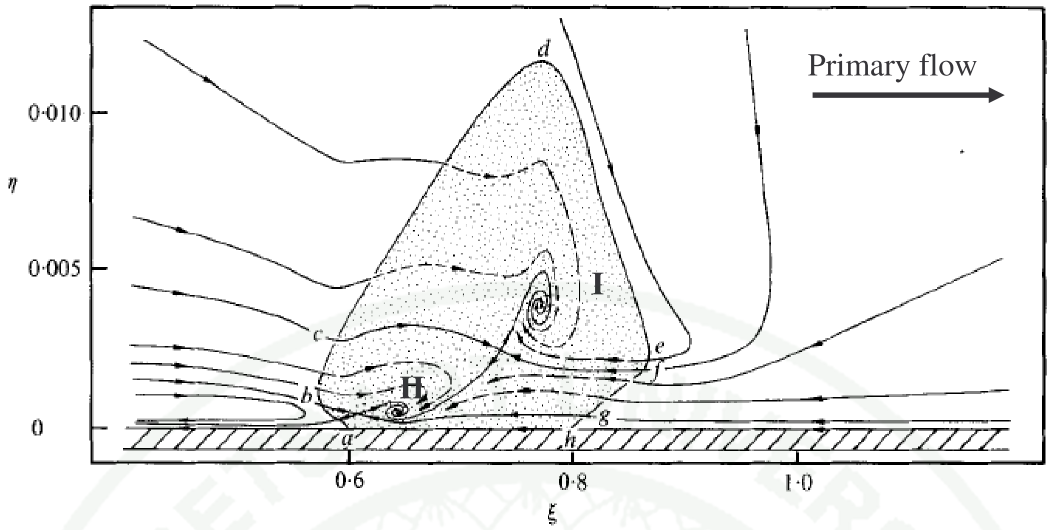

Figure 16 Particle trajectories diagram.

Source: Cantwell *et al*. (1978)

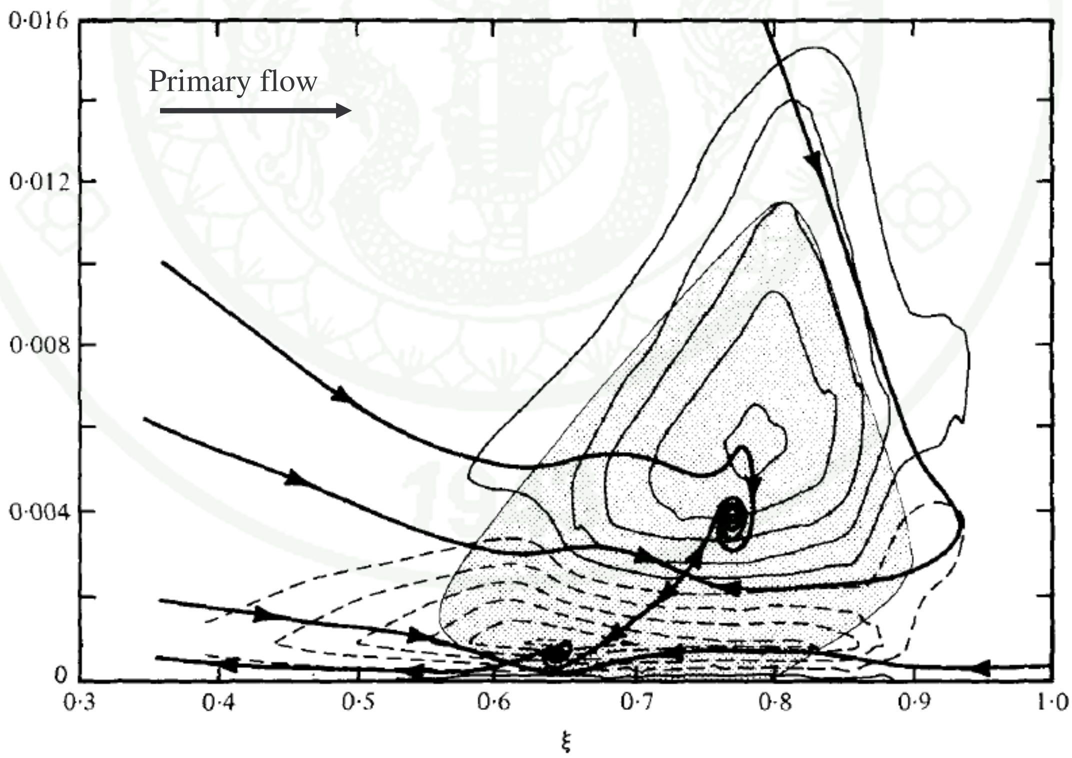

Figure 17 Temperature contour in the conical co-ordinate.

Source: Van Atta and Helland (1980)

The heat transfer mechanism of the spot is found to be strongly related to the process of entrainment. Using technique that combines PIV and thermochromic liquid crystals measurement, Sabatino and Smith (2002) conclude that the overhang region at the leading edge and the body of the spot have little influence on the surface heat transfer. Gutmark and Blackwelder (1987) describe the spot overhang as former near wall turbulence, which has ejected and convected away from the wall and finally does not influence the surface properties. Van Atta and Helland (1980), Antonia *et al*. (1981), and Gutmark and Blackwekder (1987) determined that the fluid within the spot is at higher temperatures than for similar laminar conditions. This suggests that the spot body is the most likely an amalgam of warm fluid that has been accumulated from prior ejections of surface fluid. Thus, in further downstream, heat transfer decreased when the temperature gradient between the spot body and the surface reduces. Information, obtained from PIV indicates that there is a relatively high speed fluid near the surface immediately following the passage of the spot body. Antonia *et al*. (1981) indicate that the fluid in this region is cooler, comparing to the leading edge. Thus, the heat transfer increases due to an inrush of cool fluid. Sabatino and Smith (2002) also hypothesize the relationship between the spot entrainment process and the variation in surface heat transfer of the spot as depicted in Fig. 18. The warm fluid, which is originally near wall, is entrained from the near wall region so the spot body expands by accretion of warm fluid. In the spot body region, heat transfer increases approximately 9% above comparable laminar conditions. The trailing structure in the calmed region improved surface mixing with cooler fluid that enters from upstream. This results in a peak of heat transfer of approximately 15% above laminar conditions. However, this is still much lower than turbulent characteristics. The youngest spot seems to yield the largest percentage increase in the surface heat transfer because it entrains the less warm fluid inside. At this point, heat transfer here is very close to turbulent boundary layer.

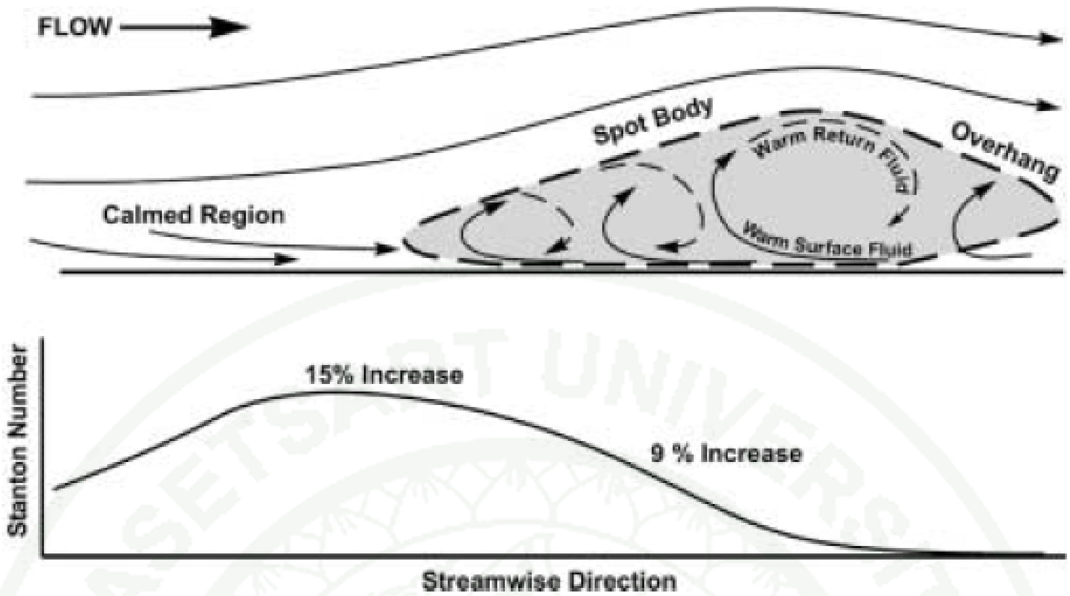

Figure 18 Relation between Stanton number and the entrainment process.

Source: Sabatino and Smith (2002)

The entrainment process, which directly responds for the growth mechanism of turbulent spot, is also investigated as the spot propagates downstream. Wygnanski *et al*. (1976) presents this process by the streamlines and indicate that, at the leading interface of the spot, the entrainment is most efficient near the surface and drops slowly with increasing y. This phenomenon is also observed by Cantwell *et al*. (1978) as previously described. Gad-El-Hak *et al*. (1981) explain this process at the front part of turbulent spot that this region has been swept over the slower near wall laminar flow, producing a large overhang of the spot's leading edge as shown in Fig. 19. The dye, released in the near wall region firstly separates into several lumps, possibly due to a strong vertical velocity component. These discrete regions have a particular wavelength of approximately one or two thicknesses of laminar boundary layer. Wygnanski *et al*. (1982) show the vector distribution of velocity perturbation at leading and trailing edge as depicted in Fig. 20. This presents that the gulping process at the front interface is relatively strong in near wall region while it is weak at trailing edge. However, the nibbling process outstandingly performs above the near wall region at the trailing edge.

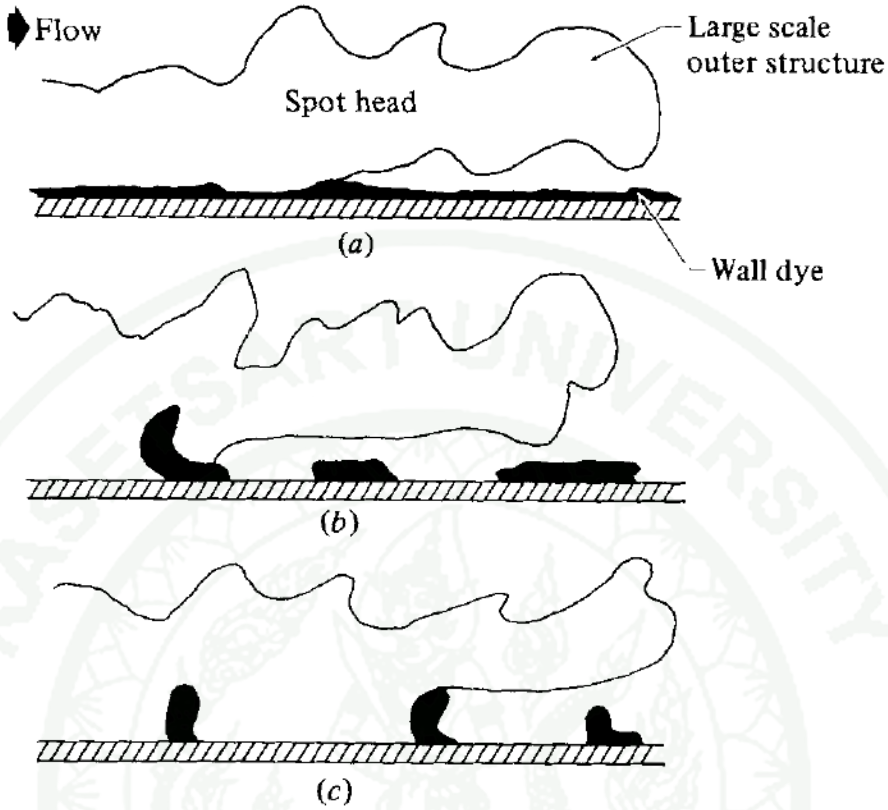

Figure 19 Entrainment process at the leading edge.

Source: Gad-El-Hak *et al*. (1981)

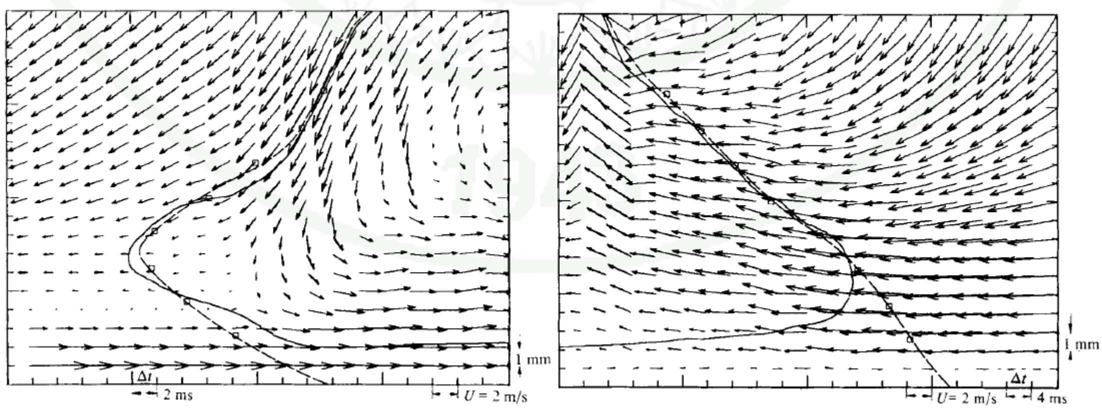

Figure 20 Velocity distribution at leading and trailing edge.

Source: Wygnanski *et al*. (1982)

3.3 Coherent structures within turbulent spot.

From the measurement by Van Atta and Helland (1980), it is believed that the misleading results are associated by establishing the ensemble averaged structure of the spot from averaging at different reference such as leading edge, trailing edge of the spot as well as the location of the spot generator as expressed by Wygnanski *et al*. (1976), Cantwell *et al*. (1978), Van Atta and Helland (1980), and Antonia *et al*. (1981). The method will definitely mask the presence of internal structure inside turbulent spot. However, further studies, focusing on the flow visualization by Perry *et al*. (1981) and Gad-El-Hak *et al*. (1981) are described on the presence of many substructures within individual turbulent spot. Matsui (1980) remarks that many kinds of vortices, that is, hairpin, ring, wavy and winding, are observed. The number of these substructures increases with the streamwise distance and they propagated downstream at approximately the same velocity, following Sankaran *et al*. (1988). The propagating velocity, inclination and length scales of these substructures correspond to the characteristics of hairpin vortices. The new substructures are formed near the trailing edge of the spot. The presence of several distinct vortex structures is confirmed using hot and cold wires by Antonia *et al*. (1981), Wygnanski *et al*. (1982), and Sakaran *et al*. (1988). The measurements using PIV by Sabatino and Smith (2002) and Schröder *et al*. (2008) are also detectable the presence of vertical structure within the spot. From many flow visualization researches, hairpin or horseshoe or Λ-shape vortices are proposed as the primary structure of turbulent spot. Coherent rows of four eddies are identified while several rows appears in the plan view as substructures of turbulent spot, following Itsweire and Van Atta (1984). The slightly different results are obtained using an array of X probes aligned in the direction normal to the surface by Sankaran *et al*. (1991). They exhibited clear evidence of five distinct eddies of turbulent spot as shown in Fig. 21. These correspond to those obtained by Wygnanski *et al*. (1982).

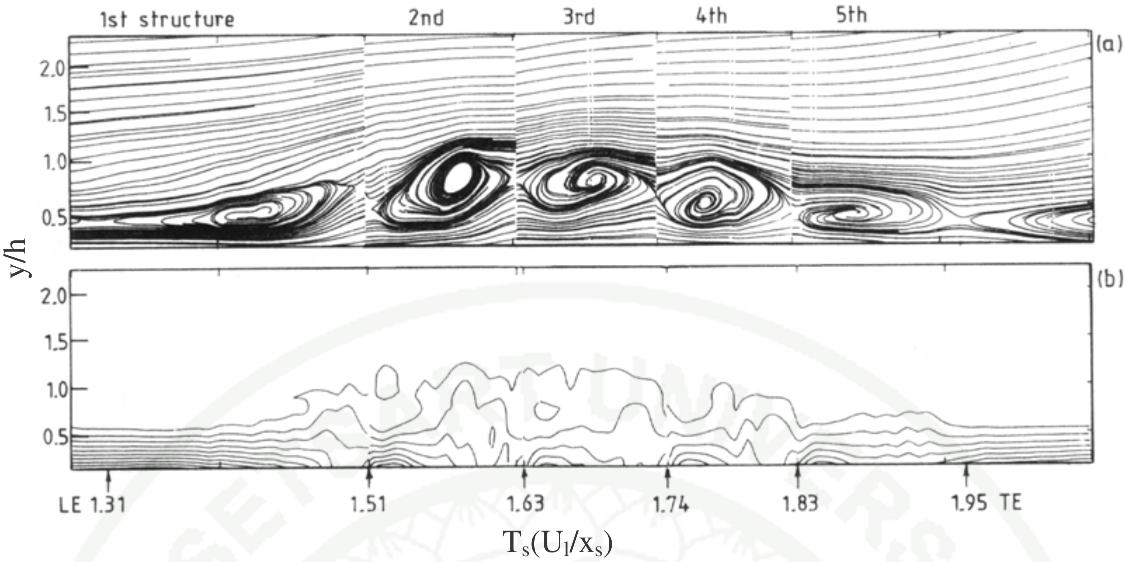

Figure 21 Five major vortices within turbulent spot.

Source: Sankaran *et al*. (1991)

Hairpin vortex, suggested as the primary structure of turbulent spot, was visualized by Acarlar and Smith (1987). The experiment was carried out under the hypothesis that hairpin structures are associated by the breakdown of the low speed streak structures, developing adjacent to the surface beneath turbulent boundary layer. When the flow is properly disturbed, an oscillation breaks down into horseshoe vortices as depicted in Fig. 22. They are carried downstream by the mean flow and stretch out by the wall shear layer. This stretching process elongates the horseshoe shaped vortices into hairpin-type vortices. When the heads and legs of the vortices lift-up from the surface, they are more stretched. The trailing of its legs, locating near the wall create the local lateral pressure gradients which cause the accumulation, concentration, and lift-up of low-momentum fluid between the counter-rotating legs, following Ersoy and Walker (1985). The location of the secondary streamwise vortices, forming outboard of the counter-rotating legs of the hairpin vortices and extend downstream. These secondary vertical structures are weaker than the horseshoe vortex, observed in the measurement of Makita and Nishizawa (2001).

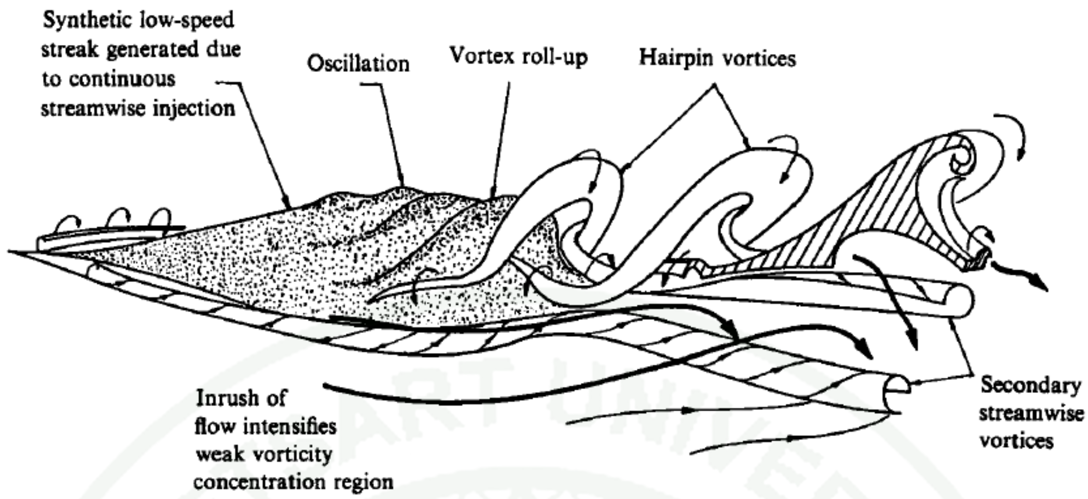

Figure 22 Breaking down of turbulence.

Source: Acarlar and Smith (1987)

Haidari and Smith (1994) further investigate the evolution of hairpin vortices using both dye and hydrogen bubble visualization techniques in conjunction with the hot-film anemometer in a water tunnel. They suggest that a turbulent spot is an agglomeration of smaller flow structures as depicted in Fig. 23. The initial hairpin vortex, initiated by the injection process, is referred to as the primary vortex. The formation of the subsidiary vortices is caused by the inviscid deformation of the collective vortex lines, comprising the primary vortex. More new hairpin vortices, developing outboard of the symmetry plane of the initial vortex is created laterally by additional spanwise deformation. It is also found that the subsidiary vortices grow very rapidly and are influenced by the lateral motion of the fluid generated by the primary vortex legs. Thus, this destabilization is considered as the primary effect on the spanwise growth of turbulent spot, which is in agreement with the report of Gad-El-Hak *et al.* (1981). Furthermore, the secondary hairpin vortices are found, following the primary vortex. They are the result of inviscid/viscous interactions between outer layer fluid and surface fluid, caused by the interaction of the primary vortex with the surface. This process is similar to the formation process of the primary hairpin vortex. A lift up of low momentum fluid initiates three dimensional deformation of spanwise vorticity, which eventually gives rise to the formation of secondary vortices. In the process of the primary vortex, the low momentum region is artificially generated by the injection process.

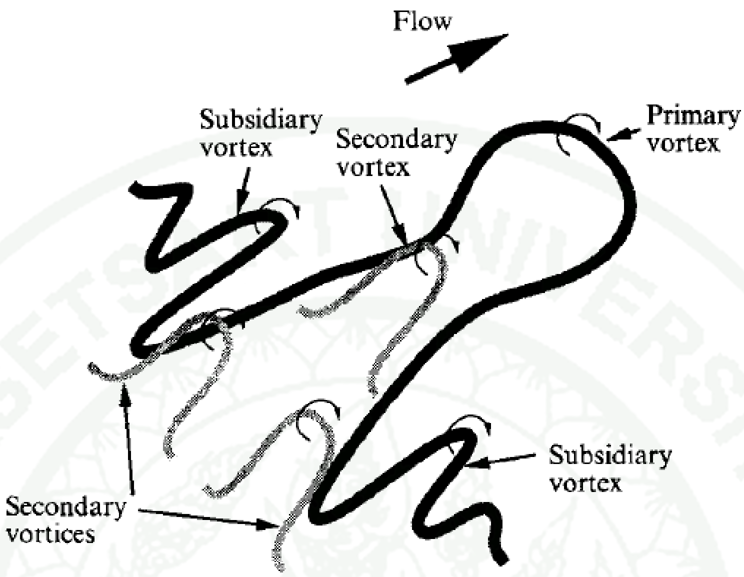

Figure 23 Structure of turbulent spot.

Source: Haidari and Smith (1994)

The process of vortex regeneration, both laterally and in the wake of the primary vortex, leads to the continued development of the hairpin vortex into a turbulent spot structure. Haidari and Smith (1994) employed a horizontal hydrogen bubble sheet to capture the spot development at the height of $y/\delta = 0.4$ and at streamwise distances of $x/\delta = 1$, 5, 10, and 30 as depicted in Fig. 24(a)-(d), respectively. Meanwhile, turbulent spot development at the height of $y/\delta = 0.1$ at the same streamwise distance is shown in Fig. 24(a')-(d'). In Fig. 24(a), the counter rotating legs lie above the plane of bubble wire and are marked by the faint tubes of bubble as labeled L. These tubes trail drop right to left below the bubble sheet, extending down towards the plate. The narrow bright bifurcated concentration of the bubbles in the plan view part of Fig. 24(a') appears in the end view as upwellings of low speed fluid, caused by the pressure-gradient-induced interaction of the legs of the vortex with near wall fluid. In Fig. 24(b), the counter rotating legs of the primary vortex are still clearly apparent in both plan and end views. This reveals the initiation of a secondary hairpin vortex, labeled S_1, which just beginning to pass through the bubble sheet. The head of the secondary vortex is found above the sheet. The near wall low momentum region develops as shown in Fig. 24(b') and evolves into two distinct low momentum regions with appreciable vertical penetration.

By Fig. 24(c), the secondary vortex has developed and moved away from the wall, appearing as the ridge – S_1. Also the two outboard secondary vortices, labeled S_2 are formed. With this appearance, the flow pattern in Fig. 24(c') begins to reflect the initiation of an additional pair of low momentum regions. As indicated in the end view, the low momentum regions near the symmetry line display the new low speed regions E, penetrating outward from the wall. The middle two low speed regions as shown in Fig. 24(c') start to be associated with wall interactions of the legs of both the primary and the secondary vortex. In this view, Li and Dengbin (2006) show the formation of the streamwise vortex that is gradually up-fling while traveling downstream as shown in Fig. 25. They further indicate that as the spot elevates to the certain height, the up-eruption movement strongly begins between two vortices and eventually causes breakdown of the vortices. In the mean time, the outboard regions appear to be associated with the wall interactions of the newly formed lateral secondary vortices. Finally, Fig. 24(d) and (d') illustrate the appearance of the spot-like structure. It is found that the continued evolution of existing vortices and the development of new vortex structures are under the viscous-inviscid interactions, resulting in the systematic development of a turbulent spot. The further details of hairpin vortex filament are recently visualized by Bernard (2011).

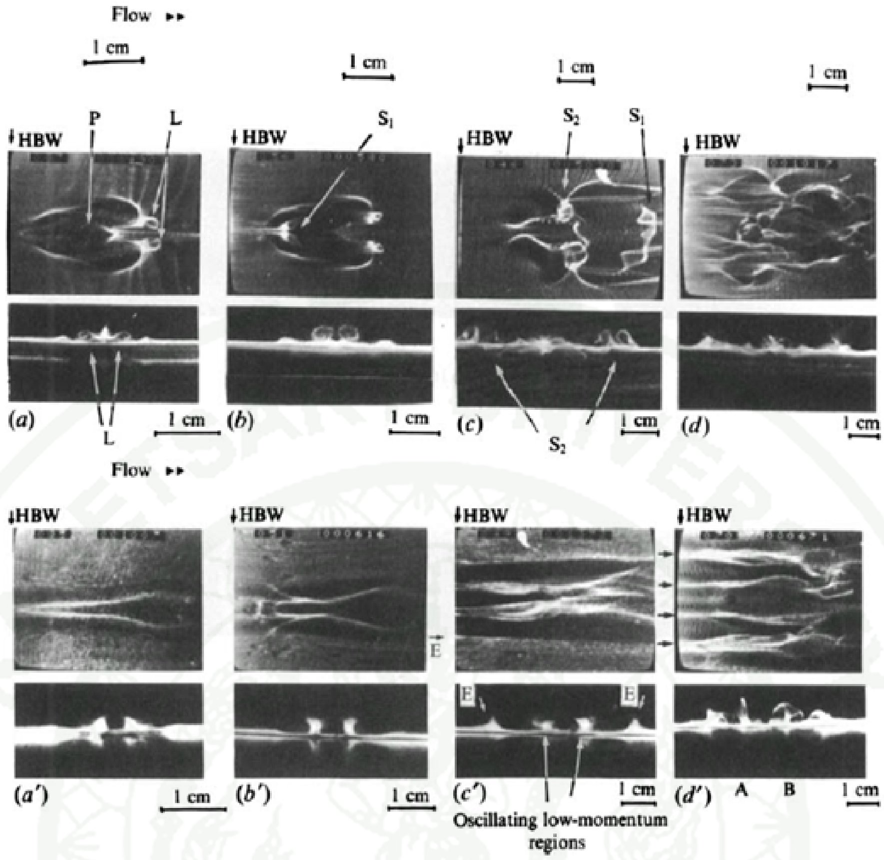

Figure 24 The process of vortex generation.

Source: Haidari and Smith (1994)

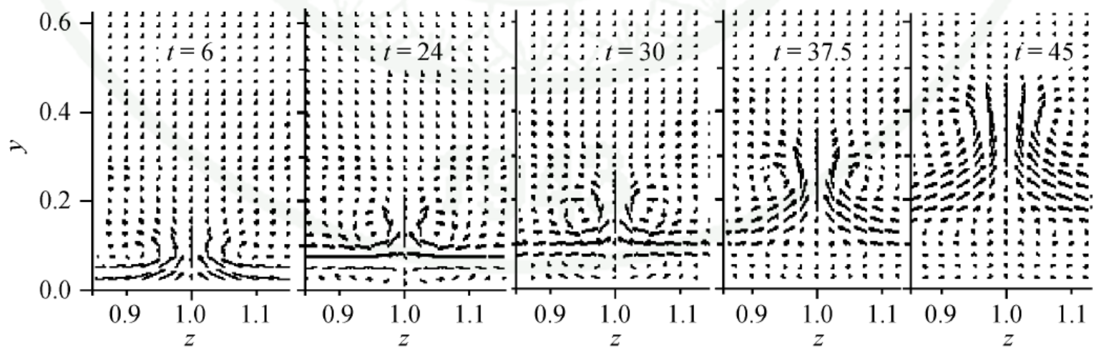

Figure 25 Development of the vortex filaments.

Source: Li and Dengbin (2006)

Details of evolution of turbulent spot are further revealed using a direct numerical simulation – DNS by Singer and Joslin (1995). A short pulse of injecting fluid blocks part of the usual boundary layer flow, which later forms a high pressure region at upstream. A strong hairpin vortex formed just downstream of the high pressure region while a weak hairpin vortex emerges but no longer participates the development. A pair of U-shaped vortices was observed beneath the hairpin vortex legs. It is consistent to the laterally displaced secondary vortices, reported by Haidari and Smith (1994). However, any subsidiary vortices, the cause of the lateral growth of the spot are not observed in this simulation. Singer (1995) used the same code of DNS to investigate the early of the turbulent spot formation, called "young turbulent spot". The obtained results are consistent with those obtained by Haidari and Smith (1994). The structure and the early development stage of the primary and secondary vortices are visualized as depicted in Fig. 26. Singer (1995) also reported that the overhanging region of the turbulent spot is composed of older, less intense vortices. These older structures propagate downstream very rapidly and result in the streamwise growth of the overhang region of turbulent spot.

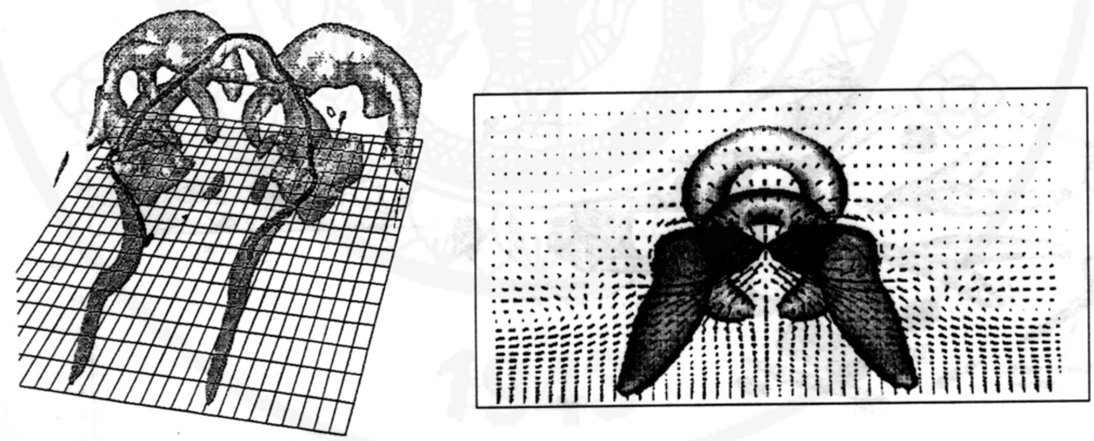

(a) (b)

Figure 26 (a) Structure of primary vortex, (b) Early stage of primary and secondary vortices.

Source: Singer (1995)

The computational study is further using a numerical method for predicting all three unsteady velocity components by Johnson (1999). This work is extended from the contribution of Johnson (1998). He shows that the calmed region consisted of two layers. The lower layer is fluid which has entered the rear of the perturbed region and has been swept towards the surface to replace low momentum fluid, extracted by hairpin vortex. The top layer is high momentum fluid which is also swept towards the surface but only temporarily fills the space vacated by the low momentum fluid, before becoming entrained into the hairpin vortex. The high momentum stream of fluid which sweeps through the calmed region to become entrained within the hairpin vortex mixes with a second stream of the low momentum fluid which passes beneath the leading edge of the spot before becoming entrained into the vortex. Both streams are ejected into the middle layer of the spot where mixing out continues. The high local shear rate, associated by the mixing of these two streams, result in the turbulent bursting observed within the spot. The uppermost layer in the spot is primarily fluid from the free stream, drawn towards the wall in the calmed region. The lowest layer, referring to the viscous sub layer is fluid close to the wall, passing beneath the spot unperturbed and is not entrained by the hairpin vortex but is diverted around the edge of the calmed region.

The spot structure, which primarily comprises the hairpin vortices, is fully presented using a spectral DNS code by Strand and Goldstein (2010). Fig. 27 shows the multiple overlapping and entwined hairpin and streamwise vertical structures that make up the growing spot. The hairpins are presented throughout the spot. The spot structure is more complex and interwined at the center and hairpin legs do not necessarily align fully with the streamwise direction. In mature turbulent spot, a wide variety of hairpin size is apparent. These structures are consistent to the results, reported by Wu and Moin (2010). Their calculation by DNS shows the multiple turbulent spots under boundary layer transition and at least two of them are in the process of merging. Numerous hairpin vortices are tightly packed inside each turbulent spot. Red color in Fig. 28 indicates that some of the hairpins in the spot reach the local boundary layer edge. The turbulent spots move downstream with different speeds at their leading and trailing fronts. Finally, these turbulent spots catch up with the trailing edge of the downstream continuous turbulent region.

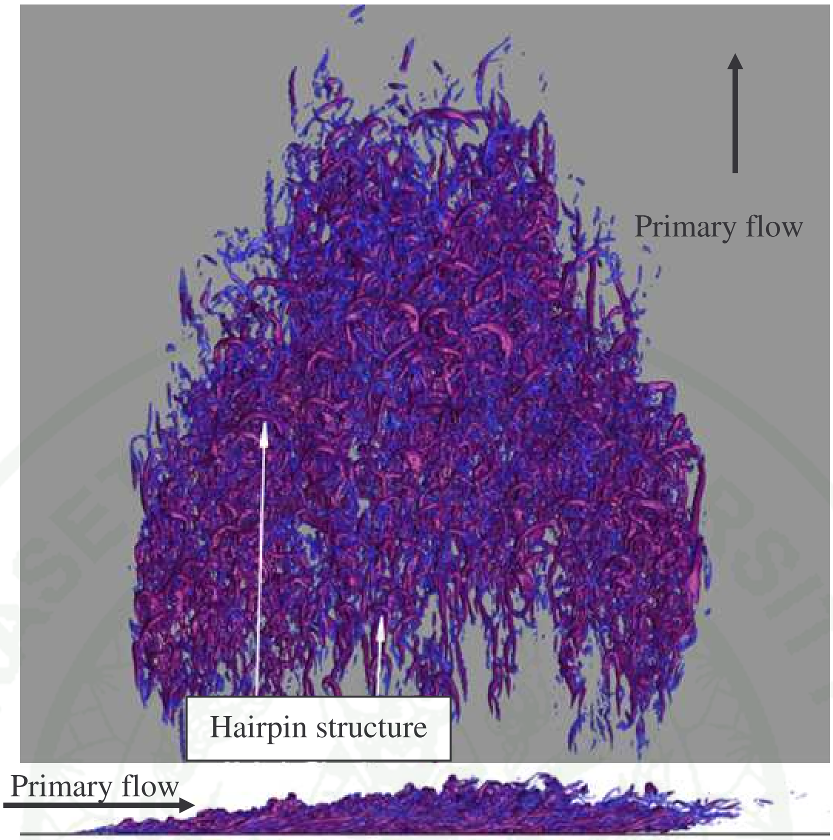

Figure 27 Hairpin vortices within turbulent spot.

Source: Strand and Goldstein (2010)

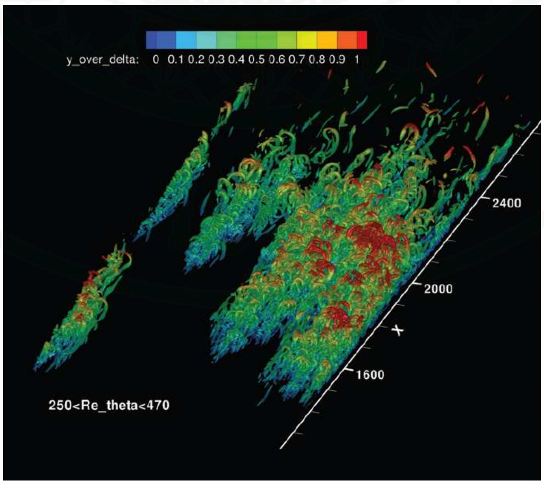

Figure 28 Velocity gradients in transition zone.

Source: Wu and Moin (2010).

4. Effects on boundary layer transition.

It has been known that the viscous drag of a turbulent boundary layer can be up to four or five times greater than of a laminar layer. To achieve the benefits of better heat transfer by the turbulence, the more energy source should be substantially provided. An elongation in transition not only yields the advantages of the partial turbulent but also reduces the pressure loss in the system due to the surrounding laminar. Also, a retraction in transition may lead to the more precise calculation when the prediction in this flow region is not yet completely understood. From literature reviews, the parameters, affecting the stretching and retracting of the transition length are pressure gradients, free stream turbulence, surface roughness, flow separation, surface curvature, compressibility, heat transfer, and film cooling. However, surface roughness, surface curvature, compressibility and heat transfer which influence the spot production rate are generally five or ten times less than the effect of pressure gradient, following Mayle (1991). Therefore, in order to yield the precise calculation on the boundary layer transition, these affecting factors should be taken in account. In this section, only primary factors i.e. pressure gradient, free stream turbulence and surface roughness are reviewed.

4.1 Effect of pressure gradient

In general, when a fluid flows past an object other than a flat plate, the pressure is not constant in the direction along the body surface, depending on the profile of curvature, following Munson *et al*. (2006). On flat plate, a decelerating flow, relating to an increasing pressure of an adverse pressure gradient, the boundary layers tend to be destabilized and the velocity profiles have a point of inflexion, following Schlichting (1979). On the other hand, the absence of inflexion point and stabilization appear under an accelerating flow or a favorable pressure gradient. The reduction of destabilization, caused by the favorable pressure gradient is clearly visualized by the spreading angle of the turbulent wedges, following Chong and Zhong (2012). They found that the spreading angles of the wedge, obtained by both the temperature and shear stress sensitive liquid crystals become smaller as the level of favorable pressure gradient increased. Clark (1993) indicates that the propagation rates at spot leading edge are about constant fractions of the local free stream velocity while the convection rate at the trailing edge does not directly scale as at the leading edge. Clark (1993) plotted the fractional propagation rate against the acceleration parameter, K, defined as

$$K = \frac{\upsilon}{U_\alpha^2}\frac{dU_\alpha}{dx} \qquad (2)$$

The plot shows that the fractional propagation rate at the leading edge of turbulent spot is constant throughout a range of K from zero up to $3*10^6$. Meanwhile, the rate at the spot trailing edge decreased with the lower K. Thus the growth of turbulent spot is inhibited by a favorable pressure gradient. The evolution of the turbulent spot under the favorable pressure gradient is studied by Katz *et al*. (1990). The growth rate of the spot significantly reduces in all three directions. It is much shorter and narrower in comparison with the spot under zero pressure gradient at comparable distances and Reynolds numbers. Also, the spot shape occurs as a rounded triangular arrowhead with the trailing interface, straight and perpendicular to the direction of the main flow. Furthermore, not only the wave packets, trailing behind the spot are absent, but the laminar boundary layer surrounding the turbulent spot is more stable. This is consistent to the investigation of Cantwell *et al*. (1978), owning to the favorable pressure gradient that exists in their experiment. These results lead to the occurrence smaller spreading angle in this acceleration flow. Chong and Zhong (2005) investigate three dimensional structure of turbulent spot and its dependence on the streamwise pressure gradients. The structure under the zero pressure gradient is depicted in Fig. 29(a) is compared to the others with increasing favorable pressure gradients. In the figure, the positive velocity perturbations, shown in light grey, appears thin flat while the negative perturbations are presented in dark grey. This comparison shows that the stronger pressure gradient results in a shorter wing over which the height of spot decreases rapidly.

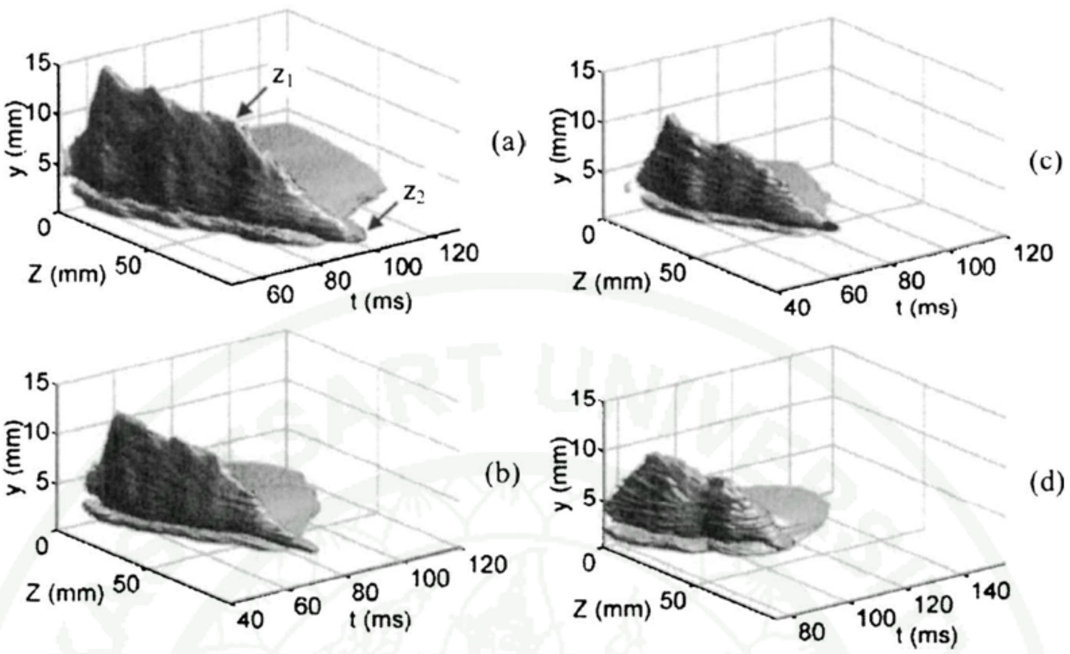

Figure 29 Half structures of velocity perturbation under various favorable pressure gradients.

Source: Chong and Zhong (2005)

The behaviors of the turbulent spot under the influence of an adverse pressure gradient are studied by Gostelow *et al*. (1993), Van Hest *et al*. (1994), Seifert and Wygnanski (1995), and Zhong *et al*. (2000). They all agreed that the spreading rate is increased under the adverse pressure gradient. Gostelow *et al*. (1993) observed an accelerated destabilization of the flow in the adverse pressure gradient. This relates to the existence of high amplitude waves near the spot. Also, Gostelow *et al*. (1996) reported that the turbulent spot under this pressure gradient has a relatively blunt nose, comparing to the others in zero and favorable pressure gradient. Zhong *et al*. (2000) employed the coating temperature sensitive liquid crystals to visualize the thermal footprints of turbulent spots under the pressure gradient. They specified the level of the adverse pressure gradient using the pressure gradient parameter - λ_θ defined by Thwaites as

$$\lambda_\theta = \frac{\theta^2}{\upsilon}\frac{dU_\alpha}{dx} \tag{3}$$

Their strongest level of adverse pressure gradient is -0.08, very close to the critical value of -0.082, indicating that the laminar boundary layer is near the verge of separation. They observed that the spot grows faster in the spanwise direction, referring to the increasing half spreading angle when the pressure gradient increases as depicted in Fig. 30. With the higher pressure gradient, the propagation rate of the leading edge increases while that of the trailing edge decreases as shown in Fig. 31.

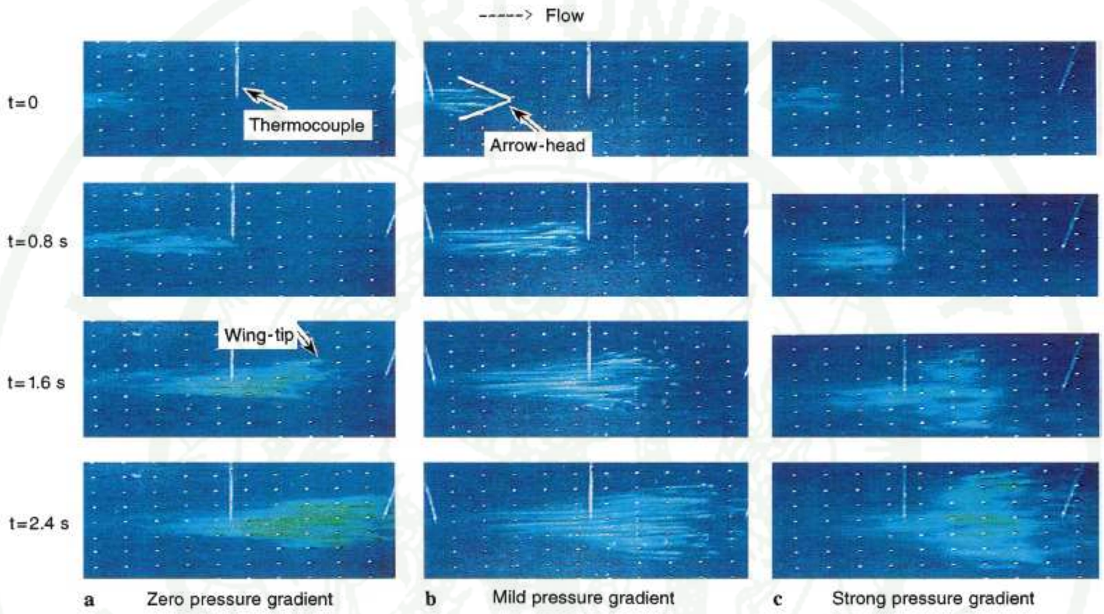

Figure 30 Thermal footprints of turbulent spot under various adverse pressure gradients.

Source: Zhong *et al*. (2000)

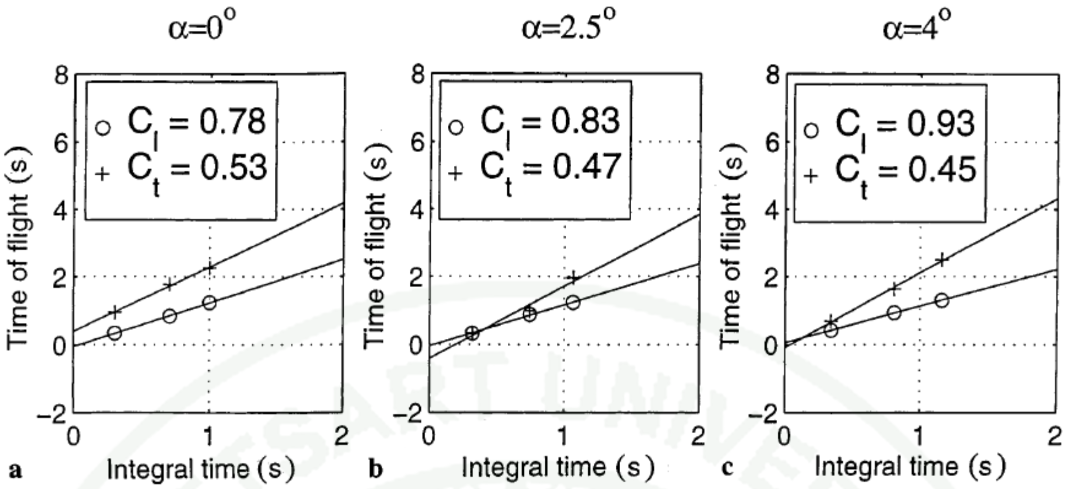

Figure 31 The propagation rate of the leading and trailing edges of the spots under various adverse pressure gradients.

Source: Zhong *et al*. (2000)

Gostelow *et al*. (1996) summarized the celerities and spreading half angle of turbulent spot under favourable, zero and adverse pressure gradients obtained by various researchers as shown in Fig. 32 (a) and (b). It should be noted that these data are measured at the height of $0.05 \leq y/\delta_L \leq 0.35$ where δ_L is the thickness of larminar boundary layer. These plots apparently indicate that the turbulent spot convects downstream with the constant propagation rate at the leading edge under all levels of pressure gradient. With the reduction of λ_θ, the celerity at the trailing edge decreases while the half spreading angle increases. These mean that turbulent spot expands in streamwise and spanwise direction under adverse pressure gradient, comparing to the structure that is subjected the zero gradient of pressure. In the mean time, the favorable pressure gradient provides the smaller structure of turbulent spot.

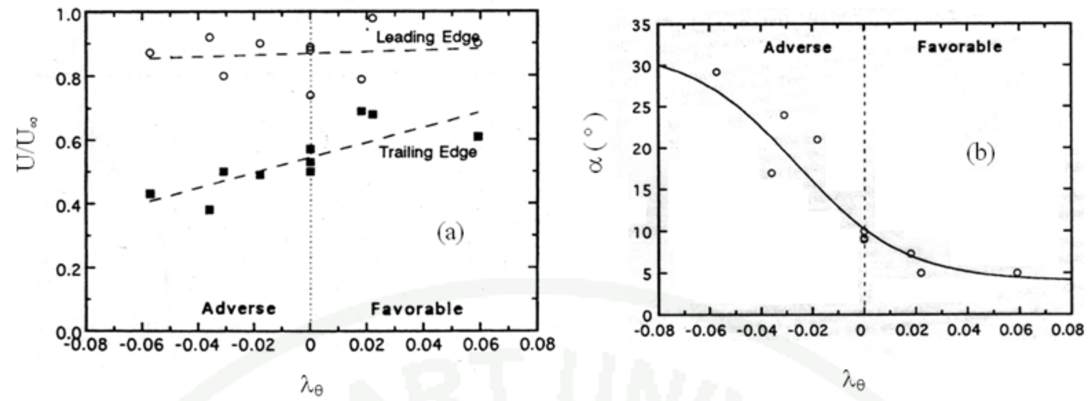

Figure 32 Variation of turbulent spot parameters as a function of pressure gradient parameter, (a) The celerities at the leading and trailing edges, (b) Half spreading angle.

Source: Gostelow *et al*. (1996)

4.2 Effect of free stream turbulence

The free stream turbulence is the one of parameters, affecting the onset and length of transition. Details in the investigations on the effect of free stream turbulence on boundary layer transition are found in Abu Ghannam and Shaw (1980), Narasimha (1985), and Hogendoora and de Lange (1997). Mayle (1991) compiled data of momentum Reynolds number at transition onset and spot production rate against the free stream turbulence intensity for transition in zero pressure gradient flows from various researchers. Linear variations are found as the relations of

$$\mathrm{Re}_{\theta t} = 400 * Tu^{-5/8} \tag{4}$$

$$\hat{n}\sigma = 1.5 * 10^{-11} Tu^{7/4} \tag{5}$$

$$\hat{n} = g\upsilon^2 / U^3 \tag{6}$$

where $\mathrm{Re}_{\theta t}$ is the Reynolds number based on momentum thickness at transition, g is the number of spots, formed per unit spanwise length per unit time and

Tu is the free stream turbulence intensity expressed as a percentage. These relations are presented as shown in Fig. 33.

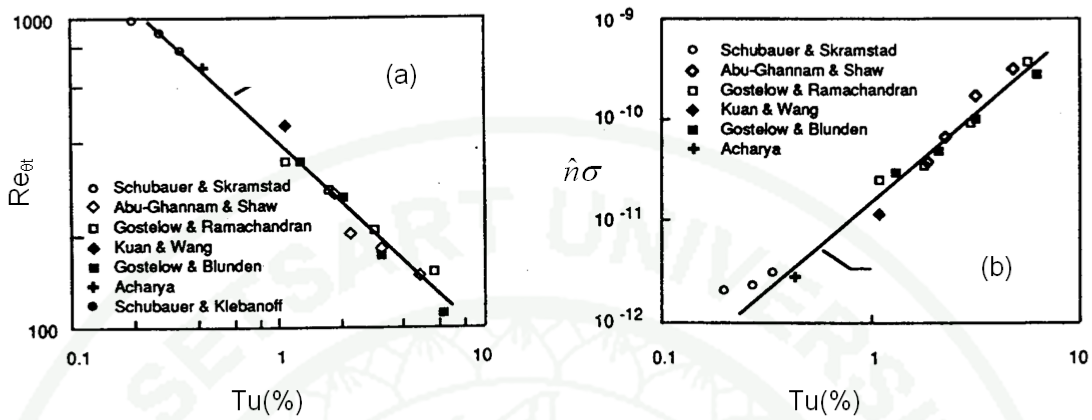

Figure 33 Variation of the onset and production rate as a function of free stream turbulence, (a) Momentum Reynolds number at the onset, (b) Spot production rate.

Source: Mayle (1991)

Yaras (2007) examines the sensitivity of this structure to the free stream turbulence. Fig. 34 shows the comparison of the perturbation velocity fields in the turbulent spot under the low, moderate and high free stream turbulence, set approximately at 1%, 3%, and 5%, respectively. The weakening of the perturbation is detected when the free stream turbulence intensity increases. Despite the smaller magnitudes of the velocity perturbations, the streaky structure is noted to remain. The hairpin vortices are still observable at higher levels of free stream turbulence. The arrowhead shape structure, noted at low free stream turbulence is not retained at the higher levels of turbulence intensity. Instead, multiple longitudinal protrusions are observed in the rms velocity fluctuation field on both leading and trailing sides of turbulent spot as depicted in Fig. 34 (c). These are visible in both cases of the moderate and high turbulence levels. The spanwise locations of these protrusions correspond to the high velocity streaks in perturbation velocity contour as shown in Fig. 34 (b)

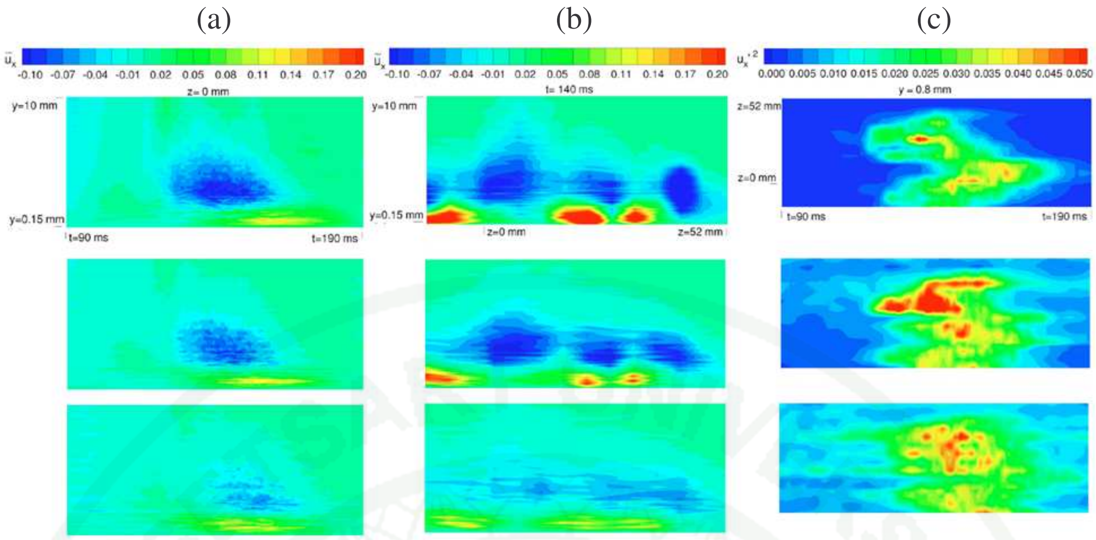

Figure 34 (a) Velocity contour on y-t plane under low, mild, high Tu, (b) Velocity contour on y-z plane under low, mild, high Tu, (c) rms velocity contour on z-t plane under low, mild, high Tu.

Source: Yaras (2007)

4.3 Effect of surface roughness

Roughness on the surface of turbine blade can give a significant effect on the blade passage flow, directly involving the region of transition. The level of surface roughness on a gas turbine blade can vary in height from 2 to 160 μm, following Taylor (1990). Modifications of boundary layer over blade surface by surface roughness has been shown to reduce turbine aerodynamic efficiency but it increases the surface heat transfer rate, following Kind *et al*. (1998) and Bons and McClain (2003). However, the length of transition zone is controllable by the large scale of surface rougness such as passive riblets and damping fins. Coustols and Savill (1992) and Bruse *et al*. (1993) experimentally show that the stream wise riblets can reduce turbulent drag on a surface by five to ten percent. Goldstein and Tuan (1998) indicate that the riblets work by damping the near wall spanwise fluctuations. Strand and Goldstein (2009) found that the riblets decrease the spreading angle by 12%. Also, damping fins are found to be much more effective than real textures because in the damping fin case, the streamwise vertical structures extend down to the plate while in the real texture case, the vertical structures rarely drop down into the riblet valleys. Chu *et al*. (2010) further informed that the damping fins with height of 0.87δ_L can virtually stop spanwise spreading as shown in Fig. 35. The streamwise vertical structures are nearly completely trapped between the damping fins while the heads of the hairpin vortices are struck above the fins.

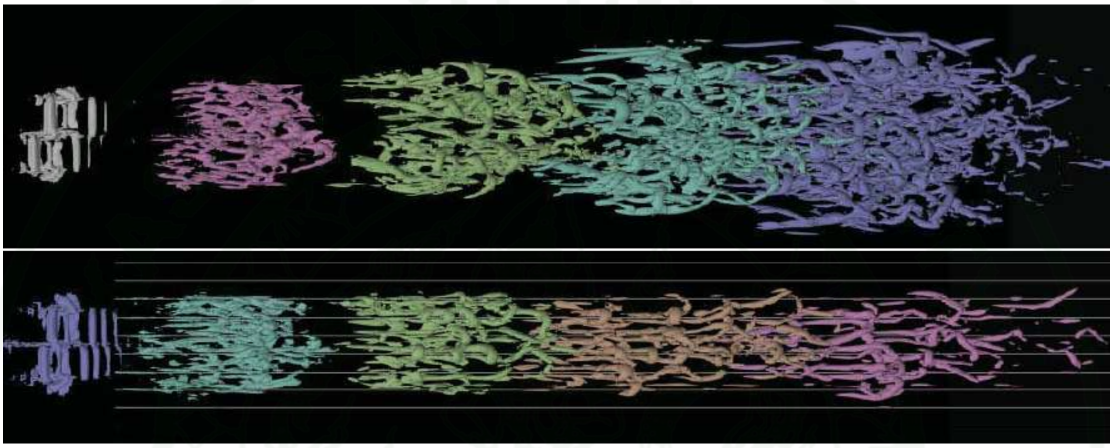

Figure 35 Evolution of turbulent spot over flat plate (upper) and damping fins.

Source: Chu *et al*. (2010)

Fig. 36(a) and (b) show the evolution of turbulent spot on a regular flat wall and spanwise slip wall, respectively. In both cases, similar hairpin structures are observed. The spanwise slip wall case produces more hairpins and grew faster in the streamwise direction, mostly by the trailing edge of the spot. However, the spots propagate downstream with nearly same spanwise spreading rates. The characteristics of turbulent spot over turned riblets wall are also observed as shown in Fig. 37. In the figure, black solid lines mark the spreading of the spot over flat wall. On the riblets wall, the spanwise spreading of the spot seems to be reduced. Furthermore, they found that, at the wing tips, spanwise vorticity is turned into streamwise vorticity by the tilting terms. This is a cause of turbulent spot spreading, localized near the wall in the spot wingtips.

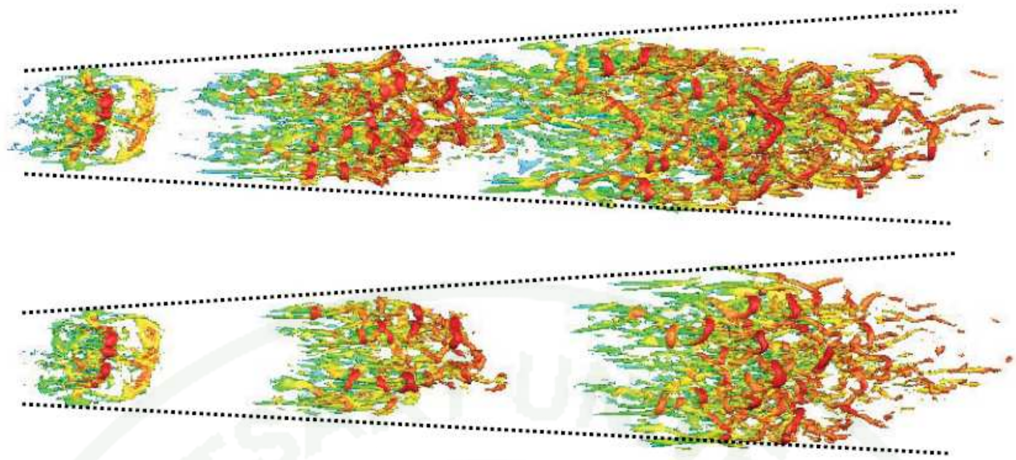

Figure 36 Turbulent spot over spanwise slip wall (upper) and normal flat wall (lower).

Source: Chu *et al*. (2010)

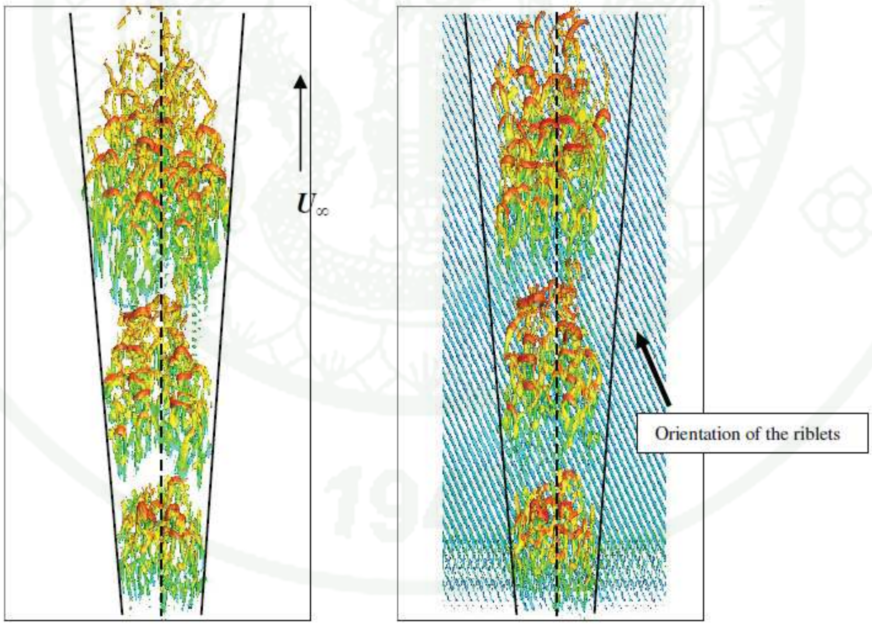

Figure 37 Turbulent spot over regular flat wall (left) and turned riblets (right).

Source: Chu *et al*. (2010)

Chernoray *et al*. (2012) confirm these results and further indicate that the riblets prevent the transformation of the Λ-structure into a turbulent spot. This leads to a decay of this perturbation, not only the spreading rate but also its amplitude as depicted in Fig. 38.

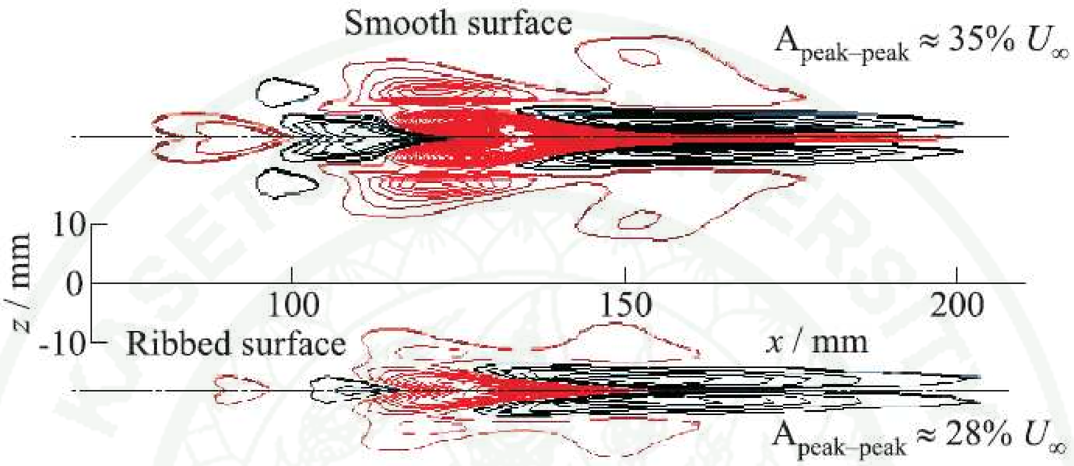

Figure 38 Contour diagrams of constant velocity fluctuations on the smooth (upper) and ribbed (lower) flat plate.

Source: Chernoray *et al*. (2012)

MATERIALS AND METHODS

Materials

In this chapter, the design and role of the low turbulent water tunnel is presented. Details of subsystems, employed through the experiment are also explained. Finally, the flow conditions under various adverse pressure gradients are described.

1. Low free stream turbulence water tunnel

The closed loop low free stream turbulence water tunnel was used in the present study to investigate the flow and heat transfer characteristics of turbulent spot under bypassed boundary layer transition. Fig. 39 shows the model of the low free stream turbulence water tunnel. Its structure was split into 4 primary sections, which were receiving tank, flow conditioning section, contraction section, and test section. The receiving tank was used as water reservoir with capacity of 900 liters for the present study. A 2.5 HP centrifugal pump was installed at the most upstream of the system to supply the continuous flow over flat plate at Re, varying from 50,000 to 187,500 based on the streamwise distance of 0.6 m from leading edge of the plate. Reduction in Re was possible by adjusting the globe valve at the rear part of test section. The first part of the tunnel was supply tank, functioning as the water container for the main flow. The most energy of the high flow rate and turbulence of the water, boosted by the water pump, were absorbed by this section.

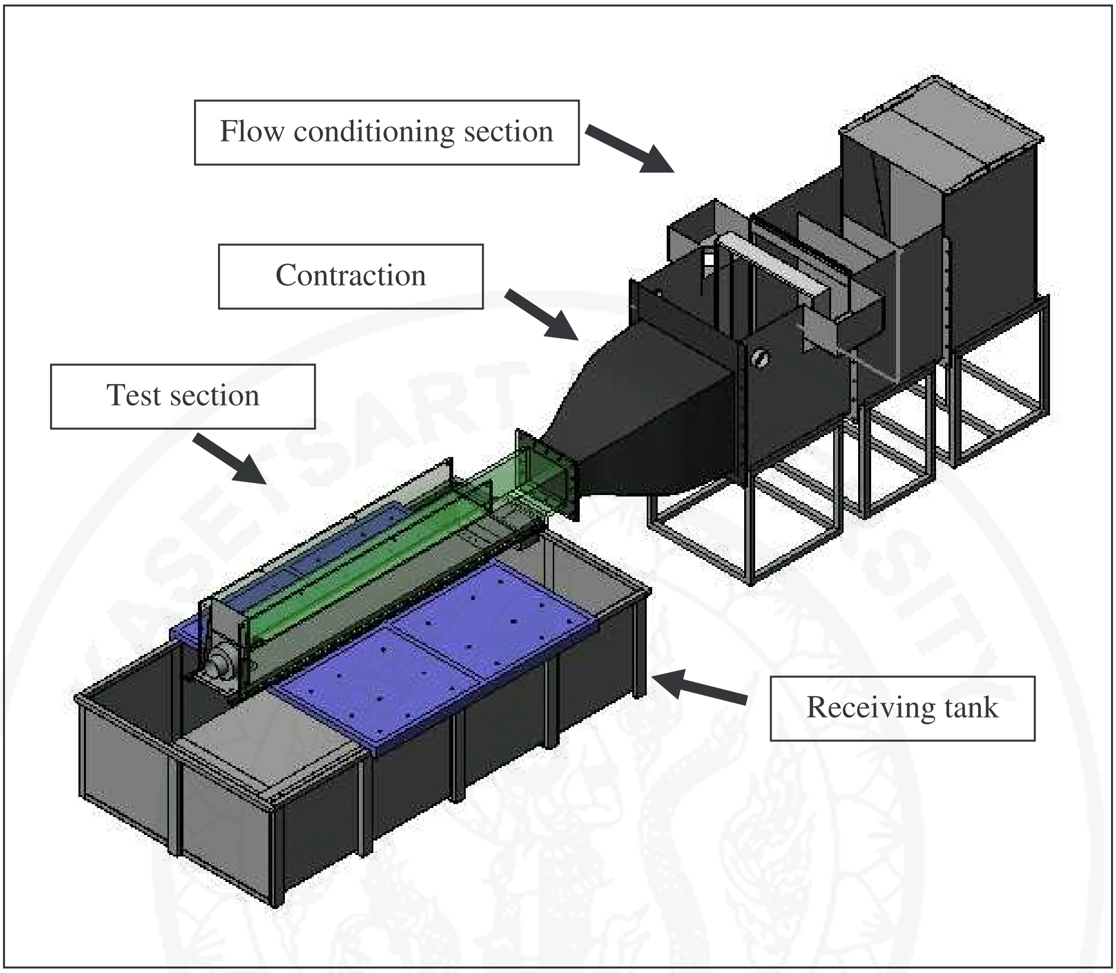

Figure 39 Model of the low free stream turbulence water tunnel.

The flow conditioning section was installed between the supply tank and the contraction as shown in Fig. 40. In this section, the turbulence of flow was decreased until it satisfied the appropriate flow condition. This section is consisted of filters, honeycomb and screens. Water filter was made from synthetic fiber. It was installed at upstream of honeycomb to filter all dirt and particles before the water flows through the test section. Furthermore, the thick filter fully prevents the excess turbulence of the main stream. The uniform flow direction was ordered by honeycomb, constructed from small pipes, having diameter and length of 0.012 m and 0.08 m, respectively. The screens were installed before the entrance of contraction. By this part, the turbulent intensity of the free stream flow was reduced.

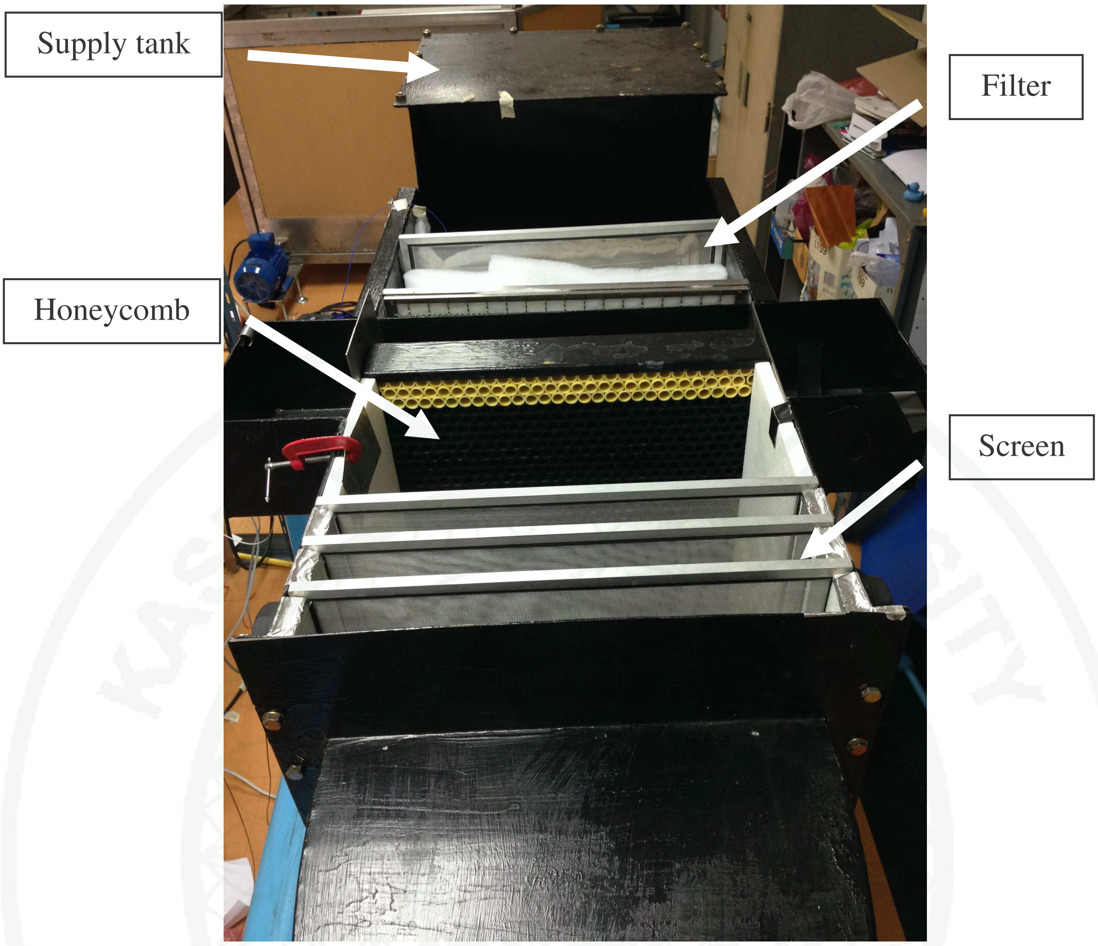

Figure 40 Flow conditioning section of the water tunnel.

The role of contraction section was to increase the mean free stream velocity while the fluctuating velocity was decreased by the influence of contraction ratio, following Batchelor (1970). In the recent study, the wall shape of the contraction was established by 4^{th} orders-polynomial equation, derived under the boundary conditions at both inlet and outlet, following Rassame *et al*. (1998). When the equation was governed, both upside-downside and left-right side shapes of the contraction surface were obtained in Fig. 41.

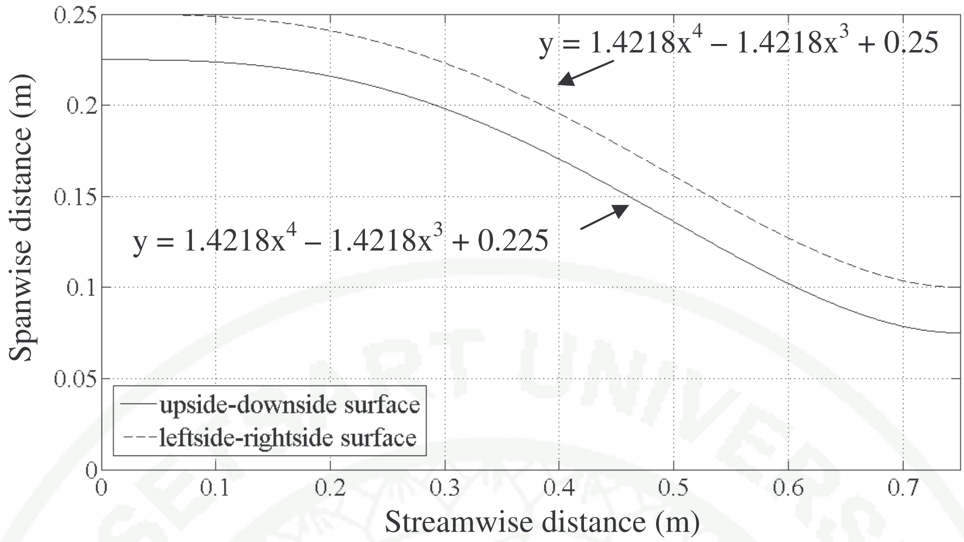

Figure 41 Structural shape of the contraction.

The experiment was carried out in the test section, which has a section of 0.2 m wide by 0.15 m high. It was made from 10 mm thick of Perspex to strengthen its structure. The early stage of the flow had been particularly bled out to refresh a new boundary layer along leading edge of the flat plate as shown in Fig. 42. During experiment, the aluminum plate was heated by 9 strip heaters, closely arranged below the heated plate to perform an isothermal surface under thermal boundary layer. All heaters were discretized for partly control by Proportional-Integral-Derivative, PID controllers. Local temperature signals were measured from three stations of type-K thin leaf thermocouple, at 40, 58 and 78 mm from leading edge. Underneath the heaters, a thermal insulator with high thermal resistance was laid to prevent unwanted loss power. Two aluminum rectangular bars were also assembled below to support both heaters and the insulator over air gap. A black PVC sheet with thickness of 100 μm was well bonded on the top of aluminum surface. With the different thermal conductivity, it was found that the plastic sheet plays an important role of thermal damper. Hence, it was possible to perform a continuously constant temperature contour on heated surface.

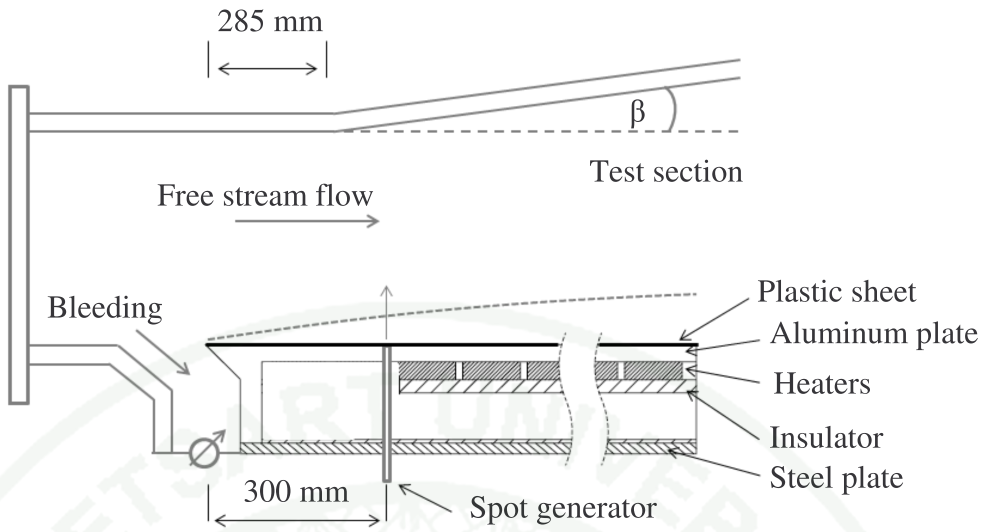

Figure 42 Test section of the water tunnel.

Spot generator was set up at 300 mm downstream from leading edge. This system was directly controlled by Programmable Logic Controller, PLC board. Instability was induced by injecting water through a 1 mm diameter hole using solenoid valve as depicted in Fig. 43. From the diagram, it is found that a water tank is set up to reserve the water of this injecting system. Before the pulsing water is injected, a diaphragm tank, receiving the adjustable air pressure from an air pump, would stabilize the water pressure in the pipe line. Thus, the pressure of injecting water was kept constant by this auxiliary system.

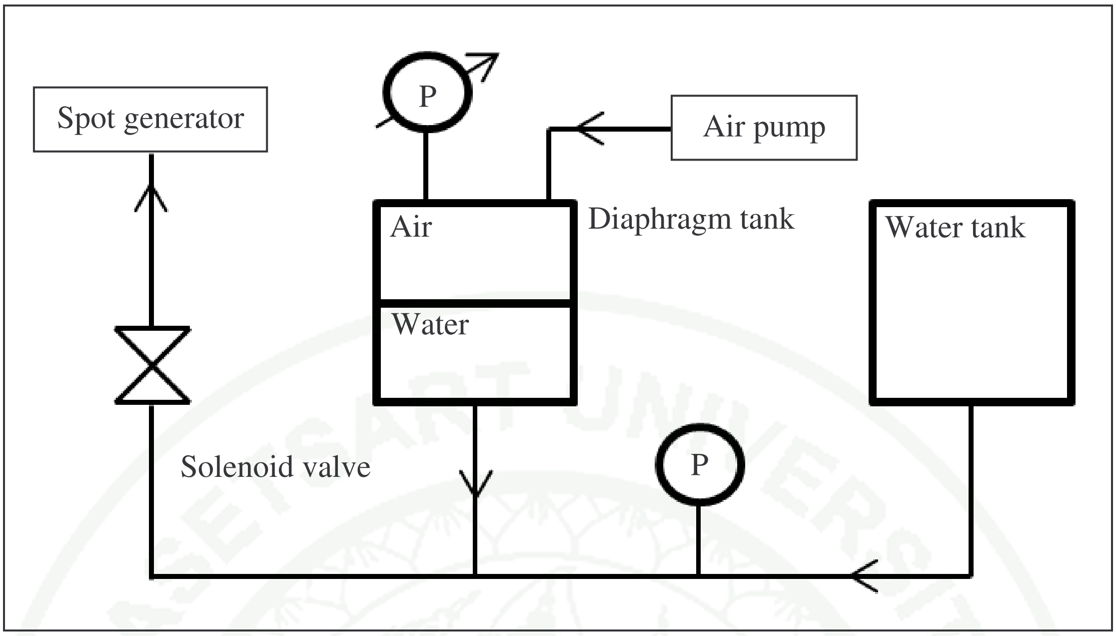

Figure 43 Turbulent spot generating system.

In the present experiment, the study was roughly separated into two types, the investigation of turbulent spot on the surface and within the flow. Thus, the optical system was manipulated differently to satisfy the needed conditions of each visualization technique. In the study of thermal footprint of turbulent spot, the induced flow was clearly exhibited by the liquid crystals, coated of about 20 μm thick on the top of plastic sheet. The used TLCs were micro-encapsulated Chiral Nematic type, commercially manufactured by Hallcrest. Its active range started from 27°C and ended up at 29°C. It was mixed with CC300 binder to upgrade the degree of water resisting by the fraction of 3 parts of binder : 1 part of LCs. On the most top, a thin layer of clear varnish was over-coated to prevent the degradation of reflective property by water. Two 70 watts-fluorescence bulbs with diameter of 1 inch were assembled besides test section as shown in Fig. 44. Their white light, containing all required spectral wavelengths from red to blue was fully shined on the coated plate by glossy reflectors. A handy video camera was mounted in elevation of 1.5 m above test surface to acquire series of image.

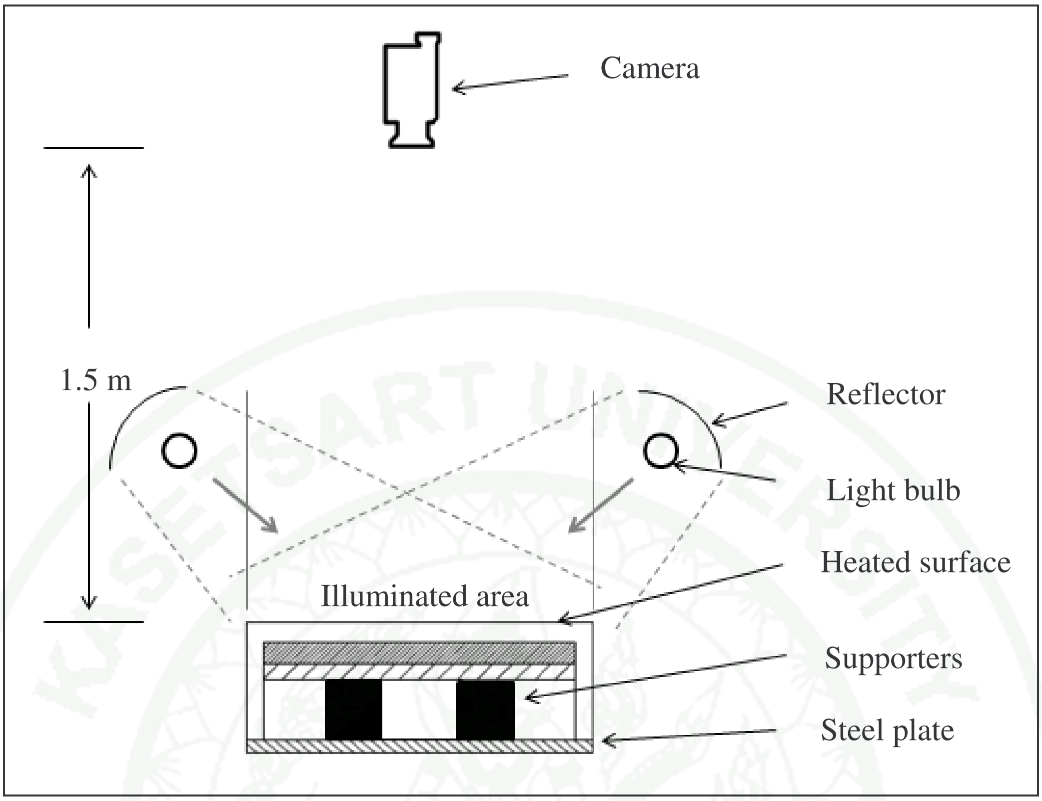

Figure 44 Optical set up for the test of coating liquid crystals.

The study of turbulent spot interior within the flow was carried out under the optical setup, using LED diodes. The released light was continuously white color, suitable for this visualization technique. The LED diodes were cold light, ensuring no excess heat from the light that transmitted to the considered fluid. The thin light sheet of approximately 1 mm was established by 1 mm slit that was mounted by the distance of 40 cm from the diode. More light intensity could be prepared by increasing a number of LED diode. In the present study, eight LED diodes were utilized for the light, which has the length of 30 cm. Nikon D90 CCD-camera, mutually employed with f 1.8 lens to grab the series of image during turbulent spot evolution in both top and side views as shown in Fig. 45 and 46, respectively. Through the experiment, distance between the camera and the light plane was at 1.5 m.

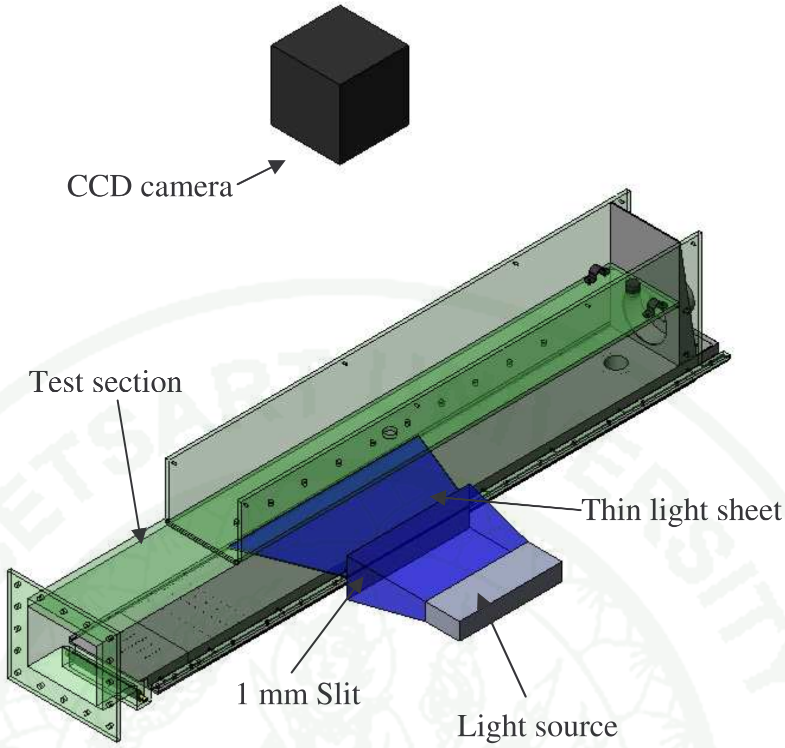

Figure 45 Optical set up when turbulent spot was observed from top view.

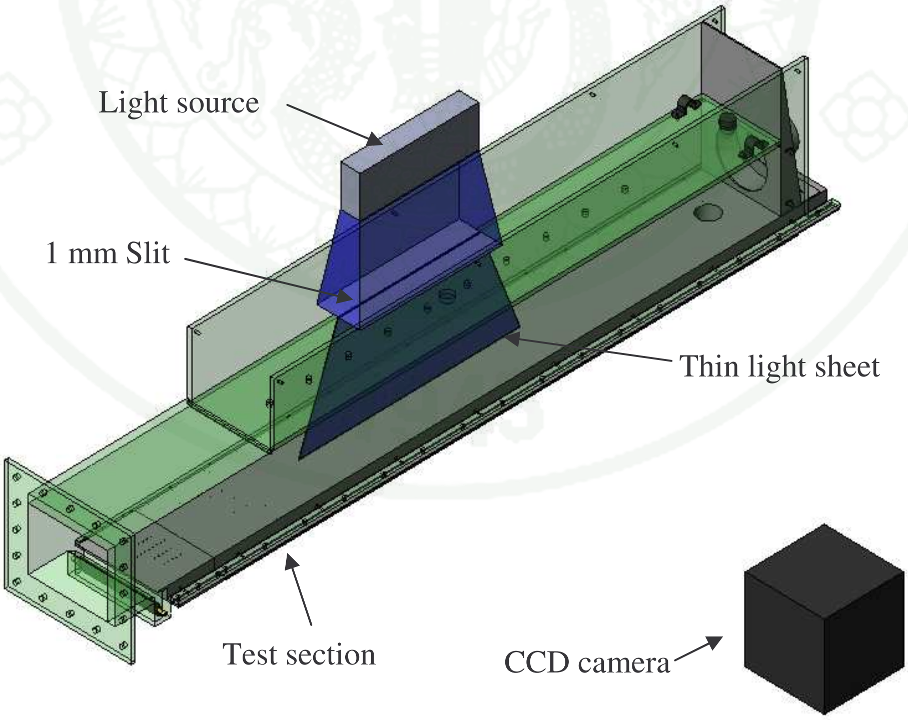

Figure 46 Optical set up when turbulent spot was observed from side view.

By this technique, structure of turbulent spot was visualized by both milk solution and slurry liquid crystals that were released from the most upstream portion of the test plate via holes of 1 mm diameter. The milk solution was provided by mixing milk and water by fraction of 5 : 1. It is presumed that fattiness of the milk retards diffusion of the dyed solution into the main bulk of water. In the mean time, it provides the condition of good visibility due to its high reflective properties. Moreover, milk's density and dynamic viscosity are between 1027 – 1033 kg/m^3 and 0.0015 Ns/m^2 which are very close to the water, after Hui (2007). Meanwhile, the concentration of slurry liquid crystals in the water was at 1% by weight. The solution was kept in the dye chamber, installed underneath the plate near leading edge as shown in Fig. 47. The pressure was set by the same method of spot generating system. However, the sedimentation of slurry liquid crystals must be prevented by adding a small pumping line to the chamber. Further information in this visualization technique could be found in the published reports of Elder (1960), Cantwell *et al*. (1978), and Gad-El-Hak *et al*. (1981). When all components of the low free stream turbulence water tunnel had been assembled as shown in Fig. 48, the flow conditions will be reported in the next topic.

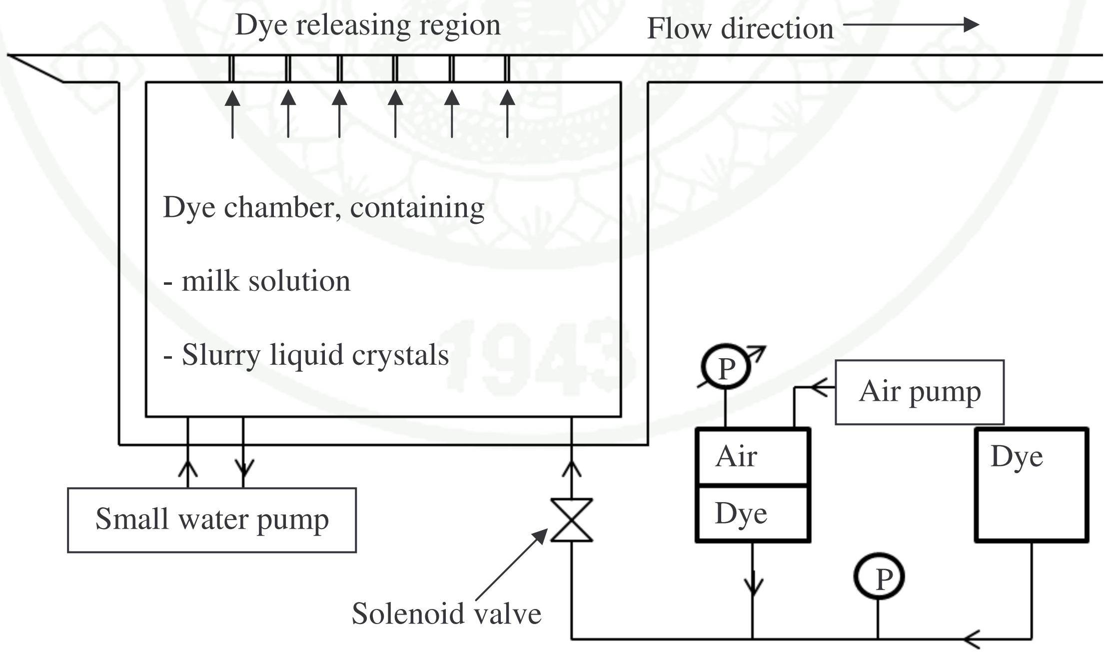

Figure 47 Dye releasing system.

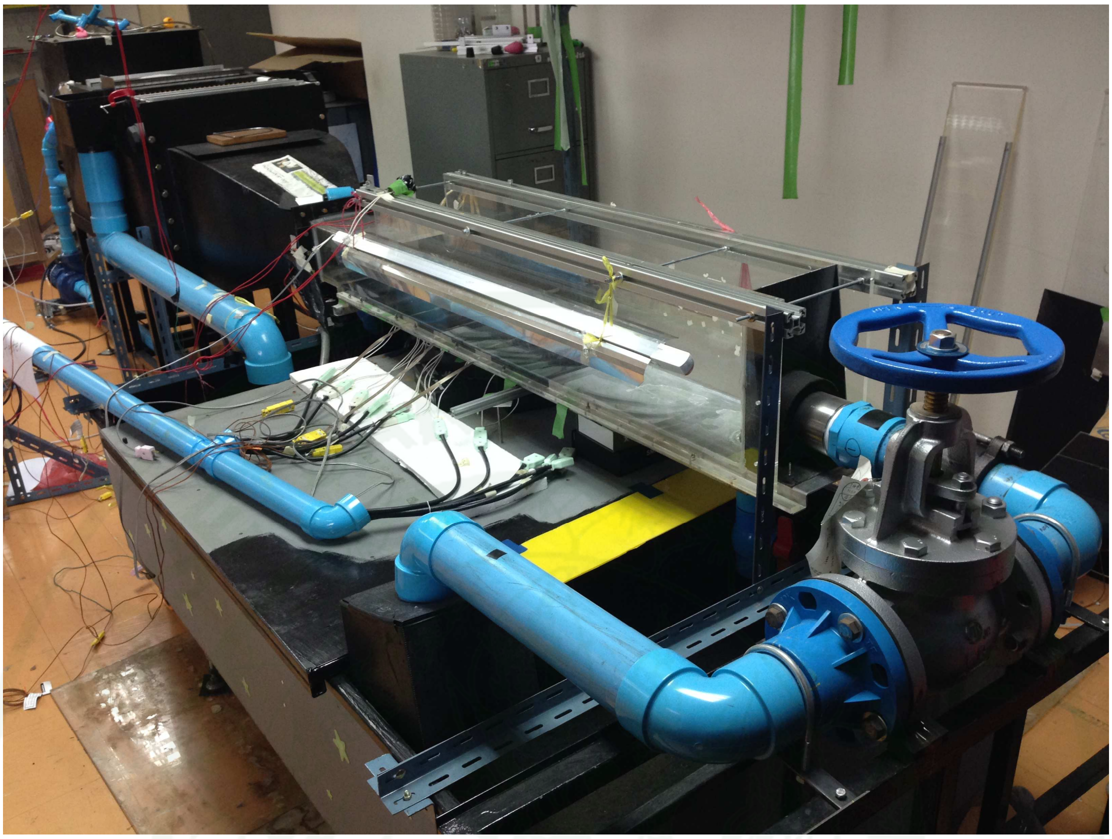

Figure 48 Low free stream turbulence water tunnel.

2. Flow conditions

As informed previously, one of the most important parameters that affect on the boundary layer transition is pressure gradient along streamwise direction. Hence, this study focuses on the characteristics of artificially generated turbulent spot under the influence of zero, mild, and strong adverse pressure gradients, established by tilting the roof of test section as shown in Fig. 42. The pivot of the tilted roof was at 285 mm downstream from leading edge of the test plate so the effect of pressure gradient covered almost entire of the test plate including spot generator. The level of pressure gradient depended on the elevated angle, β of the tilted roof. In this study, mild pressure gradient was set at 2° while strong level was at 4° from horizontal line. The free stream velocity at upstream of the tilting point was kept constant at 0.17 m/s through the experiment. At downstream of the pivot, the free stream velocity at various points along the plate was measured using turbine flow meter. The distributions of free stream velocity under mild and strong adverse pressure gradients are illustrated in Fig. 49.

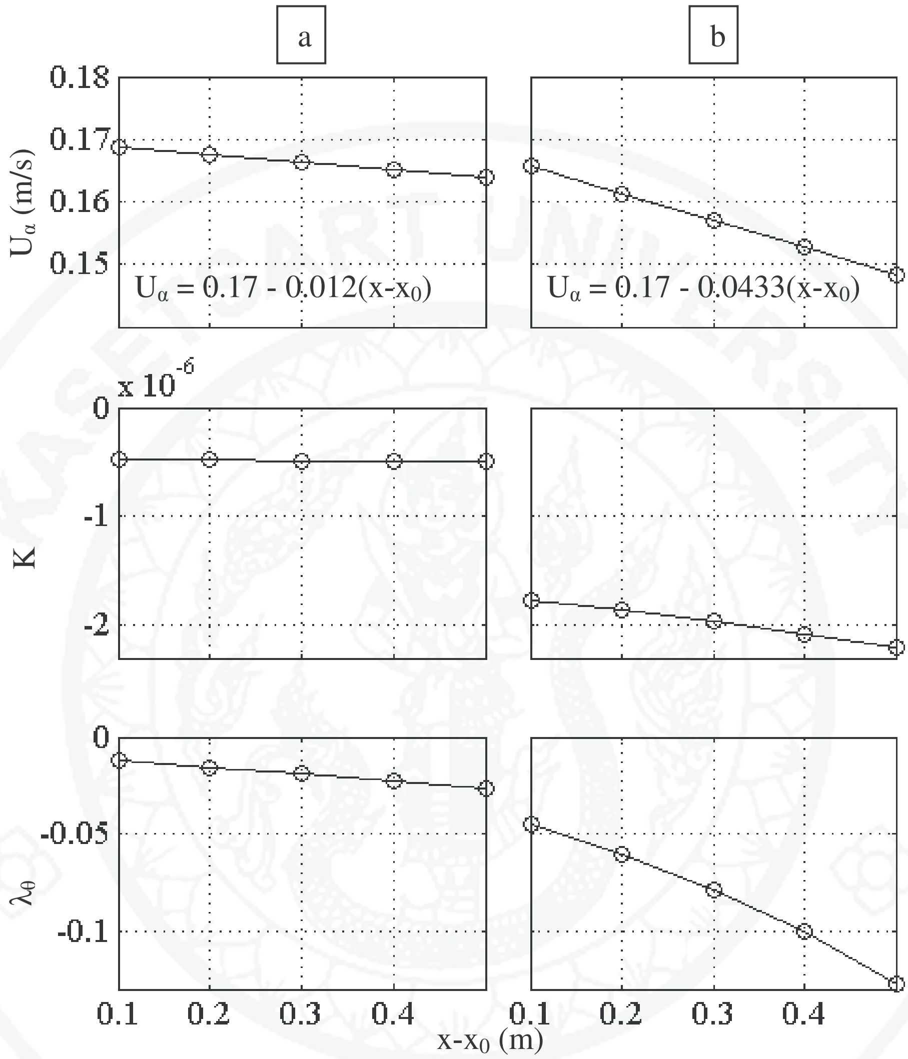

Figure 49 Flow conditions under (a) mild pressure gradient and (b) strong pressure gradient.

From the distribution of free stream velocity under pressure gradient as shown in Fig. 49(a), it was represented by Howarth's profile following Howarth(1938) as :

$$U_\alpha = U_0 - a(x - x_0) \tag{7}$$

where U_α is the local free stream velocity under pressure gradient, U_0 is the velocity at upstream of the pivot, a is a constant, and x_0 is the distance from leading edge of the test plate to the tilted point. Besides, Fig. 49 also showed the distribution of acceleration parameter (K) and pressure gradient parameter defined by Thwaites (λ_θ), respectively. Their expressions were found as :

$$K = (\upsilon / U_\alpha^2) \cdot (dU_\alpha / dx) \tag{8}$$

$$\lambda_\theta = (\theta^2 / \upsilon) \cdot (dU_\alpha / dx) \tag{9}$$

where υ is kinetic viscosity, and θ is the laminar boundary layer momentum thickness - θ was calculated from the standard correlations by Thwaites as :

$$\theta^2 = \theta_0^2 + (0.45\upsilon / U_\alpha^6) \int_{x_0}^{x} U_\alpha^5 dx \tag{10}$$

where θ_0 is the momentum thickness at $x = x_0$. It was yielded from :

$$\theta_0 = 0.671 x_0 / \sqrt{\mathrm{Re}_{x_0}} \tag{11}$$

where Re_{x0} is the Reynolds number based on the distance from the leading edge to the tilted point. From Fig. 49, it was found that the acceleration parameter and pressure gradient under the strong pressure gradient outstandingly decreased, comparing with the mild level. Moreover, the obtained turbulence intensity of the freestream flow was found at 0.925% using Dantec fibre film probe type 55R11. Measurements of velocity profile under unheated laminar boundary layer were conducted at 0.5 m from the leading edge. With the increased adverse pressure gradient, the velocity at near wall region as shown in Fig. 50 is less than the profile of Blasius. It shows that this flow condition is very near to the separation of the flow. At this point, boundary layer thicknesses were found at 8.6, 9.4, and 10.6 mm at zero, mild, and strong pressure gradients, respectively. The obtained λ_θ under strong pressure gradient were found at -0.06037. It was more than a critical value of -0.082, which is the verge of separation, given by Thwaites.

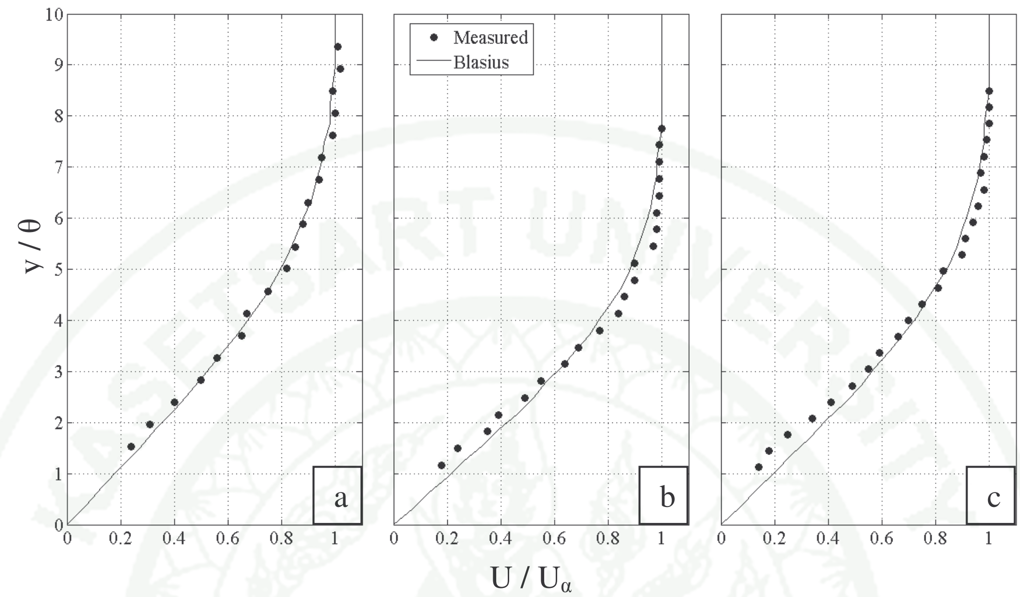

Figure 50 Velocity profiles under various adverse pressure gradients at streamwise distance of 0.5 m from leading edge of the heated plate.

Methods

In this chapter, the use of both coating and slurry thermochromic liquid crystals are described. When temperature of thermal footprint is obtained by the technique of coating liquid crystals, analytical solution is needed to convert temperature domain into convective heat transfer coefficient and heat flux. Thus, deduction of heat transfer coefficient and heat flux is also presented. Besides, technique called "Centroid Averaging Technique", developed to construct the probable structure of turbulent spot on different plane is proposed.

1. Image processing and calibration process.

Coating and slurry thermochromic liquid crystals were employed in the present experiment to capture substructure of artificially generated turbulent spot. Liquid crystals are substance that is in phase of liquid but it is responsible for color reflecting behavior like crystals. Over few decades, it has been used as fully temperature sensors in variety of flow visualization applications. TLCs are capable to selectively reflect human-eyed wavelength as a function of temperature. Generally, it appears as thick milky matter and exhibits coloring birefringence when the temperature reaches its active range. It is usually used as spray to cover a black surface. As temperature increases, the coated surface turns red, yellow, green and blue. It becomes clear again above the upper limit. It is found that these color changes are reversible and repeatable if its molecules are not physically damaged and chemically degraded. Its responsible time is only 3 ms that is short enough for fluid and heat transfer applications. However, encapsulated process can strengthen the molecule of TLCS so it is typically conducted to fix these damaging issues. Selectable range of commercial TLCs starts from 30 °C to 120 °C in a bandwidth of 0.5 °C to 20 °C. The color, scattered by liquid crystals was recorded in RGB format. The RGB system is the basic color space, containing three primary colors as depicted in Fig. 51(a). Although there is an existence of various color spaces, Hue, Saturation, Intensity – HSI format is often selected in order to precisely present the appearing color as shown in Fig. 51(b). Hue varies from 0 to 1, corresponding to a pure color component from red, until magenta, and then back to red again. Intensity, numerically, determined as the average value of red, green, and blue components indicates overall brightness of the color. Saturation displays purity/grayness of color. Purer colors have a saturation value close to 1. In the current study, Hue signal in HSI color space was used to present the occurring color, scattering by TLCs while Saturation and Intensity were mutually employed to improve their quality. All recorded RGB data were later extracted and directly converted to HSI color map by following relations, presented by Russ (2002).

$$H = \cos^{-1}(Z) \qquad \text{if} \qquad G \geq R \tag{12}$$

$$H = 2\pi - \cos^{-1}(Z) \qquad \text{if} \qquad G < R \tag{13}$$

$$Z = (2B - G - R)/(2 \cdot \sqrt{(B-G)^2 + (B-R)/(G-R)}) \tag{14}$$

$$I = (R + G + B)/3 \tag{15}$$

$$S = 1 - \min(R, G, B)/I \qquad \text{if} \qquad I > 0 \tag{16}$$

$$S = 0 \qquad \text{if} \qquad I = 0 \tag{17}$$

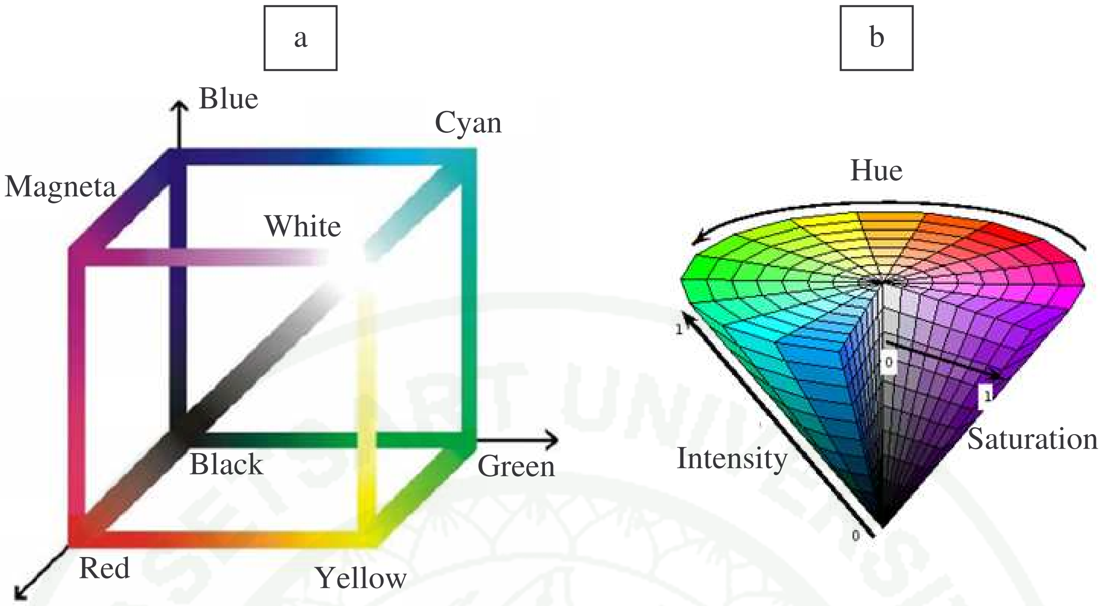

Figure 51 (a) Diagram of RGB color space and (b) Diagram of HSI color space.

Before the experiment on the boundary layer transition was carried out, a color-temperature relation of TLCs must be established as calibration process. The constant visible spectrums on tested surface were collected by the recorder with the frame rate of 25 frames per second. In the test of coating liquid crystals, the elevated temperature started from 26.6 °C to 28.7 °C in every 0.3°C. In each step, the heated surface was kept to be constant for about 20 minutes. Their color was initially defined as percentage of red, green, and blue signals that blend together in RGB color space. When Hue signal was extracted from the color at the specified temperature, the accurately calibrated correlation was performed as

$$T = 58.48270856 \cdot H^3 - 61.24566302 \cdot H^2 + 23.15642190 \cdot H + 23.89758685 \quad (18)$$

Therefore, this equation was responsible for the change of Hue value to the local temperature as shown in Fig. 52, through the experiment. The goodness of fit was found at $R^2 = 0.9987$.

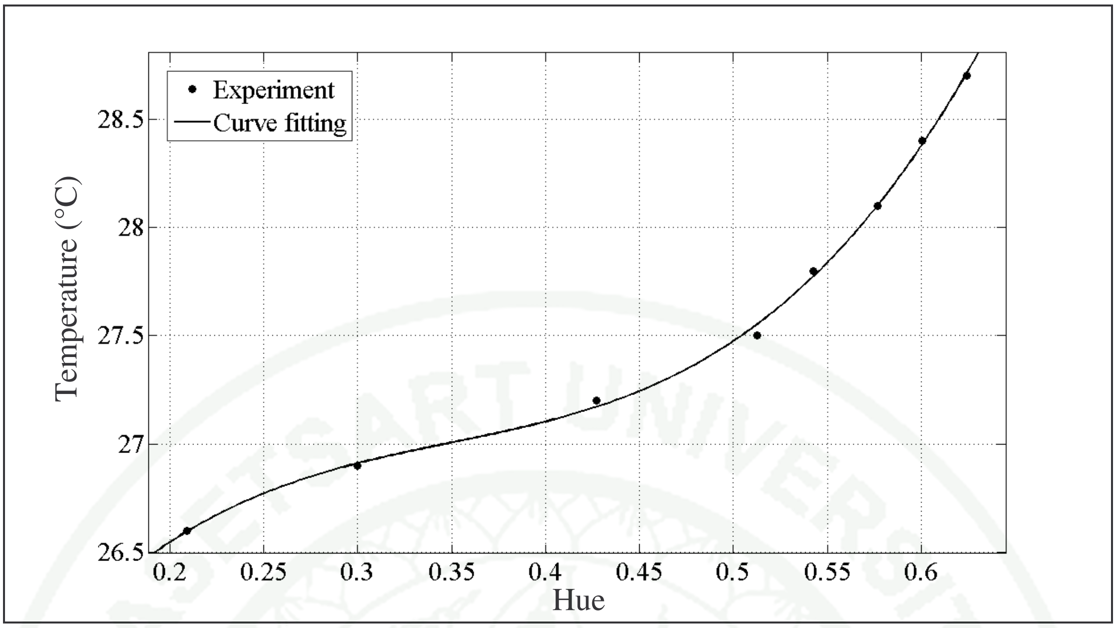

Figure 52 Calibration curve of coating liquid crystals.

A specific system was built for calibration process of slurry liquid crystals as depicted in Fig. 53. This was established because the test section was too large to contain the dispersed solution of slurry liquid crystals for calibration process. However, optical set up, the primary error factor after Dabiri (2008), was maintained as in the experiment on boundary layer transition. The test chamber, having the width of 3 mm was filled by the prepared solution. Perspex, used to enclose the working fluid has thickness of 10 mm in the reason of the good sight and thermal insulator. Another side of the chamber was 3 mm thick aluminum plate. This aluminum plate was in between the solution and flowing water, circulated by a small water pump. Via this plate, heat was transferred from the circulating water to calibration chamber. Contours of wavelengths were achieved by illumination of the white light as explained in the previous chapter. Elevated free stream temperatures during calibration were detected by thermocouple, mounted in the chamber. Every step in the calibration test, the solution was kept constant for about 20 minutes to reach steady state condition. The same as in the calibration process of coating liquid crystals, only color information in region at thermocouple tip was recorded at each specified free stream temperature. The temperature signal was directly sent to PID controller to control heater of 250 Watts, installed in water bath. Thus, relation between free stream temperature and the solution were found as shown in Fig. 54. From the test of the bypassed transition, the solution of TLCs was prepared with concentration of 1% by weight. When it was released from the dye chamber, the plate surface was fully covered by a thin film of the liquid crystal solution. After the spot initiation, the solution was dispersed through the spot body with the varied concentrations, which were less than 1%. Thus, the calibration process was conducted to yield the information of Hue-Temperature relation of the solution at different concentrations as shown in Fig. 54. Concentrations of 0.1% and 0.075% by weight of the liquid crystals in water were selected in this test and they showed the consistency between themselves. Moreover, the repeatable characteristic of liquid crystals was confirmed in this study. Therefore, the relation between hue and temperature was obtained as :

$$T = 178.34845345 \cdot H^5 - 272.36788106 \cdot H^4 + 163.24720985 \cdot H^3 - 8.44427302 \cdot H^2 + 7.90610586 \cdot H + 23.46747976 \tag{19}$$

where the goodness of fit was found at $R^2 = 0.9569$.

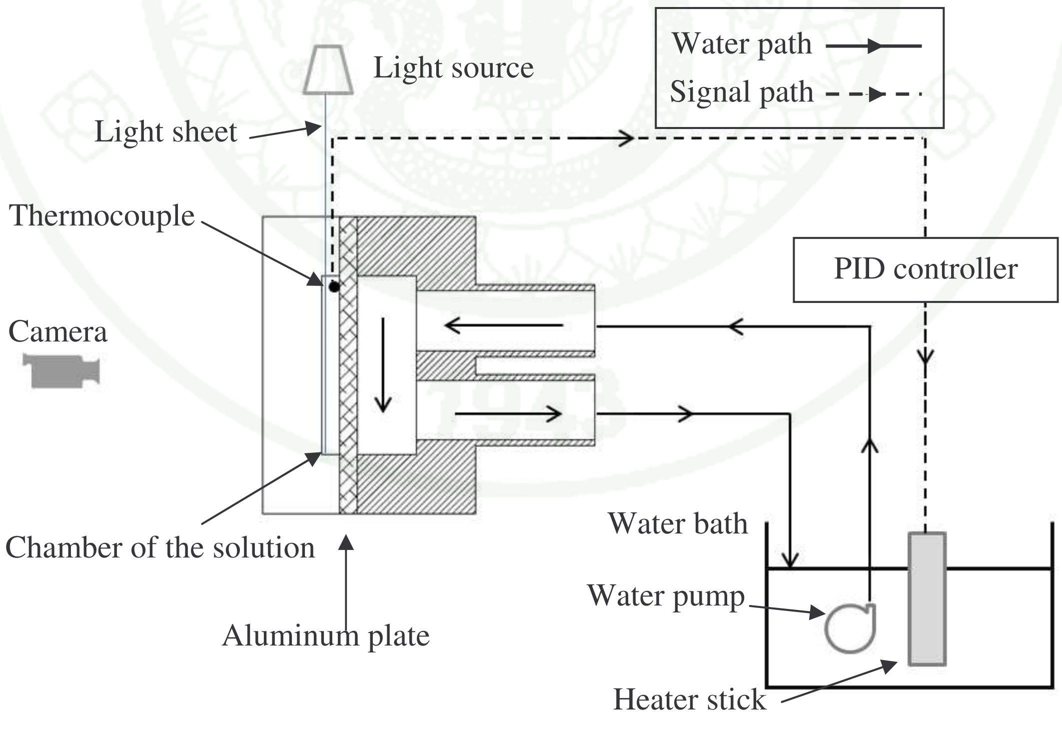

Figure 53 Calibration system.

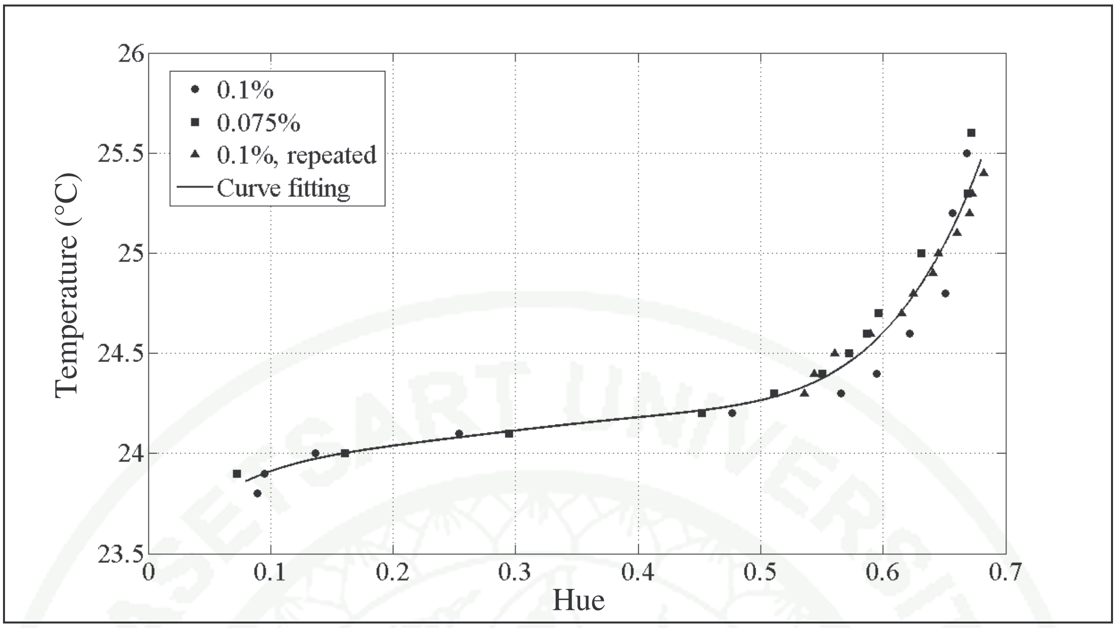

Figure 54 Calibration curve of slurry liquid crystals.

2. Deduction of convective heat transfer coefficient and heat flux.

It has been known that heat flux contours underneath turbulent spot can represent the shape of spot footprint, following Kittichaikarn *et al*. (1999). The determination of local convective heat transfer coefficient is necessary in order to obtain heat flux from principal relation of heat convection. There are many analytical solutions of transient conduction that is suitable for the application of coating liquid crystals. One of the most effective, developed from the finite difference equations, called "energy balance method". This approach enables to analyze many different phenomena, following Incropera *et al*. (2007) and Cengel (2003). Firstly, equation of conservation of energy is :

$$\dot{E}_{in} + \dot{E}_g = \dot{E}_{st} \qquad (20)$$

where $\dot{E}_{in}$, $\dot{E}_g$, and $\dot{E}_{st}$ are energy inflow, energy source, and energy storage, respectively. Six adjacent nodes from six directions will influence the energy exchange on central node without internal heat generation as :

$$\sum_{i=1}^{6} q_{(i)\to(m,n,o)}^{t+\Delta t} = \rho V C_p \frac{T_{m,n,o}^{t+\Delta t} - T_{m,n,o}^{t}}{\Delta t} \tag{21}$$

where q is rate of heat transfer, ρ, V, and C_p are density, controlled volume, and specific heat capacity of the plastic sheet, respectively. Δt is specified interval time between two consecutive images. All heat flows are assumed to be "into the node" because each actual heat direction is unknown. "Implicit" finite difference scheme is found as a backward-difference approximation to the time derivative. This scheme provides not only reduction in the amount of computational time but also unconditionally stable state. Unlike explicit, this solution needs no restrictions on Δx and Δt. In this study, a control volume of plastic sheet was established as the interior node m,n,o as shown in Fig. 55. Node m,n,o were considered at time of t and t + Δt, referring to 2 consecutive frames of recorded images. Energy exchange in four lateral nodes was influenced by heat conduction. The node subjected to the free stream flow on upper side. On this side, heat convection occurred and heat transfer coefficient was evaluated. Finally, lower side was adjacent to the aluminum plate. Temperature at this point was determined by :

$$T_{m,n,o-1} = \frac{q \cdot \Delta z}{k(\Delta x \cdot \Delta y)} + T_{m,n,o} \tag{22}$$

It should be noted that this method was conducted under the assumption that $T_{m,n,o-1}$ is constant. Thus, in order to find $T_{m,n,o-1}$, q could be directly obtained under the condition of laminar flow as in the basic relation of :

$$q = h_x (\Delta x \cdot \Delta y)(T_{m,n,o} - T_{\alpha}) \tag{23}$$

where h_x is a local heat transfer coefficient in laminar flow over flat plate and can be obtained from formulation of unheated starting length as :

$$h_x = \frac{0.332 \cdot \mathrm{Re}_x^{1/2} \cdot \mathrm{Pr}^{1/3}}{[1-(\xi / x)^{9/10}]^{1/9}} \cdot \frac{k}{x} \tag{24}$$

where Re_x is local Reynolds number. Pr is Prandtl number and ξ is the length of unheated starting section. Thus, $T_{m,n,o-1}$ would be substituted into Equation 21 to achieve the spatial distribution of convective heat transfer coefficient and heat flux.

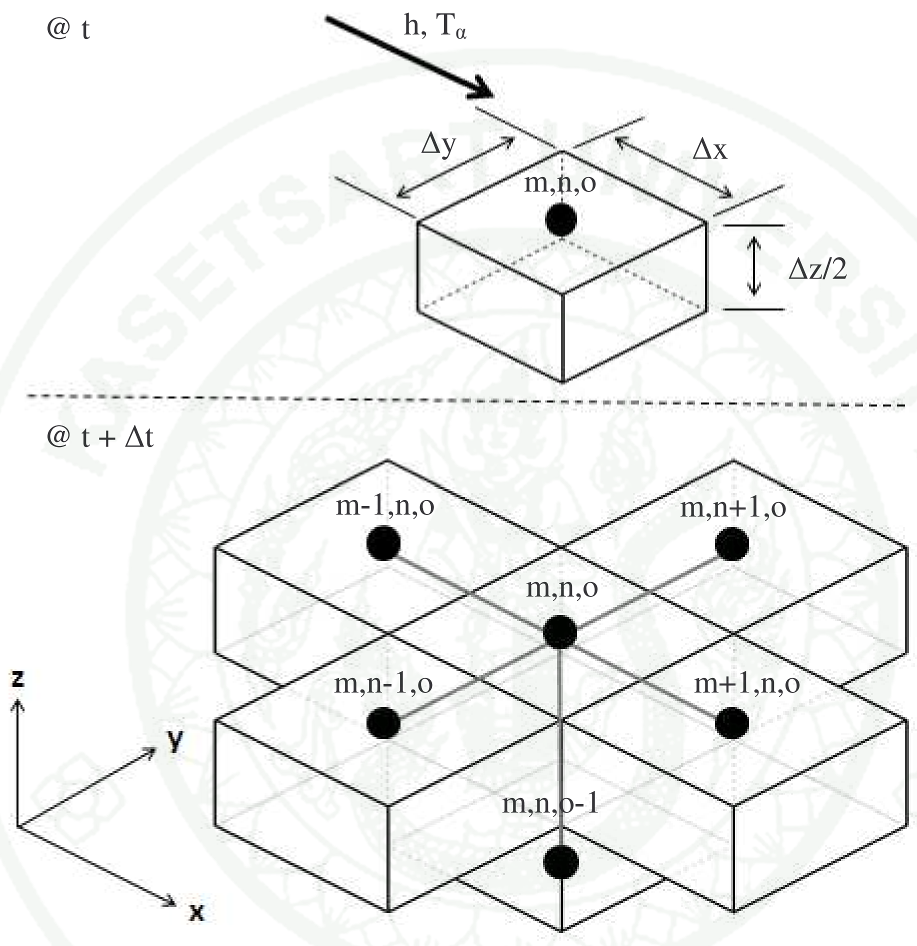

Figure 55 Map of adjoining nodes in implicit scheme.

3. Centroid averaging technique.

It has been known that boundary layer transition is covered by both unsteadiness and randomness. Information on turbulent spot substructures, provided by velocity and temperature distribution, was typically measured from different individual spots at the different measuring station and time. To identify a single large structure, averaging method must be implemented such as the ensemble-averaging method of velocity perturbation as reported by Wygnanski *et al*. (1982), Antonia *et al*. (1981), and Chong and Zhong (2005). Before the structure is constructed, the average is created by respect of the position of spot feature such as its leading edge, hump, trailing edge as well as the location of spot generator. After that, the signal traces were aligned at that specified feature. These results would reveal more details near the respective interface. This method was strongly effective on the space-time information, obtained by hotwire anemometer. However, as the substructure in space-space domain is investigated, the centroid of each individual structure should be focused. Thus, the centroid averaging technique was firstly proposed to find the instantaneous representative structure of turbulent spot. In the present study, 15 different individual turbulent spots were chosen for the determination. Fig. 56(a) shows five examples from all fifteen turbulent spots, directly yielded from the experiment. Their image quality was initially improved by method of background subtraction. Each component of R, G, and B signals of the spot image was directly subtracted by its background. It was found that only spot structure was detected and the sharp bound appeared as depicted in Fig. 56(b).

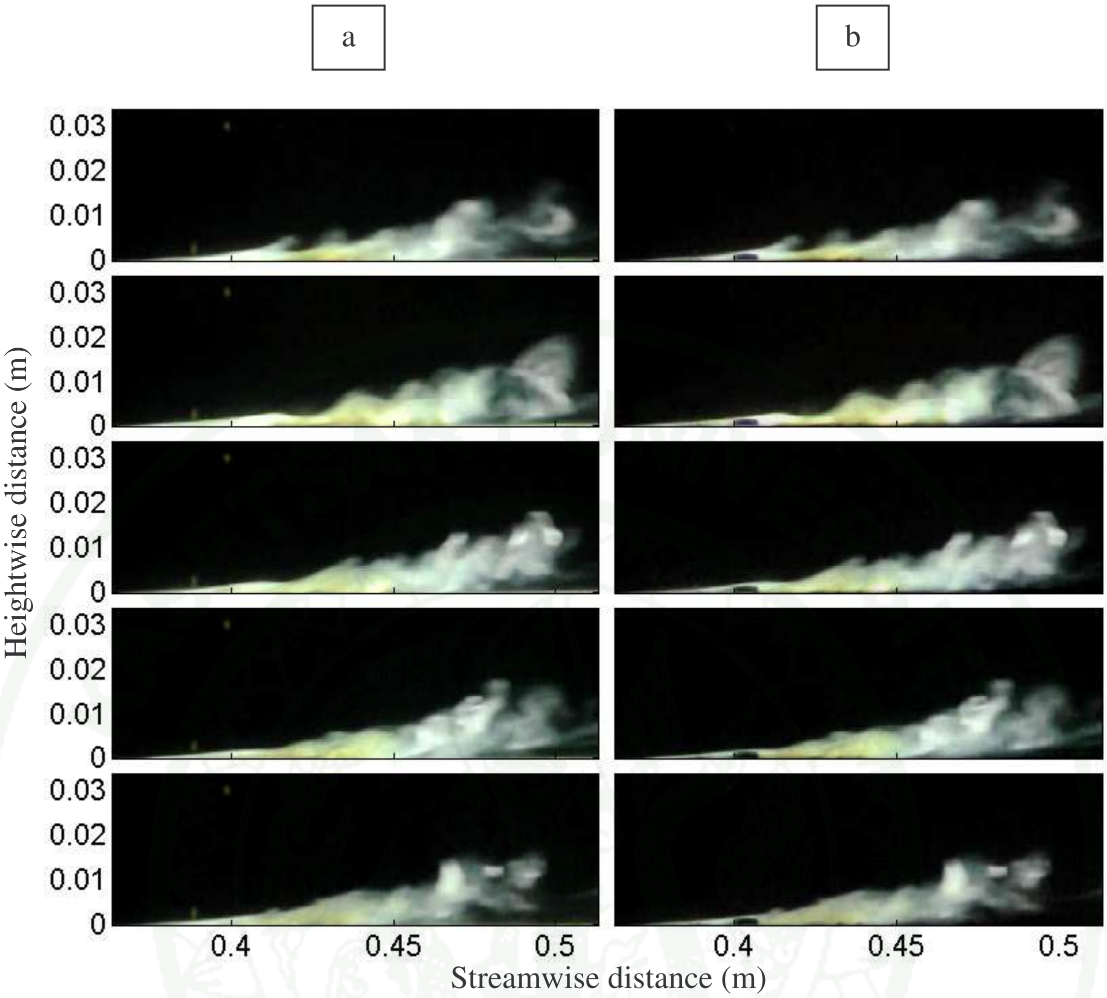

Figure 56 (a) Five individual turbulent spots., (b) Five individual turbulent spots after improvement using background subtraction process.

Fig. 57 shows the shape of five individual turbulent spots from Fig. 56(b). They were taken in the same domain and non-dimensionalized in both heightwise and streamwise direction by comparing to the obtained maximum distance of height and length, respectively. It was found that their structures were slightly different in shape and location. To align all structure reasonably, the centroid location of each structure was needed as reference point. Typically, in image processing method, the structure was discretized into small areas as pixel. It was used to approximate the centroid by :

$$\overline{X} = \frac{\sum_i A_i \overline{x}_i}{\sum_i A_i} \tag{25}$$

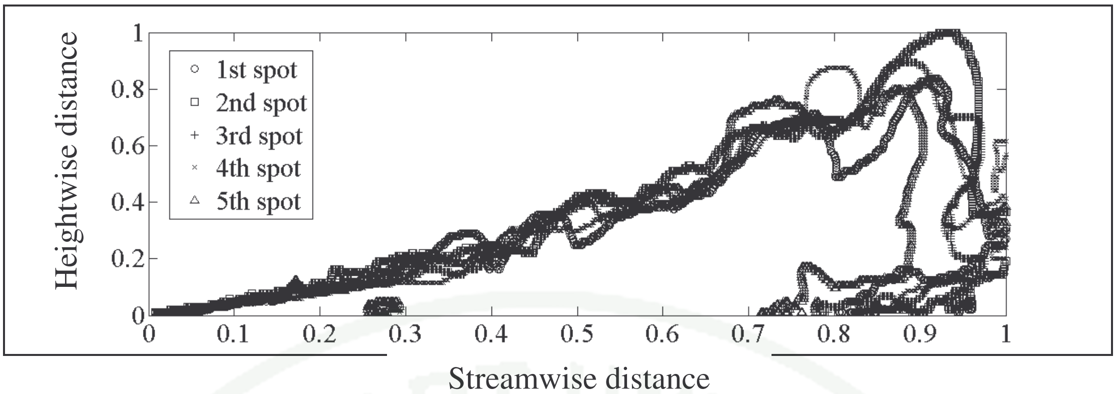

Figure 57 Shape of five individual turbulent spots in non-dimensionalized domain.

After a centroid of all structures was achieved, this point would be proposed as the final position of the obtained structure. It was the reference point that all centroids of each individual structure were shifted to. When the spot structures were aligned, point by point averaging was performed. However, the results show that a yielded laminar-turbulent interface was not clearly identified. Therefore, the threshold value was selected through a trial and error procedure until the interface between the laminar and turbulent region was identified and consistent to itself on all other planes.

RESULTS AND DISCUSSION

This chapter presents results, yielded from the current study. The investigation of turbulent spot structure was carried out by 3 different techniques. The first technique is the use of coating thermochromic liquid crystals to capture the characteristic of turbulent spot footprints on the test surface. In the second technique, milk solution was used as medium to obtain the shape of turbulent spot. And the last, slurry liquid crystals were released instead of milk into the test section to reveal thermal structure within spot body. The formation rate and thermal parameters of artificially generated turbulent spots were compared to those, reported by the other researchers. The effect of adverse pressure gradient on characteristics of turbulent spot was also discussed in this chapter.

1. Thermal footprints of turbulent spot

1.1 Thermal characteristics of turbulent spot footprint under zero pressure gradient

Fig. 58(a)-(h) show series of RGB images of the footprint underneath artificially generated turbulent spot, propagating downstream from left to right. It was found that the thickness of boundary layer at the spot generator, δ_0 was equal to 7 mm so the time could be directly normalized as $\tau = t / (\delta_0 / U_\alpha)$. Selected interval time was set to be 0.4 s or $\Delta\tau = 9.72$ that corresponds to 10 from 25 frames, grabbed in 1 second. The first image started at 0.8 s or $\tau = 19.43$ after disturbance injection. All consecutive images were recorded from 0.34 m to 0.6 m on streamwise direction. These corresponded to a normalized streamwise distance from 5.71 to 42.86 when it was defined as $(x - x_0) / \delta_0$. On y-axis, zero was set at midpoint and span out about 0.06 m laterally. This was equal to a normalized spanwise distance of 8.57 when it was defined as z / δ_0. Heated surface, initially showing uniformly blue color that was consequence of thermochromic liquid crystals started at the normalized streamwise distance = 4.29. Beyond unheated zone, it was found that turbulent spot occurred as a group of green streaks, convecting downstream. An appearance of each green streak apparently exhibited unsteady characteristic under random effect of transitional boundary layer. However, with the interference of saturation and intensity signal, color in RGB colormap couldn't be purely illustrated.

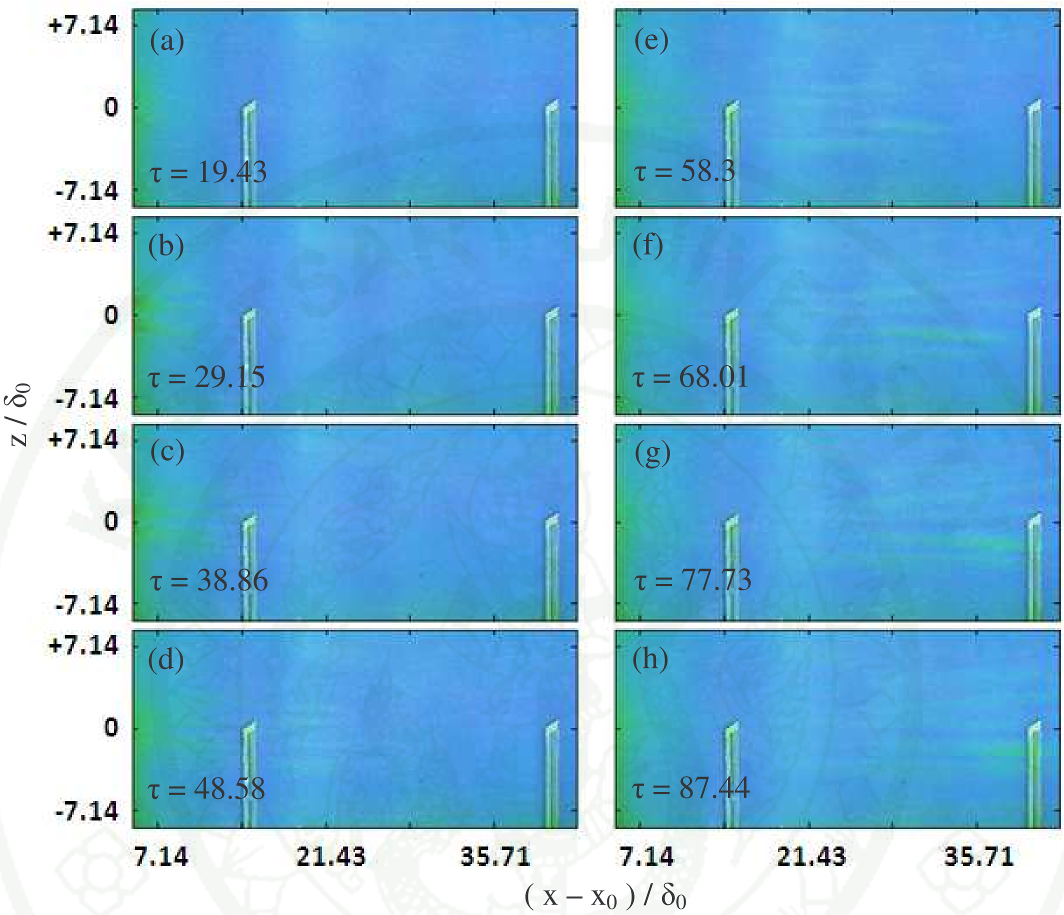

Figure 58 RGB images of thermal footprint under zero pressure gradient.

The problem of perturbed signal was solved by transforming color system from RGB to HSI. It was found that Hue component from HSI presented the pure color, scattered by TLCs as depicted in Fig. 59(a)-(h). Without interference of Saturation and Intensity components, Hue contour could provide a clear vision on streaky structure. Besides, on the left side of each image, there was a green strip that lay along spanwise direction. This is transition in thermal zone between heated surface and unheated area, preceding the recorded zone. Also, the color signal on both thermocouple, on 0.4 and 0.58 m from leading edge of the test plate, were presented incorrectly. Unlike the blacken surface of the plastic sheet, liquid crystals were coated directly on the shining metal of thermocouples. This caused an error when Hue signal was extracted from this region. Therefore, these issues were screen out by image processing technique.

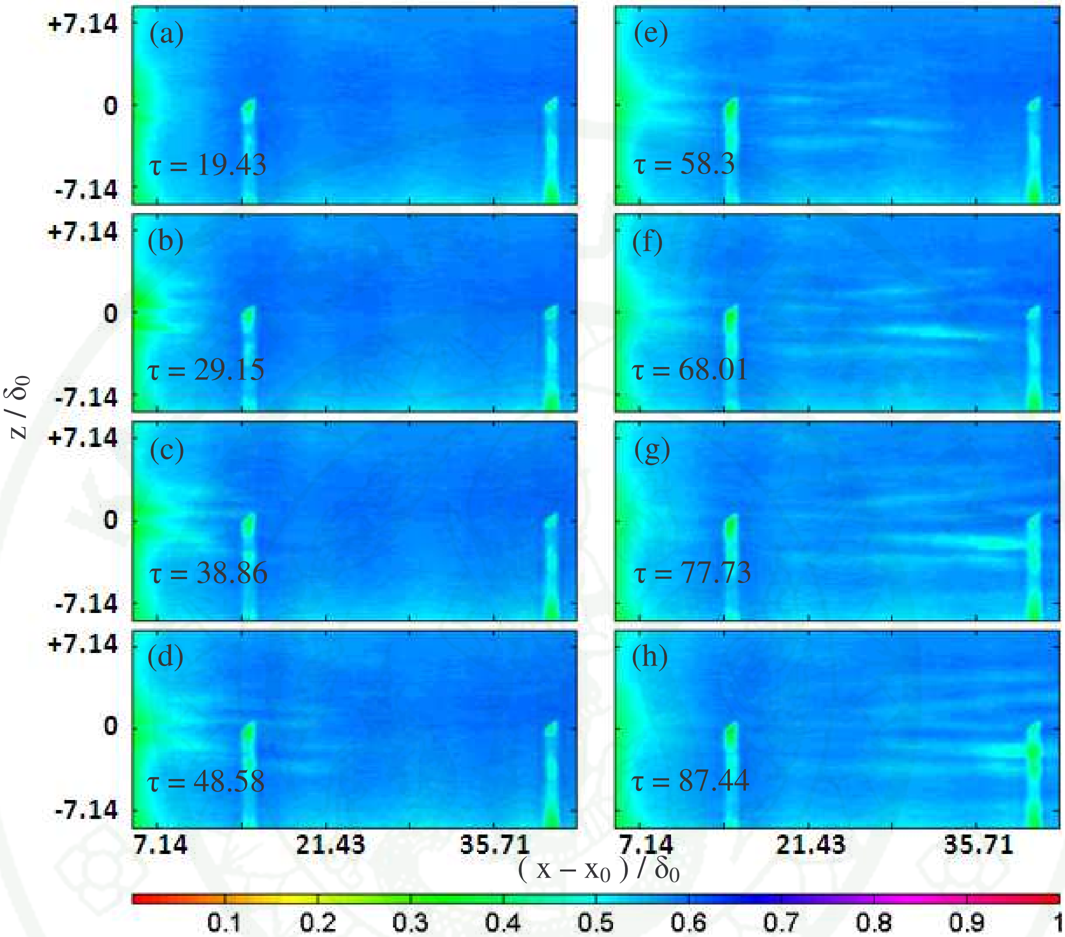

Figure 59 Hue images of thermal footprint under zero pressure gradient.

When the calibrated color-temperature relation as described previously was applied, temperature contours were obtained. Fig. 60(a)-(h) show the spatial instantaneous temperature distribution of turbulent spot footprint from τ = 19.43 to 87.44 after disturbance injection with Δτ of 9.72. The temperature (°C) was reported by the below colorbar. Before spot arrival, surface temperature was uniformly kept at about 28.3°C-28.4°C as shown in Fig. 60(a). It was found that the footprint at early stage was capable to partly cool down the test surface with the relatively lowest temperature. This was because turbulent spot came with the relatively low temperature of upstream water, measured at 23.6°C. As turbulent spot firstly attached the heated region under thermal boundary layer, the great difference in temperature between the surface and incoming vortex within turbulent spot resulted to the maximum chilled temperature of 27.4°C as shown in Fig. 60(b). However, Fig. 60(g) shows point of the relatively lowest temperature, induced by only the influence of turbulent spot. This emerged at the core of main streaky structure.

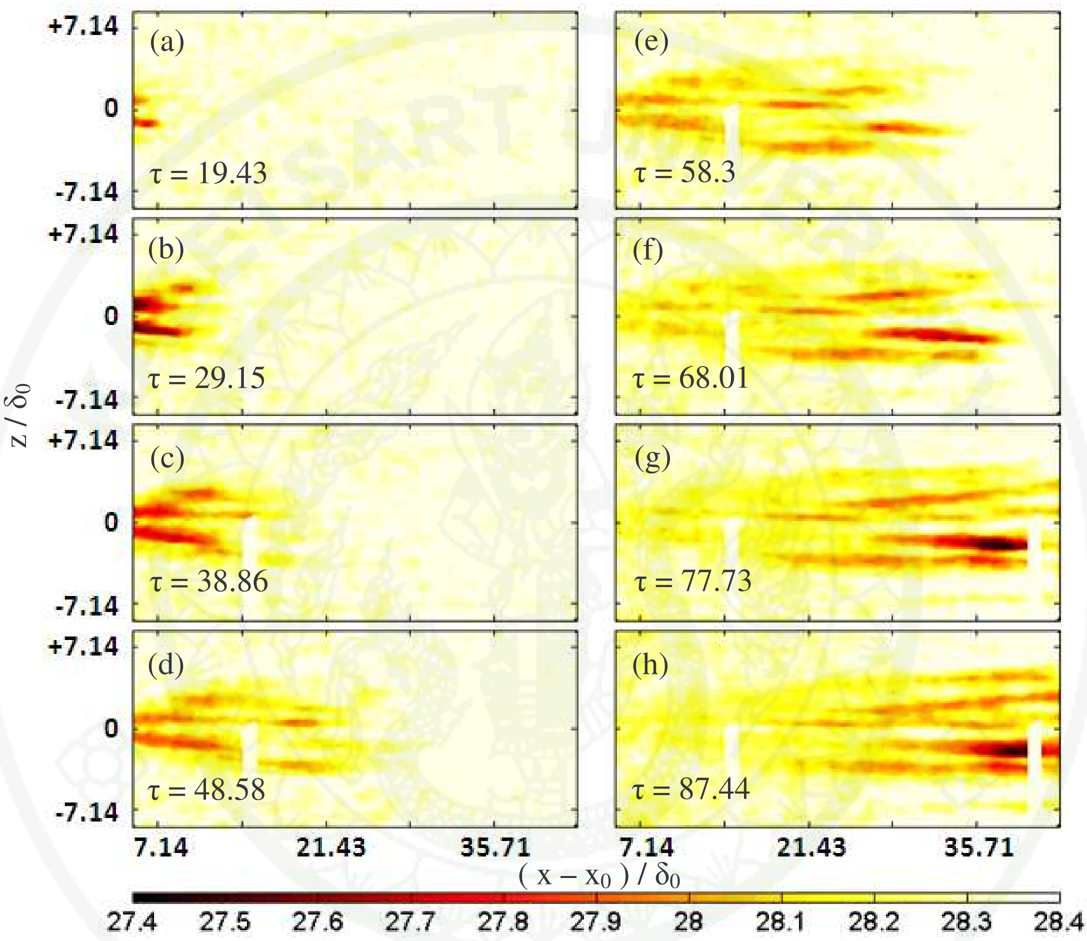

Figure 60 Temperature contour of thermal footprint under zero pressure gradient.

An analytical formula, developed from energy balance method mutually with "Explicit" finite difference approach was used to achieve the spatial distribution of instantaneous convective heat transfer coefficient underneath turbulent spot as depicted in Fig. 61(a)-(h). The below color bar shows the value of heat transfer coefficient(W/m^2K). Without the effect of the great temperature difference at the most upstream of the heated area, the value of heat transfer coefficient increased when it moved further downstream. The maximum value was up to 840 W/m^2K when it traveled beyond the normalized streamwise distance of 35.71. This confirmed that the footprint was capable to transfer heat mostly at the center of each streak.

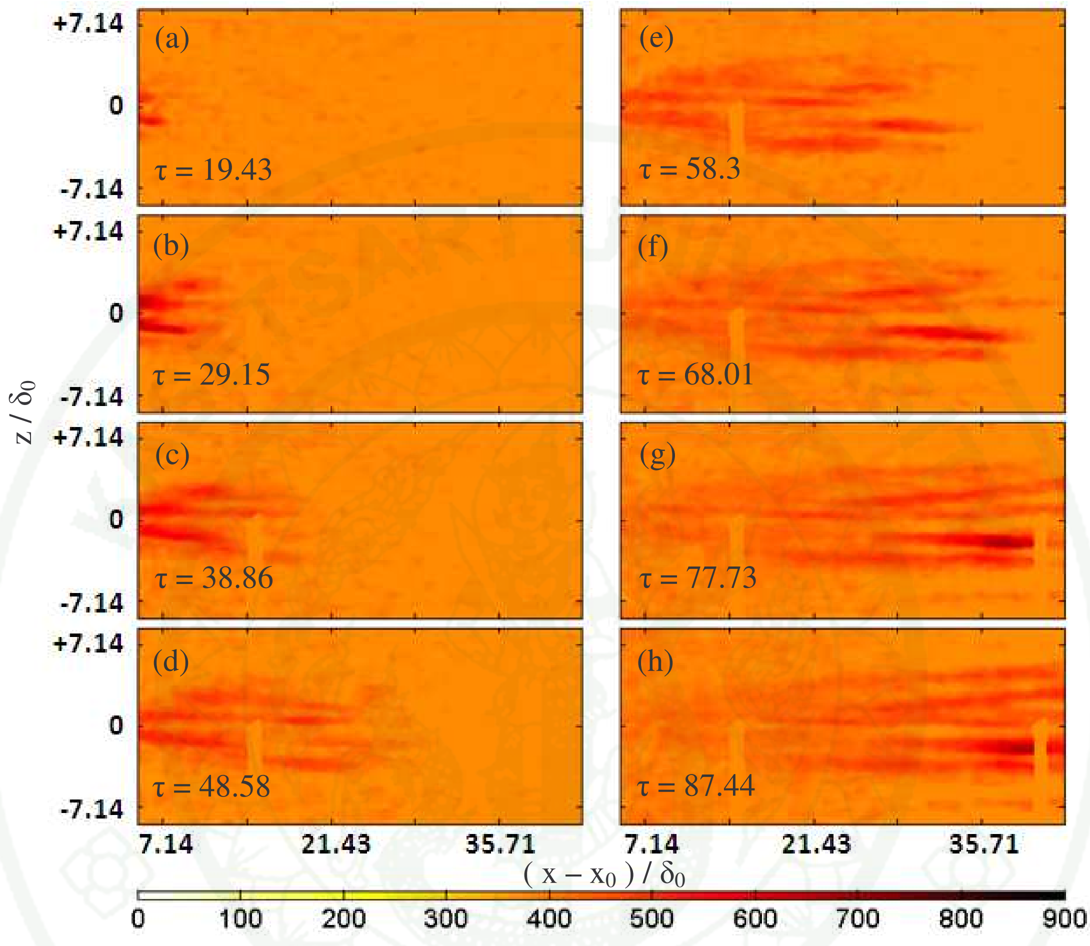

Figure 61 Contour of convective heat transfer coefficient of thermal footprint under zero pressure gradient.

1.2 Thermal characteristics of turbulent spot footprint under adverse pressure gradient

In this topic, all results were presented as the spatial instantaneous temperature and convective heat transfer coefficient distribution under the influence of mild and strong adverse pressure gradient. It was found that the cooled area appeared after turbulent spot was initiated by injecting water. As occurred under zero pressure gradient, the temperatures within the spot footprint in early stage were relatively low due to the highest difference between temperature of incoming fluid and heated surface. However, temperatures in each pressure gradient were not outstandingly different but the chilled area increased when the level of pressure gradient increased. The lowest temperature inside the footprint was measured near the right end of the images as shown in Fig. 62(a)-(h) and 63(a)-(h).

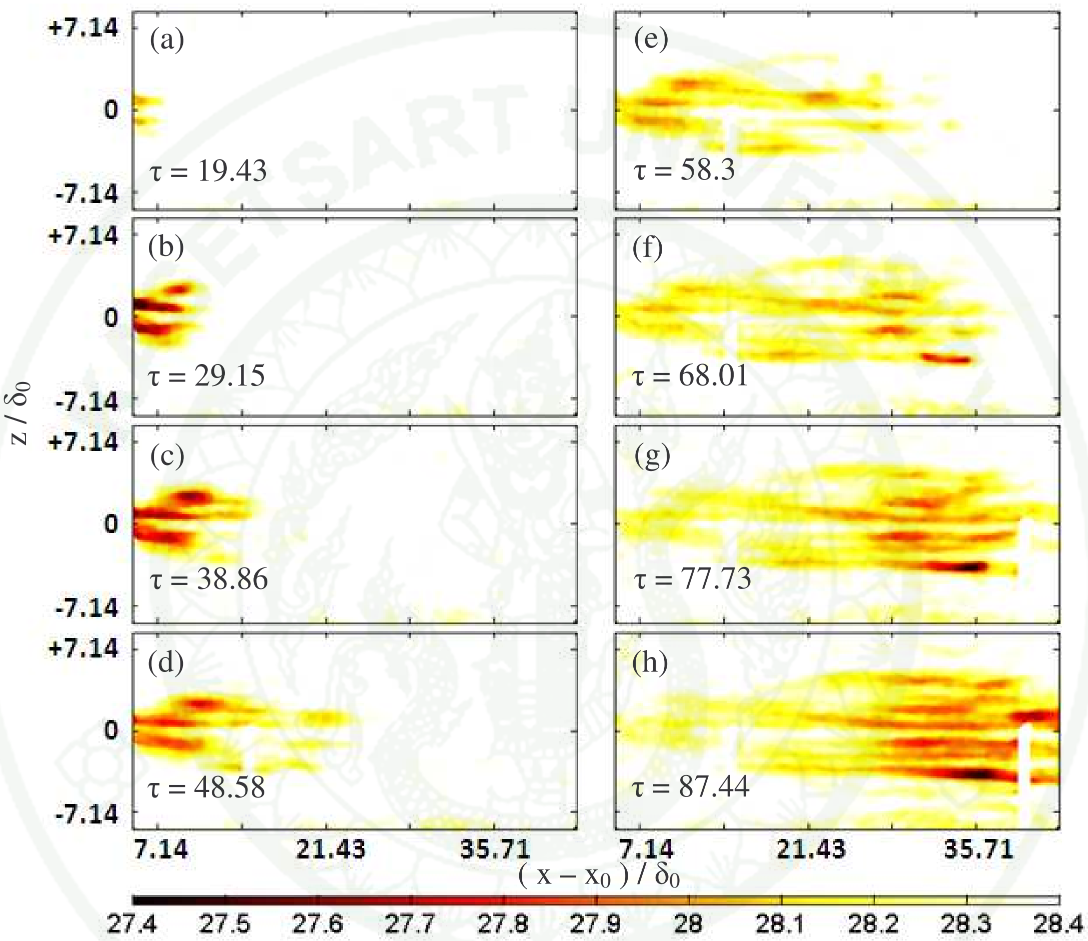

Figure 62 Temperature contour of thermal footprint under mild adverse pressure gradient.

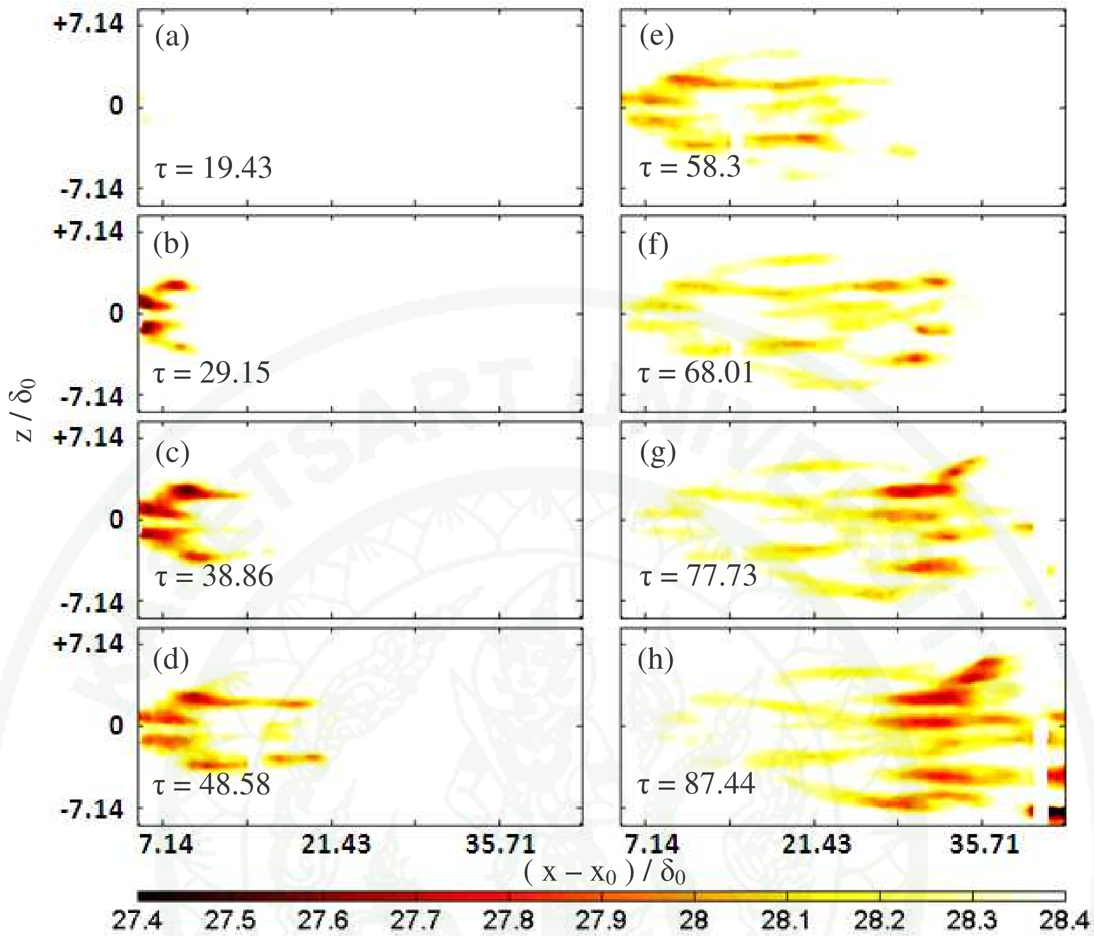

Figure 63 Temperature contour of thermal footprint under strong adverse pressure gradient.

The spatial instantaneous of convective heat transfer coefficient distribution of turbulent spot footprint under mild and strong pressure gradient were depicted in Fig. 64(a)-(h) and 65(a)-(h), respectively. Obtained data trend was similar to heat transfer coefficient at $\lambda_\theta = 0$. The maximum heat transfer coefficients were found at the core of each streak within the footprint. It was clearly seen that the value of the coefficient inside induced streaks increased when the level of pressure gradient was stronger. Therefore, it was found that pressure gradient along streamwise distance affected not only the local boundary layer as described previously, but also the heat transfer ability of turbulent spot. Therefore, in both mild and strong level of pressure gradient, the characteristics in convective coefficient behaved like turbulent spot under ZPG except the width of the footprint.

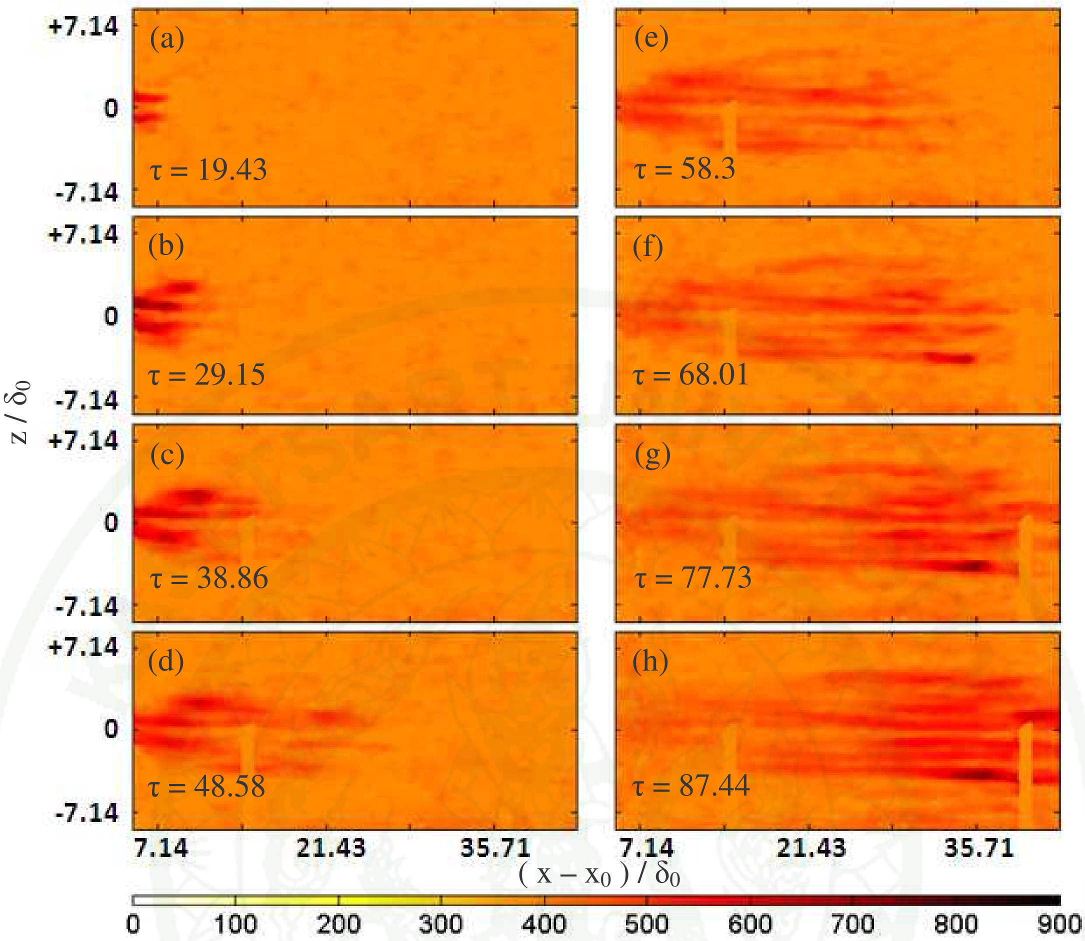

Figure 64 Contour of convective heat transfer coefficient of thermal footprint under mild adverse pressure gradient.

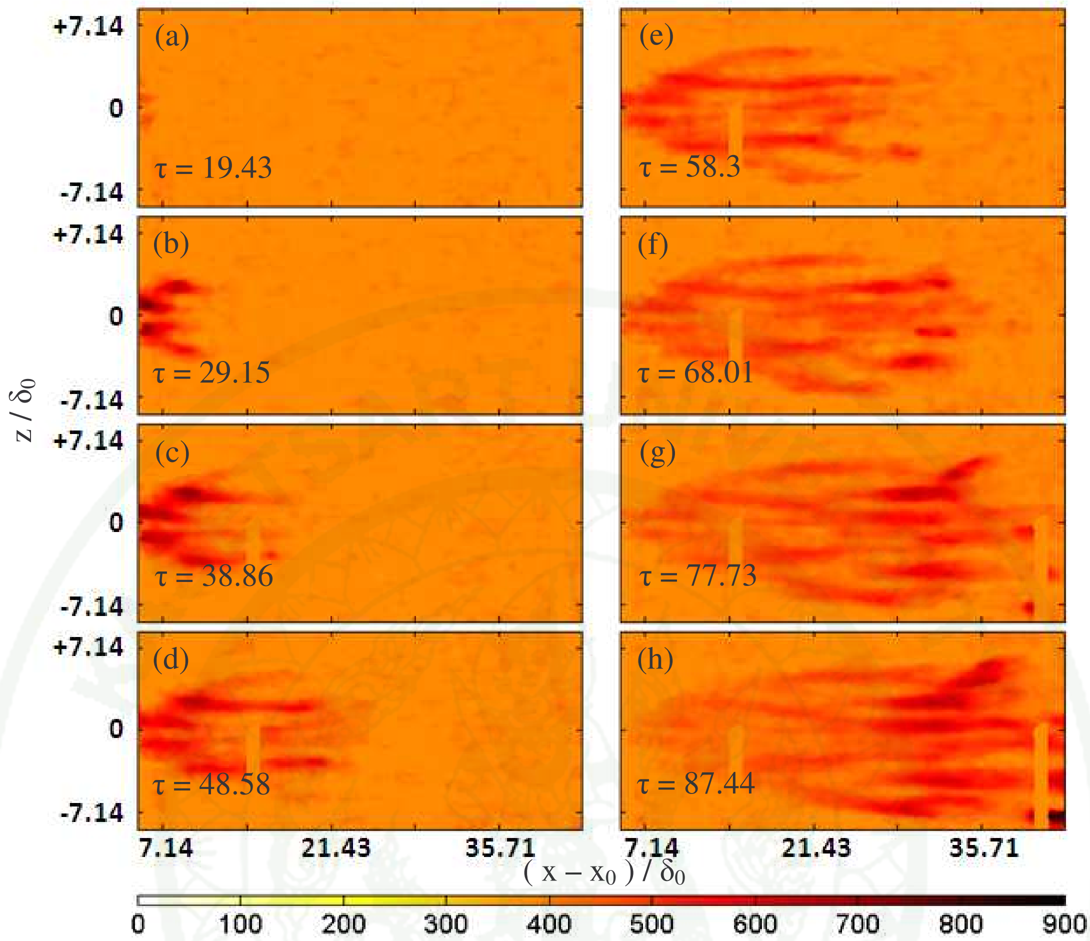

Figure 65 Contour of convective heat transfer coefficient of thermal footprint under strong adverse pressure gradient.

1.3 Structure and development of turbulent spot footprint under ZPG

Series of consecutive images of the spatial instantaneous heat flux were obtained by governing the fundamental equation of heat convection to visualize internal mechanism and development of thermal footprint underneath turbulent spot as shown in Fig. 66(a)-(h). It should be noted that the yielded heat flux from this technique includes only part, induced by unsteady turbulence as

$$\dot{q}_t = \dot{q}_{total} - \dot{q}_l \tag{26}$$

The threshold value for all heat flux contours was set to be 10% of $\dot{q}_{t,\max}$ following Kittichaikarn(1999). When the thermal footprint propagated downstream from left to right, it grew in both streamwise and spanwise direction. Corresponding to temperature and heat transfer coefficient, heat flux at early stage reached the maximum due to the effect of temperature difference between incoming water and heated plate. The heating value, responsible by only influence of spot footprint could be found since Fig. 66(e). It was found that the internal structure of the footprint mainly consisted of random streaks. These were an important consequence of the secondary vortices that were randomly generated within turbulent spot. It was also found that each streak had the average width of 1 cm. Generally, it transferred heat amount around 200-300 watt/m^2 while the maximum heat flux of 900 watt/m^2 was found at center of the main streak as depicted in Fig. 66(g). The development mechanism at wingtips could be found as point A in Fig. 66(c). Streaky structure initiated like small induced spot. It later grew among the longer streak and became lateral part of turbulent spot footprint as seen at point A in Fig. 66(d). This was caused by destabilization process near turbulent spot wingtips, suggested by Corrsin and Kistler (1955). Unlike destabilization of the unstable laminar boundary layer on the verge of turbulent region, leading edge of turbulent spot prolonged by the classical entrainment process. At the front edge, turbulent spot gulp the relatively low temperature fluid inside when it moved forward. Consequently, the leading edge of spot footprint occurred as small spots at the most downstream of the structure. These small spots later grew longer as seen at point B in Fig. 66(d) and (e). Moreover, turbulent spot trailing, found in heat flux form is shorter than those in the temperature distribution. It was because the image of spatial instantaneous heat flux was derived from energy balance equation, including the storage energy. The effect of this term caused the spot trailing in temperature image delayed in turning back into the uniformly steady value after spot arrival. It result the longer trail and error as found in temperature distribution image. This agreed to the results that found by Kittichaikarn (1999). Thus, the analytical solution that formed from energy balance approach was capable to reveal the true shape of the thermal footprint of turbulent spot. This trialing zone of the footprint was widely known as becalmed region. It played role of calming all fluctuating behaviors after spot passed and also eliminated discontinuity between turbulence region at spot head and laminar region at far behind turbulent spot.

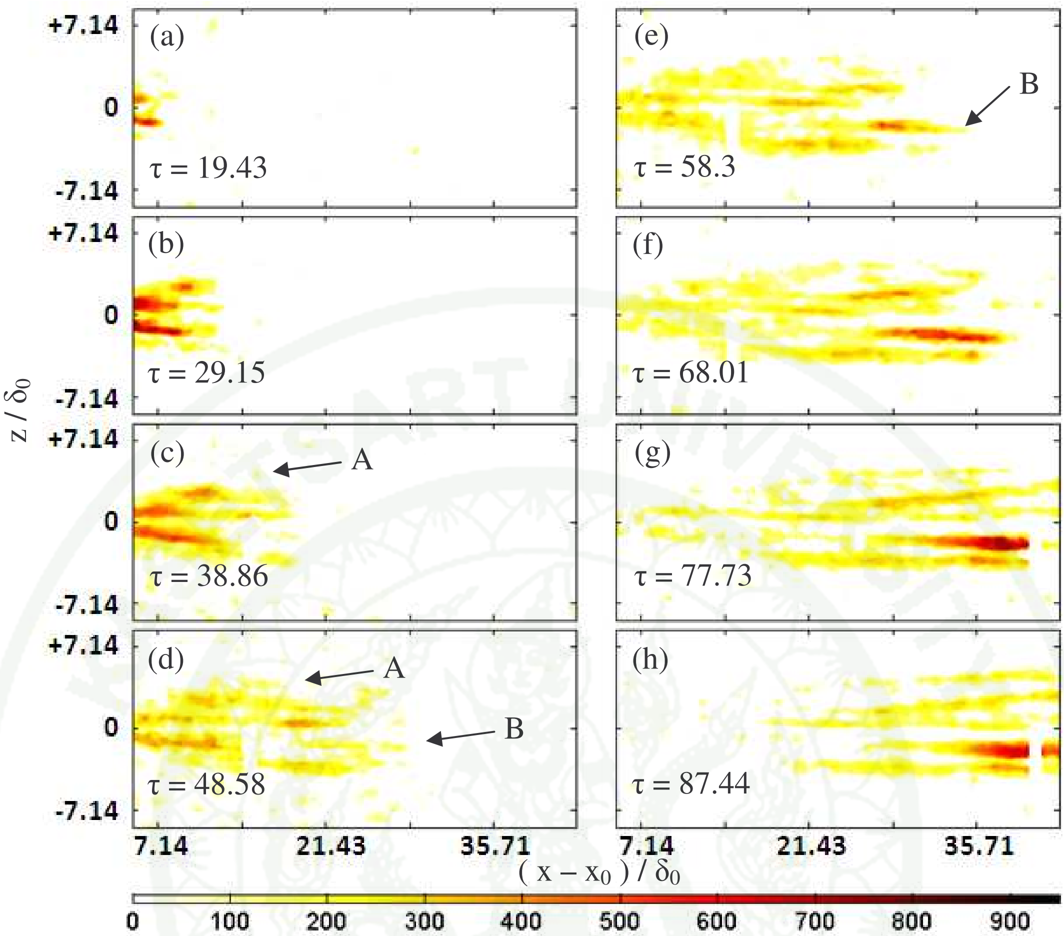

Figure 66 Heat flux contour of thermal footprint under zero pressure gradient.

It has been known that the boundary layer transition was covered by random effect of unsteady phenomenon. However, the presence of some unique characteristics exists by observation. Therefore, method of establishing representative structure of thermal footprint was developed by an averaging determination to indicate the consistent behavior of artificially generated turbulent spots. The footprint structure resulted from pixel-by-pixel averaging of 15 individual spot footprints, presented in heat flux contours. Before averaging process, the contour was initially non-dimentionalized. Bound of the structure was identified at the same threshold value as in heat flux contour. Thus, the spatial distribution of representative structure in Fig. 67(a)-(h) obtained from

$$\dot{q}_{avg} = \frac{\dot{q}_{total} - \dot{q}_l}{\dot{q}_{\max}} \tag{27}$$

All images of representative structure of thermal footprint were also presented from τ = 19.43 to 87.44 after injection. The below colorbar exhibits the variation of non-dimensional heat flux of representative structure as it convected downstream from left to right. After disturbance injection, the representative structure of turbulent spot footprint in early stage showed that the stabilized flow initially broke down into turbulence as four streaky shapes at spot frontal. Two of the most lateral streaks clearly tended to grow in spanwise direction. In the mean time, they propagated downstream with the same speed as two middle streaks. In this stage of development, spot shape should be depicted as “hand-like” as shown in Fig. 67(a)-(b). Unlike in spanwise direction, the footprint stretched outstandingly in streamwise direction from τ = 38.86 to 68.01 after disturbance injection. The four frontal streaks still convected down stream with relatively equal velocity. The shape of becalmed region firstly occurred as one long trail as show in Fig. 67(f). By observation, it was found that this trailing region gradually faded out and later took place as 2 tails-like, which corresponding to the results of Itsweire and Van Atta (1984).

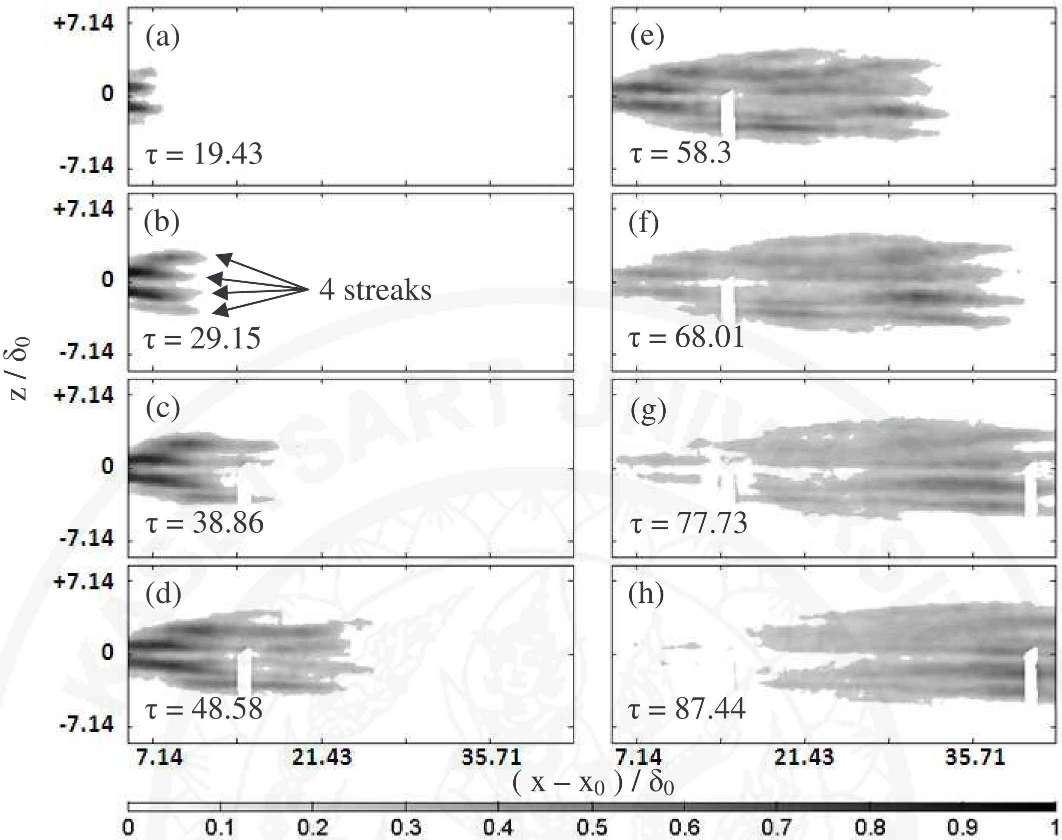

Figure 67 Representative structure of young thermal footprint under zero pressure gradient.

Moreover, the evolution of thermal footprint at the normalized streamwise distance between 28.57 - 50 was further visualized as shown in Fig. 68(a)-(h). At the most spanwise of the footprint, the 5^{th} and 6^{th} streaks were found at both sides of lateral bound of the structure as depicted in Fig. 68(d). They were induced and added as part of the spot footprint. Besides, at the normalized time of 126.29 after injection, it was found that the middle frontal streak was piercing forward. At this point, arrow head shape was apparently formed as shown in Fig. 68(f). Therefore, the existence of young turbulent spot could be achieved before two additional streaks appeared. After the appearance of these streaks, the classical mature turbulent spot was obtained. This corresponded to the suggestion by Wygnanski *et al*. (1982) that the spanwise of the spot was linear along longtitudinal direction from the spot generator larger than 40 cm. Also, Kittichaikarn (1999) found that half spreading angle of young turbulent spot is in range of 4°- 6°. Conversely, at the mature state of, the angle was approximately

10°. Also, Fig. 68(h) showed becalmed region that occurred as fading area on the left side of the image.

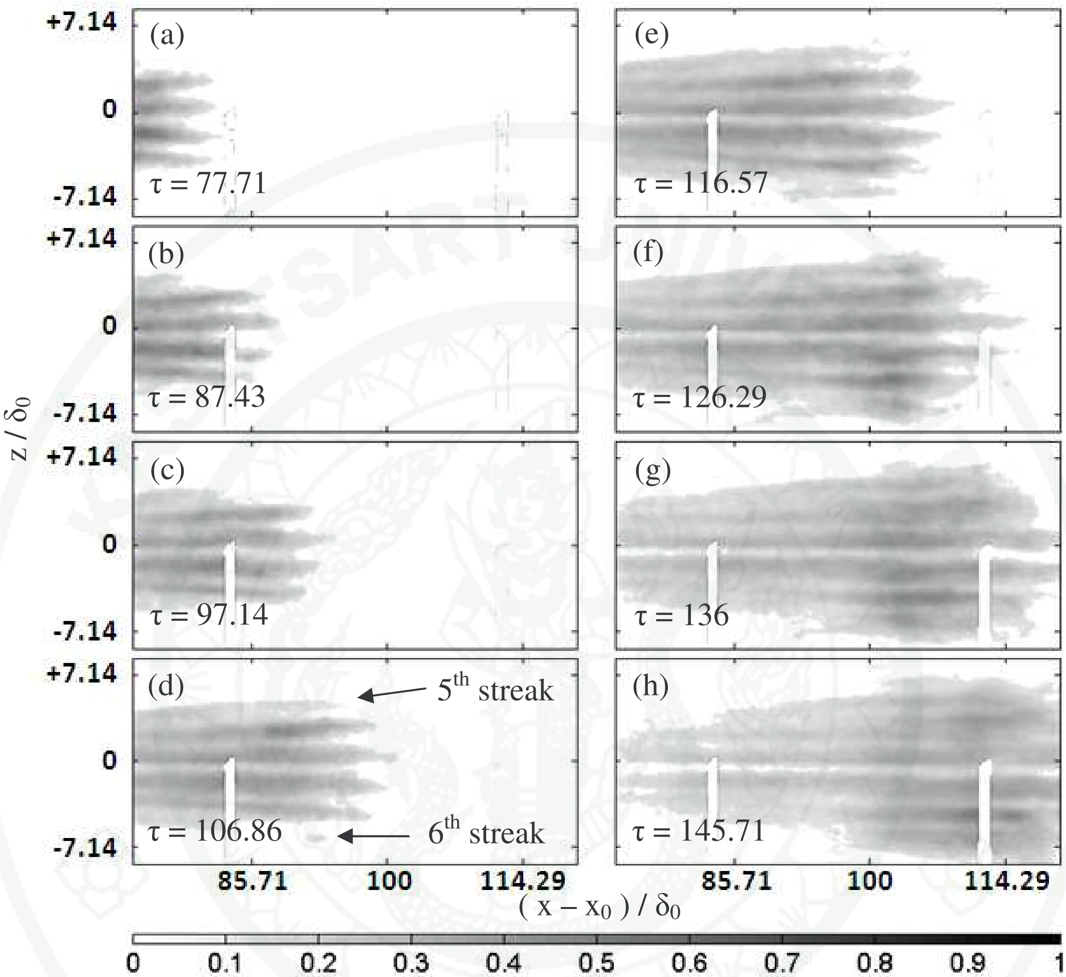

Figure 68 Representative structure of mature thermal under zero pressure gradient.

1.4 Structure and development of turbulent spot footprint under adverse pressure gradient

The consecutive frames of heat flux beneath turbulent spot under mild and strong adverse pressure gradient, plotted in Fig. 69(a)-(h) and 70(a)-(h), respectively, were obtained by the same algorithm as the footprint under zero pressure gradient. When the footprint propagated downstream from left to right, it was found that the pattern of heat transfer mechanism was similar even the level of pressure gradient increased. The footprint started with high heat transfer due to the refreshment of thermal boundary layer at the left end of images. It provided high heat rate again when it convected downstream. It was also clearly found that not only the size of the footprint but also the maximum heat flux increased under higher pressure gradient. The structure was more round, which was in agreement with the observations of Gostelow *et al*. (1996). Besides, becalmed region was observed at trailing area behind spot body. It appeared as streaky structure and gradually vanished after spot passed.

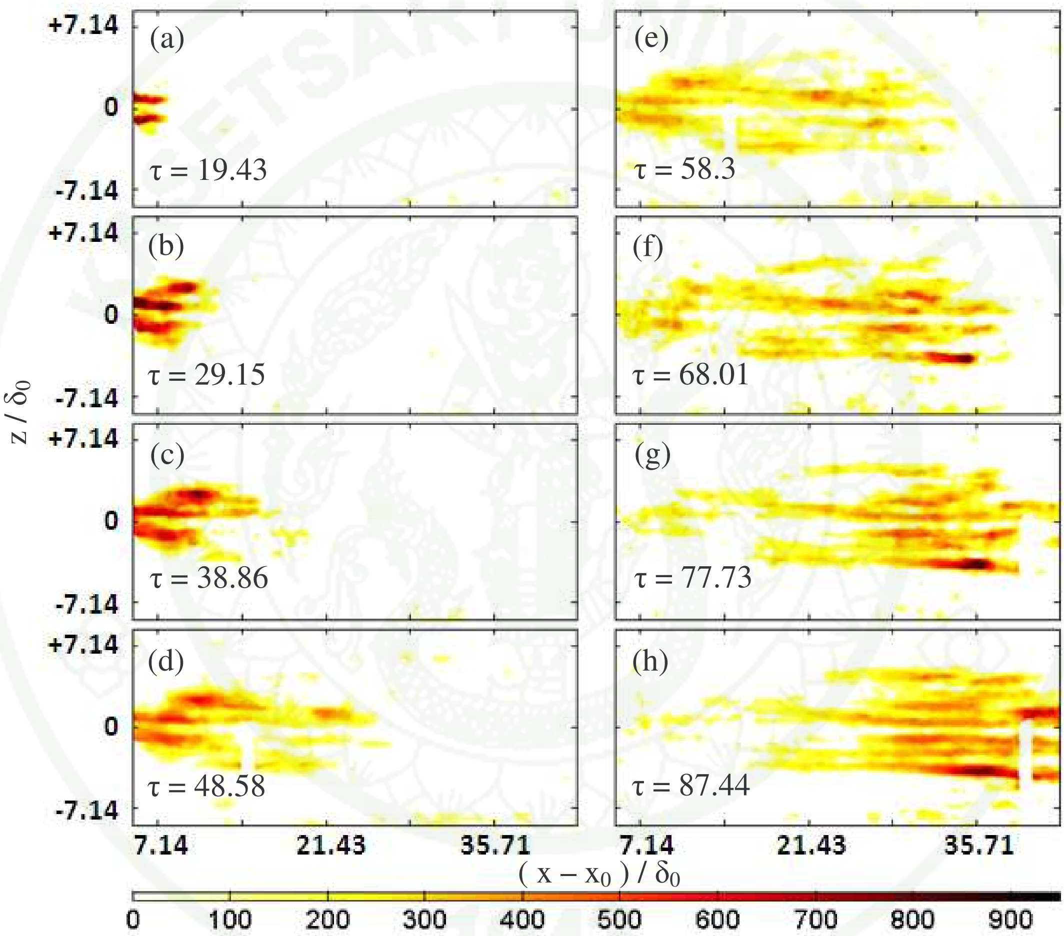

Figure 69 Heat flux contour of thermal footprint under mild adverse pressure gradient.

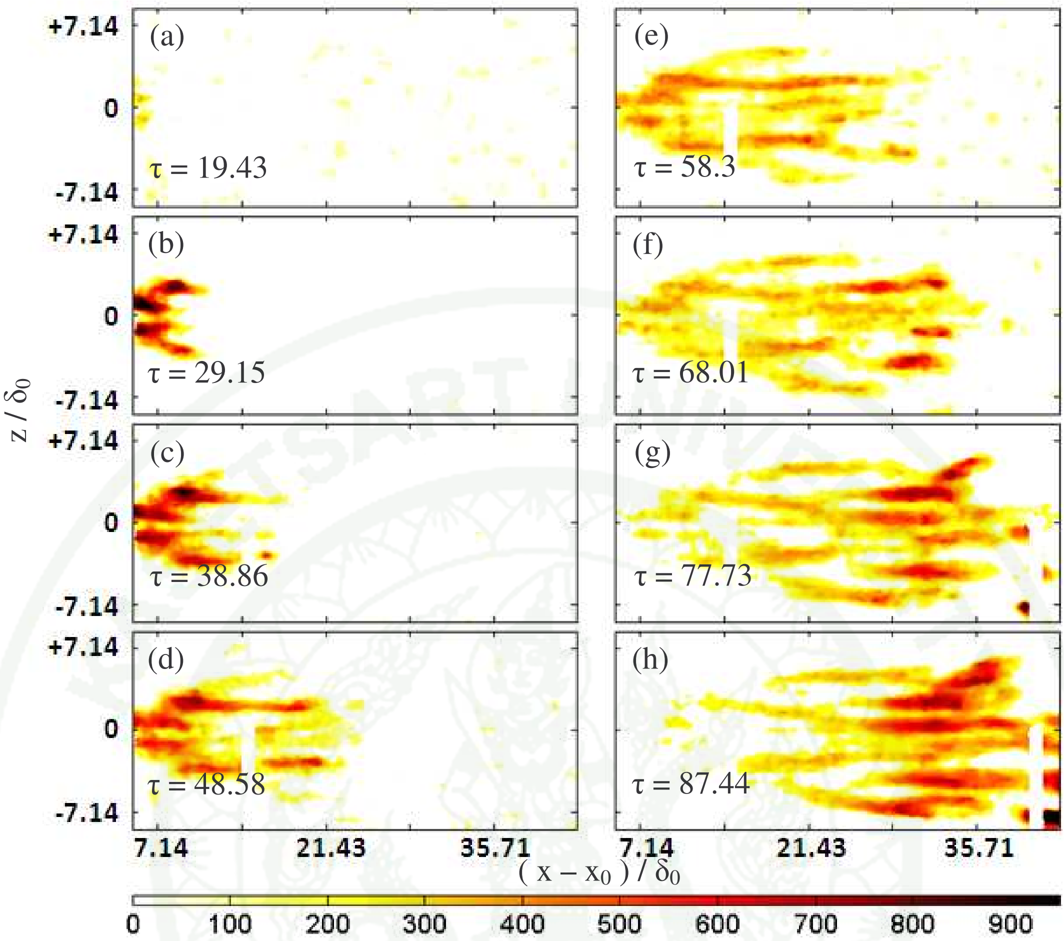

Figure 70 Heat flux contour of thermal footprint under strong adverse pressure gradient.

Fig. 71(a)-(h) and 72(a)-(h) show the consecutive images of the spatial instantaneous representative structure of thermal footprint beneath the artificially generated turbulent spot under mild and strong adverse pressure gradient, respectively. These could confirm that size of the footprint increased when the level of pressure gradient increased. After disturbance injection, the representative structure at λ_θ = -0.01574 and λ_θ = -0.06037 also show that the near wall turbulence within turbulent spot broke down into four frontal streaks as the footprint under λ_θ = 0. Moreover, the 5th and 6th streaks, induced by new subsidiary vortex, found by Haidari and Smith (1994), were also seen near both wingtips as shown in Fig. 71(e) and 72(e). These additional streaks occurred quicker if the pressure gradient is stronger. Thus, this could confirm that the increased level of adverse pressure gradient directly accelerated the growth of turbulent spot.

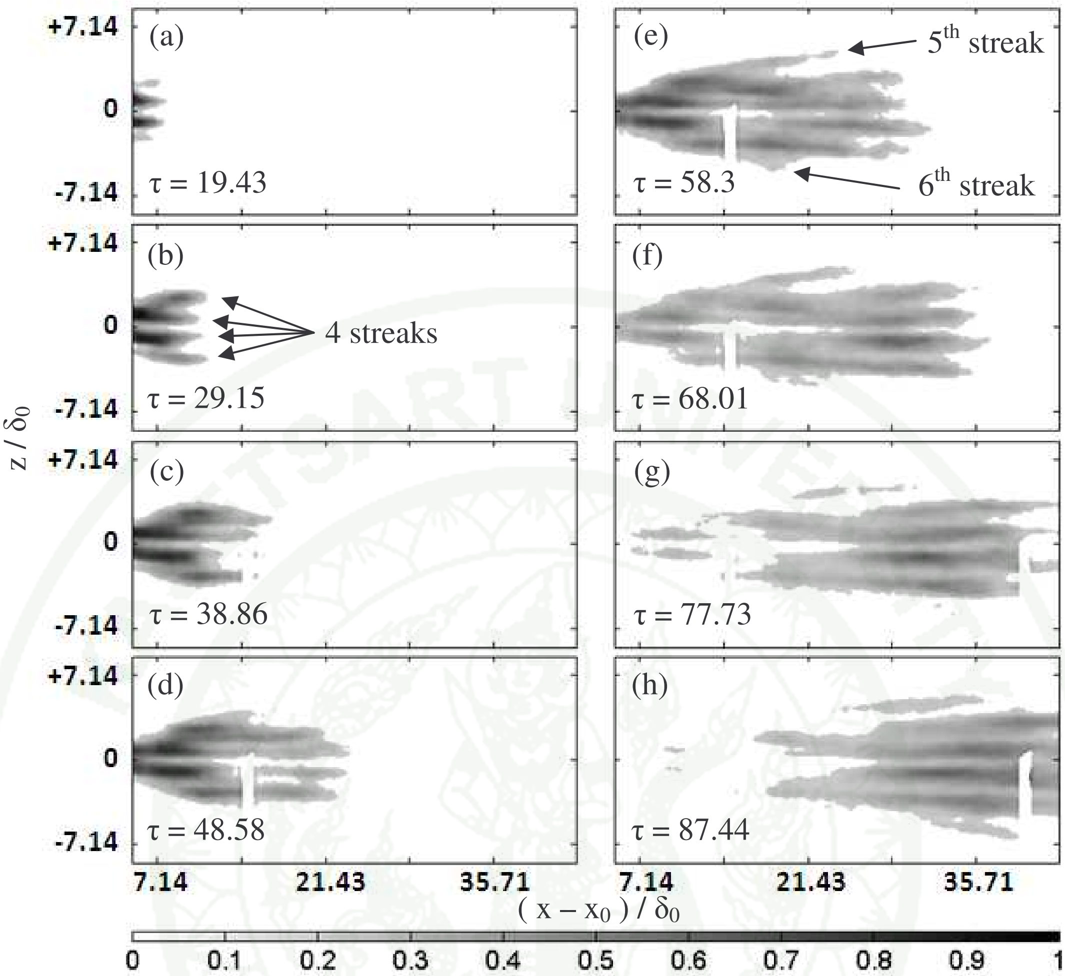

Figure 71 Representative structure of thermal footprint under mild adverse pressure gradient.

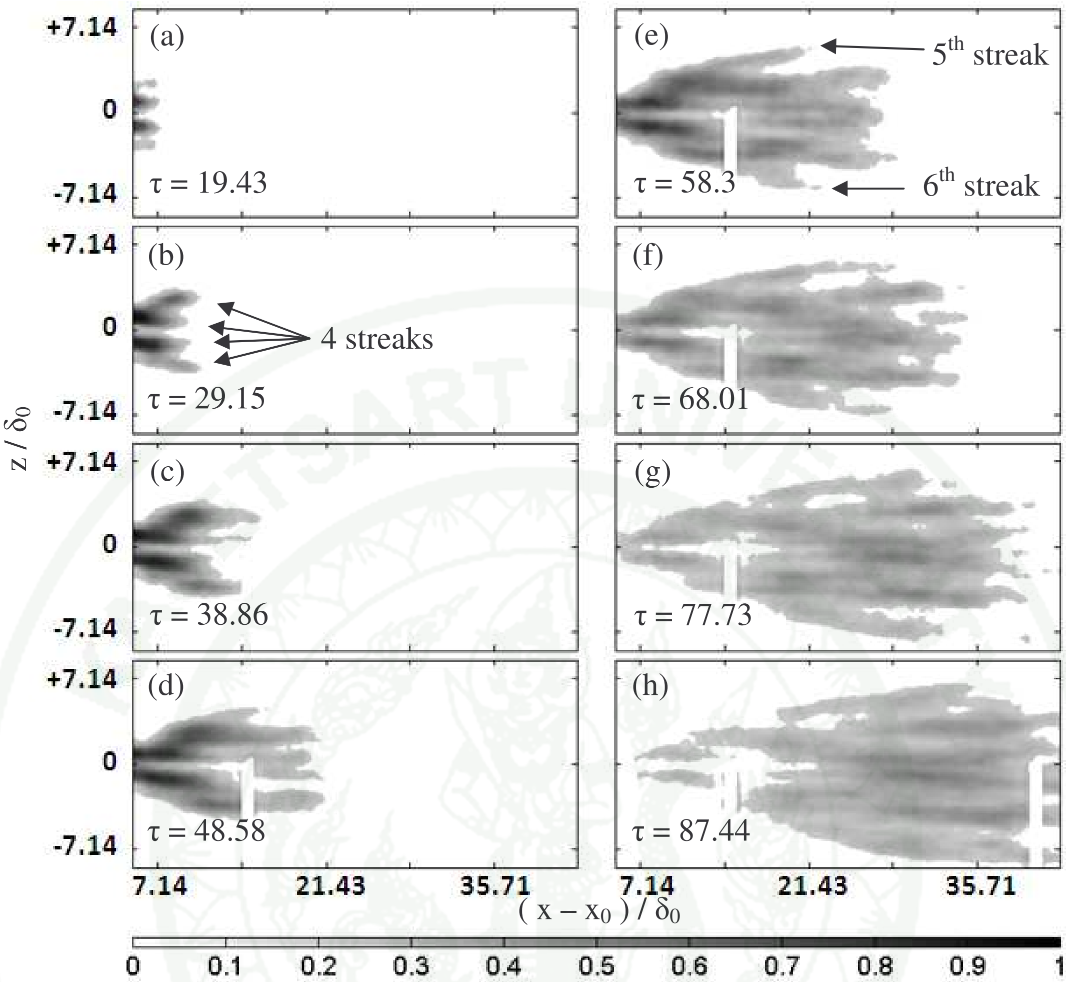

Figure 72 Representative structure of thermal footprint under strong adverse pressure gradient.

1.5 Turbulent spot footprint parameters

Turbulent spot footprint parameters, comprising propagation rates at leading edge, trailing edge, and end point of becalmed region, as well as half spreading angle under zero pressure gradient, obtained from the present experiment and those reported by the other researchers are listed in Table 1. The propagation rate of leading edge, trailing edge, and becalmed region, as well as half spreading angle were obtained by the consideration of distance over specific time from the consecutive heat flux contours. Location of the footprint's leading edge was identified by the most downstream point of the contour. Trailing edge of turbulent spot located on the wavy line, marked on the maximum heat flux across the spot width as shown in

Fig. 73. The estimated location of trailing edge was deduced by averaging the streamwise position of each point on the wavy line. Thus, becalmed region were on the upstream area of this line. At the end of this region, spot celerity of becalmed region could be determined. Moreover, it is found that the wingtips of the footprint are on the junction of this wavy line and its most spanwise tip. Trajectories of wingtips were formed by superimposing the contours of heat flux of thermal structure at five consecutive frames. The locus of wingtips was later fit by straight line. It should be noted that the method assumed that locus of wingtips was linear. Half angle, created by these two trajectory lines was reported as half spreading angle as depicted in Fig. 74.

Table 1 Turbulent spot parameters under zero pressure gradient obtained at the height of $0 < y/\delta \leq 3.5$ mm from the surface.

Study	C_{LE}	C_{TE}	C_{BC}	α°
Schubauer & Klebanoff (1955)	0.88	0.5	0.29	10
Sankaran *et al.*(1988)	0.74	0.53	-	9
Hofeldt(1996)	0.88	0.56	0.32	10
Kittichaikarn(1999)	0.83	0.56	0.31	6
Chong & Zhong(2005)	0.83	0.54	-	8.6
Chong & Zhong(2013)	-	-	-	6.8
Present study[1]	0.73 ± 0.03	0.55 ± 0.02	0.36 ± 0.01	6.8 ± 0.02
Present study[2]	0.74 ± 0.03	0.57 ± 0.02	0.32 ± 0.01	6.8 ± 0.02
Present study[3]	0.79 ± 0.03	0.53 ± 0.02	0.33 ± 0.01	10 ± 0.02

[1]Note the parameters of young spot obtained from the classical technique.

[2]Note the parameters of young spot obtained from the averaging technique.

[3]Note the parameters of mature spot obtained from the classical technique.

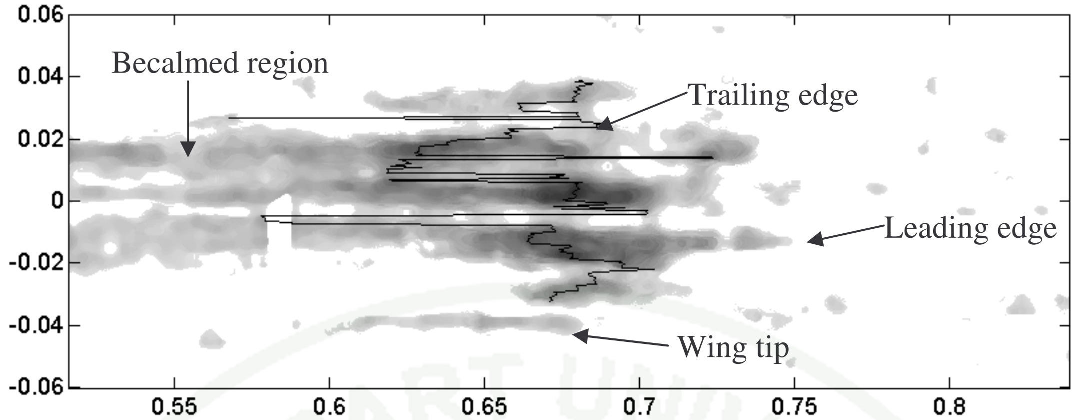

Figure 73 structure of thermal footprint beneath the artificially generated turbulent spot at freestream velocity of 0.17 m/s.

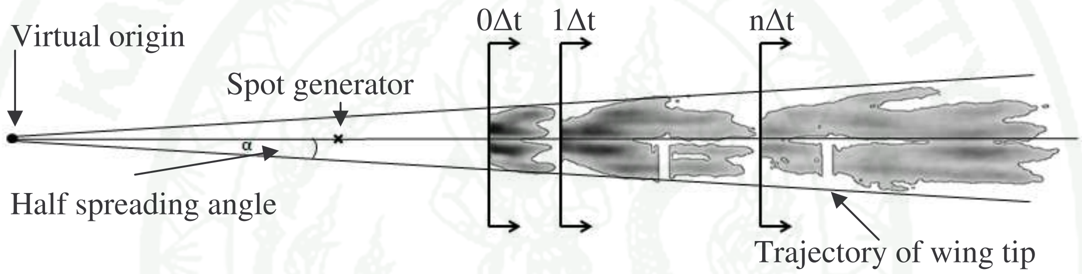

Figure 74 Measurement of virtual origin and half spreading angle of turbulent spot.

From the present study, the parameters were achieved by two techniques, consisting of the classical one, parameter determination on the individual turbulent spot footprint. Another focused on the representative structure as mentioned previously. In addition, the parameters, yielding from the mature footprint were also presented. Celerities at leading edge, trailing edge, and becalmed region were obtained at 0.73, 0.55, and 0.36, respectively by classical technique. It was found that they were quite similar to those obtained by the representative structure, comprising 0.74, 0.57, and 0.32 at leading edge, trailing edge, and end point of becalmed region, respectively. Therefore, this was a strong evidence to confirm reliability of the representative structure determination. This method provided not only the accuracy but also a shorter processing time. Also, it was found that, when the turbulent spot was at mature state, celerity at leading edge of the footprint was dramatically increased from 0.73 to 0.79 while celerity at other parts was remaining quite constant. Also, the half spreading angle changed from 6.8° to 10°. This raising angle caused by the additional streaks. These results clearly supported the hypothesis on the mechanism of young turbulent spot, made by Kittichaikarn (1999). It was noted that the difference between immature and mature state strongly affected on celerity at leading edge and half spreading angle.

Comparing to those reported by the others, it was found that the parameters of mature footprint were in a good agreement. It should be noted that Sankaran *et al*. (1986), Kittichaikarn (1999) and Chong and Zhong (2013) achieved all parameters from thermal structure of turbulent spot while Schubauer & Klebanoff (1955), Hofeldt (1996), and Chong and Zhong (2005) used hot wire anemometer. However, good agreement between spreading angle, determined by shear stress and temperature sensitive liquid crystals was confirmed by Chong and Zhong (2013). Therefore, all reported data could be directly compared. Moreover, only Kittichaikarn (1999), Chong and Zhong (2013) and the present experiment employed coating liquid crystals to yield the qualitatively and quantitatively spatial behavior of the footprint. These obtained results were recorded exactly on the plane of surface which is impossible for any measurement probe. Unlikely, spot parameters, presented by Schubauer & Klebanoff (1955), Sankaran *et al*. (1988), and Hofeldt (1996), were obtained at the height of $0 < y/\delta \leq 3.5$ mm from the surface. As the spot footprint was under the influence of adverse pressure gradient, its parameters were recorded as shown in Table 2. Also, in this table, the results were compared to those obtained from the other researchers.

Table 2 Turbulent spot parameters under adverse pressure gradients obtained at the height of $0 < y/\delta \leq 3.5$ mm from the surface.

Study	λ_θ	C_{LE}	C_{TE}	C_{BC}	$\alpha°$
Zhong *et al*. (2000)	-0.08	0.74	0.42	0.22	13
Present study (SAPG)	**-0.06**	**0.65 ± 0.03**	**0.44 ± 0.02**	**0.22 ± 0.01**	**11.4 ± 0.02**
Gostelow *et al*.(1996)	-0.057	0.872	0.431	0.25	29.2
Van Hest (1994)	-0.036	0.92	0.38	0.1	17
Zhong *et al*. (2000)	-0.03	0.78	0.49	0.27	9
Present study (MAPG)	**-0.016**	**0.71 ± 0.03**	**0.49 ± 0.02**	**0.28 ± 0.01**	**8.9 ± 0.02**

when turbulent spot was under influence of adverse pressure gradient, spot celerities could be directly obtained from particular velocity of the footprint over constant freestream velocity of water. It should be noted that, under adverse pressure gradient, freestream velocity decreased along streamwise direction. If the celerity was assumed to be constant through the two successive points on the surface, algorithm was altered as

$$C = \frac{1}{\Delta t}\int_{x1}^{x2} \frac{dx}{U_\alpha(x)} \tag{28}$$

where C is spot celerity, Δt is the interval time between two successive distance of x1 and x2. $U_\alpha(x)$ is freestream velocity function as shown in Fig. 3. Details of measurement technique in this study were reported by Zhong *et al*. (2000). The present study provided celerities of the footprint under mild pressure gradient of 0.71, 0.49, and 0.28 at leading edge, trailing edge, and the end point of becalmed region, respectively. They became 0.65, 0.44, and 0.22 under strong pressure gradient. It was found that, unlike half spreading angle, the value of celerities tended to decrease when λ_θ decreased. The half spreading angle were found at 8.9° and 11.4°

when the footprint experienced the mild and strong pressure gradient, respectively. From Table 1, it should be noted that there was only results from Zhong *et al*. (2000) that turbulent spot parameters were measured on exact surface. Consequently, not only the celerity at leading edge but also the half spreading angle, reported by Gostelow *et al*. (1996) and Van Hest (1994) were relatively higher. It was found that their high celerities were measured on the elevated locations. This caused the apparently higher value because this location had relatively less shear force, generated by viscous boundary layer. This phenomenon was also found as the appearance of velocity profile under boundary layer and it strongly affected on propagation rate of turbulent spot at leading edge. Also, the higher half spreading angle were from the presence of wave packet, measured by Gostelow *et al*. (1996). However, spot parameters, obtained in this study were in agreement with those reported by Zhong *et al*. (2000). Besides, the distance-time diagrams, presenting the three stages of the flow along the streamwise direction of spot under various pressure gradient are also shown in Fig. 75.

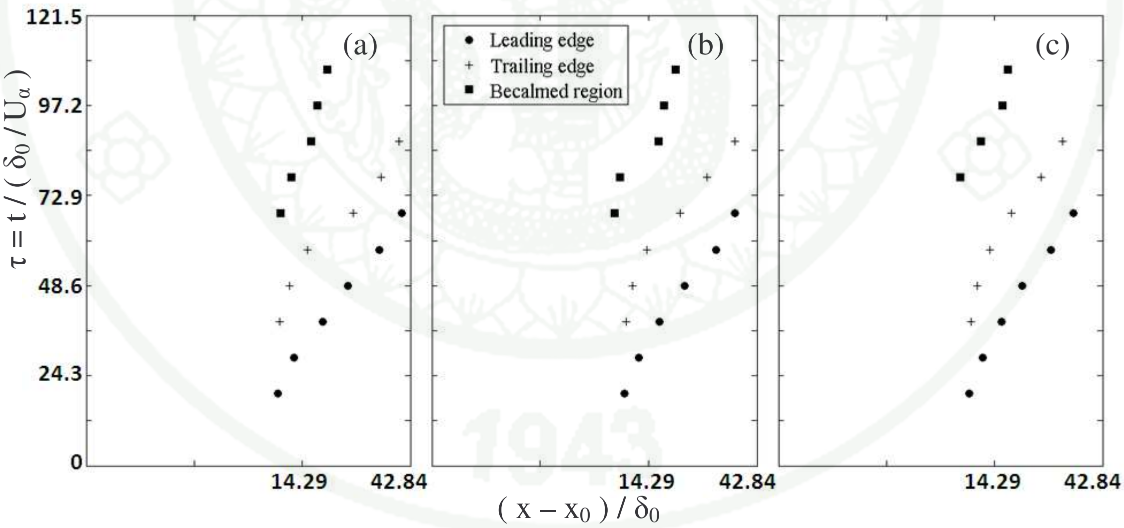

Figure 75 The distance-time diagram, used to present the propagation rate under (a) zero, (b) mild, and (c) strong adverse pressure gradient.

Moreover, it is found that the virtual onset of turbulent spot was not on the position of actual spot generator but it located farther upstream. It should be noted that, during experiment, spot generator was fixed at 0.3 m from leading edge of the test surface under all pressure gradients. Thus, these onset locations were directly comparable. It was found that the obtained virtual onsets relied on the locations of 0.167 m, 0.222 m, and 0.267 m from leading edge of the test plate under zero, mild, and strong pressure gradient, respectively. The different distance between point of disturbance generator and virtual onset decreased when adverse pressure gradient increased as found in Fig. 76.

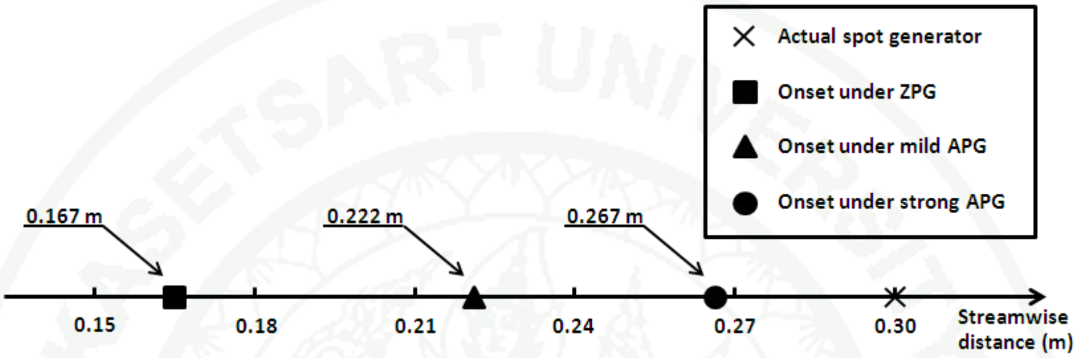

Figure 76 The locations of virtual onset of turbulent spot footprint under variations of pressure gradient.

2. 3D structure of turbulent spot

In this topic, all turbulent spot data were detected using milk solution as dye. When the dye was released from the dye chamber as described previously in chapter 3, the plate surface was completely covered by thin film milk. After turbulent spot was initiated by spot generator, the thin film dye rapidly broke up and dispersed throughout the spot body. However, the mechanism in turbulent breaking down by the spot generator must be explained in details as shown in Fig. 77. Green food coloring, diluted in the water, was injected through the hole of 1 mm diameter of spot generator when the thin layer of milk dye had been covering the plate surface as shown in Fig. 77(b). It was found that the injecting water pulled up particular milk after the green solution ran out as illustrated at oval line A in Fig. 77(c). Nevertheless, there was an occurrence of inertia at the region, following this injecting water. At this moment, this suction drew milk from the surface as shown by oval line B in Fig. 77(d). When this fluid lump propagated downstream as shown in Fig. 77(f), the near wall turbulence broke down and turbulent spot was eventually created. Thus, hairpin vortex, considered as the main part of turbulent spot was initiated and bypassed transition began.

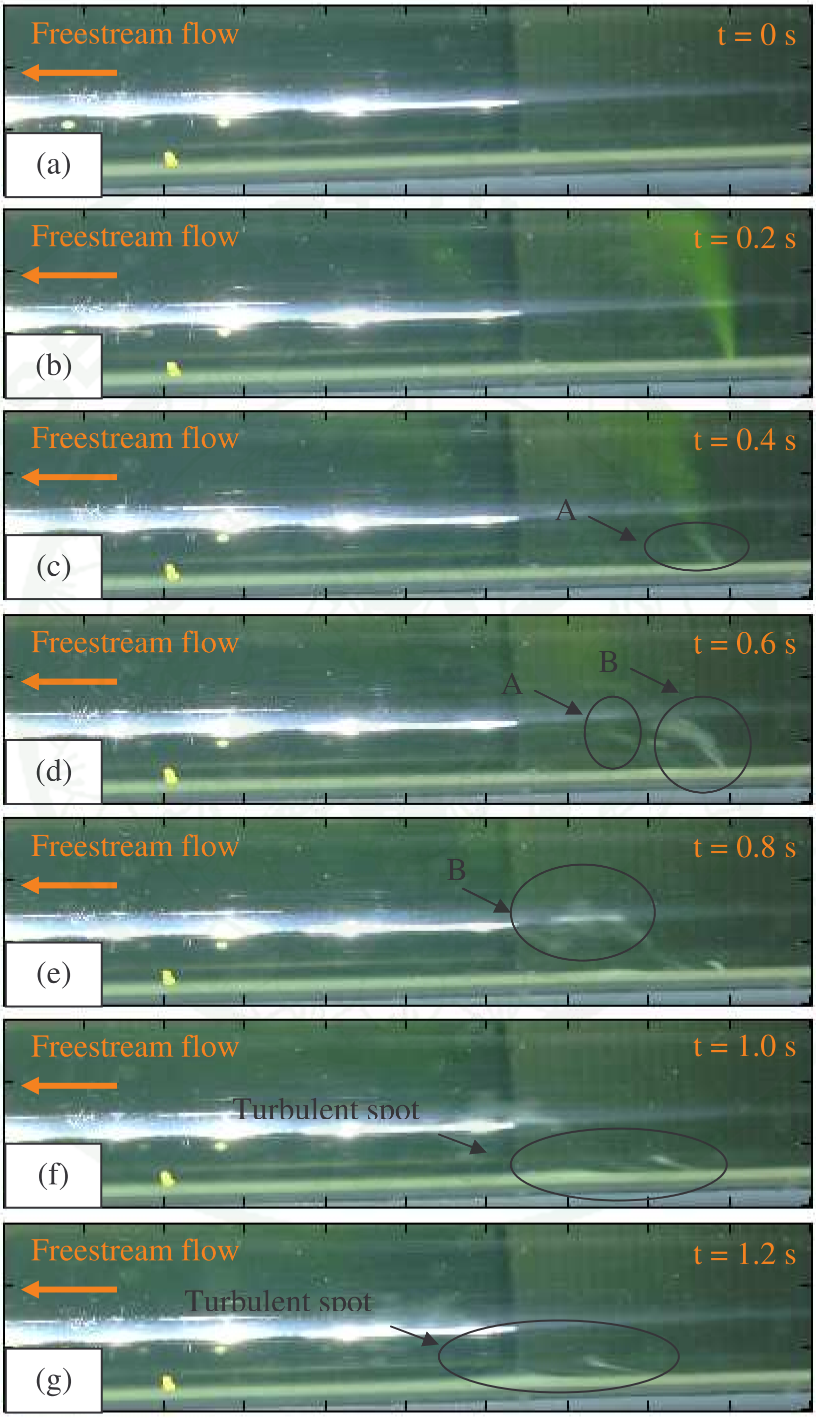

Figure 77 Mechanism of turbulent breaking down by spot generator.

Although researchers had conducted the flow visualization on turbulent spot using this technique, no one extracted spot information by image processing technique. Here, in this topic, turbulent spot was investigated, using the developed image processing program in different planes within its structure. All data were presented in three sub topics as

2.1 Turbulent spot information on the plane perpendicular to the plate surface

2.1.1 Turbulent spot development on the plane perpendicular to the plate surface under zero pressure gradient

Fig. 78(a)-(d) show series of RGB images of artificially generated turbulent spot under zero pressure gradient, propagating downstream from left to right on the plane of $z = 0$. Corresponding to the investigation on spot footprint, interval time was set as 0.4 s or $\Delta\tau = 9.72$. It started and ended at 0.8 s and 2.0 s or $\tau = 19.43$ to 48.57 after disturbance injection, respectively. All consecutive images were grabbed between 0.33 m and 0.57 m in streamwise direction. This was equal to the normalized streamwise distance between 4.29 and 38.57. In heightwise direction, zero distance was set on the test surface. The distance in this direction was normalized as y/δ_0 As explained previously, milk solution was released from dye chamber, installed upstream of the recording region. When thin milk layer fully spread out over the surface, turbulent spot was induced by injecting water. It was found that, when generated turbulent spot was illuminated by white light sheet, milk solution exhibited the good visibility due to its high reflective property as shown in Fig. 78. As the spot moved downstream, it grew in both streamwise and heightwise direction and always led by perturbation fluid. Its shape was similar to the group of hairpin vortices as reported by Chu *et al*.(2010) as shown in Fig. 78(e). Turbulent spot was high turbulent region within itself and embedded by laminar flow. It was found that it was consisted of overhang head, spot body, and becalmed region as depicted in Fig. 79. By observation, the front head of turbulent spot occurred as spanwise vorticity with the sharp edge on laminar-turbulent interface. Location on top of this vorticity was found as the highest position of turbulent spot. The empty region below this eddy was established by the entrainment that brings the non turbulent water into turbulent spot by gulping process, following Cantwell *et al*. (1978). This was clearly seen by the direction of the vorticity, rotating like bringing the laminar water into its body in this region. However, entrainment process, called nibbling, was found at the rear edge of the spot. When the hairpin vortices were induced, they nibbled the laminar fluid into its body. The new fresh water, surrounding this region, must flow in to fulfill the place of the pulled water. These were the reasons of the obtained streamline, presented by Cantwell *et al*. (1978). The vorticity was followed by spot body, integration of various hairpin vortices. In this region, milk solution was mostly pulled up from the surface into turbulent spot by the formation of each hairpin vortex. The existent hairpin vortex was pushed forward by the new one. At the same time, there was the entrainment, induced by the overhang vorticity, flow along the near wall region. These made the vortex fell down and behaved like sub vortex within spot body. Unlike the first two parts, illustrating the chaotic movement inside, calming flow was found at the trailing region. The dye in this area orderly aligned as found in laminar boundary layer. This region was denoted that becalmed region. These observations agreed with the results, reported by Chong and Zhong (2006). They constructed the structure of turbulent spot by u and v components of velocity. The results showed that turbulent spot traveled downstream with single spanwise vortex at the overhang region with the direction as found by this technique. Moreover, directions of velocity magnitude within lower portion of turbulent spot body were also agreed to the observed direction of hairpin vortices.

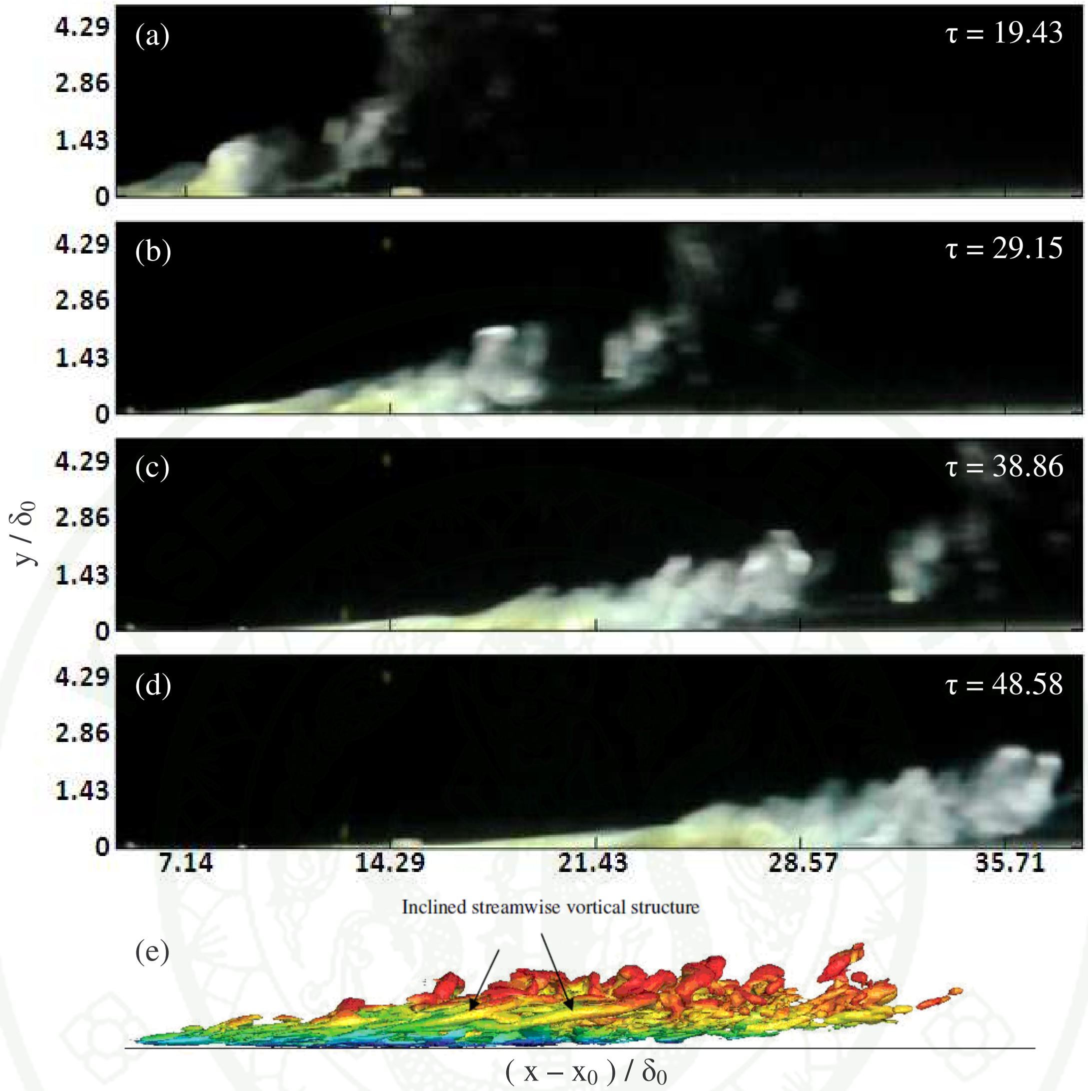

Figure 78 (a)-(d) Turbulent spot structure under zero pressure gradient on the plane z = 0 m., (e) Vortical structure of turbulent spot on flat plate.

Source: Chu *et al.*(2010)

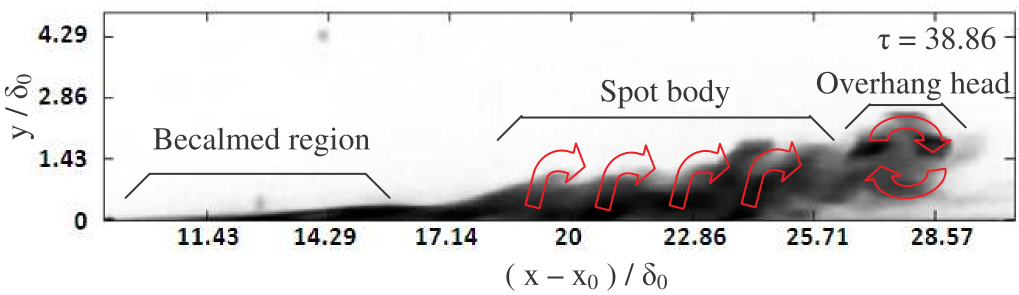

Figure 79 Flow mechanism within turbulent spot structure on the plane z = 0 m.

Fig. 80 shows the evolution of turbulent spot with colorbar of milk intensity. Three curves were directly added to the consecutive images. The highest and lowest ones show the thickness of turbulent and laminar boundary layer, respectively. In addition, the middle curve was constructed at the height of the turbulent boundary layer, originating at the spot generator with an initial thickness of laminar boundary layer at that location, suggested by Schubauer and Klebanoff (1956). It was found that the height of turbulent spot scales approximately as the height of this curve. The elevation of spot overhang was equal to the thickness of laminar boundary layer when it reached the normalized streamwise distance of 35.71 from spot generator, in agreement with results, reported by Wygnanski (1976). Furthermore, turbulent spot body was obviously split into two parts as labeled A and B in Fig. 80(d). Inside region A, the dynamic of dye filament was similar to those found in fully turbulent boundary layer. For turbulent spot under zero pressure gradient, the height of this part was found between the lowest and the middle curves. Meanwhile, part B followed the thickness of laminar boundary layer. The similarity of these distinct characteristics could be found in each different individual turbulent spot as shown in Fig. 81. It should be noted that turbulent spot developed in hightwise direction without the relation with the thickness of turbulent boundary layer. Therefore, only middle curve and thickness of laminar boundary layer were presented in Fig. 81.

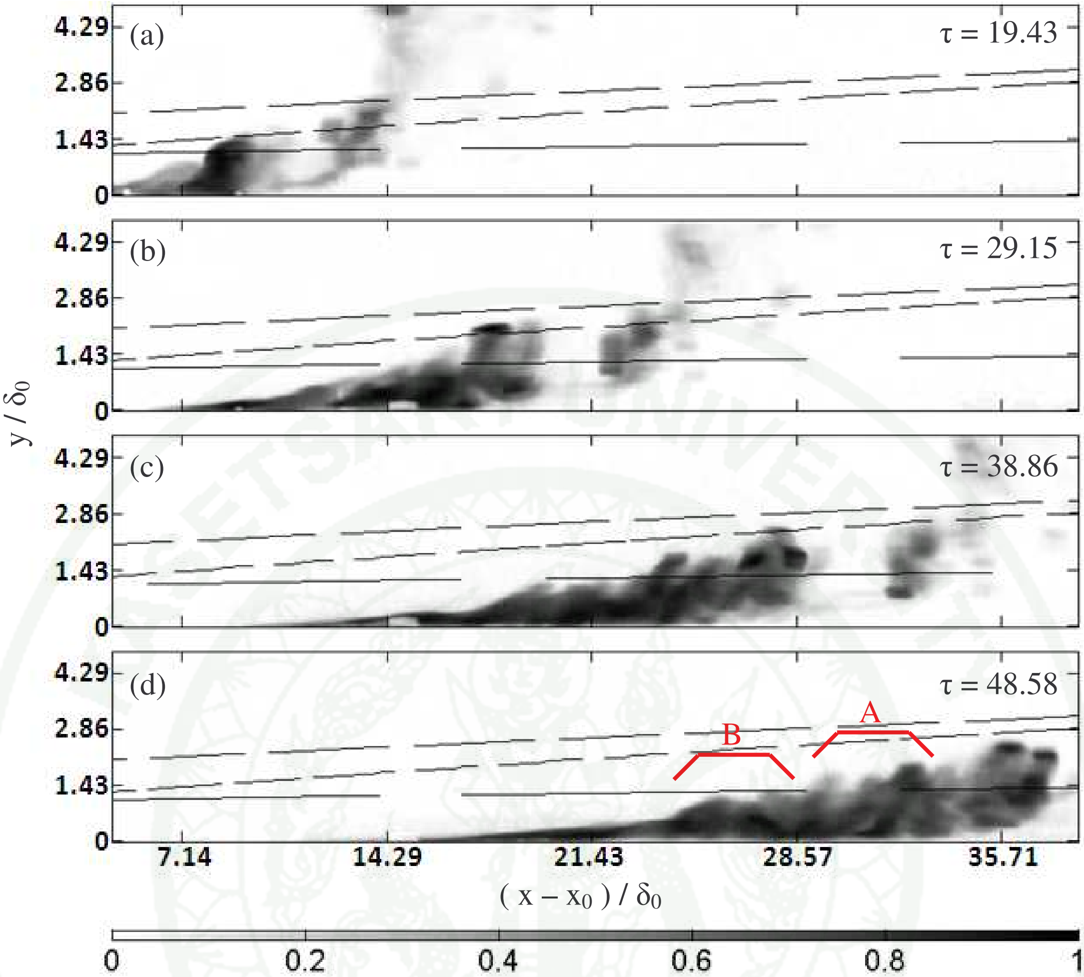

Figure 80 The spot structure with curves of boundary layers on the plane z = 0 m.

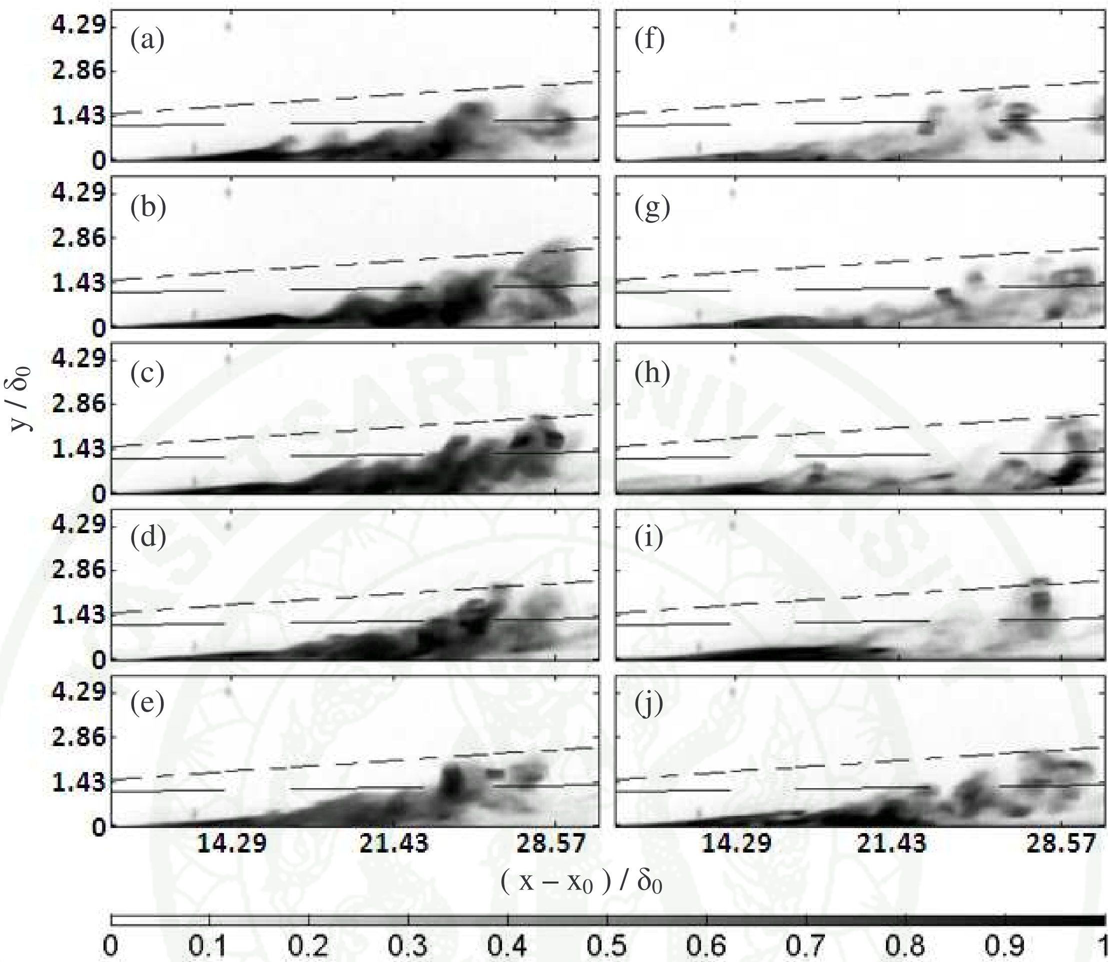

Figure 81 Ten individual turbulent spots on the plane z = 0 m at 1.6 s or $\tau = 38.86$ after disturbance injection.

From Fig. 81, it was found that each of ten individual turbulent spots behaved similarly when they propagated downstream. To eliminate the random effect that occurred if the different spots were considered, the representative structure was proposed as illustrated in Fig. 82. This structure was constructed from 15 individual spots using the centroid averaging technique. It should be noted that this representative structure emphasized on the location and the laminar-turbulent interface, bounding its structure. Thus, the whole shape of turbulent spot on the spatial contours of the plane z = 0 m was revealed. When the bound was presented, it was found that the structure consisted of the overhang head and the long tail body. The overhang tip followed the curve of laminar boundary layer. Moreover, the obtained structure also revealed the hump that was limit by the curve, created from the thickness of turbulent boundary layer that started from the thickness of boundary layer laminar at the location of spot generator. The appearance of spot features typically agreed to the shape of each individual turbulent spot. Hence, this structure was directly comparable to the representative structure on the other planes.

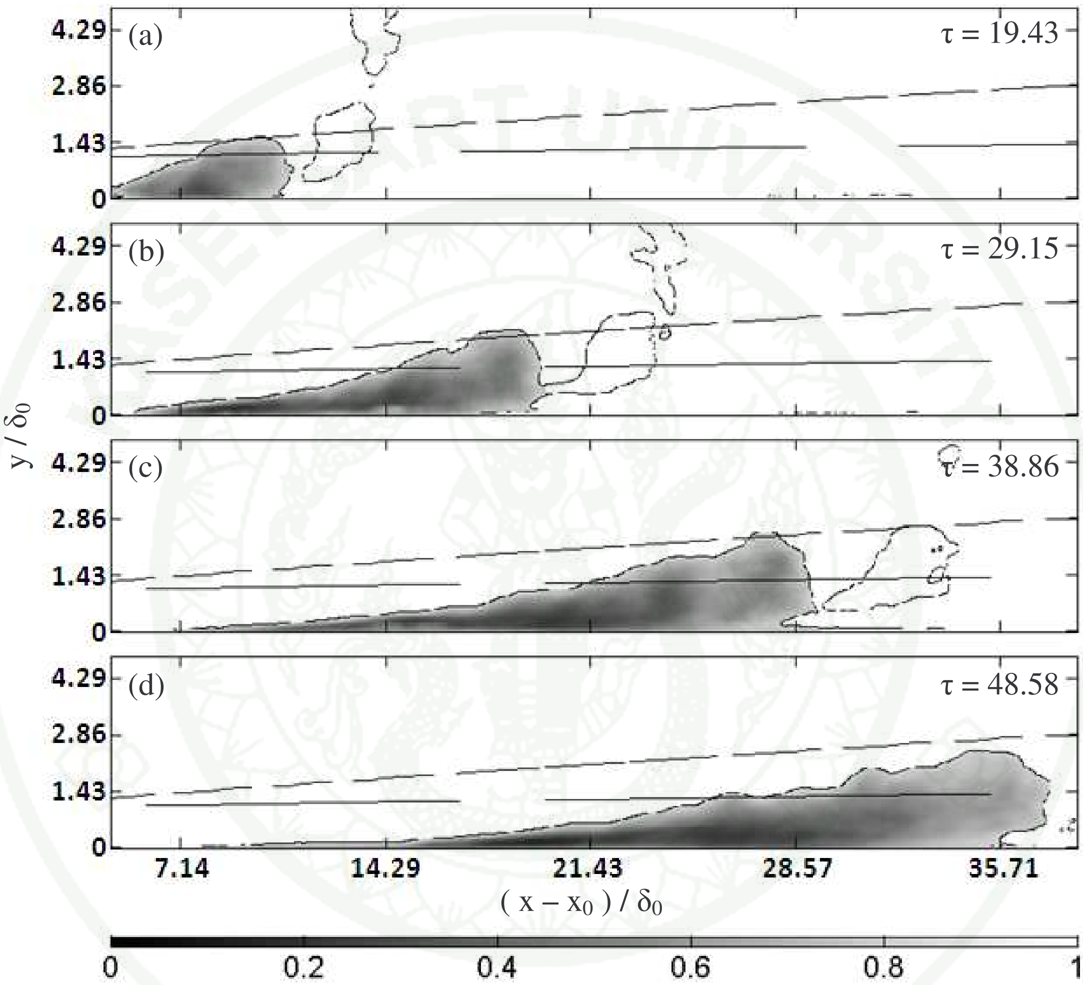

Figure 82 The representative structure of turbulent spot on the plane z = 0 m at different instant time.

Fig. 83(a)-(c) show the consecutive frames of turbulent spot on the plane z = 0, 0.01, 0.02 m, respectively. They were all illustrated in RGB signal. It should be noted that the series of image in each plane were grabbed from the different individual turbulent spot. These images show that the size of turbulent spot on the plane z = 0 was relatively larger than the other planes in both heightwise and streamwise direction. Turbulent spot on plane z = 0.01 and 0.02 m were found as the combination of various hairpin vortices. When the positions of the detected spot on the other planes were compared to the structure on plane z = 0 m, it was found that these corresponded to its body that mainly performed as a group of hairpin vortices. Thus, without its overhang head, established by the spanwise vorticity, the whole turbulent spot body primarily was the vortices that generally found in fully turbulent boundary layer as shown in Fig. 84 and 85 on the plane z = 0.01, 0.02 m. However, it was found that small vortex was occasionally appeared within spot body.

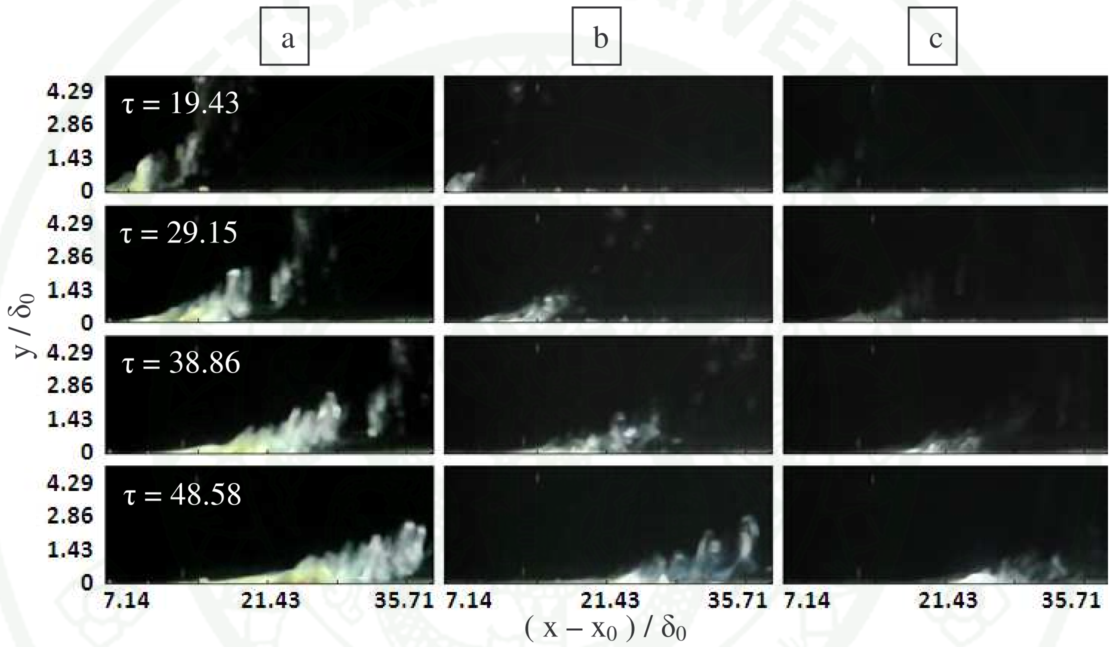

Figure 83 (a)-(c) Turbulent spot structure under zero pressure gradient on the plane z = 0, 0.01, and 0.02 m, respectively.

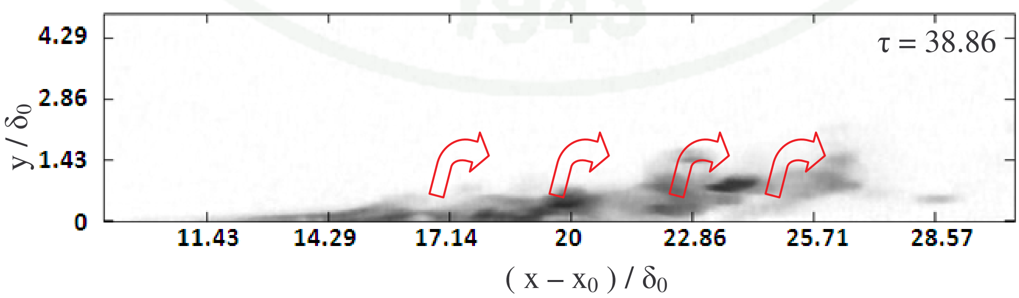

Figure 84 Flow mechanism within turbulent spot structure on the plane z = 0.01 m.

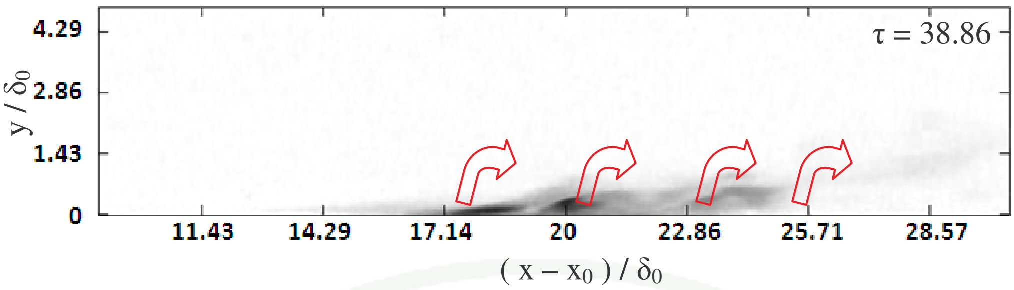

Figure 85 Flow mechanism within turbulent spot structure on the plane z = 0.02 m.

Fig. 86(a)-(c) and 87(a)-(c) show the evolution of different individual and the representative structure of turbulent spot on the plane z = 0, 0.01, and 0.02 m with the boundary layers. It was found that turbulent spot grew with different manner, comparing to the other planes. On the plane z = 0.01 m, turbulent spot hump directly acceded the created curve. Even it was slower than itself on the plane z = 0 m, the hump on the plane z = 0.01 m pierced through the laminar thickness to reach the created curve. It eventually performed like its structure on plane z = 0 as shown in the image at $\tau = 48.58$ of Fig. 86(b) and 87(b). Meanwhile, the structure on the plane z = 0.02 m still acceded the thickness of the laminar boundary layer. The tip of overhang head on the plane z = 0.01 m also obeyed the laminar thickness while the tip on the plane z = 0.02 m was below. Besides, the length of the structure was shorter on the other planes, far from the symmetry.

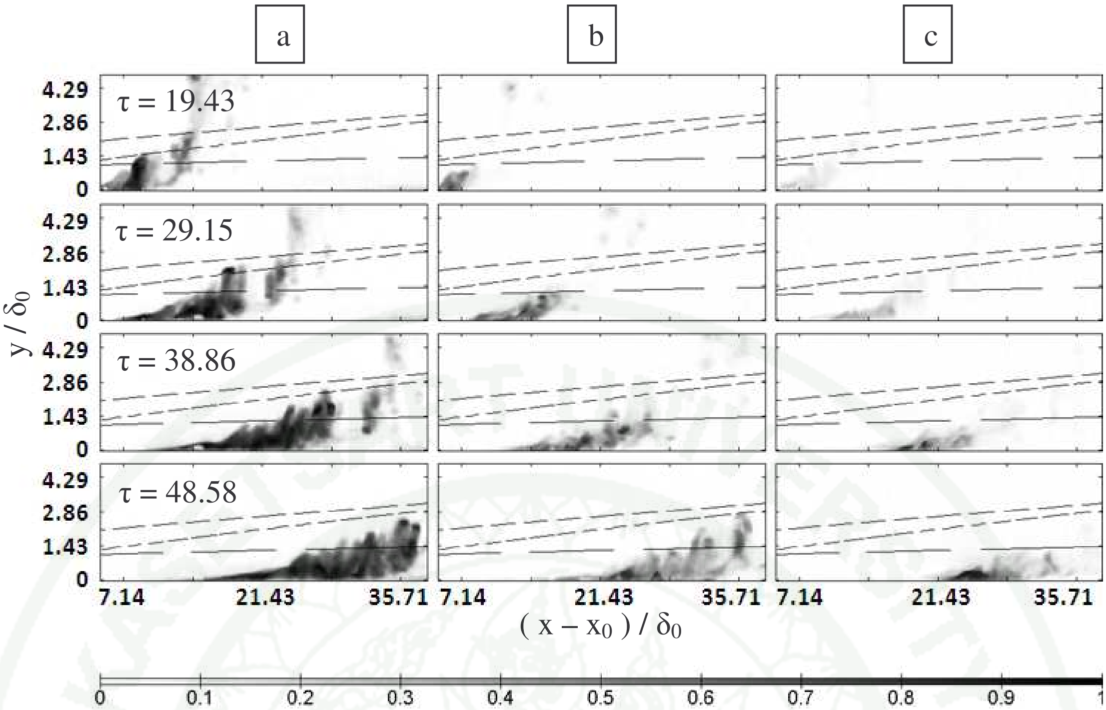

Figure 86 (a)-(c) Turbulent spot structure with curves of boundary layer under zero pressure gradient on the plane z = 0, 0.01, and 0.02 m, respectively.

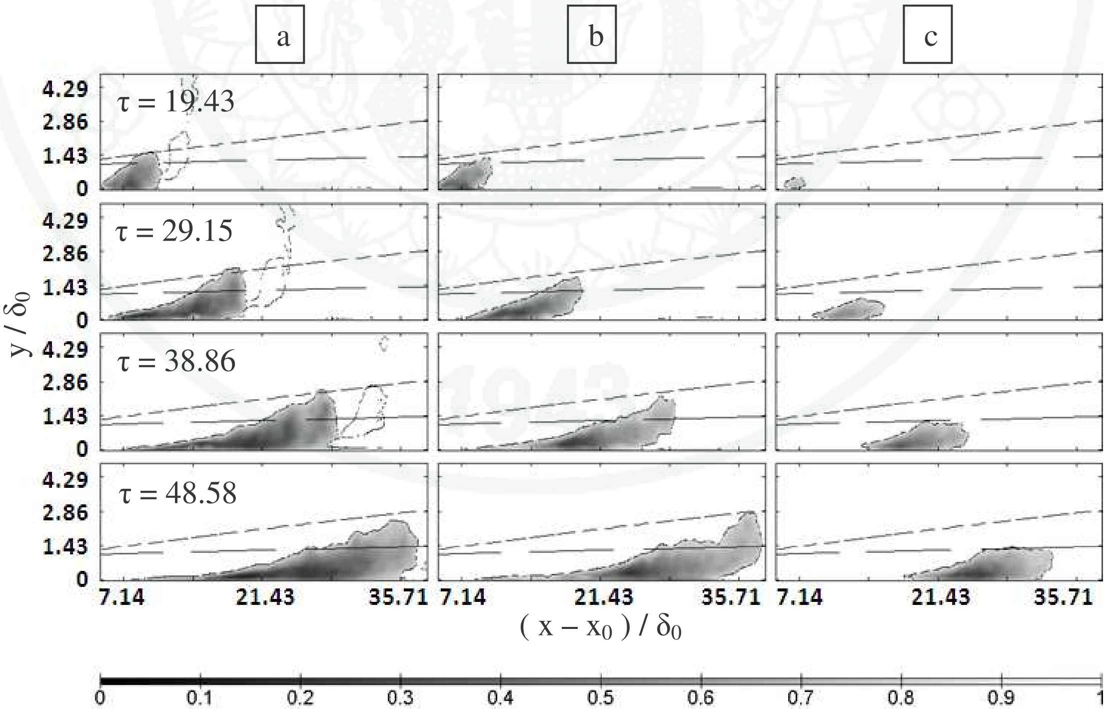

Figure 87 (a)-(c)Turbulent spot structure under zero pressure gradient on the plane z = 0, 0.01, and 0.02 m, respectively.

When the representative structures on each plane were arranged in the same domain, the structure of turbulent spot under zero pressure gradient on the plane, normal to the surface was constructed as shown in Fig. 88. The darkest structure presents the spot on the plane $z = 0.02$ m. Conversely, the grayer one shows the structure on the plane $z = 0.01$ and 0 m, respectively. It was clearly found that the size of turbulent spot on the other planes was limited by the structure on plane $z = 0$ m. In other words, it grew mostly on the symmetry plane. However, as it propagated downstream, the structure on the other planes eventually performed as on the plane of symmetry. As seen in the image at $\tau = 48.58$, it is found that the overhang head on the plane $z = 0$ and 0.01 m locate equally although they initiate differently. From this observation, the spanwise vorticity was capable to induce the surrounding flow and became bigger as it moved downstream until it decays, following Singer and Joslin (1994). Also, its tail, including becalmed region was longest on the plane of $z = 0$ m while it was shorter on the plane far from symmetry. Hence, the length of becalmed region was directly related to the level of the turbulence inside turbulent spot.

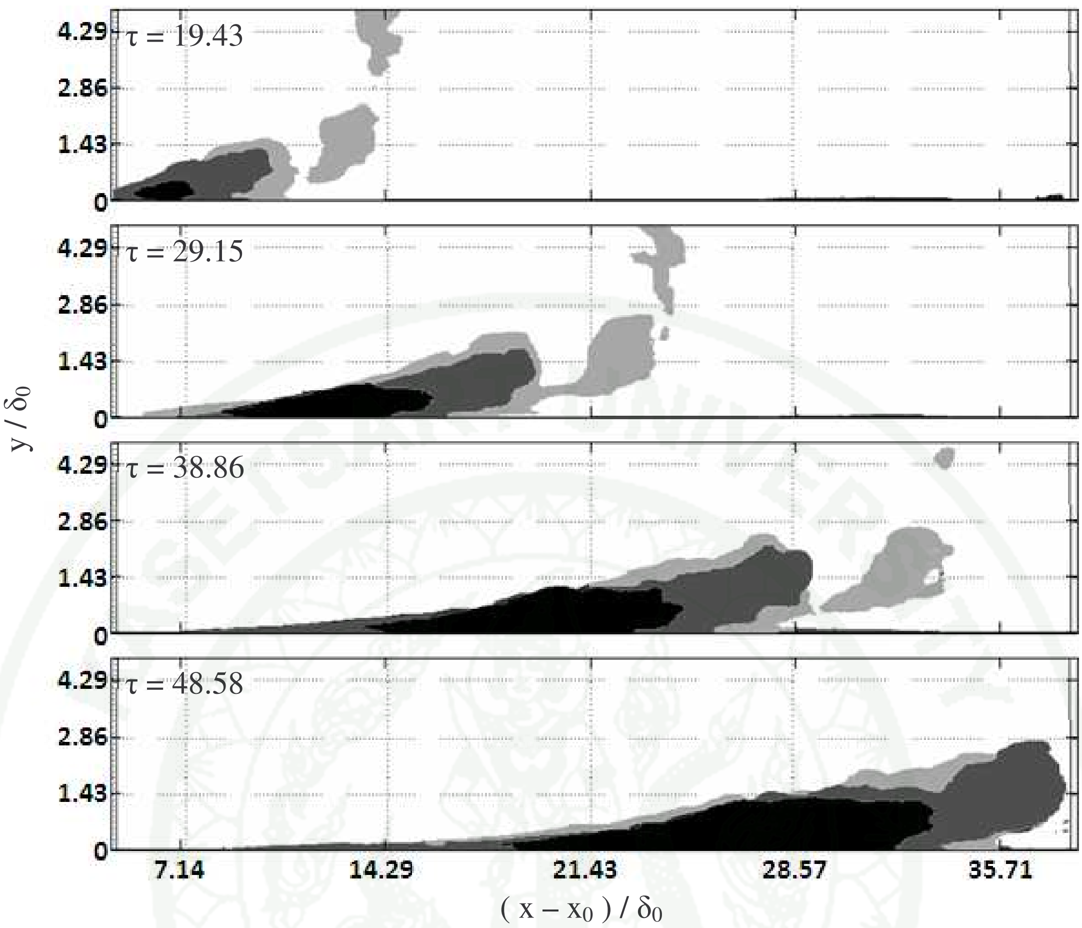

Figure 88 The whole structure of turbulent spot under zero pressure gradient.

2.1.2 Turbulent spot development on the plane perpendicular to the plate surface under the influence of adverse pressure gradient

Fig. 89(a)-(c) show individual turbulent spot on the plane z = 0 m under the influence of zero, mild, and strong adverse pressure gradients, respectively. It was found that the shapes of the spots on the plane, normal to the surface under various pressure gradients were similar. There were the presence of spanwise vorticity at the overhang head and also the group of hairpin vortices within spot body. However, there was another hump appeared on the rear interface of the spot when the level of adverse pressure gradient was increased as shown in Fig. 89(c). Comparing to results under zero pressure gradient, this hump made the spot body thicker in heightwise direction. Also, the body of the spot on the plane z = 0.01 and 0.02 m were also affected by the pressure gradient as shown in Fig. 90 and 91. Its height was increased when λ_θ was decreased.

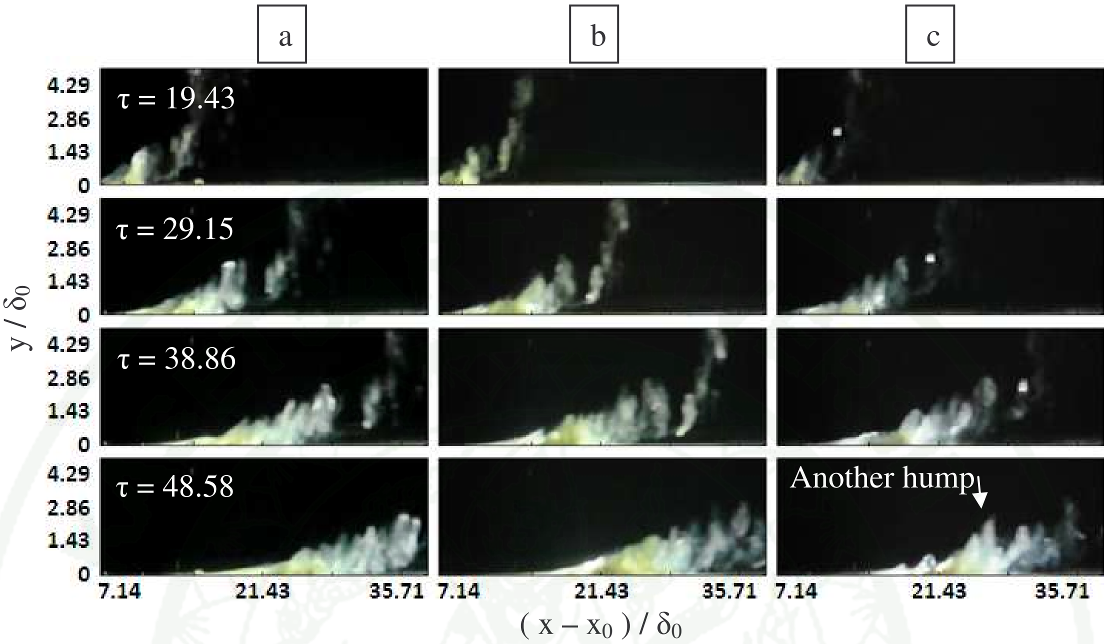

Figure 89 (a)-(c)The structure of turbulent spot on the plane z = 0 m under zero, mild, and strong pressure gradient, respectively.

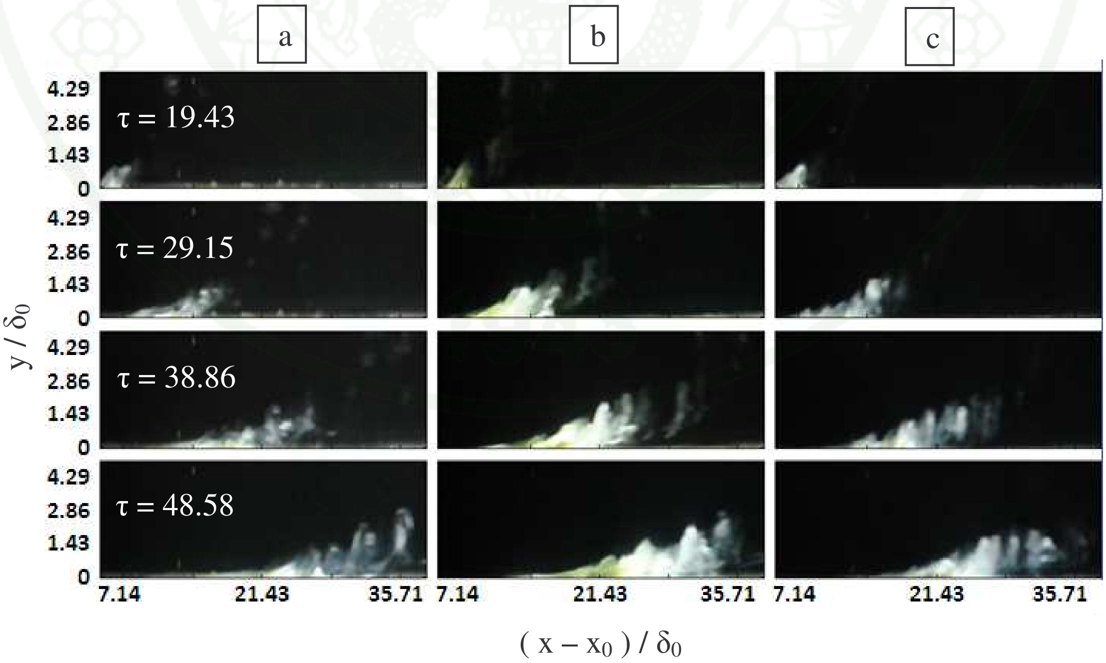

Figure 90 (a)-(c)The structure of turbulent spot on the plane z = 0.01 m under zero, mild, and strong pressure gradient, respectively.

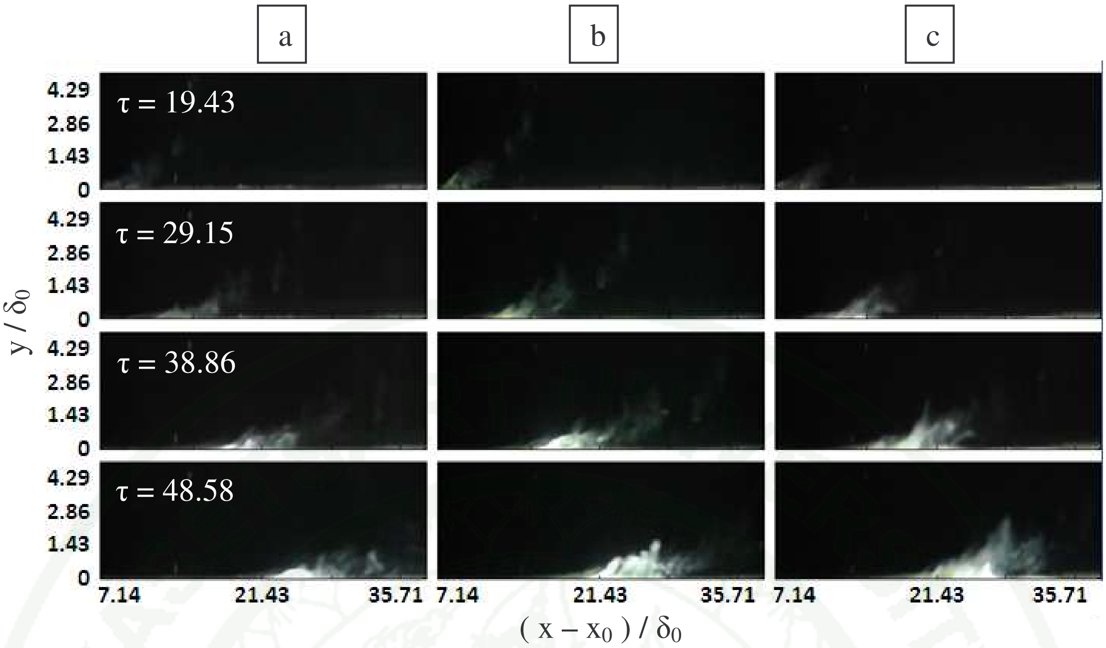

Figure 91 (a)-(c)The structure of turbulent spot on the plane z = 0.02 m under zero, mild, and strong pressure gradient, respectively.

When the boundary layers were added into the consecutive images of the spot, it was found that the height of the spot in the recorded domain was limited to the thickness of turbulent boundary layer as shown in Fig. 92, 93, and 94. The height of the new hump on the back of each spot grew beyond the laminar thickness and reached the middle curve when it convected downstream. The frontal interfaces of the overhang region were blunt. The overhang tip of turbulent spots under each pressure gradient was followed the thickness of laminar shear layer.

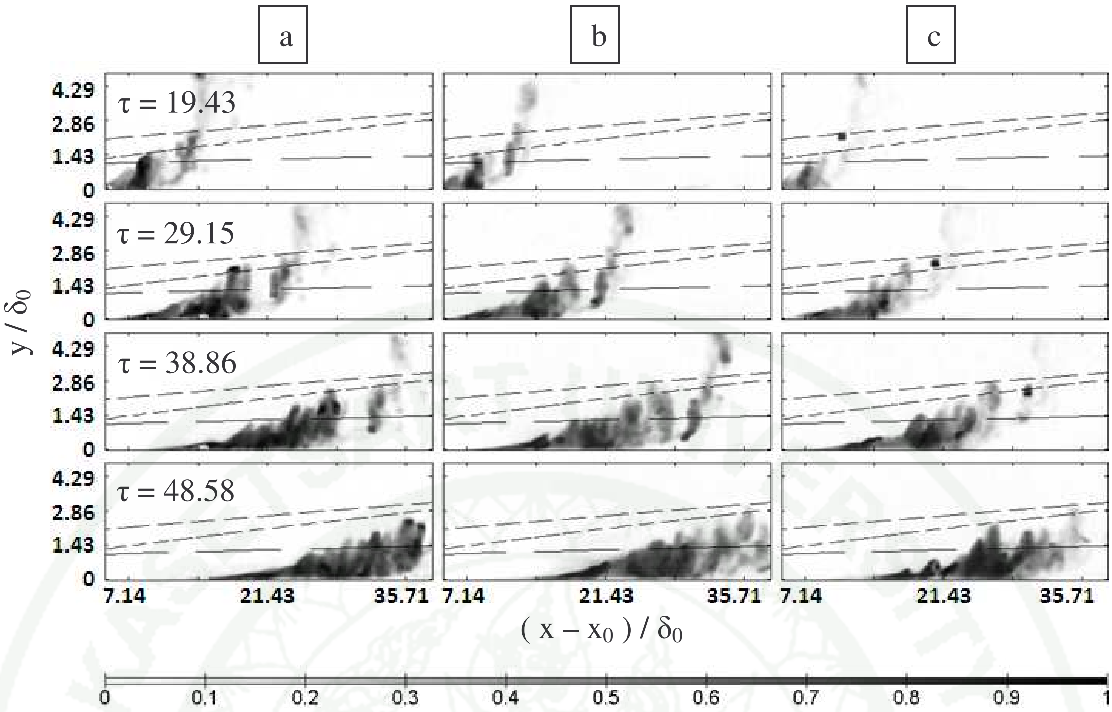

Figure 92 (a)-(c)Turbulent spot on the plane z = 0 m with the curves of boundary layer under zero, mild, and strong pressure gradient, respectively.

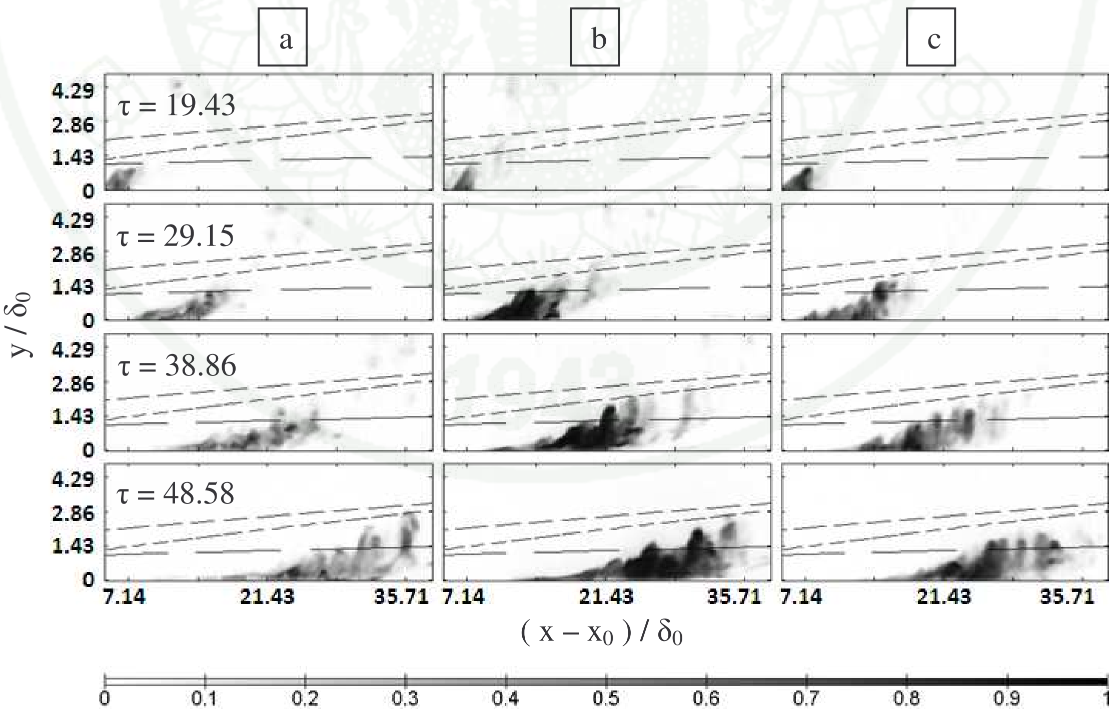

Figure 93 (a)-(c)Turbulent spot on the plane z = 0.01 m with the curves of boundary layer under zero, mild, and strong pressure gradient, respectively.

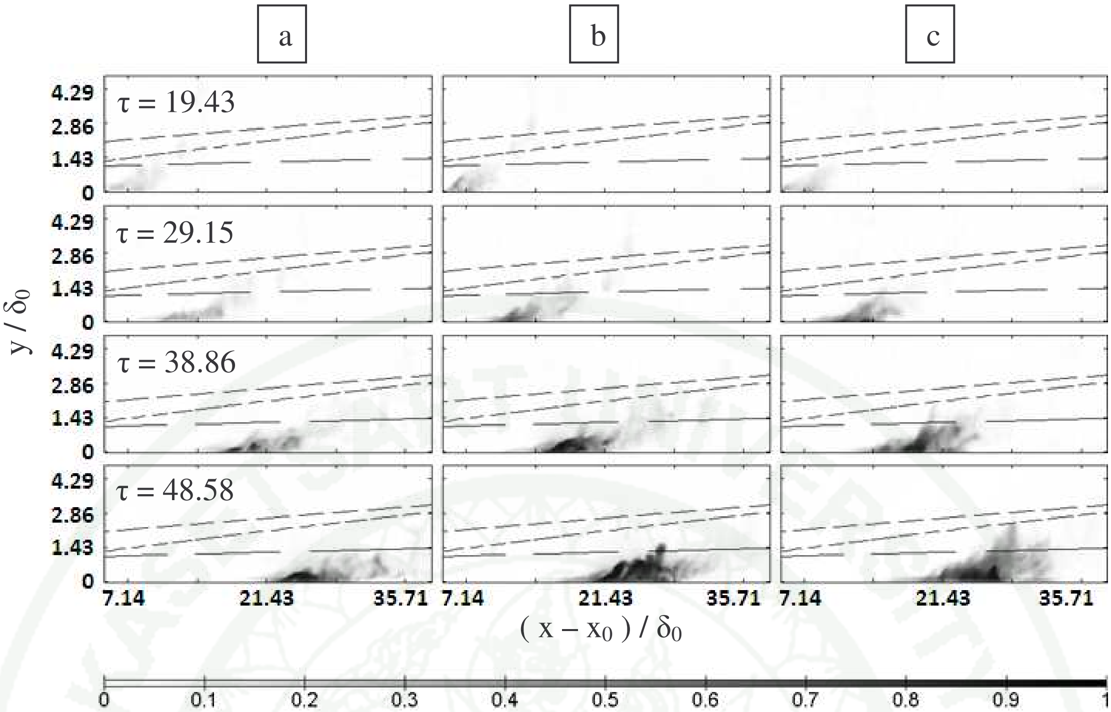

Figure 94 (a)-(c)Turbulent spot on the plane z = 0.02 m with the curves of boundary layer under zero, mild, and strong pressure gradient, respectively.

When the representative structures of turbulent spot under various adverse pressure gradients were presented as depicted in Fig. 95, 96, and 97, it was clearly found that the hump of its overhang grew higher than the thickness of middle curve. This confirmed that the height was no longer limited to this layer as the pressure gradient was increased. It was also found that the interface at its rear swelled out. This region reached the middle layer in the case of the strong pressure gradient. However, the shapes of turbulent spot on the plane of z = 0.01 and 0.02 m seemed quite similar under each level of λ_θ.

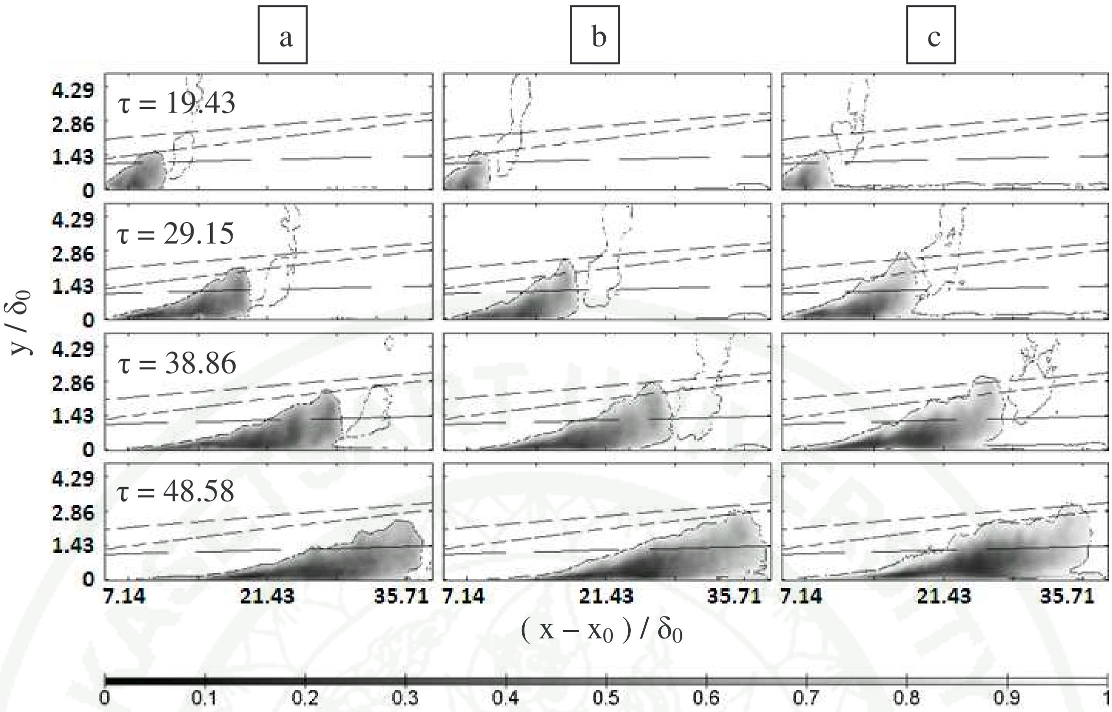

Figure 95 (a)-(c)The representative structure of turbulent spot on the plane z = 0 m under zero, mild, and strong pressure gradient, respectively.

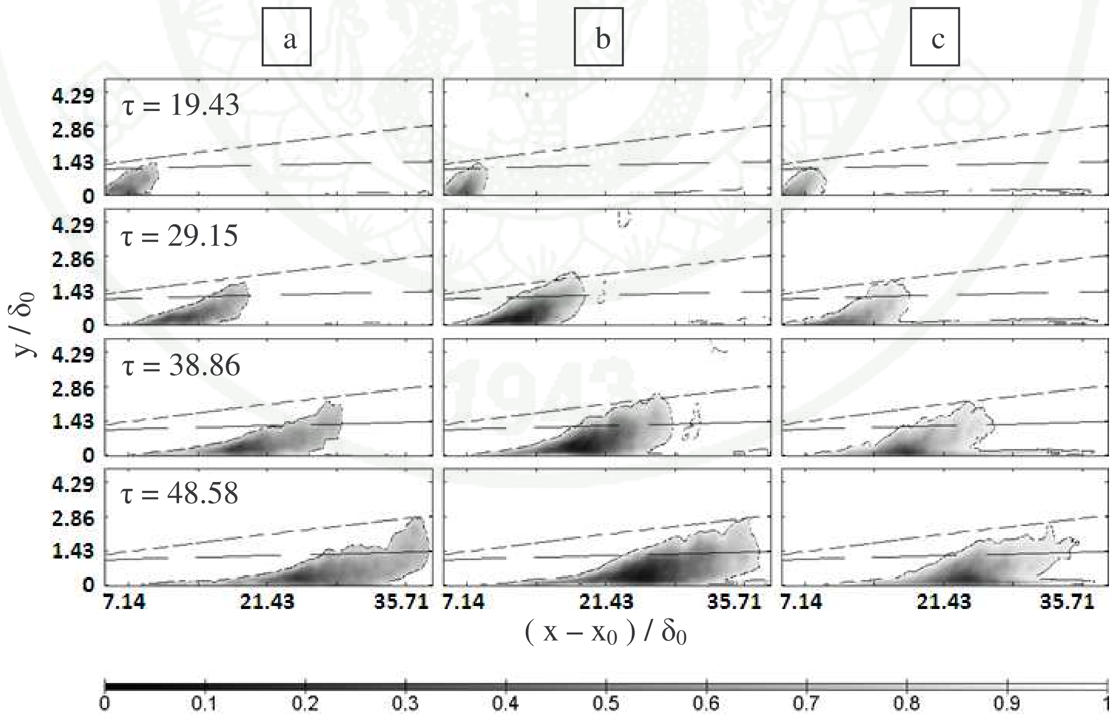

Figure 96 (a)-(c)The representative structure of turbulent spot on the plane z = 0.01 m under zero, mild, and strong pressure gradient, respectively.

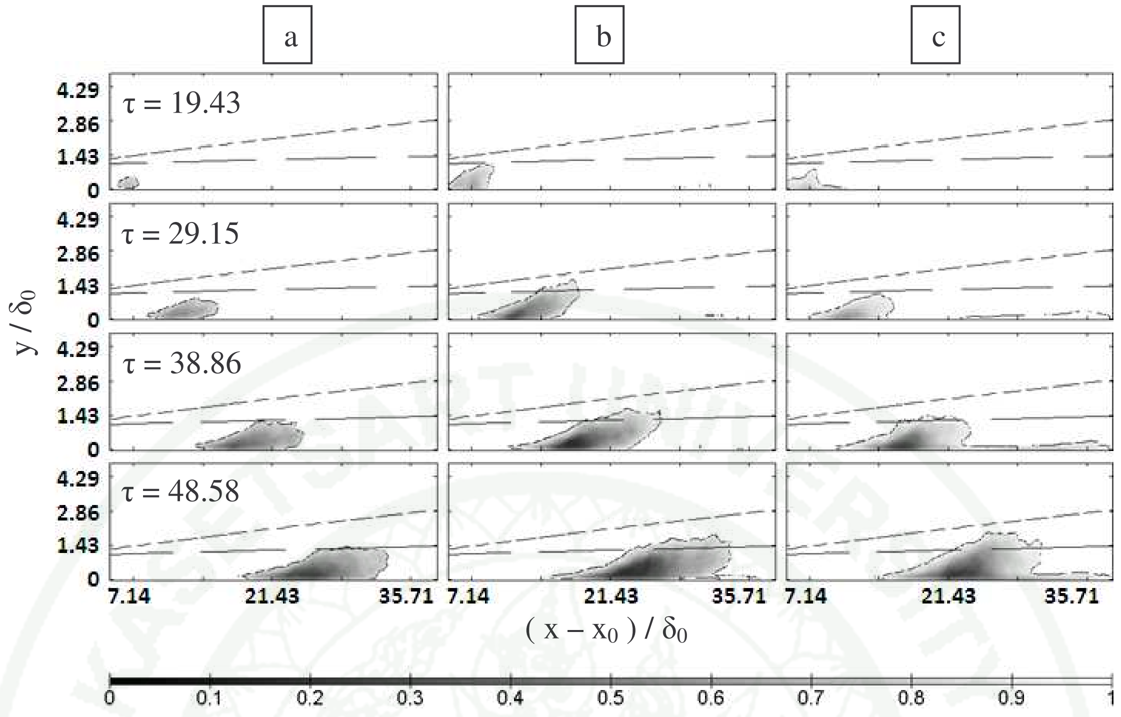

Figure 97 (a)-(c)The representative structure of turbulent spot on the plane z = 0.02 m under zero, mild, and strong pressure gradient, respectively.

Fig. 98(a)-(c) show the representative structure of turbulent spot under the influence of zero, mild, and strong adverse pressure gradients, respectively. As expressed previously, the darkest structure shows the spot on the plane z = 0.02 m. Meanwhile, the grayer one exhibits its structure on the plane z = 0.01 and 0 m, respectively. This is clear evidence, showing that the adverse pressure gradient directly affects on the whole structure of turbulent spot. It accelerates the boundary layer transition to be fully turbulent state in the quicker time. In the present study, λ_θ was decreased from 0 to -0.06037 that is very close to the verge of separation at -0.082. The structure of the spot at this low λ_θ was simply found on the mature state when it was in the late of transition region. Also, the hump of the spot grew beyond the thickness of turbulent boundary layer which did not happen under zero pressure gradient. However, it was found that the structure was blunter and propagated slower, when it underwent the stronger adverse pressure gradient. The step, created by the structure on different plane on the frontal region, also confirmed the presence of the arrow head shape of turbulent spot. Nevertheless, the arrow head-like shape were clearer if it was observed from the top view as will be discussed later.

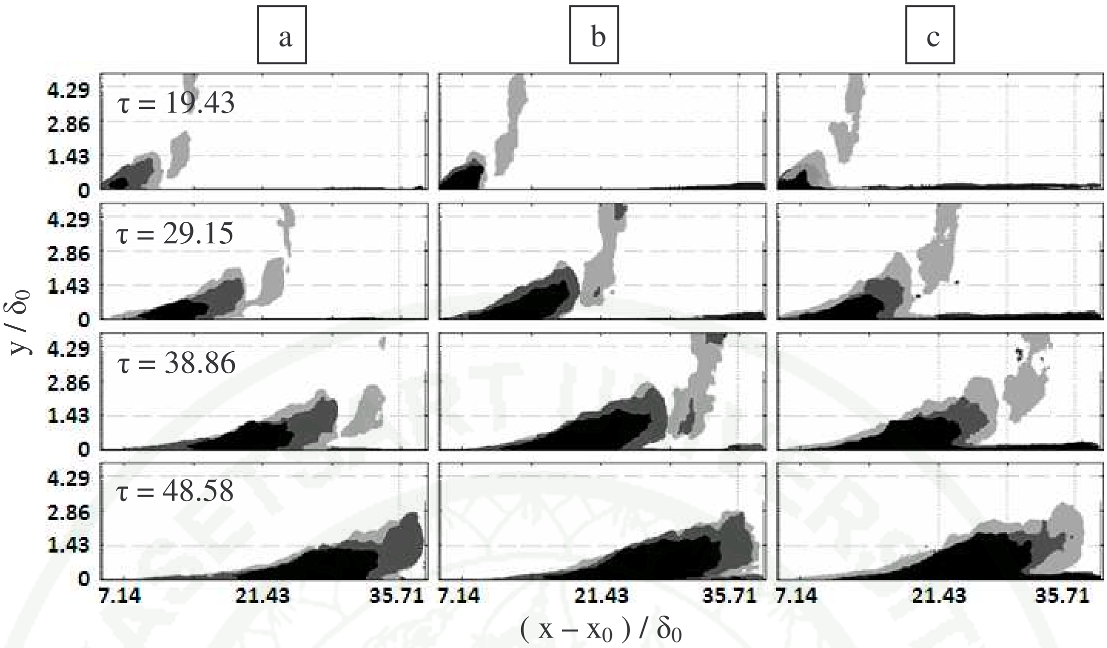

Figure 98 (a)-(d)The whole structure of turbulent spot under zero, mild, and strong pressure gradient.

2.1.3 Turbulent spot parameters on the plane perpendicular to the plate surface

By this visualization technique, spot celerity was measured at the different feature of the structure using the developed image processing code. When the hump of the structure was marked as the highest point at y_h, seven levels were localized as the measurement point on both frontal and rear interfaces of the spot as shown in Fig. 99. Thus, the celerity was obtained by these thirteen points on the laminar-turbulent interface as the spot traveled downstream. Fig. 100 shows the spatial distribution of measurement locations as they moved by the development of the spot at τ = 19.43, 29.14, and 38.86 after disturbance injection. It was found that their level was not stationary because each of them depended directly on the height of the structure.

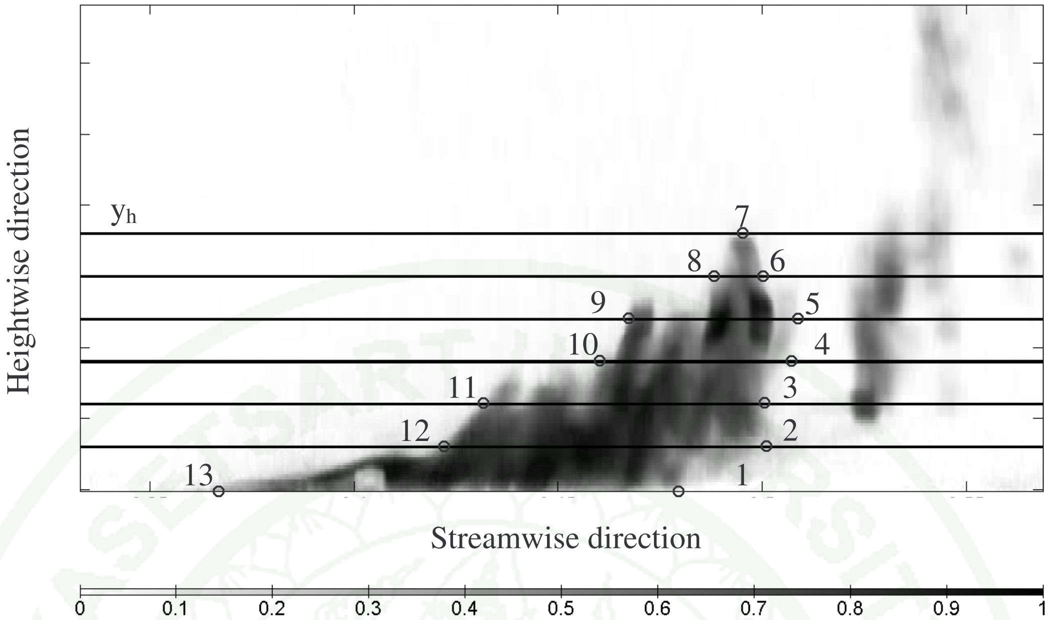

Figure 99 The measurement points on turbulent spot structure.

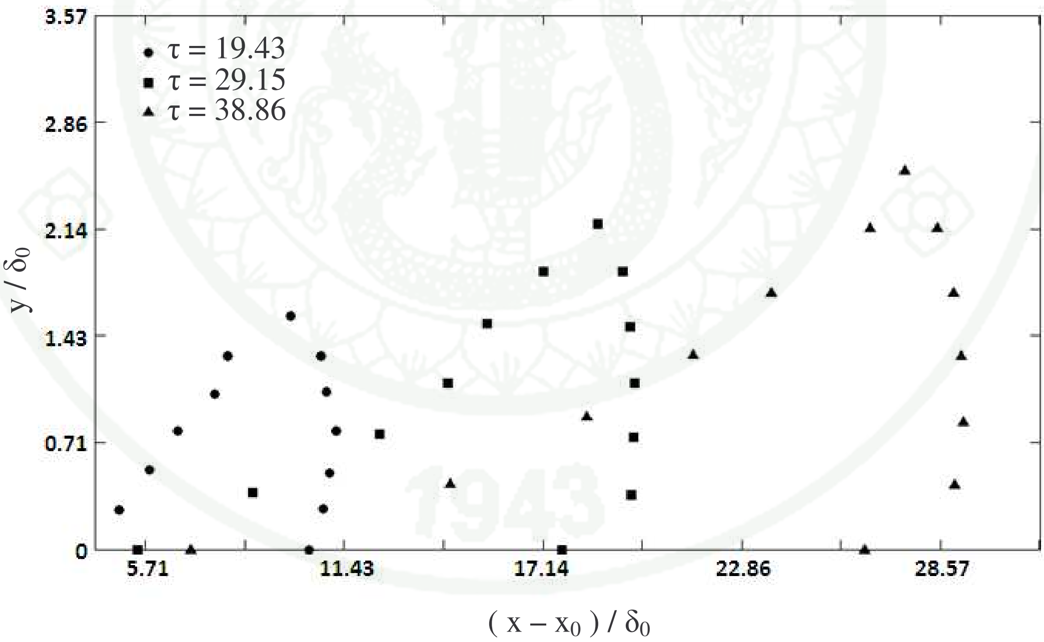

Figure 100 The measurement points on turbulent spot structure at τ = 19.43, 29.14, and 38.86 after disturbance injection.

The similarity on shape of turbulent spot structure at the normalized time of 19.43, 29.14, 38.86, and 48.57 after injection was investigated. All spots were non-dimensionalized on both streamwise and heightwise axis as depicted in Fig. 101. On streamwise direction, the most downstream interface edge was taken in account as 1 while 0 was set at the tip of its tail. Meanwhile, the hump was deemed as 1 on heightwise direction. From the results, it was found that the shape of turbulent spot at the frontal interface was quite constant. However, slight difference was found at its rear edge. The tail of younger turbulent spot occurred as a short one. Spot trail became longer as it propagated further downstream. Furthermore, the virtual onset of turbulent spot was found at intersection of the fitting lines of three different positions on the interface edge at τ = 19.43, 29.14, and 38.86. Height levels that was specified as measurement point were selected at y/y_h = 0.333, 0.667, and 1. It was found that the virtual onset was on the location of 0.1585 m downstream from leading edge of the test plate as shown in Fig. 102. It was different from the virtual onset of turbulent spot under zero pressure gradient that was reported at 0.167 m from the leading edge.

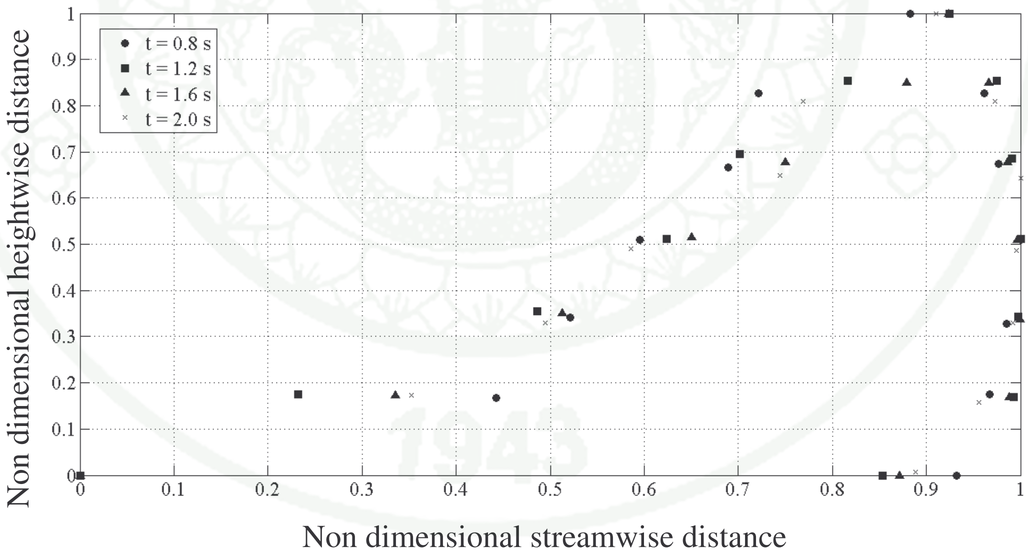

Figure 101 The similarity on shape of turbulent spot structure at the time of 0.8, 1.2, 1.6, and 2.0 s after injection.

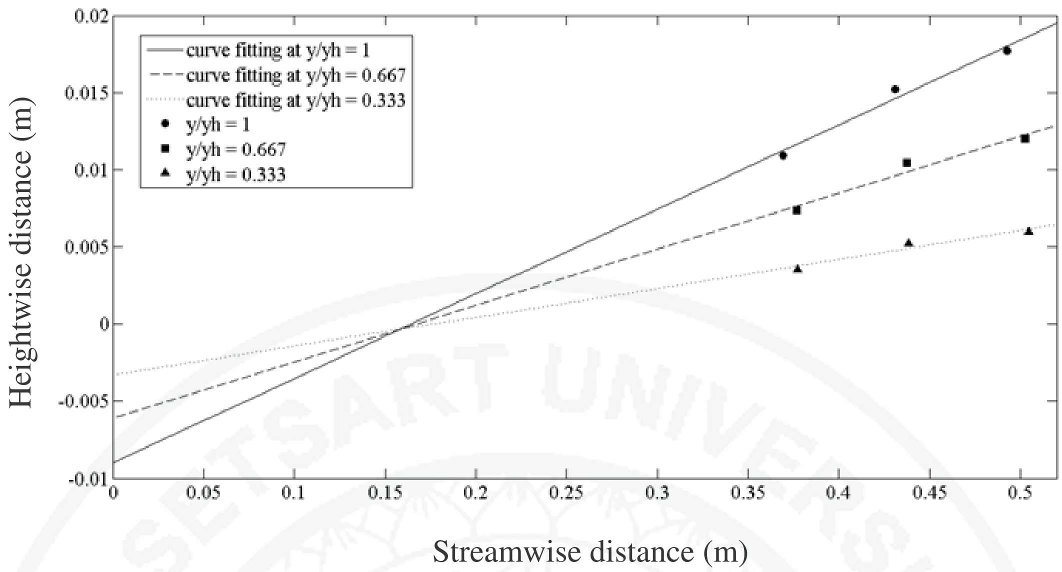

Figure 102 The prediction of virtual onset of turbulent spot on the plane z = 0 m.

The similarity of the spot structure under various adverse pressure gradients was also investigated as depicted in Fig. 103. It was found that the shape of spot structure under each pressure gradient was not apparently different, especially at the frontal edge. However, the thickness of rear interface of turbulent spot increased under the stronger adverse pressure gradient. This was a result of the increasing pressure along streamwise direction under adverse pressure gradient. This pressure obstructed turbulent spot on the main steam direction. Thus, this effect accelerated the growth rate on both spanwise and heightwise directions. Besides, the locations of virtual onset of turbulent spot under mild and strong adverse pressure gradient were also predicted as depicted in Fig. 104 and 105, respectively. They moved toward the position of spot generator as found on the surface, using coating TLCs. The location was 0.179 m from the leading edge of the aluminum plate under mild level and 0.2196 for strong adverse pressure gradient.

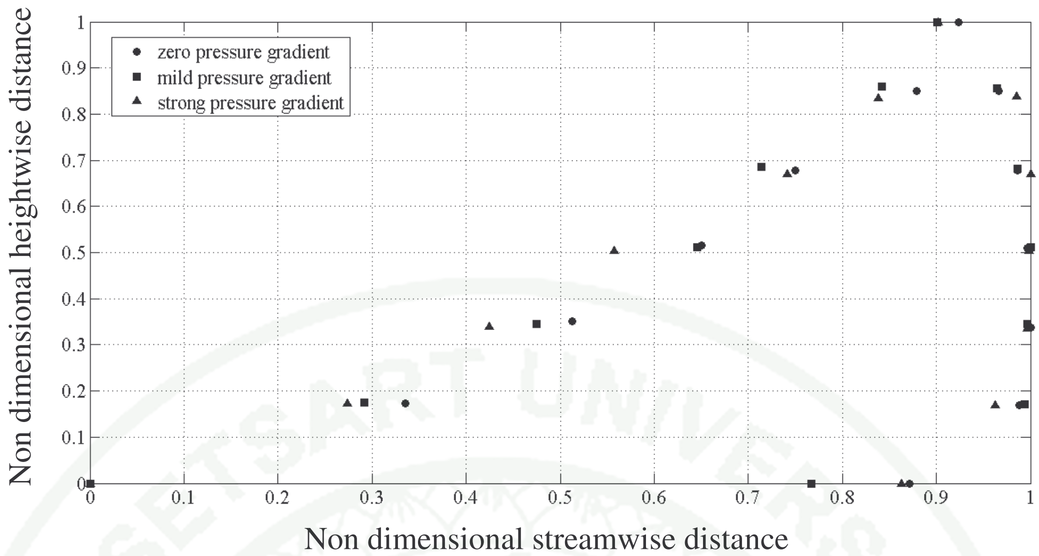

Figure 103 The similarity on shape of turbulent spot structure under zero, mild, and strong adverse pressure gradient.

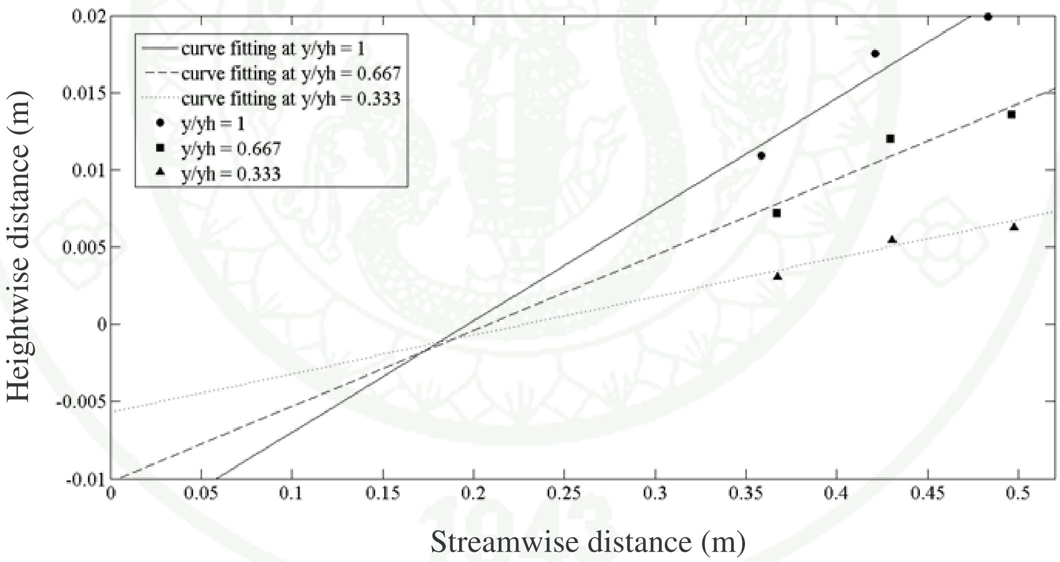

Figure 104 The prediction of virtual onset of turbulent spot on the plane z = 0 m under mild adverse pressure gradient.

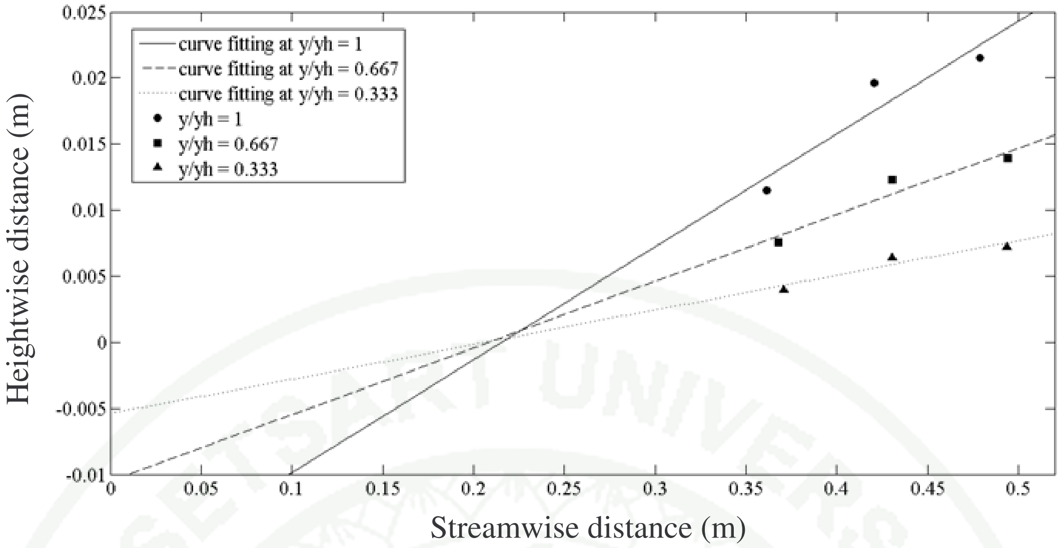

Figure 105 The prediction of virtual onset of turbulent spot on the plane z = 0 m under strong adverse pressure gradient.

2.2 Turbulent spot information on the plane parallel to the plate surface

2.2.1 Turbulent spot development on the plane parallel to the plate surface under zero pressure gradient

When the white light sheet was illuminated parallel to the surface at the position of y = 3 and 6 mm, the milk solution was also effectively reflected and revealed the shape of turbulent spot. Fig. 106(a)-(d) and 107(a)-(d) show consecutive images of turbulent spot structure on the plane of y = 0.003 and 0.006 m, respectively in RGB color space. The recorded time started at τ = 19.43 and ended at 48.58 after the injection with interval of 9.72. All images were shown by the normalized streamwise distance between -2.86 to 42.86 on the flow direction. On spanwise direction, distance was set from -8.57 m to 8.57 m. Zero distance was found at the symmetry location. Before spot arrival, the test surface was covered by milk solution. After turbulent spot was activated by injecting water, the structural shape in each instant was achieved. It was found that the white structure, presenting high fluctuation region inside turbulent spot body, grew in both streamwise and spanwise direction. The frontal interface on turbulent spot on the plane of y = 3 mm was more obtuse.

Thus, it was more like the triangular arrow head shape as shown in Fig. 107. Even the movement inside the white area was extremely random by observation, it should be remembered that this was organized by the group of hairpin vortices. Thus, its trace, shown as the empty milk area, was left behind as becalmed region. Unlike the turbulent region, the flow over this area was more orderly which was in agreement with Cantwell *et al*. (1978), Gad-el-Hak *et al*. (1981), and Perry *et al*. (1981). However, it should be noted that the structures in both Fig. 106 and 107 were from different individual turbulent spot.

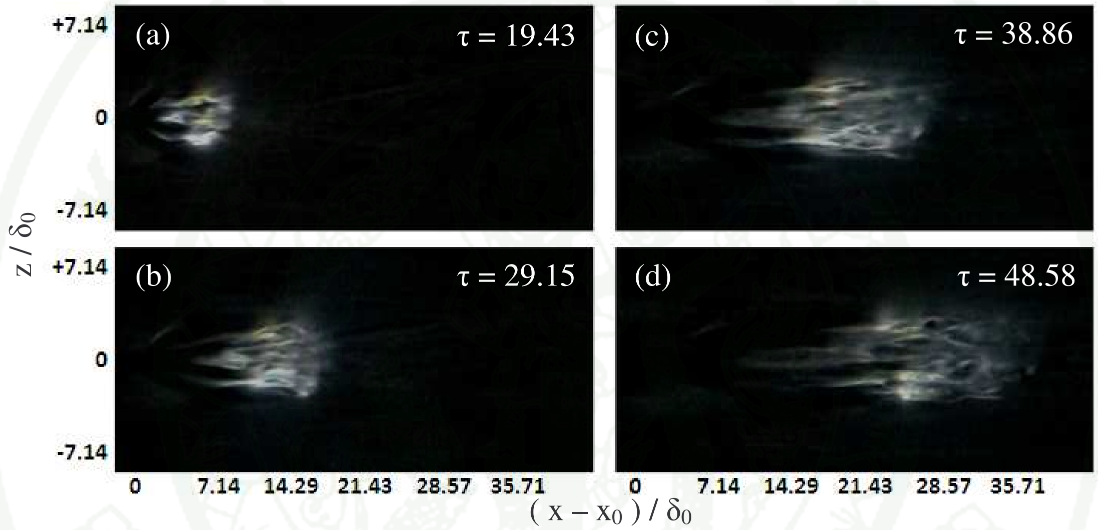

Figure 106 Turbulent spot under zero pressure gradient at y = 0.003 m.

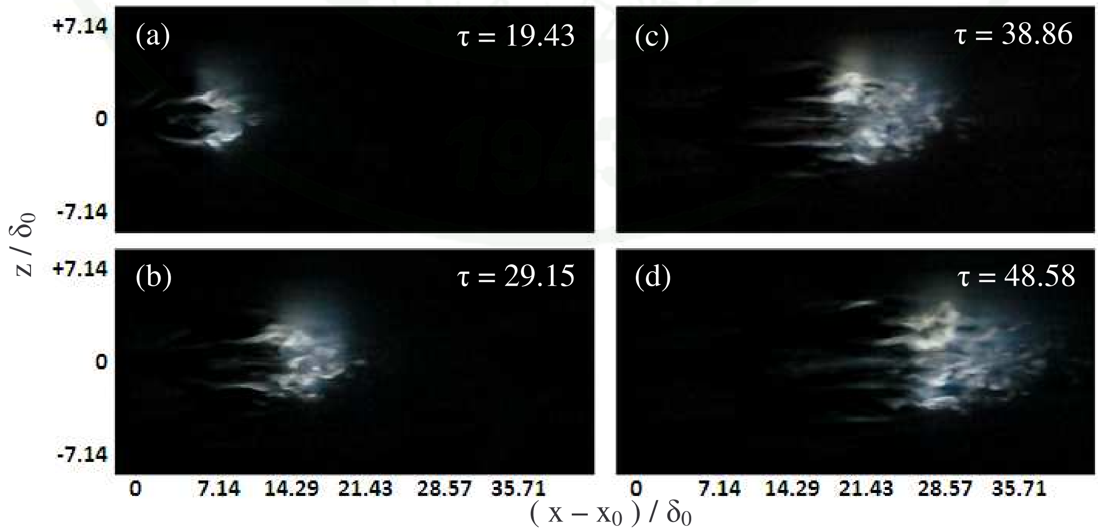

Figure 107 Turbulent spot under zero pressure gradient at y = 0.006 m.

Fig. 108(a)-(d) and 109(a)-(d) show the structure of turbulent spot from Fig. 106 and 107 after processed by the developed image processing code. In this figure, the below color bar shows milk intensity. When the backgrounds were deleted by the process of image subtraction, the sharp edge of laminar-turbulent interfaces in each instant emerged. It was found that the structure of turbulent spot was quite symmetry.

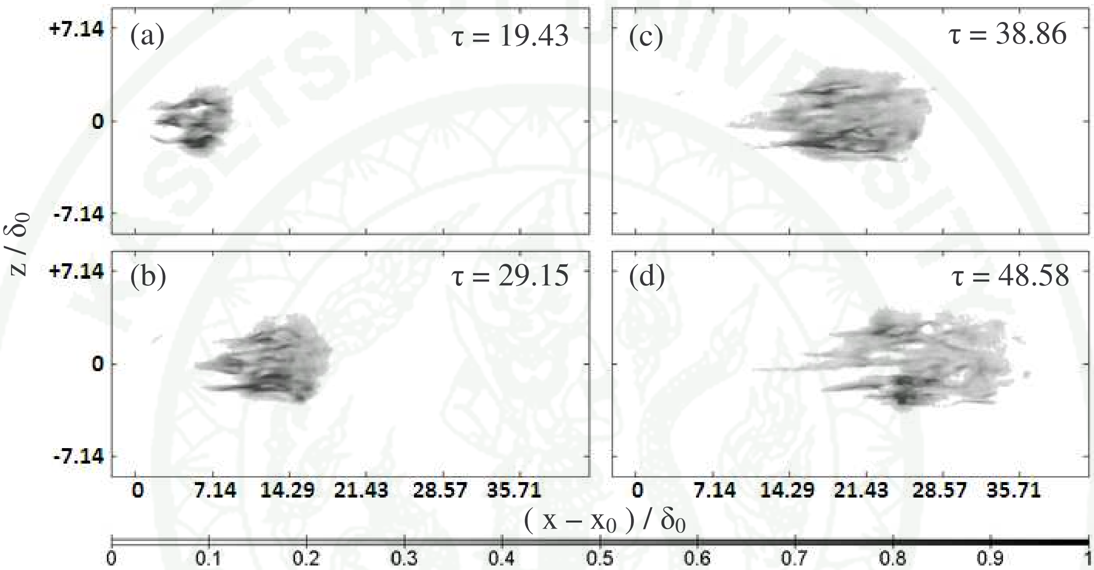

Figure 108 The structure of turbulent spot under zero pressure gradient on the plane y = 0.003 m after processed by the developed code.

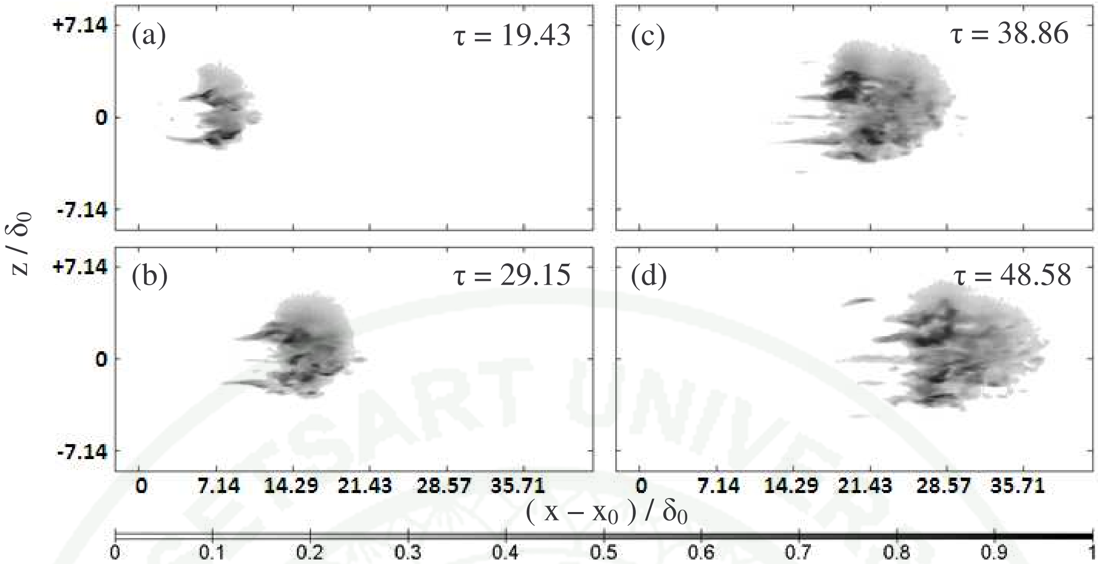

Figure 109 The structure of turbulent spot under zero pressure gradient on the plane y = 0.006 m after processed by the developed code.

In this view, the representative structure was also constructed by the centroid averaging technique. Fifteen good halves of turbulent spots were averaged and the full structure was made by mirroring. Thus, Fig. 110(a)-(d) and 111(a)-(d) show the spatial distribution of probable structure of turbulent spot on the plane y = 3 and 6 mm, respectively.

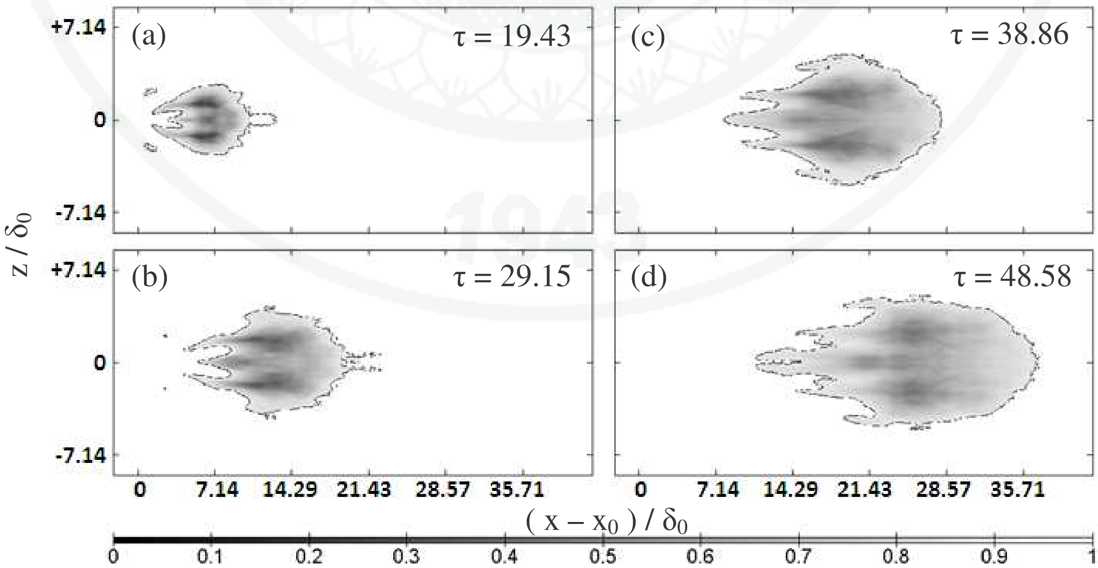

Figure 110 The representative structure of turbulent spot under zero pressure gradient on the plane y = 0.003 m.

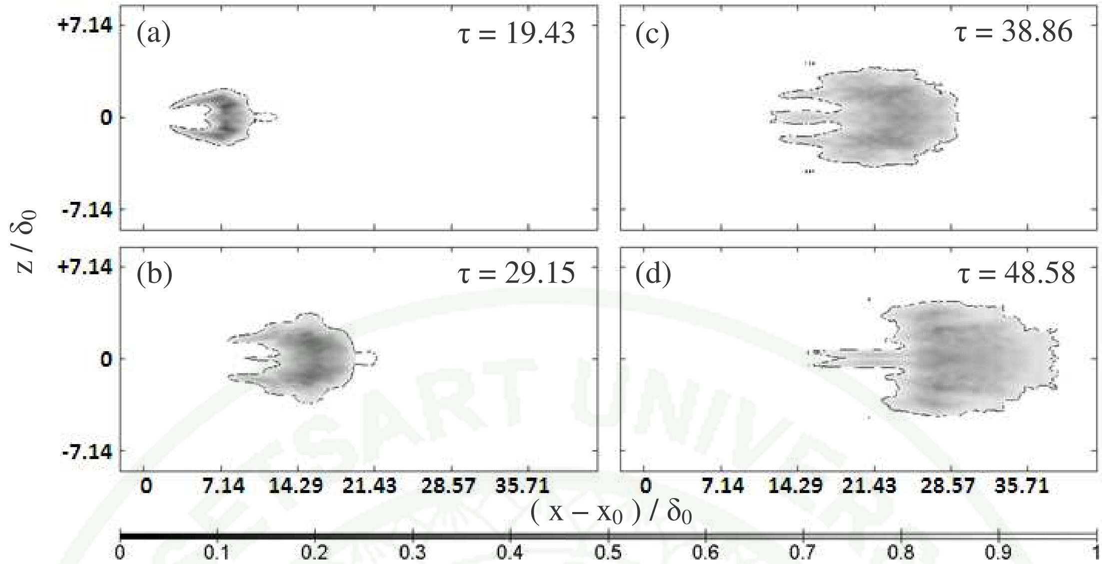

Figure 111 The representative structure of turbulent spot under zero pressure gradient on the plane y = 0.003 m.

Moreover, when the averaged structure, achieved from coating TLCs, was added to this domain, the whole spot body was built by the horizontal substructures from the plane y = 0, 3, and 6 mm as depicted in Fig. 112. It was noted that the image of plane y = 0 m started from 5.71 on streamwise direction while this technique began at -2.86. Thus the empty box was put into the domain as unheated region. In this figure, the darkest substructure presented the nearest plane while the greyer showed the farther. From the results, the presence of the spanwise overhang was identified. It was from the lateral edge of the substructure at y = 3 mm that mostly protruded, comparing to the others. Furthermore, heat exchanged area of turbulent spot, yielded by the use of coating TLCs was not exactly underneath turbulent spot body. When the image of the heat transfer structure and the substructure on the plane y = 3 mm were superimposed, Fig. 113 shows that the thermal footprint precisely placed on becalmed region of turbulent spot body. Thus, the region of the highest heat transfer of the footprint was also in this trailing of turbulent spot. Besides, the representative structure was presented from bottom view as depicted in Fig. 114. It was showed heat transfer region approximately was in the spot trailing. This was in agreement with those obtained by Johnson (1999) and Sabatino and Smith (2002).

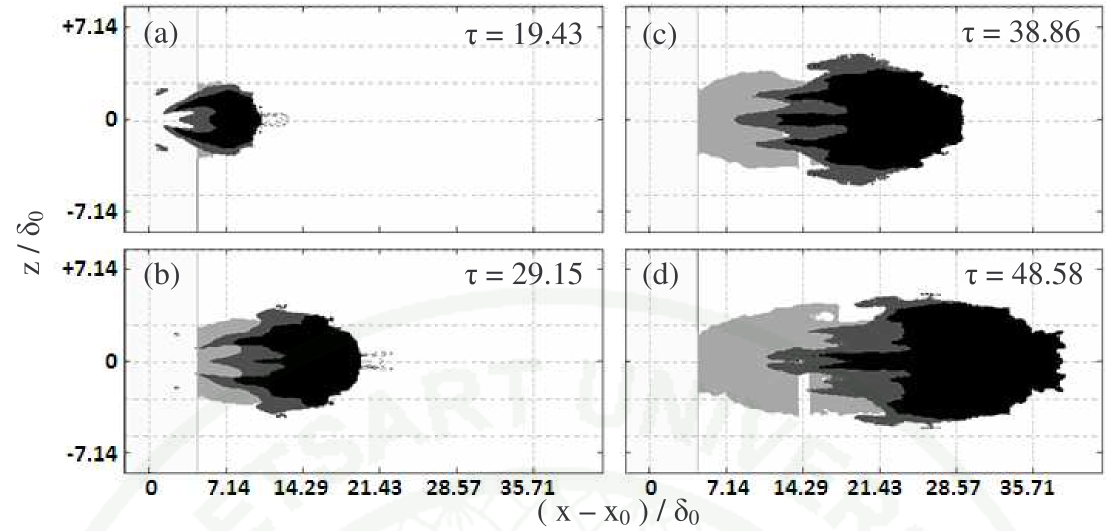

Figure 112 Top view of the whole structure of turbulent spot under zero pressure gradient on the plane parallel to the surface.

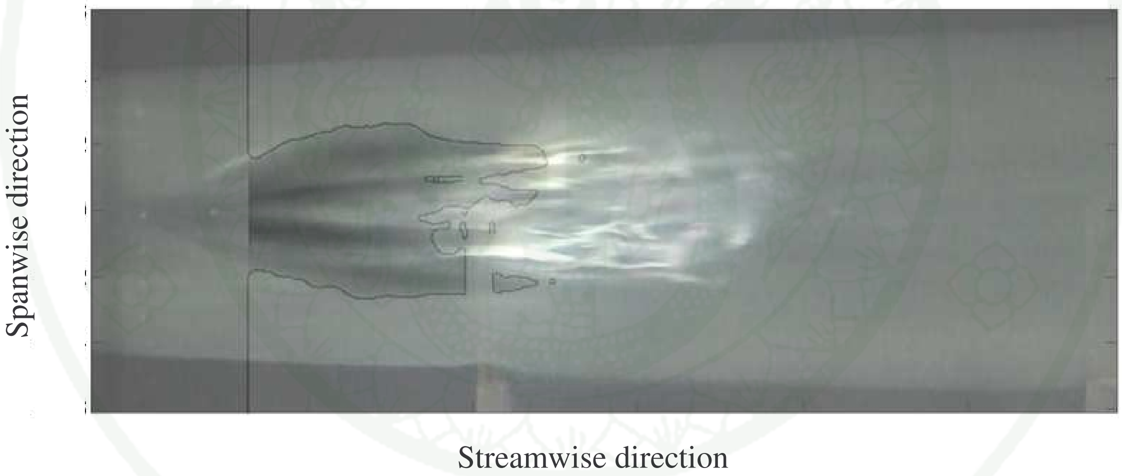

Figure 113 Superimposed images between the thermal footprint and spot body at the same instant.

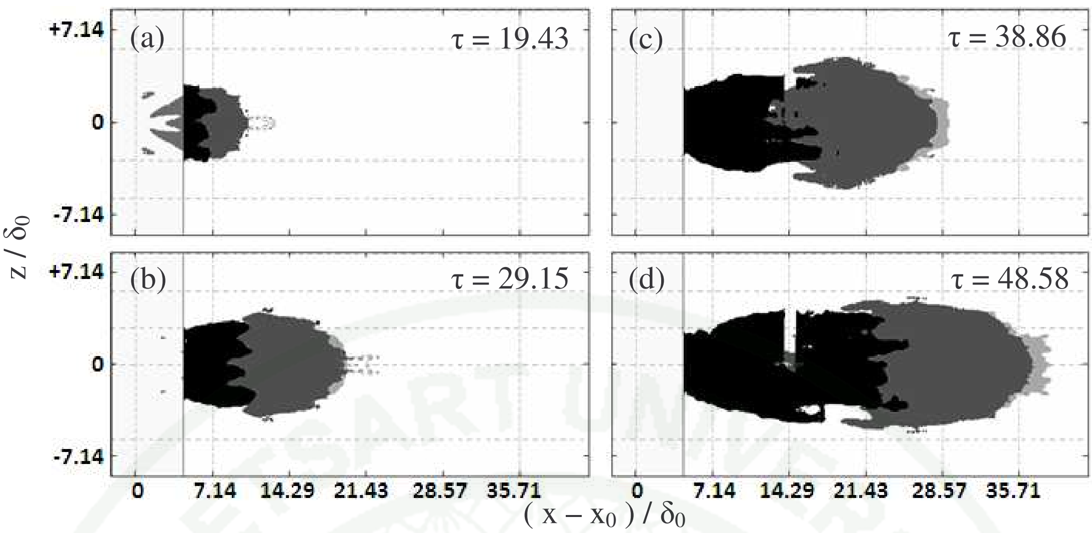

Figure 114 Bottom view of the whole structure of turbulent spot under zero pressure gradient on the plane parallel to the surface.

2.2.2 Turbulent spot development on the plane parallel to the plate surface under the influence of adverse pressure gradient

When turbulent spot was influenced by the adverse pressure gradient, the structure on the plane of both y = 3 and 6 mm behaved as shown by RGB color space in Fig. 115 and 116, respectively. It was found that the structure outstandingly grew in spanwise direction when the spot propagated downstream. All features, including turbulent spot body and the heat transfer region were also found as it experienced zero pressure gradient. However, on the plane of y = 3 mm, there were shadow on the structure beyond the symmetry line. It was because the milk solution on this plane was too thick. Especially when it underwent the strong adverse pressure gradient, the milk was much instabilized from the surface and performed as the light shield. Thus, the dark shade appeared on the opposite side of the incident edge. Furthermore, the error of scattering light also occurred as found on the spot under zero pressure gradient on the plane of y = 6 mm. Therefore, only half structures on the plane of y = 3 and 6 mm were presented as depicted in Fig. 117 and 118, respectively.

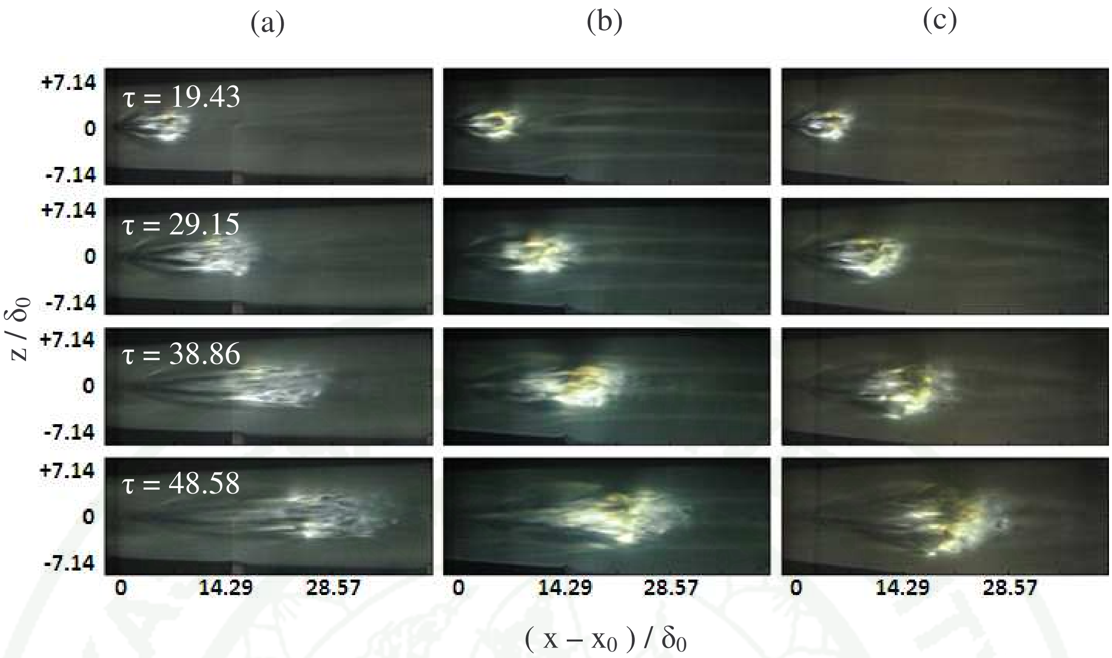

Figure 115 (a)-(c)Structure of turbulent spot on the plane y = 3 m under zero, mild, and strong pressure gradient, respectively.

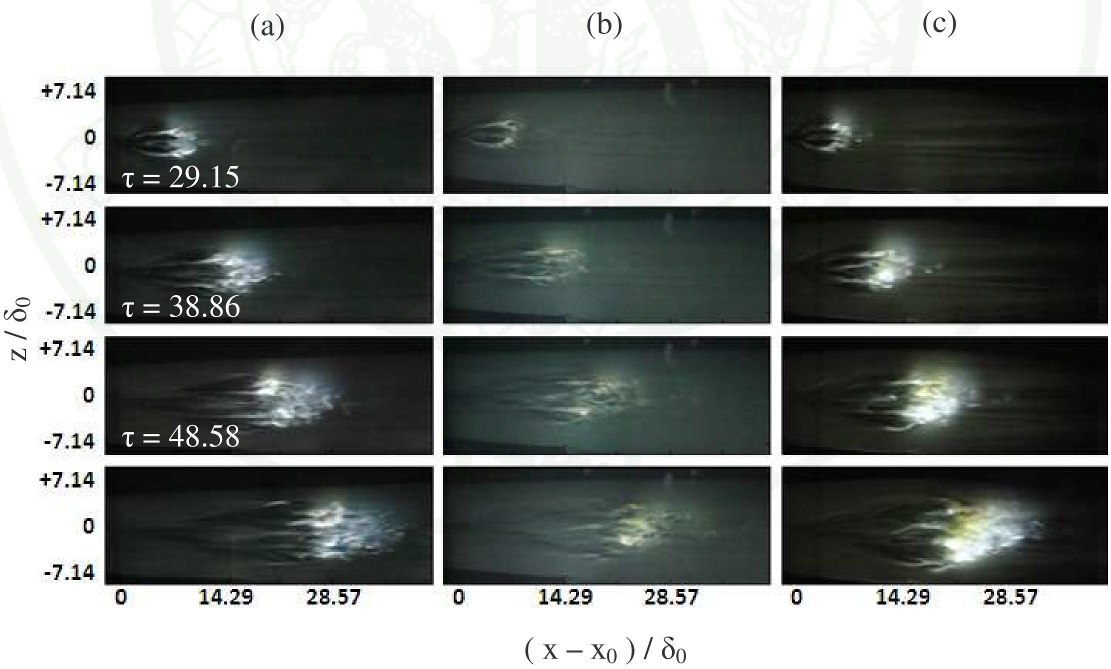

Figure 116 (a)-(c)Structure of turbulent spot on the plane y = 6 m under zero, mild, and strong pressure gradient, respectively.

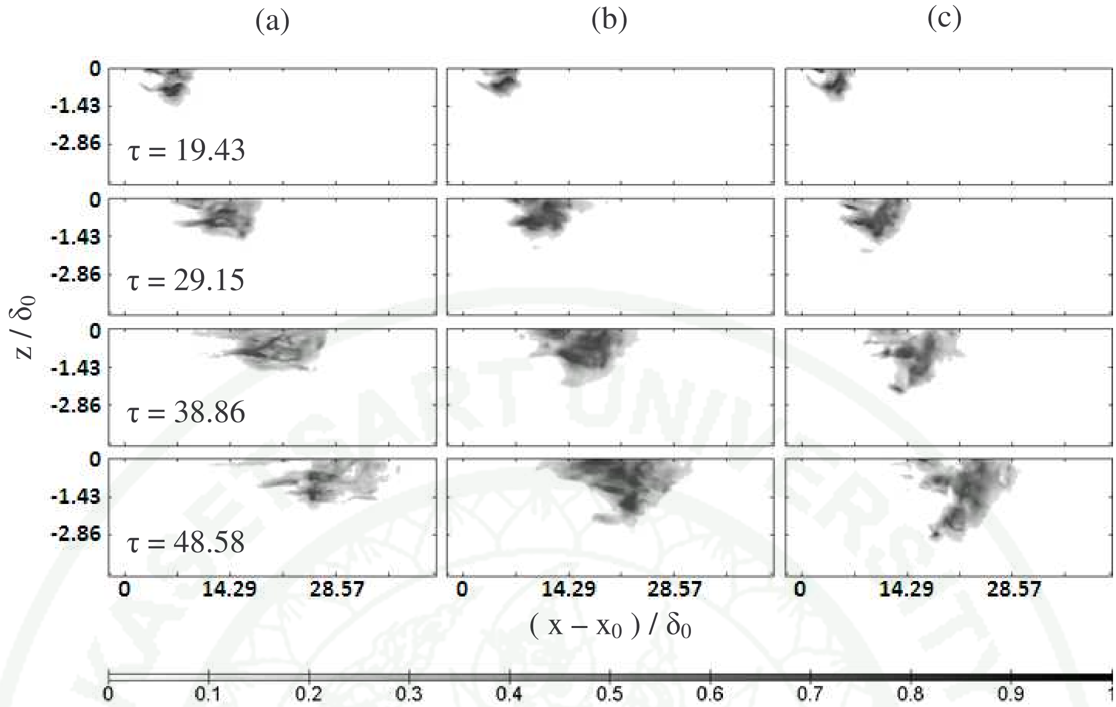

Figure 117 (a)-(c)The structure of turbulent spot on the plane y = 3 m under zero, mild, and strong pressure gradient, respectively.

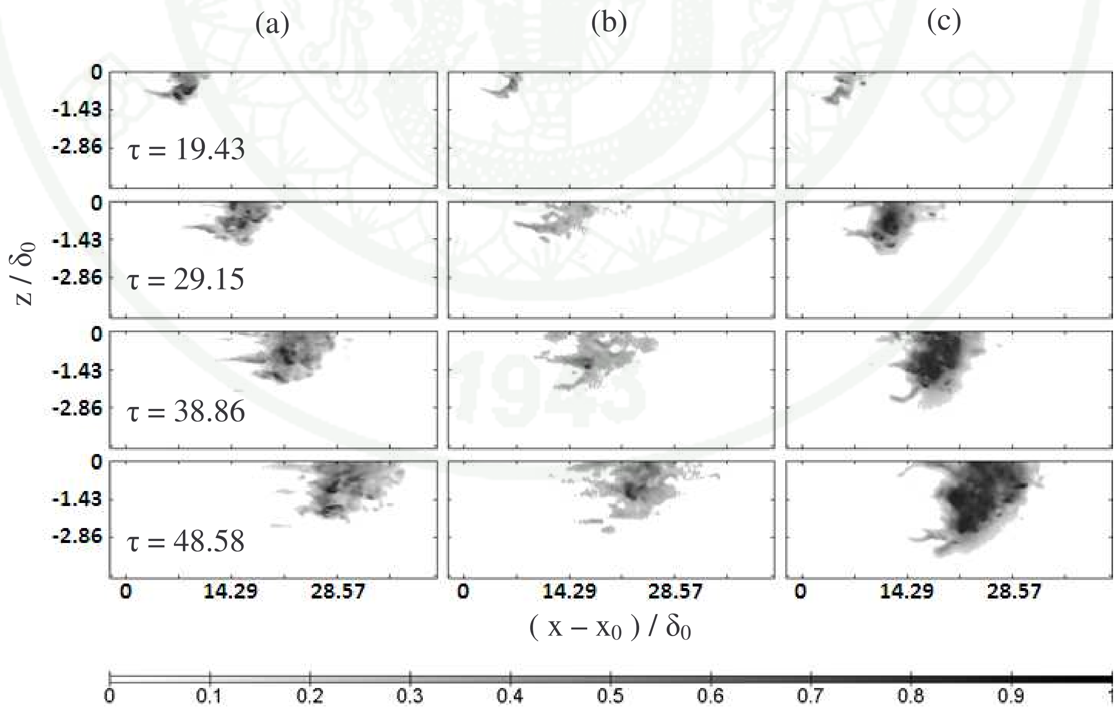

Figure 118 (a)-(c)The structure of turbulent spot on the plane y = 6 m under zero, mild, and strong pressure gradient, respectively.

Comparison of the structure under various pressure gradients was enable if the representative structures on the plane of y = 3 and 6 mm were determined as depicted in Fig. 119 and 120, respectively. Not only on its footprint but also on turbulent spot body, the adverse pressure gradient affected. The spanwise growth was apparently increased when the level of pressure gradient was increased, which contrast to the decreasing size on streamwise direction. This trend was also in agreement with its thermal footprint structure. Finally, the whole structure of turbulent spot, created from laminar-turbulent interface on the plane of y = 0, 3, and 6 mm was constructed at different instant as depicted in Fig. 121 and 122 for top and bottom view, respectively. Similar to the structure under zero pressure gradient, streamwise and spanwise overhangs could be found by the overlapped structure on frontal and lateral edge, respectively. The heat exchanged region was also found at turbulent spot trailing. The leading edge of thermal footprint corresponded to the trailing edge of turbulent spot body. The whole structure was more round under the increased adverse pressure gradient. Turbulent spot parameters, including spot celerities on leading and trailing edges and also spreading half angle will be discussed in the next topic.

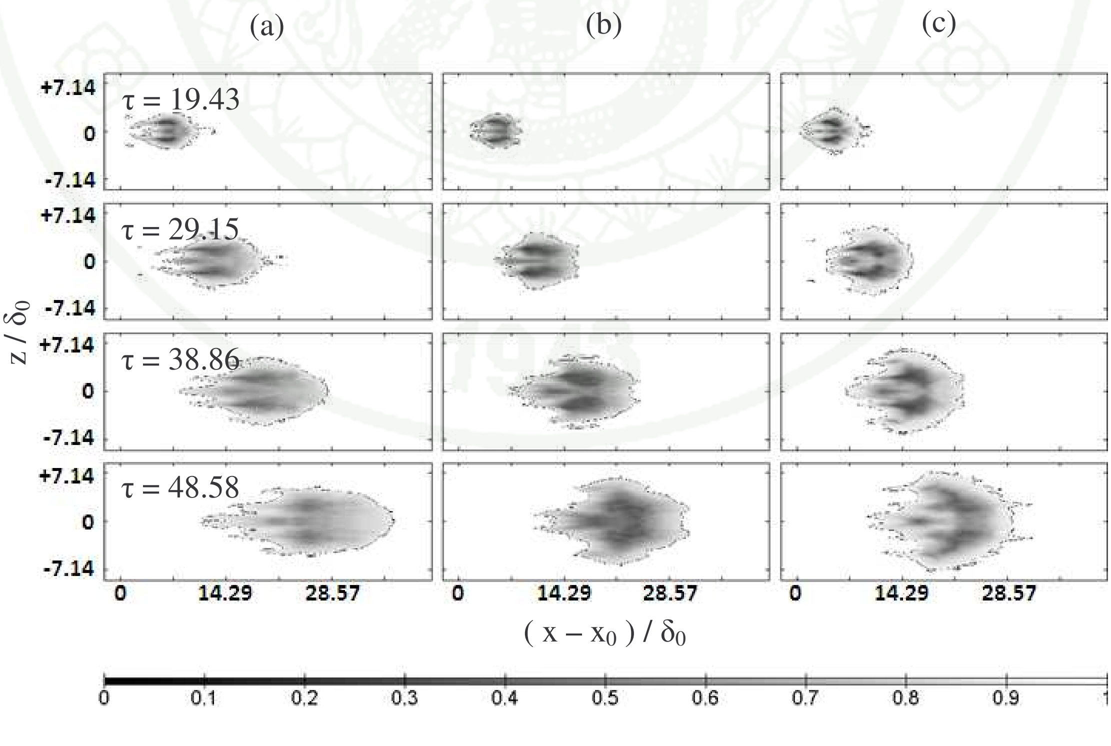

Figure 119 (a)-(c)Representative structure of turbulent spot on the plane y = 3 m under zero, mild, and strong pressure gradient, respectively.

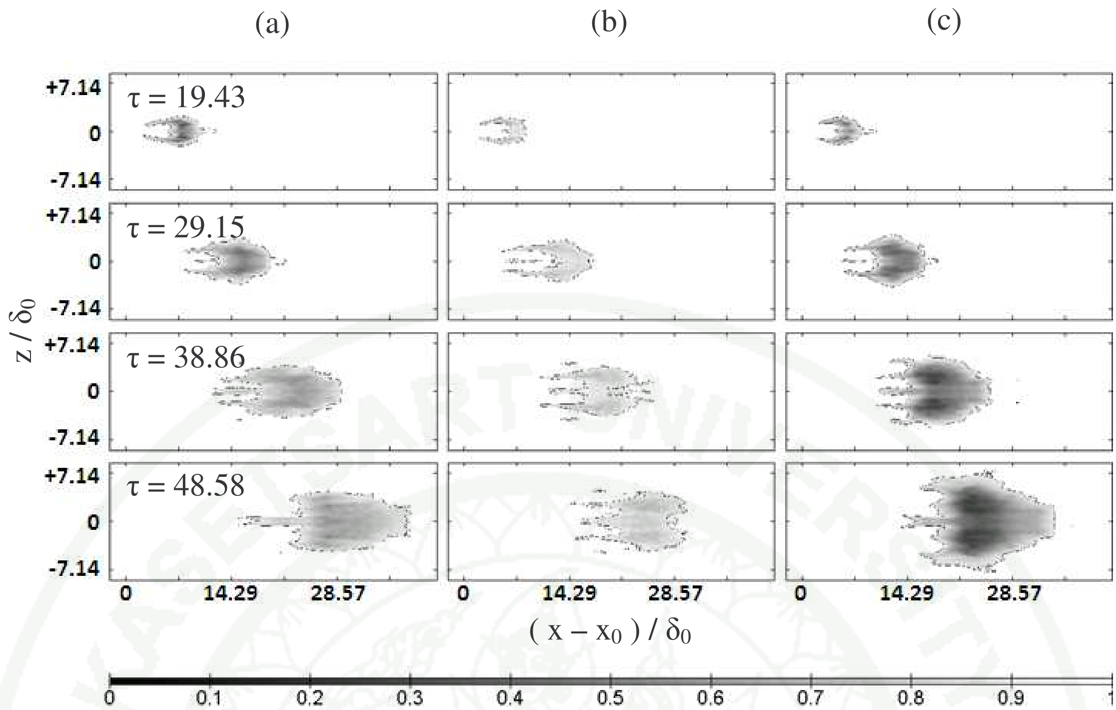

Figure 120 (a)-(c)Representative structure of turbulent spot on the plane y = 6 m under zero, mild, and strong pressure gradient, respectively.

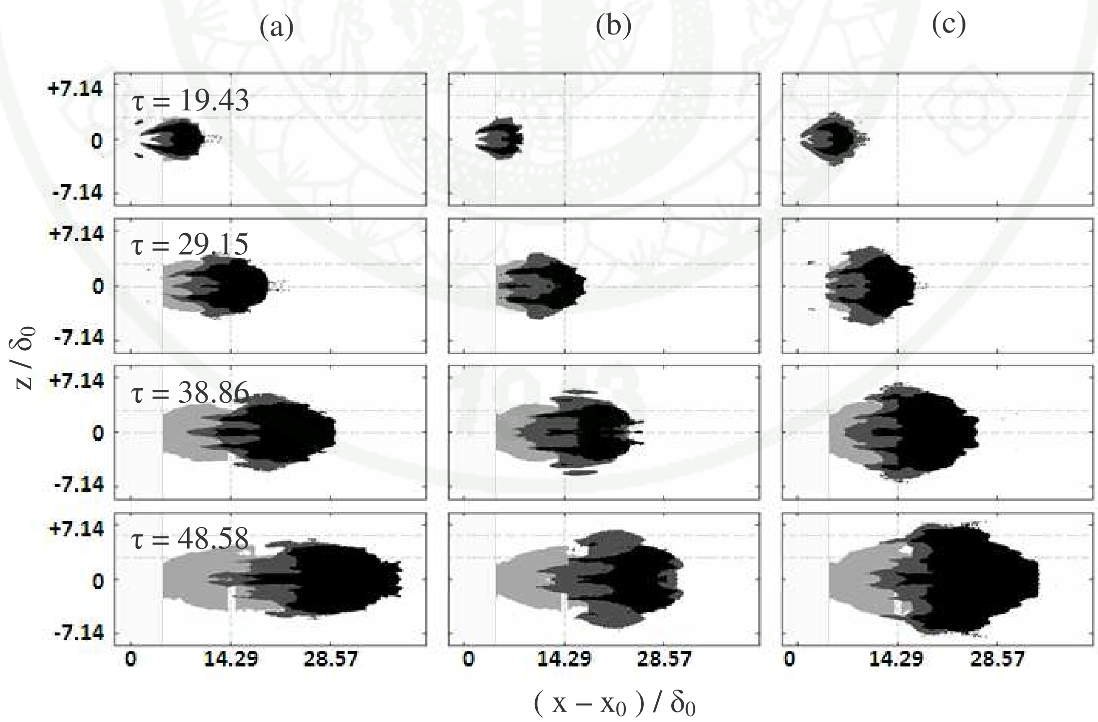

Figure 121 (a)-(c)Top view of turbulent under zero, mild, and strong pressure gradient on the plane parallel to the surface, respectively.

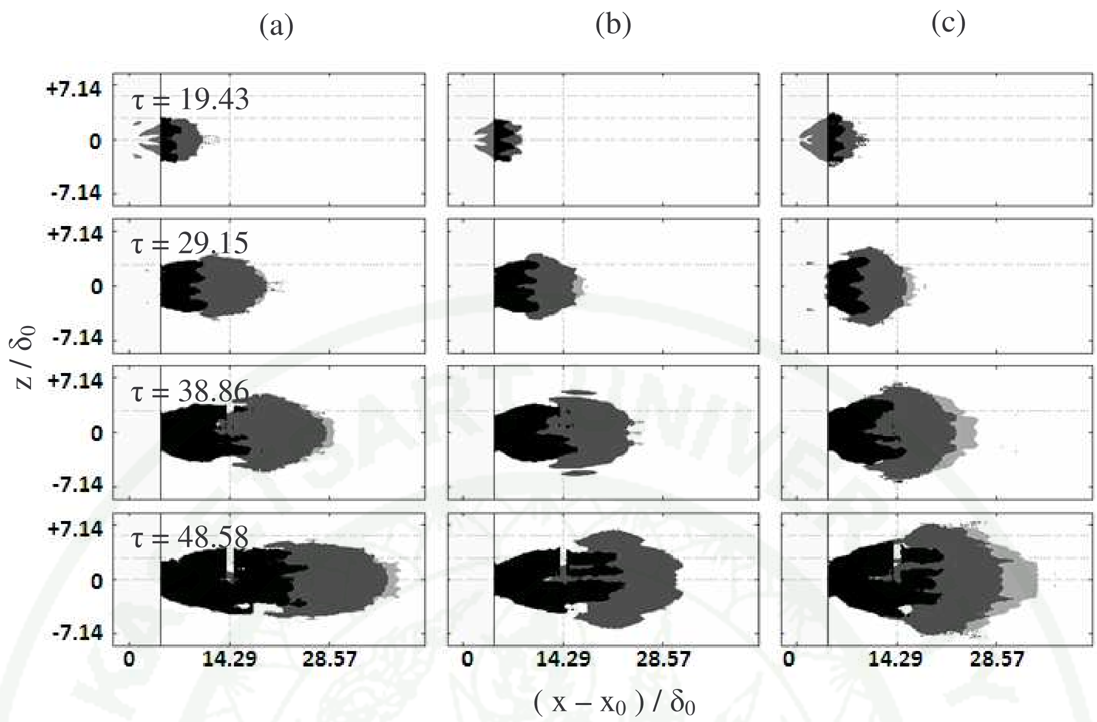

Figure 122 (a)-(c)Top view of turbulent spot under zero, mild, and strong pressure gradient on the plane parallel to the surface, respectively.

2.2.3 Turbulent spot parameters on the plane parallel to the plate surface

In this view, the turbulent spot parameters were directly measured from the representative structure. These comprised turbulent spot celerities at its leading edge and trailing edge as well as the half spreading angle. A point, at the most spanwise location of the structure was defined as turbulent spot wing tip. As it moved downstream, the trajectory of wing tip was created. Thus, the method of half spreading angle determination was similar to the one in the first visualization technique. The leading edge of the substructure was also considered at its most downstream interface. Nevertheless, the location of trailing edge was determined differently. It was found that there was an appearance of few long tails at the trailing side of turbulent spot, depending on the time of flight. Hence, all occurred positions of the trailing part were mean and finally fit as the virtual trailing edge of instantaneous turbulent spot. When it flowed downstream without the gradient of pressure, the spot parameters of the substructure on the plane of y = 3 and 6 mm were detected as shown in Table 3.

Table 3 Turbulent spot parameters on the plane y = 3 and 6 mm under the zero pressure gradients.

Study	C_{LE}	C_{TE}	α°
Schubauer & Klebanoff (1955)[1]	0.88	0.5	10
Wygnanski *et al*. (1982)[1]	0.9	0.55	9.3
Gutmark and Blackwelder (1987)[1]	0.88	0.58	9
Hofeldt (1996)[1]	0.88	0.56	10
Chong and Zhong (2005)[2]	0.87	0.57	10.6
Present study (y = 3 mm)	0.92 ± 0.04	0.48 ± 0.02	10.6 ± 0.02
Present study (y = 6 mm)	0.97 ± 0.04	0.58 ± 0.02	6.4 ± 0.02

[1]Note the parameters were obtained at the height of $0 \leq y/\delta \leq 0.35$ from the surface.
[2]Note the parameters were obtained at the height of $y/\delta_t = 0.2$ from the surface.

It was found that the celerities at spot's leading edge and trailing edge were 0.92 and 0.48, respectively at the height of 3 mm from the surface. This measuring plane was at about $y/\delta \approx 0.3$ and $y/\delta_t \approx 0.2$ where the thickness of laminar boundary layer was around 1 cm. It was found that the obtained celerity at leading edge was more than one, measured on the surface. It was realistic because the near wall substructure was dominated by viscous sub layer, dragging the fluid molecules with the higher shear force than the upper layer. Also, on this plane, the half spreading angle was found at 10.6°. This was clear evidence, showing the presence of spanwise overhang on each lateral side of turbulent spot. The relative celerities at leading edge and trailing edge were increased when they were measured on the plane of y = 6 mm or $y/\delta \approx 0.6$. Meanwhile, the spreading angle was decreased. This could be deduced that the top part of turbulent spot traveled downstream with the narrower spreading angle than the base part. This well agreed to the results obtained on the plane that perpendicular to the surface that the upper portion of turbulent spot was invisible on the plane far from the middle. Moreover, the results on the plane y = 9 mm was also carried out but they were not put in the thesis because this substructure decayed quickly as reported by Singer and Joslin (1995). Nevertheless, by observation, it was found that the structure propagated with even smaller angle than those obtained at the height of y = 3 and 6 mm. Therefore, the aspect of turbulent spot structure was narrower on the higher level.

In Table 3, the parameters were compared to those reported by other researchers. It is noted that those parameters were measure at the height of $0 \leq y/\delta \leq 0.35$ from the surface except the one, obtained by Chong and Zhong (2005), measured at $y/\delta_t = 0.2$. The celerity at the spot leading edge at $y/\delta \approx 0.3$, yielded in the present study was in agreement to the others. In the mean time, celerity at the trailing edge was slightly less than the others. This should be noted that all other parameters were achieved by the measurement of hotwire anemometer. The most results were obtained from the ensemble averaging technique, needing to shift the detected signal to its leading edge or any other reference locations. Thus, an error might be from the signal at its trailing edge that was affected by the occurred misalignment and became unclear on the measuring point. Another reasons, might be the cause of the error, reported by Wygnanski *et al*. (1982). They found that the change of Re of spot generator strongly influenced on celerity at spot trailing edge. The higher Re, the lower celerity at this location was found. In addition, the half spreading angle, obtained in this study also agreed with the other results. Therefore, this comparison confirms the reliability of this technique.

Furthermore, turbulent spot parameters on both planes of y = 3 and 6 mm were also measured under the influence of adverse pressure gradient as shown in Table 4. It also should be noted that the parameters, reported by the other researchers were measured at the height of $0 \leq y/\delta \leq 0.35$.

Table 4 Turbulent spot parameters on the plane y = 3 and 6 mm under adverse pressure gradients

Study	λ_θ	C_{LE}	C_{TE}	$\alpha°$
Present study (SAPG at y = 3 mm)	**-0.06**	**0.707 ± 0.03**	**0.39 ± 0.02**	**15.7 ± 0.02**
Present study (SAPG at y = 6 mm)	**-0.06**	**0.906 ± 0.04**	**0.485 ± 0.02**	**14.9 ± 0.02**
Gostelow *et al*. (1996)[1]	-0.057	0.872	0.431	29.2
Van Hest (1994) [1]	-0.036	0.92	0.38	17
Gostelow *et al*. (1993) [1]	-0.031	0.8	0.5	24
Seifert and Wygnanski (1994) [1]	-0.018	0.9	0.49	21
Present study (MAPG at y = 3 mm)	**-0.016**	**0.78 ± 0.03**	**0.43 ± 0.02**	**13.4 ± 0.02**
Present study (MAPG at y = 6 mm)	**-0.016**	**0.95 ± 0.04**	**0.53 ± 0.02**	**7.2 ± 0.02**

[1]Note the parameters were obtained at the height of $0 \leq y/\delta \leq 0.35$ from the surface.

From the data, achieved in the current study, it was found that the celerity decreased at both leading and trailing edges while the spreading angle increased when the level of adverse pressure gradient increased. The trend of the parameters on the farther plane from the wall was similar to the case of zero pressure gradient. However, the spreading angle was relatively wider than the one obtained from its footprint. Thus, the spanwise overhang also occurred under the influence of adverse pressure gradient. In Table 4, the variations on spot celerities and the half angle could be seen. Especially, the half spreading angle, achieved in the present study was relatively less than those reported by the others. Re, Re of spot generator, the presence of wave packet near the wingtip etc., found that they directly affected on the shape of the spot were the main cause of this inconsistence.

3. Thermal structure of turbulent spot

In this topic, the spatial temperature distribution within turbulent spot was achieved using the slurry thermochromic liquid crystals. All experimental procedures in this test directly followed the previous technique. Only dye type was changed from milk to be the solution of the liquid crystals, diluted in the water with the proper fraction. The experiment was carried out on both views as the previous test, including the plane perpendicular and parallel to the plate surface. Also, the turbulent spot parameters were reported and discussed in this topic.

3.1 Thermal characteristics of turbulent spot on the plane perpendicular to the plate surface

3.1.1 Development of thermal structure of turbulent spot on the plane perpendicular to the plate surface under zero pressure gradient

Similar to the previous test, the liquid crystals solution was gently released from the dye chamber at the most upstream of the flat plate. When the thin layer of the solution fully covered the plate surface, turbulent spot was initiated by the injecting water at spot generator. The evolution of generated turbulent spot was recorded through the normalized streamwise distance between 8.57 to 38.57. Meanwhile, the normalized heightwise distance remained between 0 to 4.71. During the test, the free stream temperature was kept constant at 23.6°C while the plate surface was set at 25.4°C. This temperature range was found to be fully fit on the active range of this liquid crystal, expressed by its calibration curve. Fig. 123(a) shows the consecutive images of individual turbulent spot on the central plane of z axis. Even it has a lower degree of reflection, the obtained structure of turbulent spot, introduced by the slurry liquid crystals, was fairly similar to which yielded by milk solution. The obtained color, scattering from the thin sheet of white light, was firstly recorded as RGB signals. Firstly, turbulent spot exhibited an orange color at the normalized time of 19.43. Then, it turned green and blue when the spot propagated further downstream from left to right. These color signals were converted to Hue component and lastly transformed to temperature via the Hue-Temperature relation curve. It was found that the appeared color corresponded to the non-dimensional temperature within spot body as shown in Fig. 123(b). The below color bar defined the dimensionless temperature, established from

$$T_{non\text{-}dimension} = (T - T_{\alpha})/(T_s - T_{\alpha}) \quad (29)$$

where T_{α} and T_s are free stream and surface temperatures, respectively. In the images of thermal structure of turbulent spot, the three curves, described in the previous technique, were added into the contour. It was found that slurry liquid crystals could efficiently provided qualitative and quantitative information of temperature perturbation within turbulent spot interior. At first, turbulent spot was formed with the low temperature as depicted in the first image of Fig. 123(b). Then, the temperature in upper portion region of the spot was higher and followed by the relatively low value at its trailing at τ = 29.14 after the injection. Finally, the almost entire structure was diffused by the high temperature fluid except the near wall region and its trailing part.

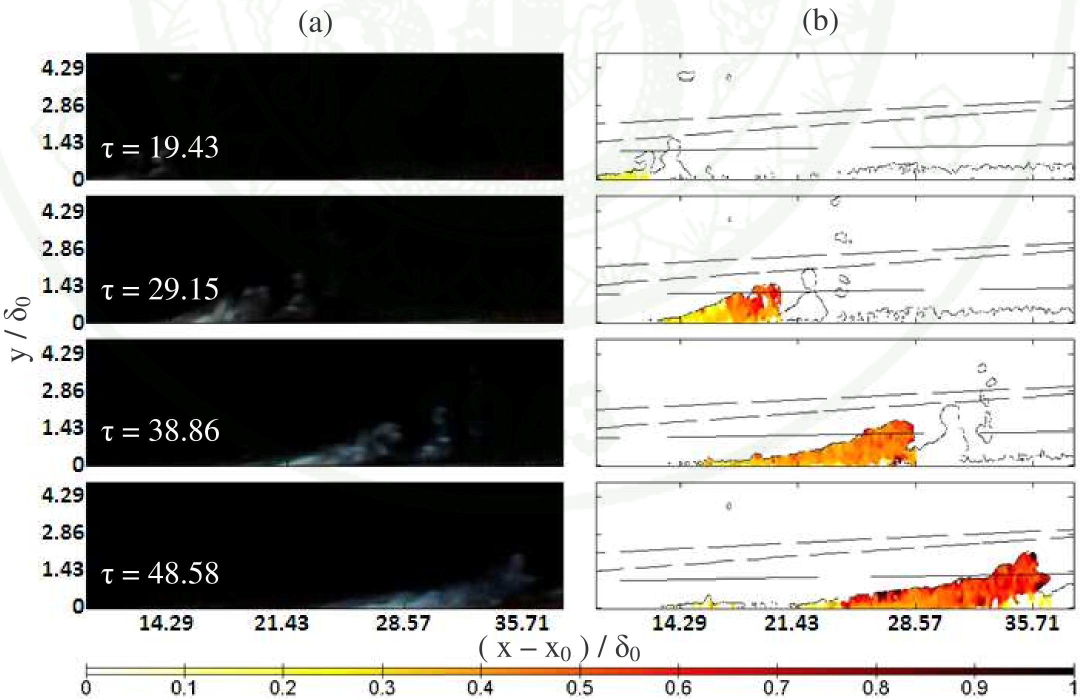

Figure 123 (a) Structure of individual turbulent spot, exhibited by slurry liquid crystals on the plane z = 0 m., (b) Thermal structure of individual turbulent spot on the plane z = 0 m.

However, due to the random effect of turbulent flow, the representative structure was also proposed to see the probable thermal structure by the centroid averaging method, described previously. From the results as illustrated in Fig. 124, it was found that the young structure of turbulent spot cenvected heat from the hot surface by the aid of hairpin vortices. The dimensionless temperature was found to be 0.1 – 0.2 over entire structure at the normailized time of 19.43. The relatively high temperature region of about 0.3 - 0.4, from the heated surface was found at the lower part of the body. It was pulled up and diffused over entire structure at the normalized time of 48.57. There was a strong connection between this results and v component of velocity, reported by Chong and Zhong (2006) as shown in Fig. 10. It revealed that the near wall fluid within turbulent spot flowed on upward direction. This was clear evidence, showing that the hotter near wall water was accumulated into its body via the existence of hairpin vortices as explained previously. The colder fluid on the layer above must replace the empty space on the surface via nibbling process of entrainment as seen at the becalmed region of every instantaneous thermal structure. Hence, the heat transfer via turbulent spot footprint was associated by this mechanism. However, the thermal structure at near wall region of turbulent spot, achieved in the present study, was different to those reported by, Van Atta and Helland (1980), Antonia and Chambers (1981), and Chong and Zhong (2006). Their structures consisted of two main parts, hotter and colder regions at upper and lower portions, respectively. It should be noted that these ensemble averaged temperature contours were constructed by the obtained signal from coldwire anemometer. Their temperature signals were relative to its local temperature, performing by thermal boundary layer. Meanwhile, the thermal contour within the structure in Fig. 124 was presented by absolute temperature. Thus, when the temperature contour was referenced by the local temperature, turbulent spot was alternately presented as shown in Fig. 125. It was found that the spot consisted of two regions that were relatively high and low temperature areas on the upper and lower portions as found by Van Atta and Helland (1980), Antonia and Chambers (1981), and Chong and Zhong (2006).

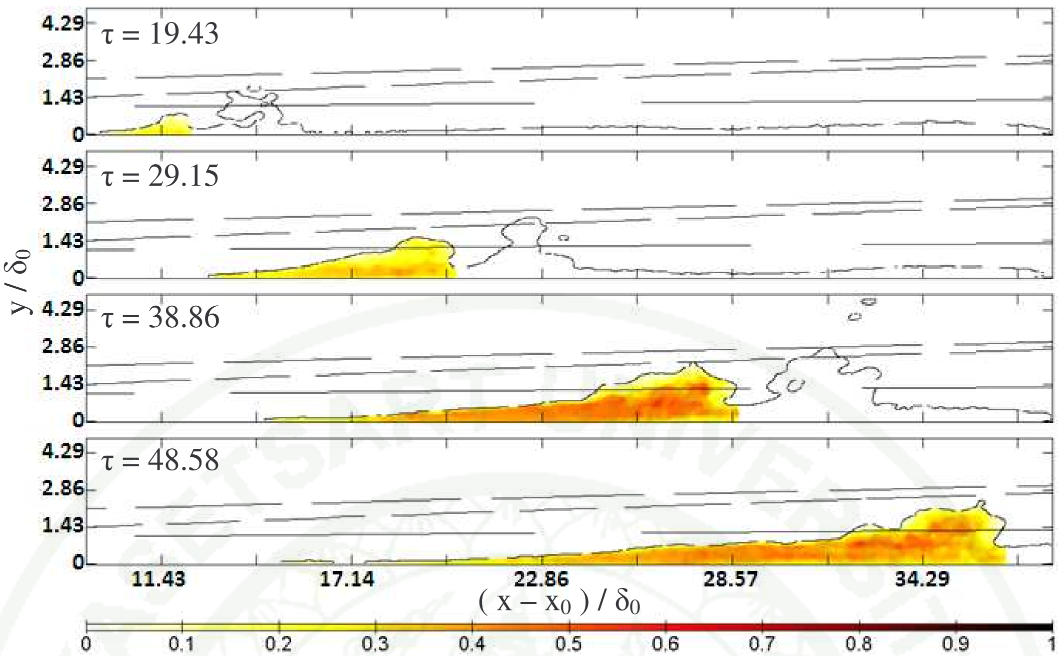

Figure 124 Thermal structure of representative turbulent spot on the plane z = 0 m.

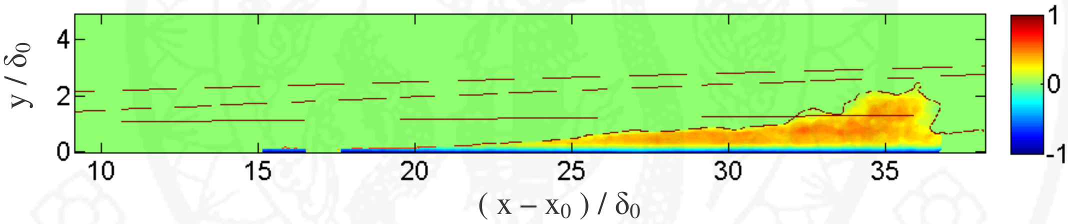

Figure 125 Temperature contour relatived by local temperature.

Fig. 126(a)-(c) show the consecutive frames of each individual turbulent spot as RGB, exhibited by the slurry liquid crystals on the plane of z = 0, 0.01, and 0.02 m, respectively. Color contours of substructure on the plane z = 0.01 m behaved like those yielded on the central plane. Meanwhile, the relatively slowest in movement and development was found on the structure on the plane of z = 0.02 m. The color on this plane at $\tau = 48.58$ remained orange while the others scattered green or blue. When the colors were transformed to the dimensionless temperature, it was found that turbulent spot had the same thermal characteristic over entire structure as shown in Fig. 127. The relatively hotter and colder regions were found at the upper and lower part, respectively.

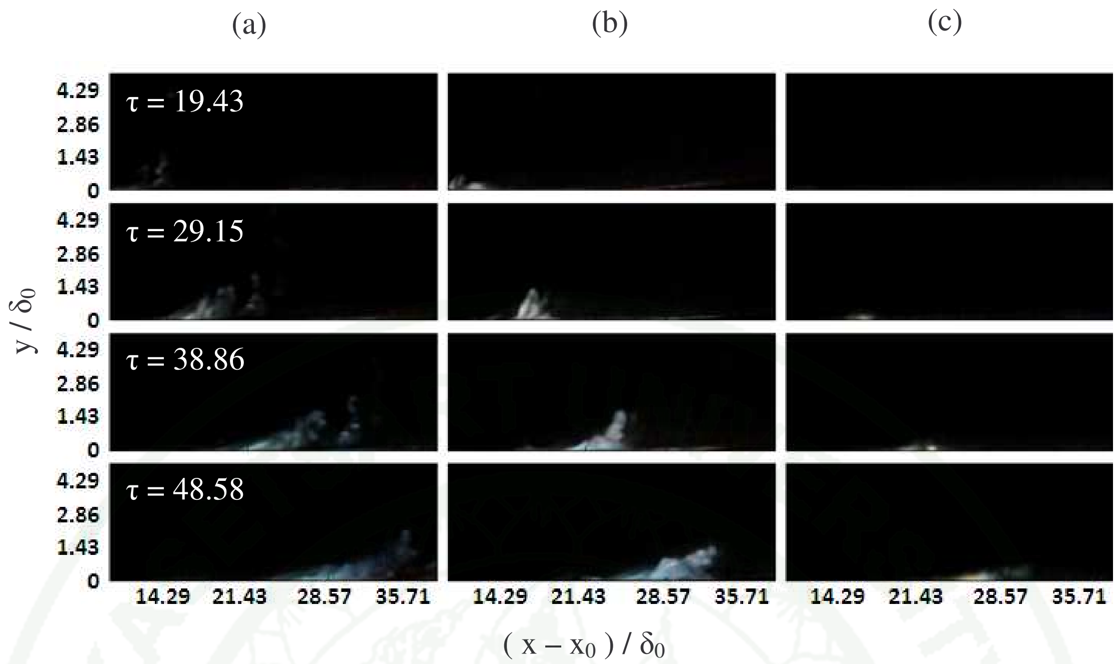

Figure 126 (a)-(c)Structure of individual turbulent spot, exhibited by slurry liquid crystals on the plane z = 0, 0.01, and 0.02 m, respectively.

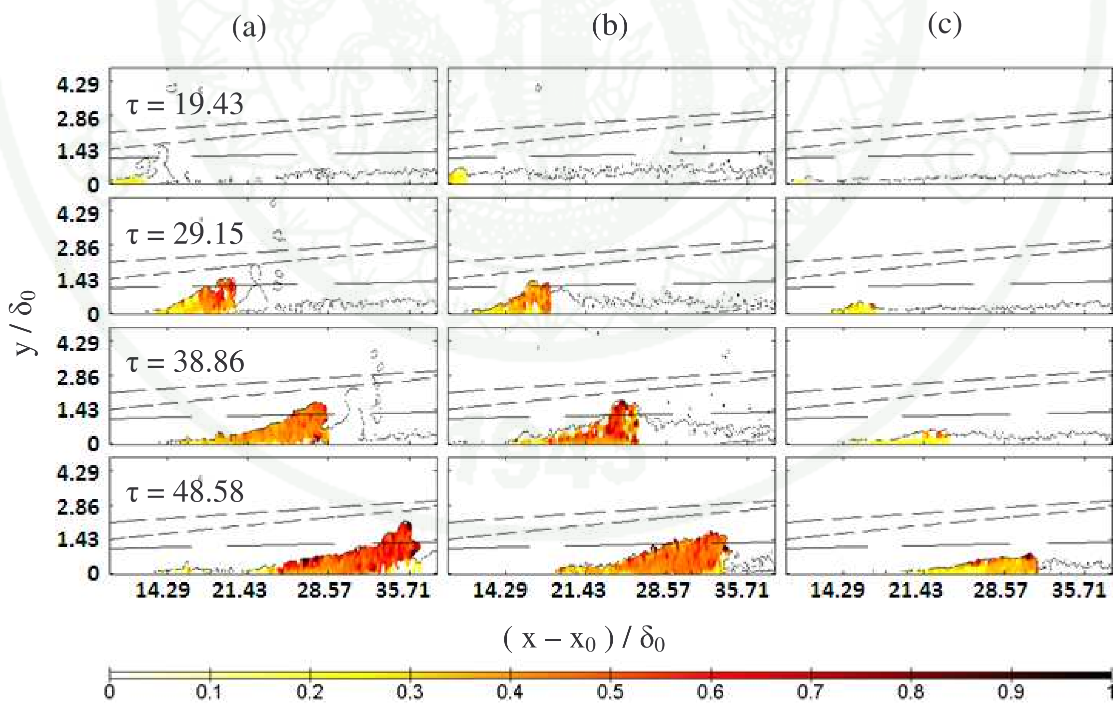

Figure 127 (a)-(c)Thermal structure of individual turbulent spot, exhibited by slurry liquid crystals on the plane z = 0, 0.01, and 0.02 m, respectively.

Fig. 128(a)-(c) depict the consecutive frames of the representative thermal structure of turbulent spot on the plane of z = 0, 0.01, and 0.02 m, respectively. They also show that the hotter fluid convected from the surface when turbulent spot propagating downstream. This behavior was found not only the central plane but also the whole structure. This signature of heat diffusion on all planes also confirmed that the whole structure of turbulent spot was tightly packed with hairpin vortices. However, the maximum temperature perturbation was approximately 0.5 inside the spot. This range of temperature perturbation was in good agreement with the maximum magnitude at upper portion of the ensemble averaged thermal structure, reported by Van Atta and Helland (1980), Antonia and Chambers (1981), and Chong and Zhong (2006).

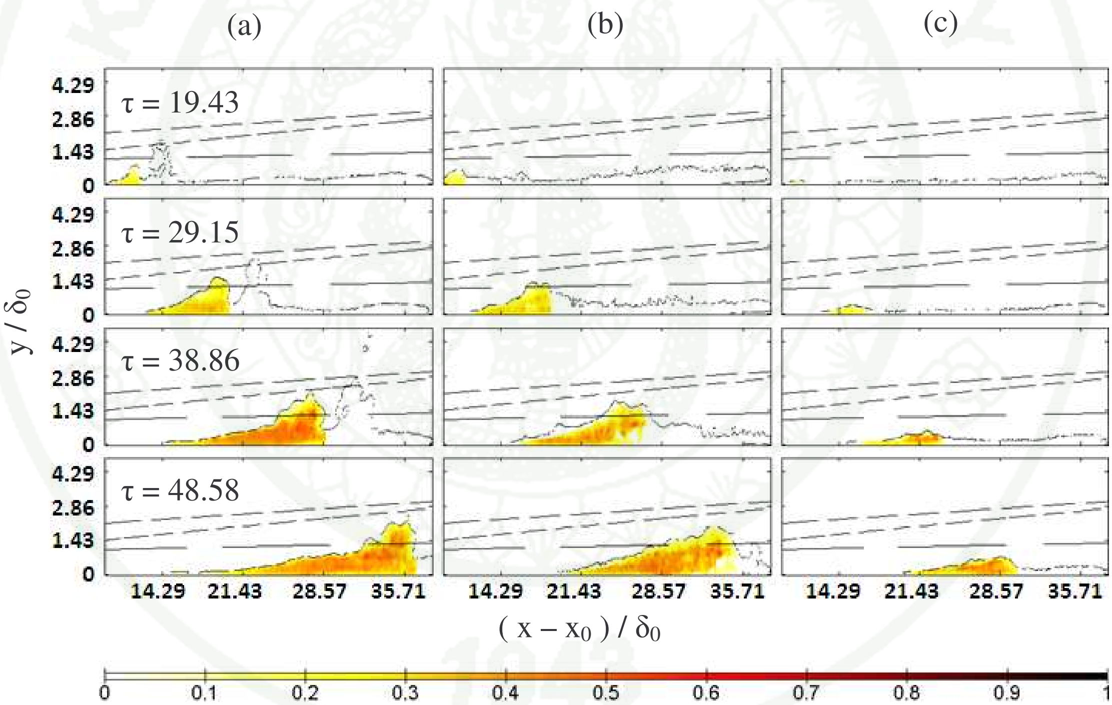

Figure 128 (a)-(c)Thermal structure of representative turbulent spot on the plane z = 0, 0.01, and 0.02 m, respectively.

3.1.2 Development of thermal structure of turbulent spot on the plane perpendicular to the plate surface under various pressure gradients

Fig. 129(a)-(c) show the consecutive images of RGB signal of individual turbulent spots on the plane of z = 0 when they were under the influence of zero, mild, and strong adverse pressure gradients, respectively. Their color was found in the same trend. After spot initiation, liquid crystals inside turbulent spot firstly exhibited the orange, corresponding to the relative low temperature. After that, it turns green and blue, referring to higher temperature when the spot propagated further into the heated zone. These coloring characteristics were also found on substructure on the plane of z = 0.01 and 0.02 m as shown in Fig. 130 and 131, respectively. By the relatively lower reflective degree of liquid crystals, comparing to milk, the size of the substructure on all planes were not apparently ordering when the level of the pressure gradient was increased as found in the previous technique. However, this issue was compensated by the qualitative and quantitative temperature information, focused in this study.

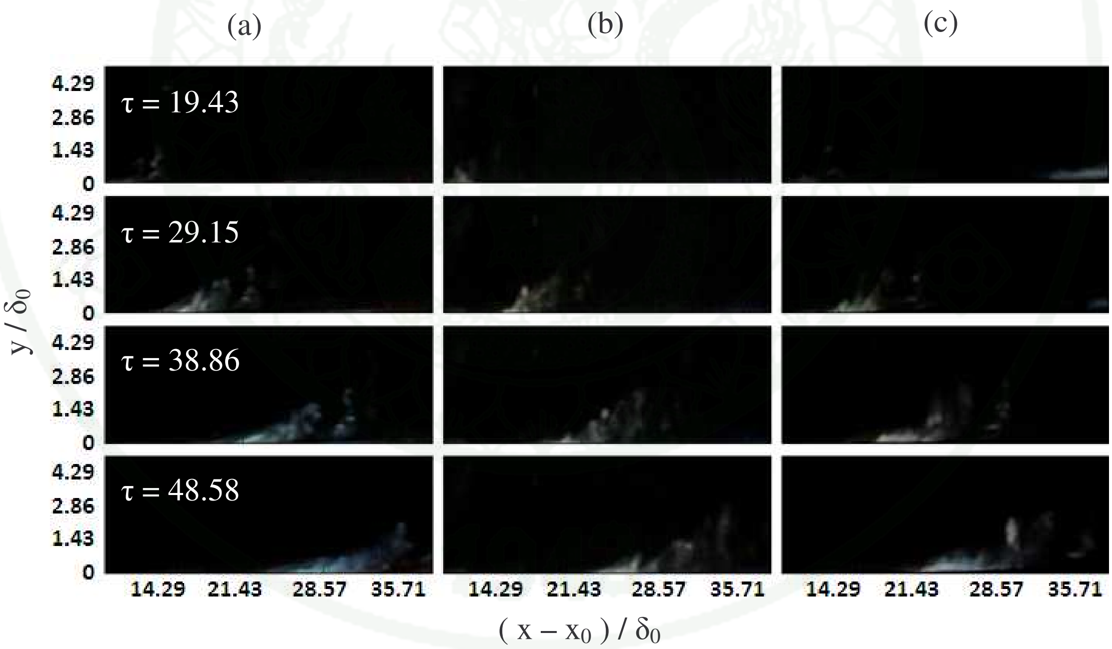

Figure 129 (a)-(c)Turbulent spot, exhibited by liquid crystals on z = 0 m under zero, mild, and strong adverse pressure gradient, respectively.

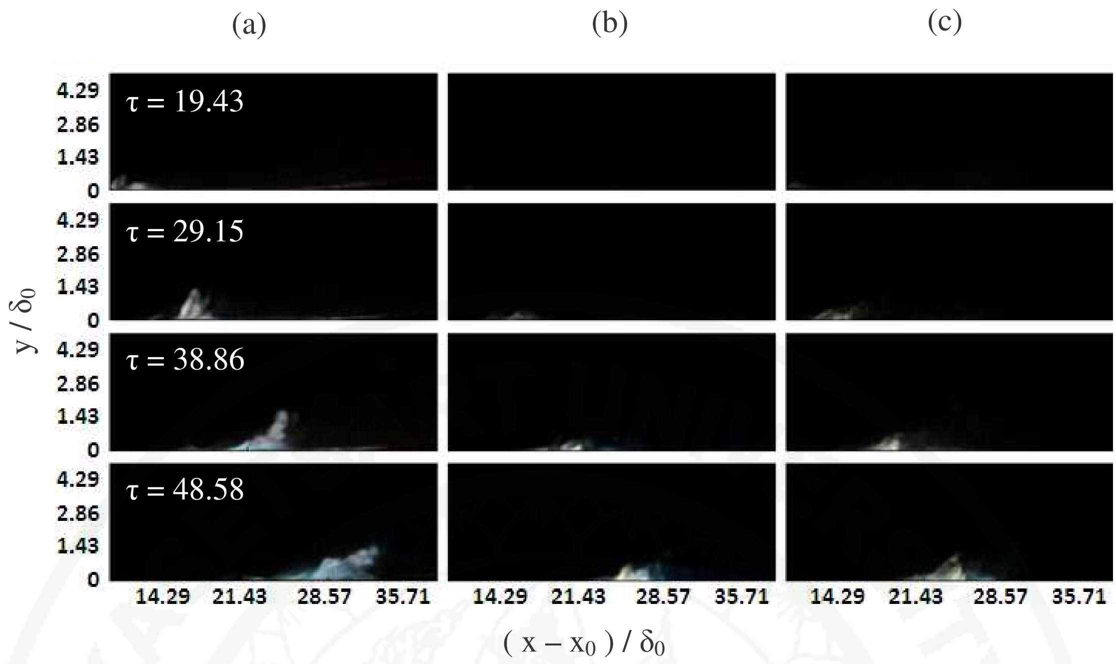

Figure 130 (a)-(c)Turbulent spot, exhibited by liquid crystals on z = 0.01 m under zero, mild, and strong adverse pressure gradient, respectively.

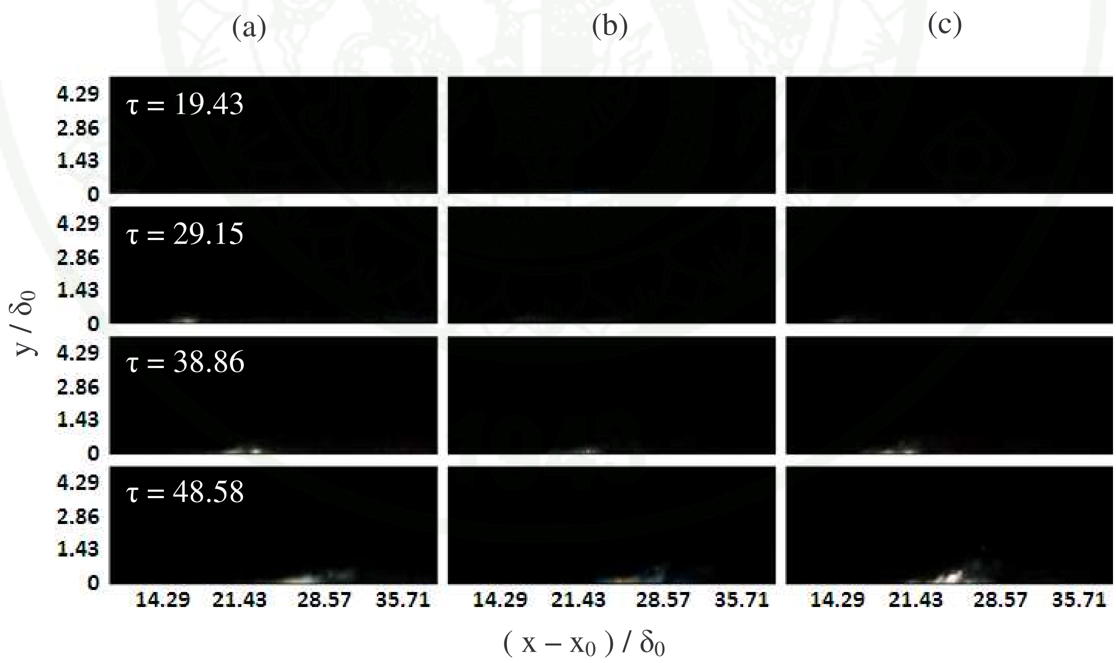

Figure 131 (a)-(c)Turbulent spot, exhibited by liquid crystals on z = 0.02 m under zero, mild, and strong adverse pressure gradient, respectively.

When the representative thermal structures were constructed as shown in Fig. 132(a)-(c), the temperature contours of turbulent spot under zero, mild, and strong adverse pressure gradients were presented. It was found that the yielded temperature perturbation was in the same range. Also, the characteristic of its thermal diffusion that the hotter fluid convected on upward direction was consistent with the structure under zero pressure gradient. Fig. 133 and 134 show the evolution of the sub thermal structure of the representative turbulent spot on the plane z = 0.01 and 0.02 m, respectively. It was found that the high temperature region, induced by the hairpin vortices was firstly accumulated at the frontal part of the substructure in both planes. Later, it dispersed to the lower region and its trailing part. Therefore, it should be concluded that the increased level of adverse pressure gradient didn't significantly affect the thermal characteristic of turbulent spot when it was investigated on the plane perpendicular to the surface.

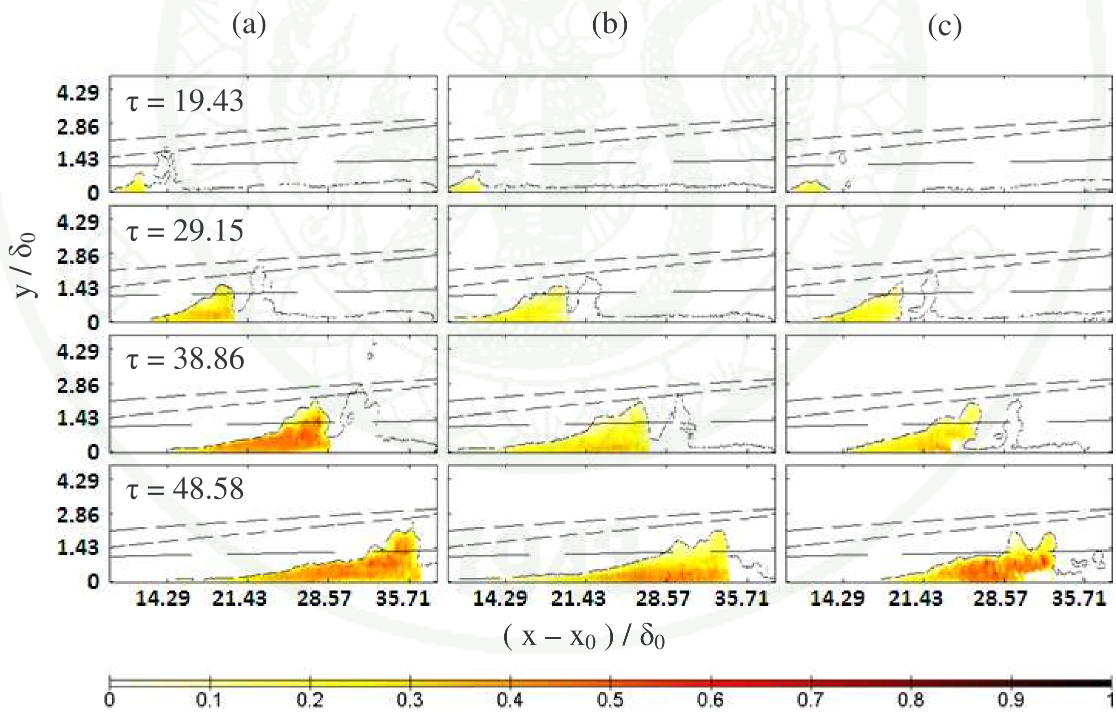

Figure 132 (a)-(c)Thermal structure of representative turbulent spot on z = 0 m under zero, mild, and strong adverse pressure gradient, respectively.

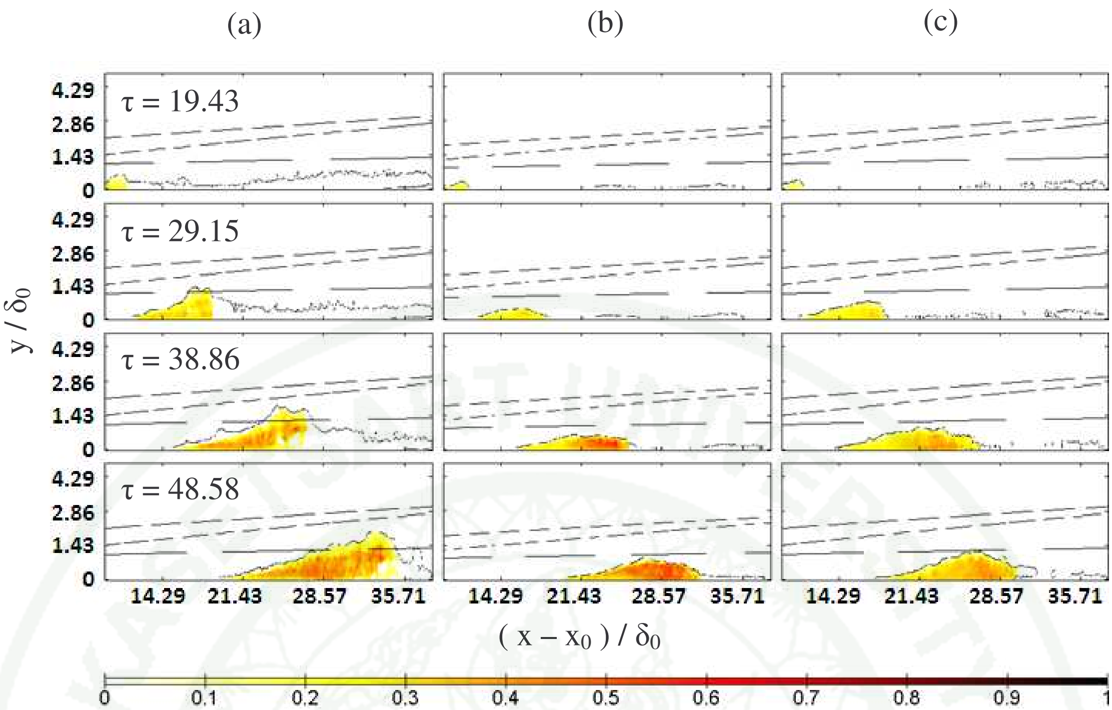

Figure 133 (a)-(c)Thermal structure of representative turbulent spot on z = 0.01 m under zero, mild, and strong adverse pressure gradient, respectively.

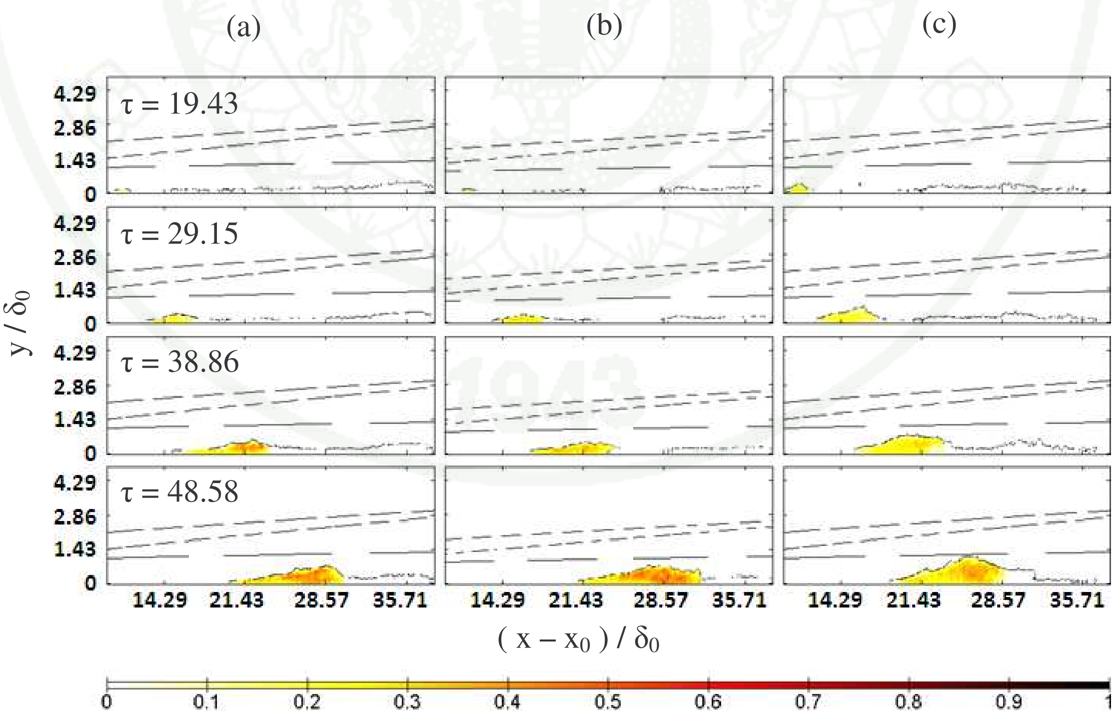

Figure 134 (a)-(c)Thermal structure of representative turbulent spot on z = 0.02 m under zero, mild, and strong adverse pressure gradient, respectively.

3.1.3 Turbulent spot parameters of thermal structure on the plane perpendicular to the plate surface

Table 5 presents turbulent spot celerity at leading edge at the most frontal interface and the hump on the plane of z = 0, 0.01, and 0.02 m. The celerity at the most frontal interface on the central plane was found at 0.84. This celerity was slightly less than those, obtained by the other researchers that were in range of 0.87 – 0.9, following Cantwell *et al*. (1978), Wygnanski *et al*. (1976), Wygnanski *et al*. (1982), and Chong and Zhong (2006). Also, celerity at the hump, found at 0.82 was similar to those reported by Wygnanski *et al*. (1982). Therefore, this confirmed reliability of the technique and the structure, exhibited by liquid crystals could be counted as evidence that this turbulent spot was the same classical turbulent spot, investigated by the other researchers.

Table 5 Turbulent spot celerity at leading edge on the height of most frontal interface and the hump on the plane of z = 0, 0.01, and 0.02 m under adverse pressure gradients.

	λ_θ	Turbulent spot celerity		
		z = 0 cm	z = 1 cm	z = 2 cm
ZPG[1]	0	0.84 ± 0.03	0.82 ± 0.03	0.65 ± 0.03
ZPG[2]	0	0.82 ± 0.03	0.77 ± 0.03	0.62 ± 0.02
MAPG[1]	-0.016	0.76 ± 0.03	0.71 ± 0.03	0.64 ± 0.03
MAPG[2]	-0.016	0.73 ± 0.03	0.62 ± 0.02	0.58 ± 0.02
SAPG[1]	-0.06	0.7 ± 0.03	0.65 ± 0.03	0.60 ± 0.02
SAPG[2]	-0.06	0.7 ± 0.03	0.55 ± 0.02	0.53 ± 0.02

[1]Note the parameter obtained at location of the most frontal interface.
[2]Note the parameter obtained at location of the hump.

From the table, it was found that magnitude of convective velocity at the most frontal interface was more than at the spot hump. Also, the celerity was greatest on the plane of z = 0 m, in good agreement with those, obtained using the milk solution. The difference of celerities, shown at each spanwise distance resulted in the formation of arrow head shape of turbulent spot. When turbulent spot was under the influence of increased pressure gradient, its celerity was apparently decreased as yielded by the other techniques.

3.2 Thermal characteristics of turbulent spot on the plane parallel to the plate surface

3.2.1 Development of thermal structure of turbulent spot on the plane parallel to the plate surface under zero pressure gradient

In this view, the thin sheet of white light also illuminated through the offset plane at the height of 3 mm and 6 mm from heated surface. When dispersed liquid crystals within turbulent spot were incident by the light sheet, color data on these planes were directly obtained in RGB format. Both heightwise and streamwise distance was equally set as the test of milk solution. Then, these yielded results were comparable. Disadvantage of this technique still be found as the diffusive light behind turbulent spot, similar to the previous technique as shown in Fig. 135(a) and 136(a). However, symmetry behavior of turbulent spot was found by sight investigation. Thus, all information of the instantaneous temperature perturbation was presented only the incident side of the spot structure. Another side of structure was constructed by mirroring the achieved data to yield the full frame of the thermal structure of turbulent spot when it propagated downstream. The obtained temperature information on the both planes was also non-dimensionalized as dimensionless parameter. From the temperature contour of individual turbulent spot, it was found that the low temperature distribution was found at the top portion of the early spot, presented as the substructure at the normalized time of 19.43 on the plane of y = 3 mm as depicted in Fig. 135(b). Hot solution from the heated surface diffused into the structure via the central front part of turbulent spot. Later, it pervaded through the considered structure when the spot traveled further under thermal boundary layer. This behavior was found to be consistent to the results from another view. Besides, the folds, parts of deformed interface which are wrapped around the vortex filaments as reported by Perry *et al.* (1981) were observed as two symmetrical lines at the normalized time of 19.43. The appeared gap between them was called a slit. Fig. 136(b) shows the temperature perturbation contour of turbulent spot on the plane y = 6 mm above the heated surface. It was found that the evolution of thermal characteristic on this height agreed with the structure, obtained on the plane of y = 3 mm. It has been known that the reflective degree of liquid crystal particle is much less than milk. Fortunately, it could visualize a detail of the substructure on the plane y = 6 mm. It was found that the turbulent spot shape on this plane consisted of two major areas that positioned symmetrically. Hence, these obtained substructures could be taken as parts of the hairpin structure of turbulent spot, described by Haidari and Smith (1994), Singer and Joslin (1995), and Singer (1995).

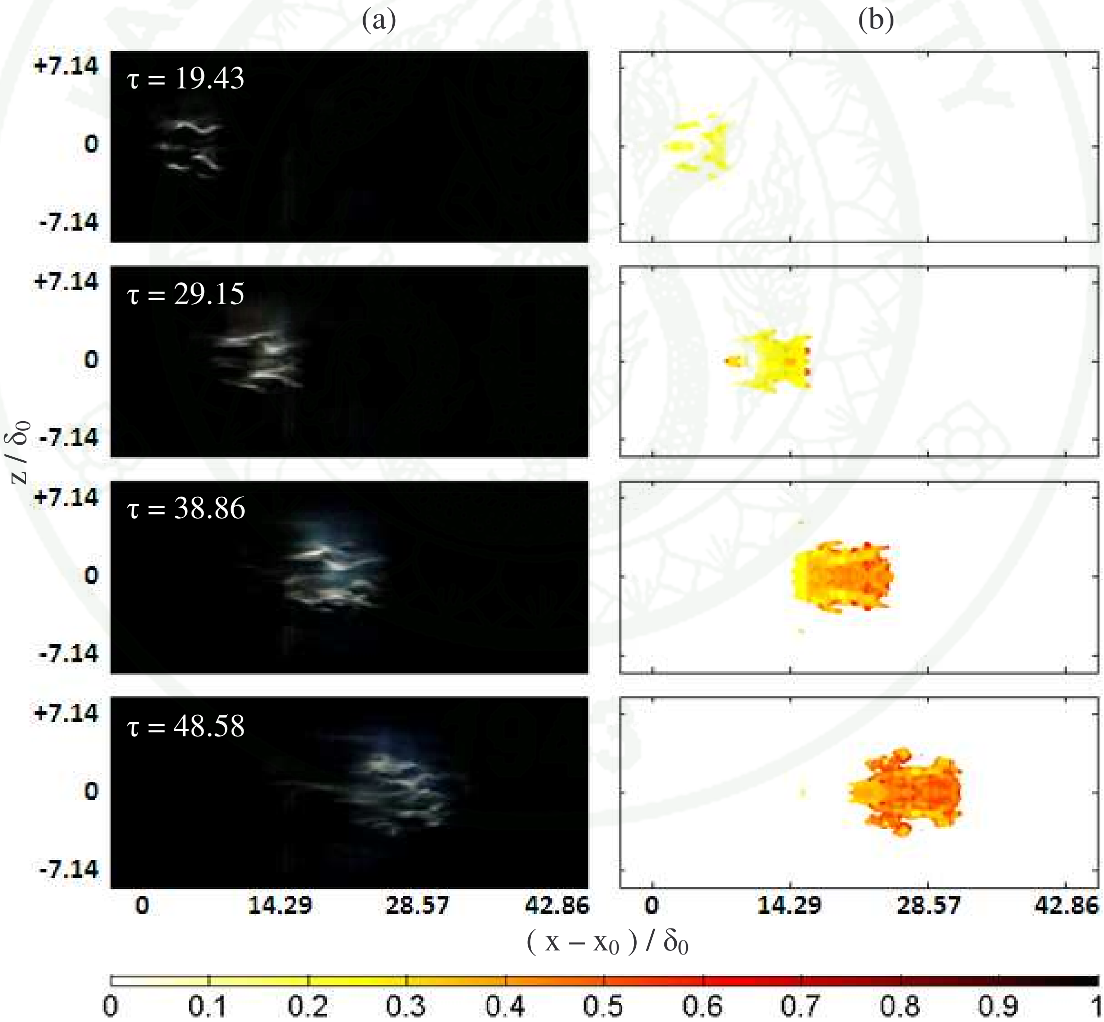

Figure 135 (a) Structure of individual turbulent spot, exhibited by slurry liquid crystals on y = 0.003 m., (b) Thermal structure of turbulent spot y = 0.003 m.

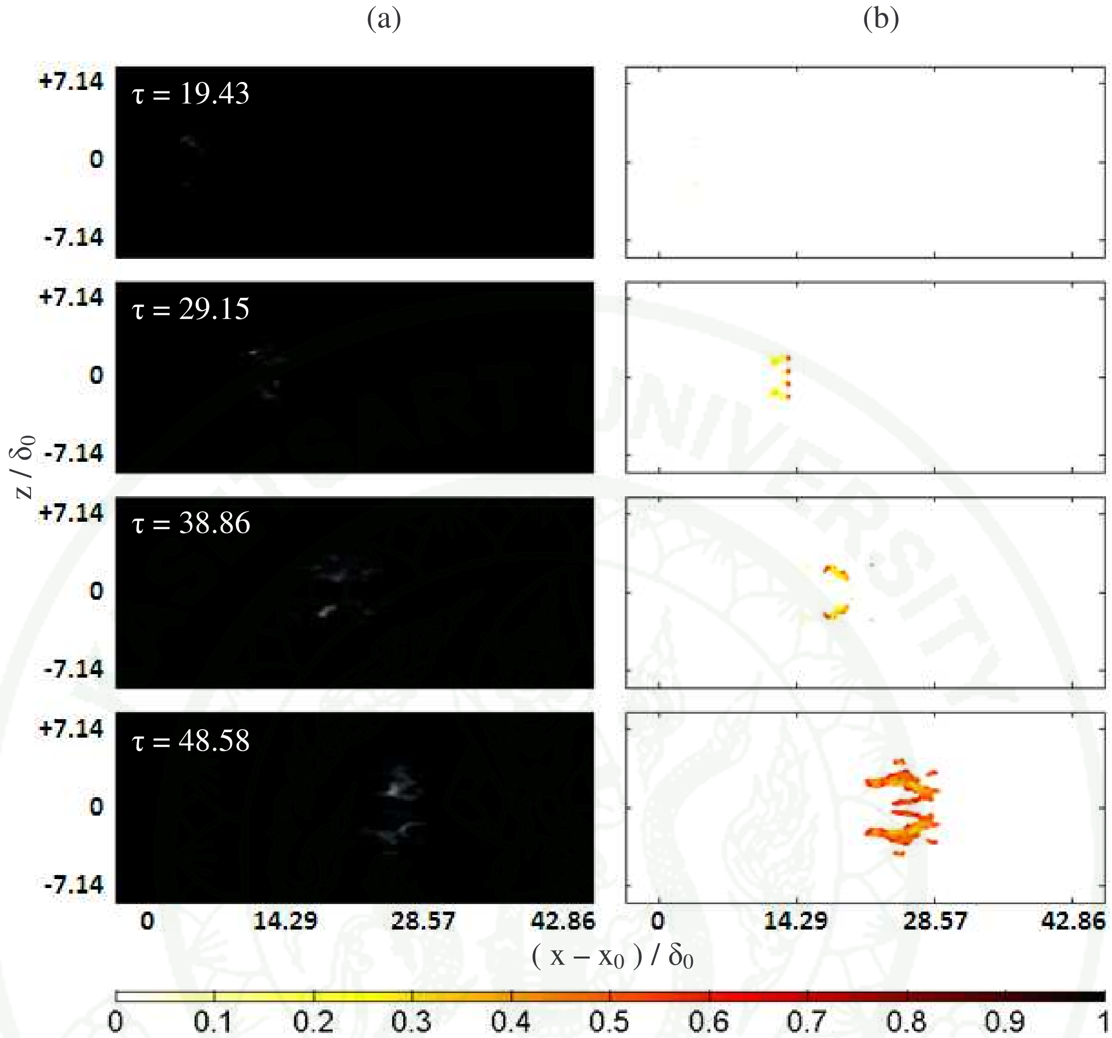

Figure 136 (a) Structure of individual turbulent spot, exhibited by slurry liquid crystals on y = 0.006 m., (b) Thermal structure of turbulent spot on the plane y = 0.006 m.

Fig. 137 (a) and (b) show the temperature distribution within the representative turbulent spot on the plane of y = 3 and 6 mm with comparable distance. It was shown that turbulent spot was initiated with the relatively low temperature even it had come across the border to heating area of the flat plate. These results agreed with those obtained from the plane perpendicular to the heated surface. The high temperature region of 0.4, reported by Van Atta and Helland (1980), Antonia and Chambers (1981), and Chong and Zhong (2006), firstly emerged on the plane of y = 3 mm at approximately $\tau = 29.14$ after the injection. Magnitude and location of the high temperature region was in good agreement with those reported by the other researchers. However, these obtained results were strong evidences to confirm that the relatively hotter fluid transported from the near heating wall region to its body via the central front region. Besides, the image detection of the spot structure by this technique also revealed the small areas near spot trailing, noted as point A as found by Glezer *et al*. (1989). They were responsible for the in-stabilization near turbulent spot wingtips to make it grow on spanwise direction. When it was related to the representative thermal foot print by the same instant, it was found that there was a connection between these areas and the 5th and 6th streaks, described previously. The hotter fluid was swept up to this local region and it was invisible on the plane of y = 6 mm. Therefore, this expressed that the behavior was deduced by the small subsidiary vortices near wingtips, introduced by Haidari and Smith (1994). In Fig. 137(b), turbulent spot was detected on the plane of y = 6 mm. The folds of vortex filaments, described by Perry *et al*. (1981) were also observed at τ = 19.43 after the disturbance. As it grew along the streamwise direction, the hot fluid from the footprint was also sent up to this region. However, the dense of high temperature fluid was relatively less, comparing to the lower level of the substructure.

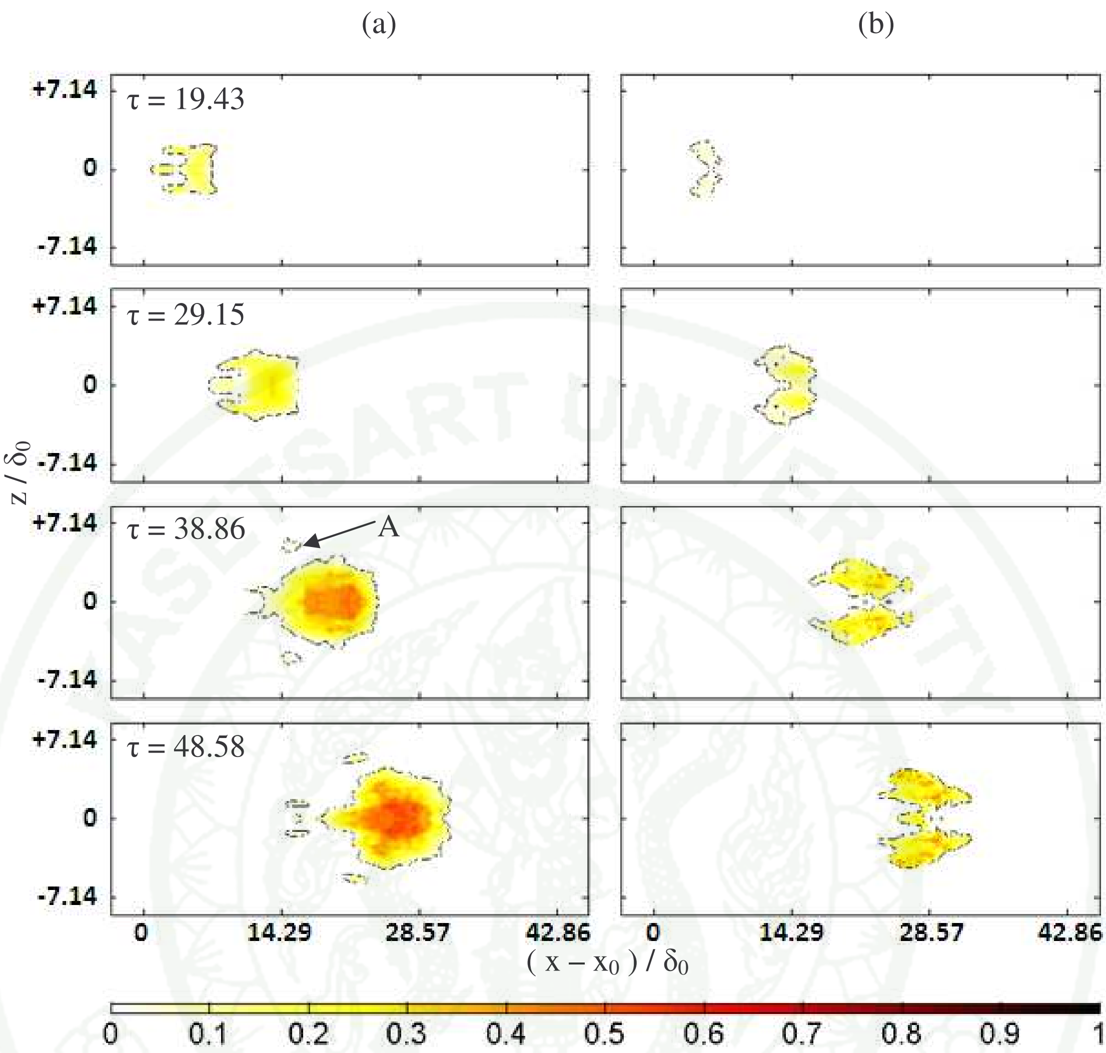

Figure 137 Structure of representative turbulent spot, exhibited by slurry liquid crystals on the plane (a) y = 0.003 m and (b) y = 0.006 m.

3.2.2 Development of thermal structure of turbulent spot on the plane parallel to the plate surface under various pressure gradients

Fig. 138(a)-(c) and 139(a)-(c) show RGB signal of individual turbulent spots, recorded when they traveled downstream under zero, mild and strong adverse pressure gradient on the plane of y = 3 and 6 mm, respectively. The folds at early stage of the development and the in-stabilization areas near wingtips were also observable. All structures appear as streaky shape, randomly emerged by the presence of the tightly pack of hairpin vortices. The observed colors were scattered by the white light, reflecting from the particle of slurry liquid crystals, dispersed through the whole structure of turbulent spot. Nevertheless, the error from an unpredictable deflection of the light after passing through the dense particles within the turbulent structure was still remaining. It is clearly seen on another side of the incident light especially under the condition of the strong adverse pressure gradient.

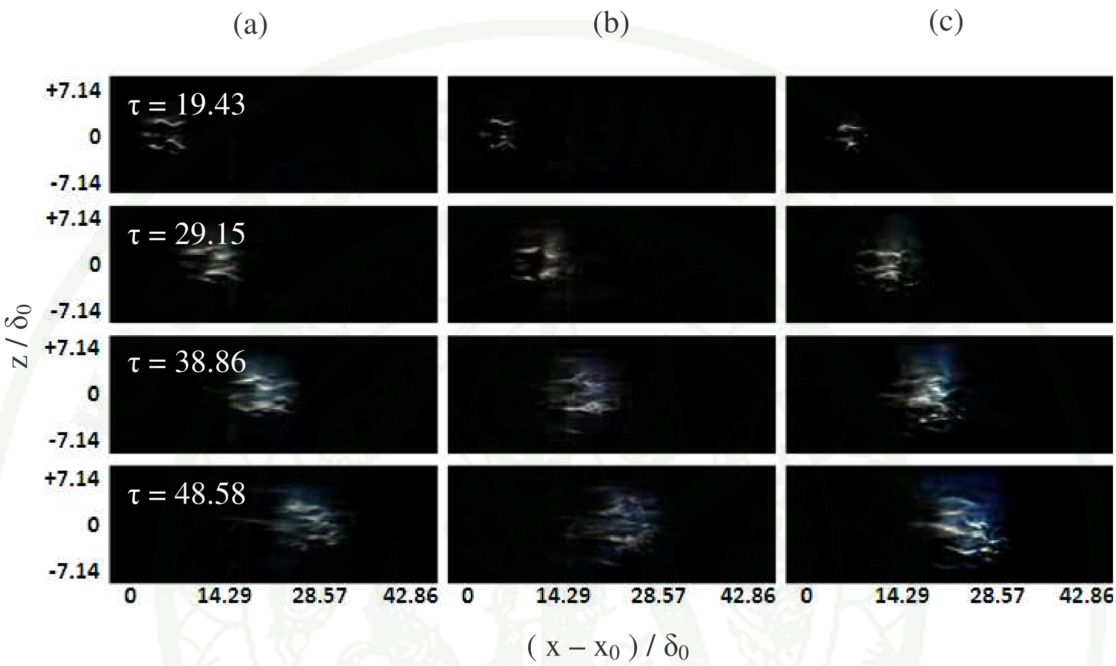

Figure 138 (a)-(c)Turbulent spot, exhibited by liquid crystals on y = 0.03 m under zero, mild, and strong adverse pressure gradient, respectively.

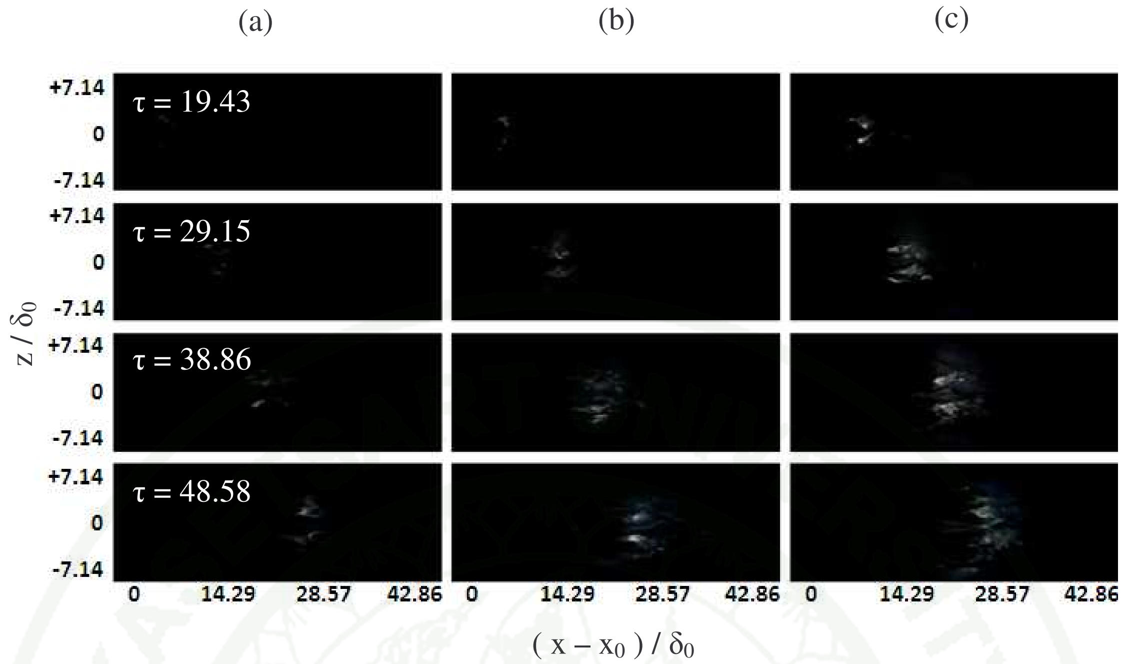

Figure 139 (a)-(c)Turbulent spot, exhibited by liquid crystals on y = 0.06 m under zero, mild, and strong adverse pressure gradient, respectively.

The representative thermal structures of turbulent spot on the plane of y = 3 mm under zero, mild, and strong adverse pressure gradients were depicted in Fig. 140(a)-(c), respectively. It was found that, when the spot confronted the higher pressure, caused by the decreasing free stream velocity, the pack of hairpin vortices tend to grew on the spanwise direction that had relatively lower pressure. The development of thermal field inside the substructure under λ_θ = -0.016 and -0.06 was similar as λ_θ = 0 that the high temperature water convected on upward direction from the heated wall via the central front region of the structure. The maximum magnitude of the dimensionless temperature under various levels of λ_θ was not outstandingly different. Fig. 141(a)-(c) show the representative thermal structures of turbulent spot on the plane of y = 6 mm under zero, mild, and strong adverse pressure gradients, respectively. It was found that the folds of vortex filaments were found in the early state of turbulent spot under all pressure gradients. Also, the in-stabilized areas, found merely on the plane of y = 3 mm at the case of λ_θ = 0, occurred at the height of 6 mm under the stronger level of adverse pressure gradient. Moreover, the location of these areas was consistent to each other on both plane as the A and B notations in Fig. 140(b) and 141(b), respectively. These areas were larger when the spot experienced the stronger adverse pressure gradient. However, the greater area, containing more hairpin vortices under the strong pressure gradient provided the higher heat transfer over flat plate. Therefore, the stronger strength in pressure gradient on boundary layer transition not only accelerated transition process on spanwise direction but also provided the better heat exchange between the surface and the free stream fluid.

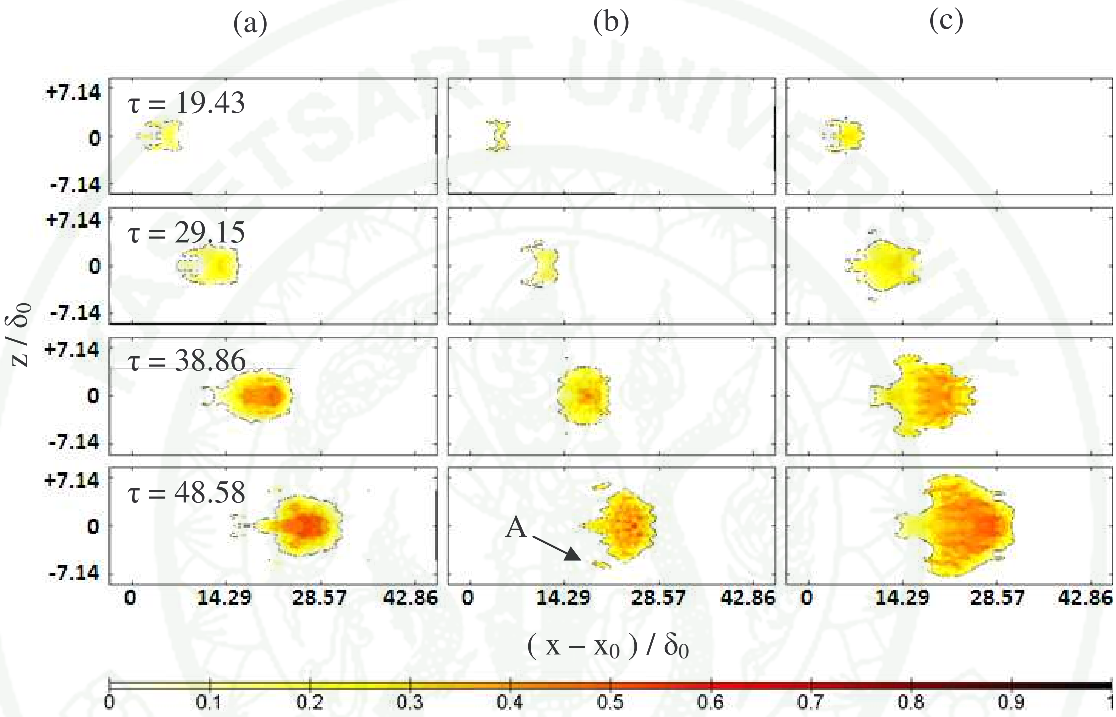

Figure 140 (a)-(c)Thermal structure of representative turbulent spot on y = 0.03 m under zero, mild, and strong adverse pressure gradient, respectively.

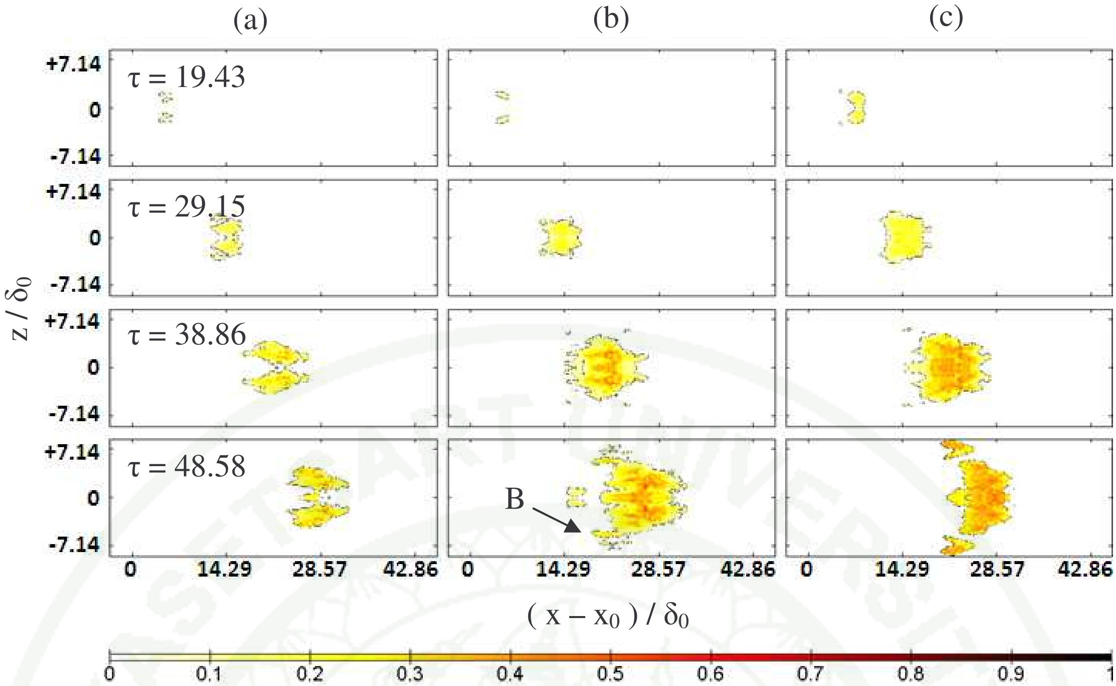

Figure 141 (a)-(c)Thermal structure of representative turbulent spot on y = 0.06 m under zero, mild, and strong adverse pressure gradient, respectively.

3.2.3 Turbulent spot parameters of thermal structure on the plane perpendicular to the plate surface

Table 6 presents Turbulent spot parameters of representative thermal structure on the plane of y = 0.003 and 0.006 m under zero, mild, and strong adverse pressure gradients. It was found that they were in good agreement with those achieved by the previous technique. Due to the increased pressure, caused by reduction of free stream velocity, spot celerity on both leading and trailing edge orderly decreased. These happened not only on the mid plane of the flow, but also through the spanwise section. The further turbulent spot propagated downstream, the more energy it employed to dominate the greater pressure drag. Thus, as explained previously, turbulent spot tended to grow on lateral direction, having the relatively lower pressure drag. These caused the wider spreading half angle in the stronger adverse pressure gradient. However, these obtained angles were also less than those reported by Gostelow *et al*. (1993), Van Hest (1994), Seifert and Wygnanski (1994), and Gostelow *et al*. (1996), mostly yielding data from hotwire anemometer. Nevertheless, the consistent spot parameters, measured under zero pressure gradient, confirmed that turbulent spot in the present study resembled the classical turbulent spot, investigated by the other researchers. Finally, these results also showed that visualization technique on the use of slurry liquid crystals could provide qualitative and quantitative information on both velocity and thermal characteristics of artificially generated turbulent spot simultaneously.

Table 6 Turbulent spot parameters of thermal structure on the plane of y = 0.003 and 0.006 m under adverse pressure gradients.

	λ_θ	C_{LE}	C_{TE}	$\alpha°$
ZPG[1]	0	0.84 ± 0.03	0.54 ± 0.02	11.1 ± 0.02
ZPG[2]	0	0.89 ± 0.03	0.69 ± 0.03	5.5 ± 0.02
MAPG[1]	-0.016	0.76 ± 0.03	0.57 ± 0.02	12.8 ± 0.02
MAPG[2]	-0.016	0.85 ± 0.03	0.55 ± 0.02	10.2 ± 0.02
SAPG[1]	-0.06	0.75 ± 0.03	0.48 ± 0.02	18.4 ± 0.02
SAPG[2]	-0.06	0.75 ± 0.03	0.57 ± 0.02	15.1 ± 0.02

[1]Note the parameter obtained on the height of 3 mm above the surface.
[2]Note the parameter obtained on the height of 6 mm above the surface.

The turbulent spot celerities at leading and trailing edges under various pressure gradients, yielded in the present study were mutually compiled with those summarized by Gostelow *et al*. (1996) as shown in Fig. 142. It was found that the spot celerities at trailing edge were in agreement with those obtained by the others. Conversely, the spot in the present study propagated with less velocity at the leading edge comparing to the others. However, the trend of the celerity at leading edge clearly showed that the front bound of the spot convected downstream slower when the level of adverse pressure gradient increased. Besides, it was also found that the half spreading angle increased when the adverse pressure gradient increased as shown in Fig. 143. It should be noted that the turbulent spot parameters, compiled by Gostelow *et al*. (1996) were measured at the mature state while the spot parameters in this study were detected at the young state. Therefore, this concluded that the maturity of turbulent spot directly affected on the spot celerity at leading edge and also the half spreading angle under the different adverse pressure gradients.

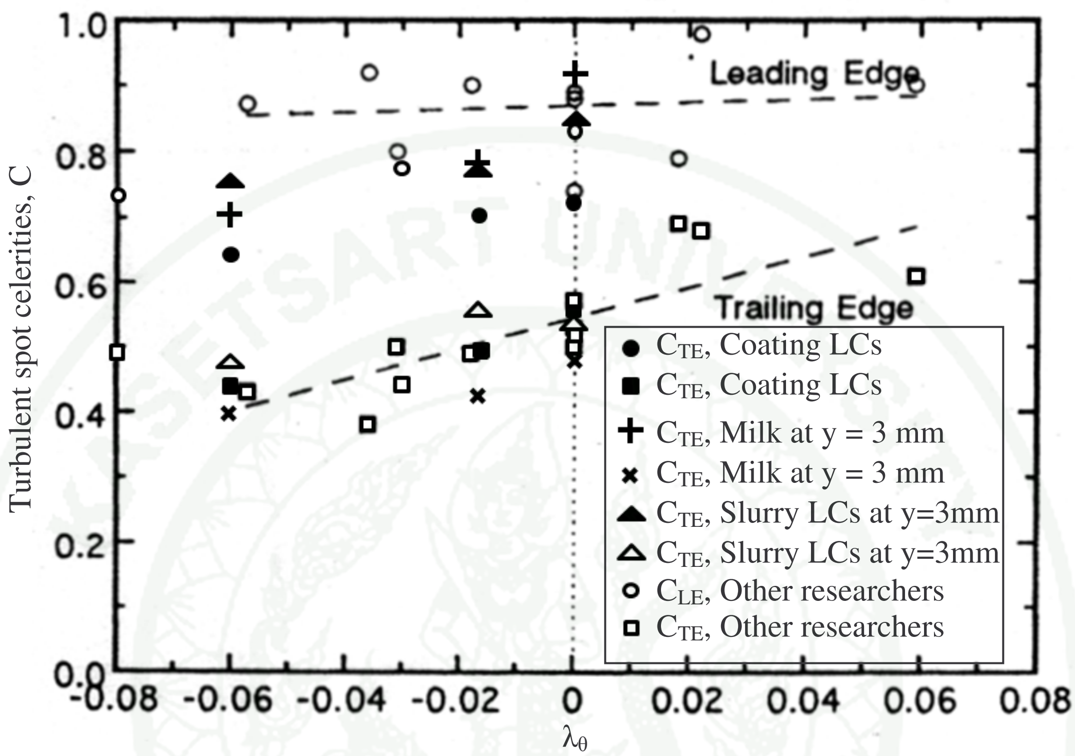

Figure 142 Compilation of turbulent spot celerities under various pressure gradients.

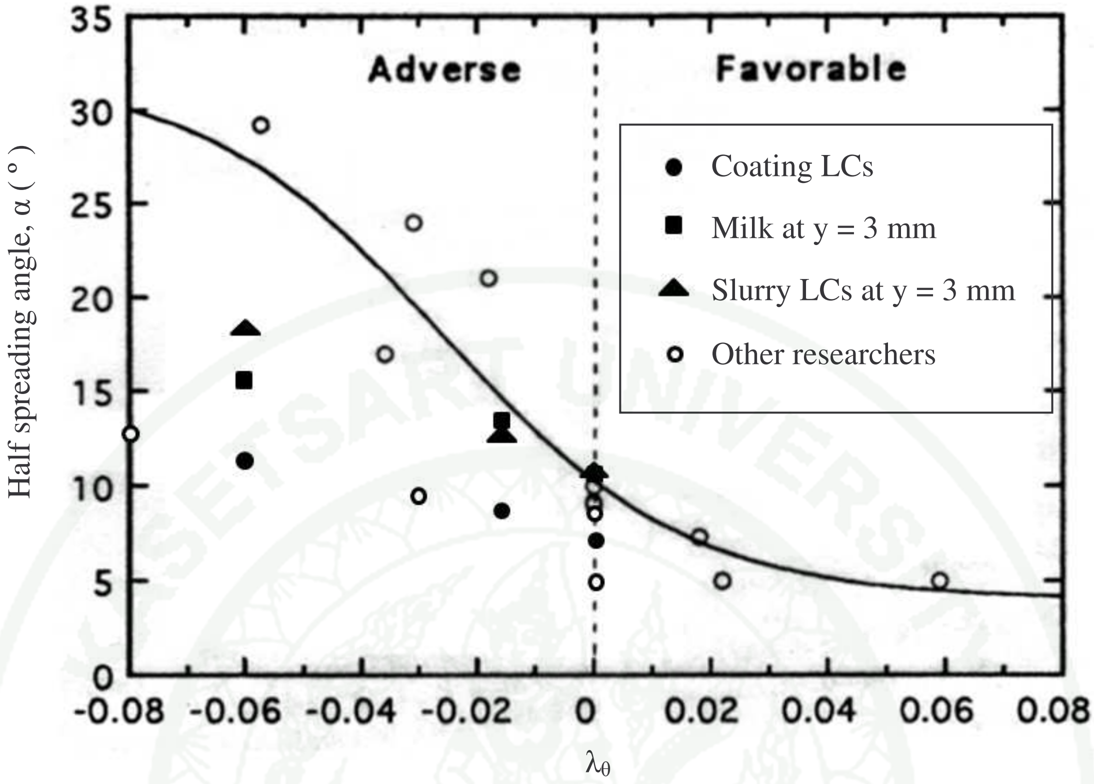

Figure 143 Compilation of half spreading angle of turbulent spot under various pressure gradients.

Following *Chen and Thyson* (1971), if the turbulent spot is assumed to have a triangle plan form, Gostelow *et al*. (1996) determined the non dimensional spot propagation parameter, σ, for the published data from

$$\sigma = (\tan \alpha) \times (C_{TE}^{-1} - C_{LE}^{-1}) \tag{30}$$

The non dimensional spot propagation parameter at different adverse pressure gradients, obtained in this study was compared to those summarized by Gostelow *et al*. (1996) as shown in Fig. 144. By the reasons above, the propagation parameter, determined from the relation of the spot celerities and the half spreading angle was less than those obtained by the other researchers. However, it was apparently found that the magnitude of the non dimensional spot propagation parameter gained when the adverse pressure gradient increased. The level of pressure gradient affected not only the non dimensional spot propagation parameter, but also the heat flux through the turbulent spot footprint. The heat flux throught the spot was measured at $\tau = 68$, which the full frame of the thermal footprint was obtained. Fig. 145 clearly showed the heat flux transferred through the spot footprint with higher rate when the level of adverse pressure increased. Therefore, from all summaries, it can conclude that the adverse pressure gradient directly influence the characteristics of both momentum and heat transfer of turbulent spot.

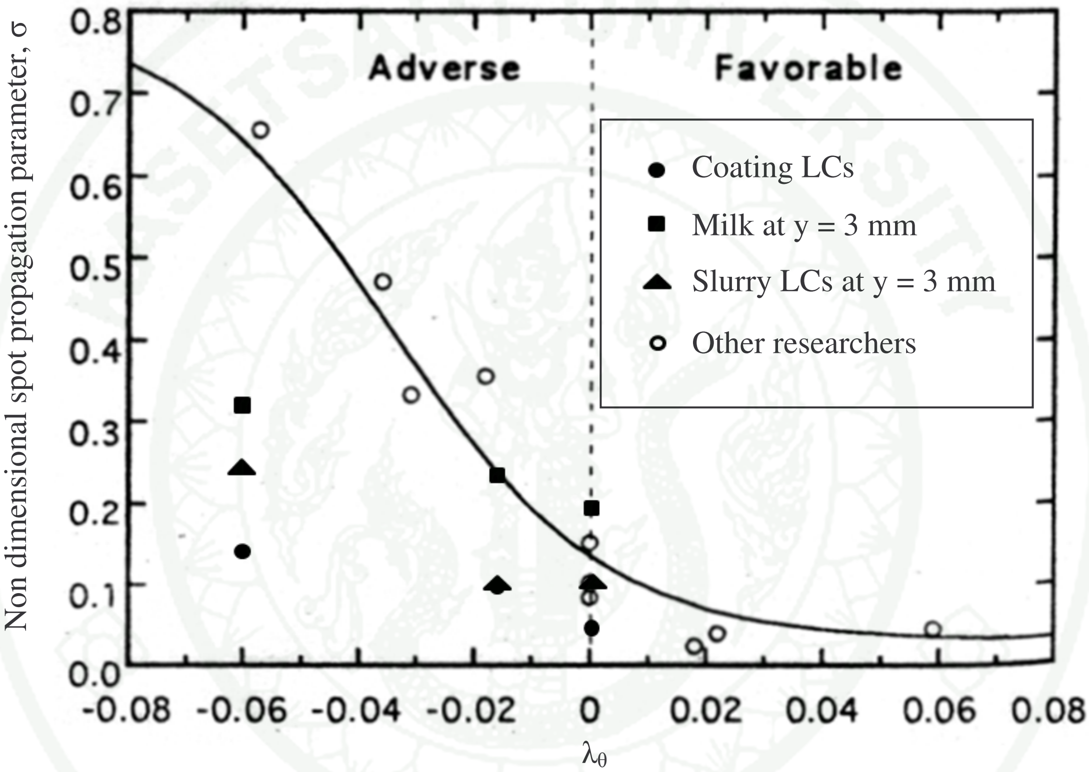

Figure 144 Compilation of non dimensional propagation parameter of turbulent spot under various pressure gradients.

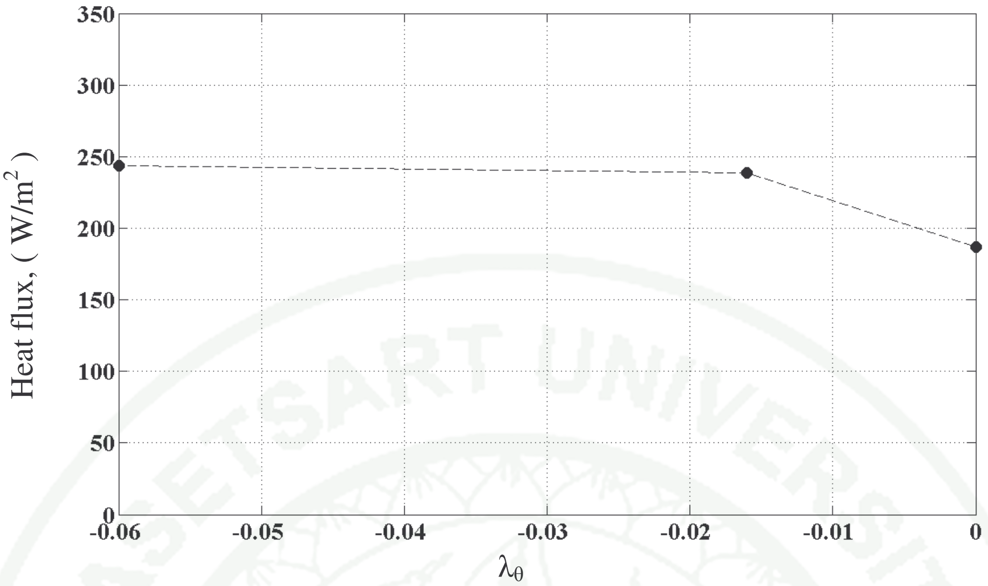

Figure 145 Heat flux through turbulent spot at various adverse pressure gradients.

CONCLUSION AND RECOMMENDATION

Conclusion

In the present study, the growth mechanism of an artificially generated turbulent spot under boundary layer transition was further investigated using three visualization techniques. The effect of various adverse pressure gradients that influenced the development of turbulent spot was also presented. From the first technique using the coating liquid crystals, characteristics of thermal footprint of turbulent spot was revealed. Firstly, the structure of thermal footprint was directly recorded in RGB color space. Turbulent spot appeared as a group of green streaks, propagating downstream. These green streaks exhibited unsteady characteristics under random effect of boundary layer transition. Spatial temperature distribution was obtained by inserting color signal into the calibrated relation of the coating liquid crystals. The lowest temperature was found at the core of each streak. This is consistent to the location of the maximum convective heat transfer coefficient and heat flux, achieved by employing an analytical formula, developed from energy balance method mutually with “Implicit” finite difference approach.

The structure of thermal foot print of turbulent spot could be directly presented by the contour of heat flux. It grew on both streamwise and spanwise directions. Each streak initiated like a small induced spot and developed among the longer streak, extending along the flow direction. Furthermore, in the current study, the representative structure of turbulent spot was proposed to reduce the consequence of randomness, dominating the turbulent region. It indicated that the thermal structure in the early stage, called “young turbulent spot”, appeared as four streaks at the spot frontal. They propagated downstream with relatively equal speed. In this stage, the footprint was depicted as “hand-like”. Also, the shape of the becalmed region was depicted as 2 tails-like. Turbulent spot became mature state when its half spreading angle changes from 6.8° to 10°, corresponding to the emerging of the 5^{th} and 6^{th} streaks at both sides of lateral bound of the structure. After this, the middle frontal streak was piercing forward and the arrow head shape was apparently formed.

In the second visualization technique, the milk solution was selected as the medium to reveal substructures of turbulent spot on different viewing planes. Also, the mechanism of turbulence breaking down by the injecting water was finely observed. After disturbance injection, the low pressure trace was created, following the injecting water. It pulled the mixed solution, flowing in the near wall region above shear layer. During these processes, the high and low pressure region instantly appeared at the upstream and downstream of the spot generator. When the instantly created inertia ran out, the high pressure fluid plunged into the low pressure region and finally a classical hairpin vortex, the primary structure of turbulent spot was generated.

This flow visualization technique showed that turbulent spot had three main parts, consisting of overhang head, spot body, and becalmed region. Each of them significantly exhibited the unique characteristic. A single spanwise vorticity was found at its overhang head since the early instant of turbulent spot generation. It appeared only near the middle plane of the flow. Location on top of this vorticity was also the highest point of turbulent spot, consistent to the height of the turbulent boundary layer, originating at the spot generator with an initial thickness of laminar boundary layer at that location. It was followed by spot body, a tight pack of hairpin vortices that was typically found under turbulent boundary layer. Calming flow occurred at the spot trailing. In this region, the dye orderly aligned as found in laminar boundary layer. The results also showed that turbulent spot propagated downstream with arrow head shape structure. When the image of thermal structure was superimposed with those obtained by the second technique, it was found that thermal footprint precisely placed on becalmed region of turbulent spot body. The thermal footprint approximately started at the trailing edge and exactly ended up at the end point of becalmed region of turbulent spot structure. In this area, the near wall fluid was swept by turbulent spot and replaced by the water, outside the near wall region. These were the reasons, explaining the cooling mechanism of the thermal footprint on the heated surface.

The heat diffusion from the heated surface to turbulent spot interior was investigated in the third visualization technique. In this test, slurry liquid crystals were used as dye instead of the milk solution. From the study, the growing mechanism of the spot was similar as those, revealed by the dye of milk solution. Besides, by the property of the slurry liquid crystals, the solution was capable to map temperature contour in fluid. Thus, it was found that the young structure of turbulent spot cenvected heat from the hot surface to its body by hairpin vortices. These vortices pulled up the hotter near wall water to the higher layer until it spread over the structure. The relatively highest dimensionless temperature within turbulent structure was only 0.4 while the highest temperature at the heated surface and the lowest temperature at the free stream was set at 1 and 0, respectively. Moreover, the relatively colder fluid was also found at the trailing region above the location of the thermal footprint. Therefore, these results fully revealed the mechanism of heat exchange under boundary layer transition.

Furthermore, from the top view, the obtained instantaneous temperature contour within turbulent spot structure also confirmed that the hotter water from the heated surface diffused on upward direction. The relatively highest temperature water was found at the central front region, consistent to the contours, reported by the others. Also, with the lower reflective degree of the liquid crystals comparing to milk, the folds of vortex filaments of the primary vortex was visible at the height of $y = 6$ mm above the surface. The hot fluid from the footprint was also sent up to this level. However, the dense of high temperature fluid was relatively less, comparing to the lower level of the substructure.

The effect of various adverse pressure gradients on the structure of turbulent spot was further determined in the present study. It was found that the pressure gradient mainly affected on the shape of the structure and the whole structure was blunter under higher level of adverse pressure gradient. Its shape was more extensive on both heightwise and spanwise directions. In the mean time, the celerity at all particular features of turbulent spot was apparently decreased comparing to those obtained under effect of zero pressure gradient. Also, distance between the virtual onset and the spot generator became nearer under the stronger adverse pressure gradient. These results were induced by the increased pressure along the flow direction, caused by reduction of free stream velocity. Then, the turbulence outstandingly grew on on both heightwise and spanwise directions, having less local pressure, comparing to the streamwise direction.

Finally, the celerities of turbulent spot at different feature such as leading edge, trailing edge, end of becalmed region etc. as well as the half spreading angle at both young and mature state of turbulent spot under various adverse pressure gradients were in excellent agreement with those reported by the other researchers. Therefore, this consistency on turbulent spot parameters confirmed the reliability of the developed techniques. Also, the turbulent spot, described its characteristics in the present study, resembled the classical turbulent spot, investigated by the other researchers.

Recommendation

Turbulent spot was investigated in the present study, mainly focused on the early stage, called "young turbulent spot". As the results of mature thermal footprint, it apparently showed different behavior. Furthermore, it has been known that boundary layer transition, developing on both suction and pressure side of turbine blade, was mostly dominated by adverse and favorable pressure gradient. Only effect of adverse pressure gradient has been investigated in the current study. Thus, it would be advantageous to determine the effect of both mature stage and the favorable pressure gradients on the growth and development on turbulent spot. Turbulent spot parameters should be obtained to fulfill view of how they change as in the realistic conditions. All achieved values would be suitable for insertion into predictive formulas for full evolution of turbulent spot under bypassed transition flow.

LITERATURE CITED

Abu-Ghannam, B.J. and R. Shaw. 1980. Natural Transition of Boundary Layers-the Effects of Pressure Gradient and Flow History. **Journal of Mechanical Engineering Science** 22 (5): 213-228.

Acalar, M.S. and C.R. Smith. 1987. A study of hairpin vortices in a laminar boundary layer . Part 2. Hairpin vortices generated by fluid injection. **Journal of Fluid Mechanics** 175: 43-83.

Antonia, R.A., A.J. Chambers, M. Sokolov, and C.W. Van Atta. 1981. Simultaneous temperature and velocity measurements in the plane of symmetry of a transitional turbulent spot. **Journal of Fluid Mechanics** 108: 317-343.

Batchelor, G.K. 1970. **The theory of homogeneous turbulence**. Cambridge University Press : 55-75.

Bernard, P.S. 2011. The hairpin vortex illusion. **Journal of Physics**: Conference Series 318, 062004.

Bons, J. P. and S.T. McClain. 2003. The Effect of Real Turbine Roughness With Pressure Gradient on Heat Transfer. **ASME J. Turbomach** 126: 333–441.

Bruse, M., D.W. Bechert, J.G. van der Hoeven, W. Hage, and G. Hoppe. 1993. Experiments with Conventional and with Novel Adjustable Drag-Reducing Surfaces. **Near-wall Turbulent Flows: Proceedings of the International Conference**. Tempe, AZ: 719-738.

Cantwell, B., D. Coles, and P. Dimotakis. 1978. Structure and entrainment in the plane of symmetry of a turbulent spot. **Journal of Fluid Mechanics** 87: 641.

Cengel, Y.A. 2003. **Heat transfer : a practical approach.** Second edition. McGraw-Hill.

Chaiworapuek, W. and C. Kittichaikarn. 2011. A Study of Free Convection using Thermochromic Liquid Crystals as Dilute Suspension in a Fluid. **Proceeding of the 25th Conference of the Mechanical Engineering Network of Thailand**, Krabi, Thailand.

Chernoray, V.G., G.R. Grek, V.V. Kozlov, and Y.A. Litvinenko. 2012. Study of the incipient spot breakdown controlled by riblets. **Progress in Flight Physics.** 3: 545-556.

Chong, T.P. and S. Zhong. 2005. On the Three-Dimensional Structure of Turbulent Spots. **Journal of Turbomachinery** 127: 545-551.

Chong, T.P. and S. Zhong. 2006. On the Momentum and Thermal Structures of Turbulent Spots in a Favorable Pressure Gradient. **Journal of Turbomachinery** 128: 689-698.

Chong, T.P. and S. Zhong. 2012. On the transverse growths of turbulent spots in a heated boundary layer with favorable pressure gradient. **J. Vis.** 15: 189-192.

Chong, T.P. and S. Zhong. 2013. On the shear stress and thermal footprints of turbulent spots at zero pressure gradient. **Journal of Mechanical Science and Technology** 27(4): 1001-1009.

Chu, J.C., J.S. Strand, and D.B. Goldstein. 2010. Investigation of turbulent spot spreading mechanism. **48th AIAA Aerospace Sciences Meeting.** Orlando, Florida.

Clark, J.P. 1993. **A Study of Turbulent Spot Propagation in Turbine-Representative Flows.** D.Phil. Thesis, University of Oxford, United Kingdom.

Coles, D. and S.J. Barker. 1975. **In Turbulent mixing in non-reactive and reactive flows.** SNB Murthy (Plenum, New York, 1975): 285-292.

Corrsin, S. and A.L. Kistler. 1955. Free-stream boundaries of turbulent flows. **N.A.C.A. Rep.** no. 1244. (Supersedes *N.A.C.A. T N* 3133.)

Coustols, E. and A.M. Savill. 1992. **Turbulent Skin-Friction Drag Reduction by Active and Passive Means: Parts 1 and 2.** Special Course on Skin-Friction Drag Reduction 8: 1-55.

Curtis, E.M., H.P. Hodson, M.R. Banieghbal, J.D. Denton, R.J. Howell and N.W. Harvey. 1997. Development of blade profiles for low pressure turbine applications. **ASME J. Turbomach** 119(3):531-38.

Dabiri, D. 2008. Digital particle image thermometry/velocimetry: a review. **Journal of Experiments in Fluids.**

Dhawan, S. and R. Narashimha. 1958. Some Properties of Boundary Layer Flow during Transition from Laminar to Turbulent Motion. **Journal of Fluid mechanics** 3: 418.

Elder, J.W. 1960. An experimental investigation of turbulent spots and breakdown to turbulence. **Journal of Fluid Mechanics** 9(2): 235-246.

Emmons, H.W. 1951. The laminar-turbulent transition in a boundary layer Part 1. **Journal of Aeronautical Science** 18: 490.

Ersoy, S. and J.D.A. Walker. 1985. Viscous flow induced by counter-rotating vortices. **Physics of Fluids.** 28, 2687-2698.

Gad-El-Hak, M., R.F. Blackwelder, and J.J. Riley. 1981. On the growth of turbulent regions in laminar boundary layers. **Journal of Fluid Mechanics** 110: 73-95.

Glezer, A., Y. Katz, and I. Wygnanski. 1989. On the breakdown of a wave packet trailing a turbulent spot in a laminar boundary layer. **Journal of Fluid Mechanics** 198: 1-26.

Goldstein, D. B. and T.C. Tuan. 1998. Secondary Flow Induced by Riblets. **Journal of Fluid Mechanics** 363: 115-151.

Gostelow, J.P., G. Hong, N. Melwani, and G.J. Walker. 1993 Turbulent spot development under a moderate adverse pressure gradient, **ASME paper** 93-GT-377.

Gostelow, J.P., N. Melwani, and G.J. Walker. 1996. Effects of Streamwise Pressure Gradient on Turbulent Spot Development. **ASME Journal of Turbomachinery** 118: 737-743.

Gutmark, E. and R.F. Blackwelder. 1987. On the structure of a turbulent spot in a heated laminar boundary layer. **Journal of Experiments in Fluids** 5: 217-229.

Haidari, A.H. and C.R. Smith. 1994. The generation and regeneration of singlehairpin vortices. **Journal of Fluid Mechanics** 277: 135-162**.**

Hodson, H.P. and R.J. Howell. 2005. Bladerow Interactions, Transition, and High-Lift Aerofoils in Low-Pressure Turbines. **Annu. Rev. Fluid Mech** 37: 71-98.

Hofeldt, A. 1996. **An Investigation of Naturally-Occurring Turbulent Spots Using Thin-Film Guages.** D.Phil. Thesis, University of Oxford, United Kingdom.

Hogendoora, C.J., H.C. de Lange, A.A. van Steenhoven, and M.E.H. van Dongen. 1997. Influence of turbulence intensity on intermittency model in by-pass transition. **ASME paper.** 97-GT-473.

Howarth, L. 1938. On the solution of the laminar boundary layer equations, **Proceedings of the Royal Society of London** series A: 547-579.

Hui, Y.H. 2007. **Handbook of food products manufacturing**. John Wiley & Sons, Inc. Hoboken, New Jersey

Incropera, F.P., D.P. Dewitt, T.L. Bergman, and A.S. Lavine. 2007. **Fundamentals of Heat and Mass Transfer.** Sixth edition. John Wiley & Sons (asia) Pte Ltd.

Itsweire, E.C. and C.W. Van Atta. 1984. An experimental investigation of coherent substructures associated with turbulent spots in a laminar boundary layer. **Journal of Fluid Mechanics** 148: 319-348

Jahanmiri, M. 2011. **Boundary Layer Transitional Flow in Gas Turbines**. Research report, Chalmers University of technology.

Johnson, M.W. 1998. Turbulent spot characteristics in boundary layers subjected to streamwise pressure gradient. **ASME paper.** 98-GT-124.

Johnson, M.W. 1999. Prediction of turbulent spot growth rates. **International Gas Turbine & Aeroengine Congress & Exhibition**. Indianapolis, Indiana.

Katz, Y., A. Seifert and I. Wygnanski. 1990. On the evolution of the turbulent spot in a laminar boundary layer with a favourable pressure gradient. **Journal of Fluid Mechanics** 221: 1.

Kind, R.J., P.J. Serjak, and M.W.P. Abbott. 1998. Measurements and prediction of the effects of surface roughness on profile losses and deviation in a turbine cascade. **ASME J. Turbomach** 120: 20-27.

Kittichaikarn, C. 1999. **A study of turbulent spots and wake induced transition using liquid crystals.** D.Phil. thesis, Department of Engineering Science, University of Oxford, UK.

Kittichaikarn, C., P.T. Ireland, S. Zhong, and H.P. Hodson. 1999. An investigation on the onset of wake-induced transition and turbulent spot production rate using thermochromic liquid crystal. **ASME paper**. no. 99-GT-126.

Klebanoff, P.S., K.D. Tidstrom and L.M. Sargent. 1962. The three-dimensional nature of boundary layer instability. **Journal of Fluid Mechanics** 95: 741-773.

Li, Z. and T. Dengbin. 2006. Nonlinear evolution of turbulent spots in the near-wall shear flow. **Science in China: Series G Physics, Mechanics & Astronomy** 49(2): 158-168.

Makita, H. and A. Nishizawa. 2001. Characteristics of internal vertical structures in a merged turbulent spot. **Journal of Turbulence** 2: N12.

Matsui, T. 1980. Visualisation of turbulent spots in the boundary layer, pp.288. **Proceedings of IUTAM Symposium on Laminar-Turbulent Transition**, ed., Eppler, R. and Fasel, H., Berlin, Heidelberg, New York.

Mayle, R.E. 1991. The Role of Laminar-Turbulent Transition in Gas Turbine Engine. **Trans. ASME Journal of Turbomachinery** 113: 509-537.

Merzkirch, W. 1987. **Flow visualization**. Academic Press, Inc. Florida.

Munson, B.R., D.F. Young, and T.H. Okiishi. 2006. **Fundamental of fluid mechanics.** 5^{th} Edition, John Wiley & Sons, USA.

Narasimha, R. 1985. The Laminar-Turbulent Transition Zone in the Boundary Layer. **Prog. Aerospace science** 22: 29.

Perry, A.E., T.T. Lim, and E.W. Teh. 1981. A visual study of turbulent spots. **Journal of Fluid Mechanics** 104: 387-405.

Rassame, S., B. Siripoorikam, S. Buensawang, Y. petitanalap, and A. Bunyajitradulya. 1998. Visualization of fluids flows using the smoke-wire technique. **Research and Development Journal of the Engineering Institute of Thailand** 9(2): 71-87.

Roberts, W.B. 1980. Calculation of laminar separation bubbles and their effects on airfoil performances, **AIAA J.** 18: 25-31.

Russ, J.C. 2002. **The image processing handbook.** CRC, Boca Raton.

Sabatino, D. and C.R. Smith. 2002. Simultaneous velocity-surface heat transfer behavior of turbulent spots. **Journal of Experiments in Fluids:** 13-21.

Sankaran, R., M. Sokolov, and R.A. Antonia. 1988. Substructures in a turbulent spot. **Journal of Fluid Mechanics** 197: 389.

Sankaran, R., R.A. Antonia, D.K. Bisset, and M. Sokolov. 1991. Flow pattern and Organisation within a turbulent spot. **Physics of Fluids** 3(6): 1560-1571.

Schlichting, H. 1979. **Boundary Layer Theory.** Seven Edition, McGraw-Hill, New York.

Schröder, A. and J. Kompenhans. 2004. Investigation of a turbulent spot using multi-plane stereo particle image velocimetry. **Journal of Experiments in Fluids:** 82-90.

Schröder, A., R. Geisler, G.E. Elsinga, F. Scarano, and U. Dierksheide. 2008. Investigation of a turbulent spot and a tripped turbulent boundary layer flow using time-resolved tomographic PIV. **Journal of Experiments in Fluids** 44: 305-316.

Schubauer, G.B. and P.S. Klebanoff. 1955. **Contributions on the Mechanics of Boundary Layer Transition.** NASA TN-3489.

Seifert A. and I. Wygnanski. 1995. On turbulent spots in a laminar boundary layer subjected to a self-similar adverse pressure gradient. **Journal of Fluid Mechanics** 296: 185-209.

Singer, B.A. 1996. Characteristics of a young turbulent spot. **Physics of Fluids** 8(2): 509-520.

Singer, B.A. and R.D. Joslin. 1994. Metamorphosis of a hairpin vortex into a young turbulent spot. **Journal of Physics of Fluids** 6: 3724.

Strand, J.S. and D.B. Goldstein. 2010. DNS of surface textures to control the growth of turbulent spots. **AIAA Journal.**

Taylor, R.P. 1990. Surface roughness measurements on gas turbine blades. **ASME J. Turbomach.** 112: 175-180.

Van Atta, C.W. and K.N. Helland. 1980. Exploratory temperature-tagging measurements of turbulent spots in a heated laminar boundary layer. **Journal of Fluid Mechanics** 100(2): 243-255.

Van Hest, B.F.A., D.M. Pesschier, and J.L. Van Ingen. 1994. The Development of a Turbulent Spot in an Adverse Pressure Gradient Boundary Layer. **Proceedings of IUTAM Symposium.** Sendai, Japan.

Wallace, J.M., G.I. Park, X. Wu, and P. Moin. 2010. Boundary layer turbulence in transitional and developed states. **Center for Turbulence Research, Proceedings of the summer Program**.

White, F.M. 1986. **Fluid Mechanics.** Second Edition. McGraw-Hill, New York, NY.

Wu, X. and P.A. Durbin. 2000. Numerical Simulation of Heat Transfer in a Transitional Boundary Layer With Passing Wakes. **Journal of Heat Transfer** 122: 248-257.

Wu, X. and P. Moin. 2010. Transitional and Turbulent boundary layer with heat transfer. **Physics of Fluids** 22: 085105.

Wygnanski, I., M. Sokolov. And D. Friedman. 1976. On a turbulent ‘spot’ in a laminar boundary layer. **Journal of Fluid Mechanics** 78(4): 785-819.

Wygnanski, I., M. Zilberman, and J.H. Haritonidis. 1982. On the spreading of a turbulent spot in the absence of a pressure gradient. **Journal of Fluid Mechanics** 123: 69-90.

Yaras, M.I. 2007. An experimental study if artificially-generated turbulent spots under strong favorable pressure gradient and freestream turbulence. **Journal of Fluids Engineering** 129: 563-572.

Zhong, S., C. Kittichaikarn, H.P. Hodson, and P.T. Ireland. 2000. Visualisation of turbulent spots under the influence of adverse pressure gradients. **Journal of Experiments in Fluids.** 28: 385-393.

Zilberman, M., I. Wygnanski, and R.E. Kaplan. 1977. Transitional boundary layer spot in a fully turbulent environment. **Phys. Fluids Suppl** 20: 258-271.

APPENDIX

UNCERTAINTY ANALYSIS

Generally, the errors in the determination of dependent variables are not known. The standard deviation of the measured quantities is often presented as the uncertainty instead. Let each of the measaured quantity is labeled as x_i and its uncertainty is labeled as Δx_i. Thus, the first measured quantity can be written as x1 ± Δx1, the second measured quantity as $x_2 \pm \Delta x_2$, etc. if f means any quantities, a function of the other quantities, $f = f(x_1, x_2,\ldots x_n)$ The uncertainty in f, labeled Δf, is:

$$\Delta f = \left[\sum_{i=1}^{n} (\frac{\partial f}{\partial x_i})^2 (\Delta x_i)^2\right]^{1/2} \tag{31}$$

Suppose that f is determined using only addition or subtraction of the other quantities as $f = a_1x_1 \pm a_2x_2 \pm\ldots\pm a_Nx_N$. The parameter a is a constant. The partial derivertives of f with respect to each quantities x_i must be firstly obtained such as $\partial f/\partial x_1 = \pm a_i$. Thus, equation can be obtained as:

$$\Delta f = \left[a_1^2(\Delta x_1)^2 + a_2^2(\Delta x_2)^2 + \ldots + a_N^2(\Delta x_N)^2\right]^{1/2} \tag{32}$$

or

$$\Delta f = \left[\sum a_i^2 (\Delta x_i)^2\right]^{1/2} \tag{33}$$

If f is calculated by using only multiplication of two measures so $f = ax_1x_2$. The partial derivertives of f with respect to each quantities x_i must be firstly obtained such as $\partial f/\partial x_1 = ax_2$. Thus, equation (31) can be expressed as:

$$\Delta f = \left[(ax_2)^2(\Delta x_1)^2 + (ax_1)^2(\Delta x_2)^2\right]^{1/2} \tag{34}$$

Dividing both sides by f gives:

$$\frac{\Delta f}{f} = \left[\frac{(ax_2)^2 (\Delta x_1)^2}{(ax_1 x_2)^2} + \frac{(ax_1)^2 (\Delta x_2)^2}{(ax_1 x_2)^2} \right]^{1/2} = \left[\left(\frac{\Delta x_1}{x_1} \right)^2 + \left(\frac{\Delta x_2}{x_2} \right)^2 \right]^{1/2} \qquad (35)$$

Even f is calculated using only division of the measured quantities, it is found that the result is similar as equation (34). From equation (34), the percentage uncertainty in f is the combination of the percentage uncertainties in x_1 and x_2. Thus, this equation is shown as:

$$\frac{\Delta f}{f} = \left[\sum \left(\frac{\Delta x_i}{x_i} \right)^2 \right]^{1/2} \qquad (36)$$

It has been known that the fractional propagation rate or celerity of the turbulent spot, C, is defined as:

$$C = U / U_\alpha \qquad (37)$$

where U_α is the free stream velocity. Also, U is the spot velocity, calculated from:

$$U = x / t \qquad (38)$$

where x is the streamwise distance that the turbulent spot propagates through the time, t. Thus, the celerity, C can be alternately expressed as:

$$C = (x) \left(\frac{1}{t} \right) \left(\frac{1}{U_\alpha} \right) \qquad (39)$$

From equation (34), the uncertainty in the spot celerity, ΔC can be determined as:

$$\frac{\Delta C}{C} = \left[\left(\frac{(\Delta x)^2}{x^2} \right) + \left(\frac{(\Delta t)^2}{t^2} \right) + \left(\frac{(\Delta U_\alpha)^2}{U_\alpha^2} \right) \right]^{1/2} \qquad (40)$$

Durinng the test, let C is the propagation rate under the free stream velocity at 0.17 m/s. Thus, U can be directly obtained as 0.17×C m/s. The uncertainty in x can be obtained from a pixel as 0.000432 m for the technique of coating liquid crystals while 0.000304 m for the technique of dye solution. The uncertainty in t is 0.04 s. Also, ΔU_α can be achieved as 0.0006 m/s from the calibration chart of the turbine flow meter series 143 from Nixon Instrumentation Company. Therefore, the sample of the calculated uncertainty in the propagation rate at leading edge, trailing edge, and the end of becalmed region are shown as in appendix table 1.

Appendix Table 1 The spot celerities and their uncertainties

Results from	C_{LE}	C_{TE}	C_{BC}
Coating liquid crystals	0.74 ± 0.03	0.57 ± 0.02	0.33 ± 0.01
Milk and liquid crystals solutions	0.84 ± 0.03	0.54 ± 0.02	-

It is known that the turbulent spot spreading half angle, α, can be determined from:

$$\alpha = \tan^{-1}\left(\frac{z}{x}\right) \tag{41}$$

Now f = $\tan^{-1}(z/x)$. The derivertive of the half spreading angle can be ontained by:

$$\frac{\partial f}{\partial z} = \frac{1}{1+\left(\frac{z}{x}\right)^2}\left(\frac{1}{x}\right) \quad \text{and} \quad \frac{\partial f}{\partial x} = \frac{1}{1+\left(\frac{z}{x}\right)^2}\left(-\frac{z}{x^2}\right) \tag{42}$$

Thus, the uncertainty in the spreading angle can be determined from equation (30) as:

$$\Delta f = \left(\left(\frac{1}{1+\left(\frac{z}{x}\right)^2} \right)^2 \left(\frac{1}{x}\right)^2 (\Delta z)^2 + \left(\frac{1}{1+\left(\frac{z}{x}\right)^2} \right)^2 \left(-\frac{z}{x^2}\right)^2 (\Delta x)^2 \right)^{1/2} \tag{43}$$

where Δz is equal to Δx. Therefore, appendix table 2 shows the calculated half spreading angles, achieved from both the coating liquid crystal and the dye solution techniques and their uncertainties.

Appendix Table 2 The spot spreading half angle and their uncertainties

Results from	Spot spreading half angle, α (degrees)
Coating liquid crystals	6.8 ± 0.02
Milk and liquid crystals solutions	6.8 ± 0.02

CURRICULUM VITAE

NAME : Mr. Weerachai Chaiworapuek

BIRTH DATE : April 24, 1982

BIRTH PLACE : Chantaburi, Thailand

EDUCATION :

YEAR	INSTITUTE	DEGREE/DIPLOMA
2004	Kasetsart University	B.Eng. (Mechanical)
2006	Trinity College, Ireland	M.Sc. (Mechanical)
2007	INSA-Lyon, France	Engineering Diploma